

# QUANTUM METROLOGY WITH CONTINUOUS MEASUREMENTS



ALEXANDER HOLM KIILERICH

PHD THESIS  
OCTOBER 2018

SUPERVISOR: KLAUS MØLMER

DEPARTMENT OF PHYSICS AND ASTRONOMY  
AARHUS UNIVERSITY



*To Leif, be all you can be.*



# English summary

The recruitment of quantum effects holds the potential to revolutionize the precision and applicability range offered by state-of-the-art sensors and measurement devices, and thereby to facilitate profound advancements in all branches of science and in our technology-based society. Quantum metrology is concerned with the theoretical and experimental aspects of this development, and with the recent advances in our abilities to manipulate, control and measure single quantum systems, its theoretical ideas are now more relevant than ever.

This PhD thesis addresses several facets of quantum metrology with a main focus on the very special role played by the measurement process in quantum theory. When a quantum system is measured, its state collapses to be consistent with the outcome. It is crucial to take this measurement backaction into account if a quantum probe system is repeatedly measured or if it is continuously monitored. We show how this may be achieved in different settings and our quantification of the measurement precision reveals that backaction can be either beneficial or detrimental to the estimation sensitivity in different circumstances. The thesis then proceeds to theorize how a measurement controlled feedback, designed to cancel the backaction, allows a topological transition in a quantum system to be observed, and how an adaptive scheme induces a Lévy flight which quickly converges to identify a dark resonance in a quantum system. Next, it presents a highly sensitive quantum thermometer which lets the sensor system, directly interacting with the thermal reservoir of interest, coherently transduce information to a second meter system, used in the read-out process. The closing inquiry reports how, in experiment and in theory, it is possible to enhance the sensitivity in magnetic resonance detection by squeezing the uncertainty in the microwave environment of a spin ensemble. I conclude by discussing some promising research directions and ideas inspired by the results presented in this thesis.

# Dansk resumé

Rekrutteringen af kvanteeffekter har potentiale til at revolutionere præcisionen og de mulige anvendelser af vores mest avancerede sensorer og måleapparater og derved til at bane vejen for betydningsfulde fremskridt i alle videnskabelige grene og i vores teknologibaserede samfund. Feltet kvantemetrologi undersøger teoretiske og eksperimentelle aspekter af denne udvikling og med de nylige fremskridt i vores evne til at manipulere, kontrollere og måle enkelte kvantesystemer, er dets teoretiske idéer nu mere relevante end nogensinde.

Denne PhD-afhandling adresserer en række facetter af kvantemetrologi med et hovedfokus på måleprocessens helt specielle rolle i kvanteteori. Når et kvantesystem måles, kollapser dets tilstand for at blive konsistent med resultatet, og hvis et kvanteprobeksystem måles gentagne gange eller observeres kontinuert, er det således afgørende at tage højde for denne måleforstyrrelse. Vi viser her, hvordan dette kan gennemføres i forskellige sammenhænge og vores kvantificering af målepræcisionen afslører, at måleforstyrrelsen kan være enten gavnlig eller ødelæggende for estimeringssensitiviteten under forskellige omstændigheder. Afhandlingen beskriver desuden, hvordan et målekontrolleret feedback kan designes til at ophæve måleforstyrrelsen og derved gøre det muligt at observere en topologisk overgang i et kvantesystem, og hvordan en adaptiv protokol inducerer en Lévy afsøgning, der hurtigt konvergerer til at identificere en mørk resonans i et kvantesystem. Dernæst præsenteres et højsensitivt kvantetermometer, som virker ved, at et sensorsystem i direkte kontakt med det termiske bad, kohærent overfører information til et metersystem, hvilket benyttes i udlæsningsprocessen. Den afsluttende undersøgelse rapporterer, hvordan det både i et eksperiment og teoretisk er muligt at øge sensitiviteten i magnetisk resonans detektion ved at klemme usikkerheden i et spinsystems mikrobølgeomgivelser. Jeg konkluderer med en diskussion af en række lovende forskningsretninger og idéer inspireret af resultaterne præsenteret i denne afhandling.

# Preface

This thesis presents the main scientific results that I have obtained during my PhD studies at the Department of Physics and Astronomy at Aarhus University, Denmark. My studies were funded by the Villum Foundation and further backed by an *Elite Research* travel grant from the Danish Ministry of Higher Education and Science. The research was conducted in the period between August 2014 and September 2018 under the supervision of Professor Klaus Mølmer. In addition, I stayed for three months during the spring of 2018 with the group of Professor Vittorio Giovannetti at Scuola Normale Superiore (SNS) in Pisa, Italy.

The next pages provide a list of my publications. A significant part of this thesis is reproduced directly from these, and each chapter begins with an explicit account of the replicated material. The results presented in the articles [1] and [2] represent research started during my undergraduate studies. As such they helped define my PhD project and will be presented in detail. Publications [3–5, 9–11] refer to projects between myself and my supervisor Klaus Mølmer, and these manuscripts will be incorporated in this thesis with only a few modifications to fit into a coherent thesis setup. During 2016 and 2017, I collaborated with a visiting PhD student, Peng Xu from Nanjing University in China. I acted to some extent as his co-supervisor during his stay, and our work resulted in the article [6] of which I am a main contributor. This paper is likewise reproduced as a chapter with only a few paragraphs rearranged.

The paper [7] stems from an experimental collaboration with the group of Professor Kater Murch at Washington University in St. Louis, USA. I have contributed with theoretical modelling and simulations but that study is at perimeter of the topic of this thesis so due to constraints of length it will not be covered in much detail. The same goes for the preprint [12] which covers the results of a project with the group of Professor Jacob Sherson at Aarhus University where I have been mainly involved in discussions and a few calculations along the way. The readers are, however, encouraged

to explore the two manuscript in the expectation that they shall find the topics enthralling.

Since the early stages of my PhD studies, I have been interacting with the experimental *Quantronics* group, headed by Professor Patrice Bertet at Université Paris-Saclay in France. This has resulted in the paper [8], reporting an experiment performed by the group on which I have been involved in the formulation of a theoretical model. The ideas, results and theoretical background of this experiment are incorporated in a chapter while non-essential experimental details are omitted.

My final publication [13] represents the outcome of my research at SNS with Vittorio Giovanttti and Antonella De Pasquale. I have been the main engine in this project and the article will be reproduced in a chapter with very minor modifications.

## Acknowledgements

During my time at Aarhus University and my PhD study, it has been my privilege to interact and enjoy good times with a great number of extraordinary people, and for this I am truly grateful. As I extend my thanks, I am bound to fail in mentioning all of them by name, lest this becomes a book of gratitude rather than a PhD thesis.

First of all, I would like to thank my supervisor Klaus Mølmer whose door, despite his busy schedule, is always open. His inquisitive mind and amazing understanding of the broad spectrum spanned by physics have been invaluable in our discussions and in the unfolding of our projects. More than that, he is simply a very nice person; always in a jolly mood, prepared to help with anything and ready with an (in)appropriate anecdote. My thank goes also to Patrice Bertet and Audrey Bienfait for arranging my visit at their lab at CEA Saclay and involving me in the exciting discussions and analyses of their experiment which have helped me develop a deeper understand of the experimental aspects of our field of research. I am likewise thankful to Vittorio Giovannetti for hosting me in his group at SNS, and whose sharp mind directed my research there towards truly interesting results. In addition, I thank his group for inspiring discussions on physics but even more for making my stay in Pisa a motivating and enjoyable experience.

The next gratitude is directed at my colleagues and friends at the institute. In particular, I am grateful to Felix Motzoi, Eliska Greplova, Lukas Buchmann, Jens Bækthøj, Jinglei Zhang, Ottó Eliasson, Jens Jakob

Sørensen, Jørgen Rørstad, Anders Justesen, Kenneth Hansen, Kristian Trelborg, Kamanasish Debnath, Philip Blocher, Albert Benseny, Nikolaj Ravn, Izhak Cohen and Kristoffer Theis Skalmstang for the wonderful mixture of joyful shenanigans and thoughtful discussions on heaven and earth and everything in-between. You guys and gals are rad. I thank also Grete Flarup for her help with everything administrative but even more so for the warm atmosphere she induces on the sixth floor. Additionally, I thank my mother for providing the illustration on the cover of this thesis.

My final and unbounded gratefulness is directed at Helene and Leif, not only for preparing my lunch box on a daily basis but much more for simply being my favourite human beings. Your company in life is my greatest privilege and my inspiration.

*Alexander Holm Kiilerich*  
Aarhus, October 2018

## List of Publications

- [1] A. H. Kiilerich and K. Mølmer, Estimation of atomic interaction parameters by photon counting, *Phys. Rev. A* **89**, 052110 (2014).
- [2] A. H. Kiilerich and K. Mølmer, Parameter estimation by multichannel photon counting, *Phys. Rev. A* **91**, 012119 (2015).
- [3] A. H. Kiilerich and K. Mølmer, Quantum Zeno effect in parameter estimation, *Phys. Rev. A* **92**, 032124 (2015).
- [4] A. H. Kiilerich and K. Mølmer, Bayesian parameter estimation by continuous homodyne detection, *Phys. Rev. A* **94**, 032103 (2016).
- [5] A. H. Kiilerich and K. Mølmer, Random search for a dark resonance, *Phys. Rev. A* **95**, 022110 (2017).
- [6] P. Xu, A. H. Kiilerich, R. Blattmann, Y. Yu, S.-L. Zhu, and K. Mølmer, Measurement of the topological Chern number by continuous probing of a qubit subject to a slowly varying Hamiltonian, *Phys. Rev. A* **96**, 010101 (2017).

- [7] D. Tan, N. Foroozani, M. Naghiloo, A. H. Kiilerich, K. Mølmer, and K. W. Murch, Homodyne monitoring of postselected decay, *Phys. Rev. A* **96**, 022104 (2017).
- [8] A. Bienfait, P. Campagne-Ibarcq, A. H. Kiilerich, X. Zhou, S. Probst, J. J. Pla, T. Schenkel, D. Vion, D. Esteve, J. J. L. Morton, et al., Magnetic resonance with squeezed microwaves, *Phys. Rev. X* **7**, 041011 (2017).
- [9] A. H. Kiilerich and K. Mølmer, Relaxation of an ensemble of two-level emitters in a squeezed bath, *Phys. Rev. A* **96**, 043855 (2017).
- [10] A. H. Kiilerich and K. Mølmer, Multistate and multihypothesis discrimination with open quantum systems, *Phys. Rev. A* **97**, 052113 (2018).
- [11] A. H. Kiilerich and K. Mølmer, Hypothesis testing with a continuously monitored quantum system, *Phys. Rev. A* **98**, 022103 (2018).
- [12] J. J. Sørensen, M. Dalgaard, A. H. Kiilerich, K. Mølmer, and J. Sherson, Quantum control with measurements and quantum Zeno dynamics, arXiv preprint arXiv:1806.07793 (2018).
- [13] A. H. Kiilerich, A. De Pasquale, and V. Giovannetti, A dynamical approach to ancilla assisted quantum thermometry, arXiv preprint arXiv:1807.11268 (2018).

# Contents

<b>Preface</b>	<b>iii</b>
<b>1 Introduction and outline</b>	<b>1</b>
1.1 Measurement backaction . . . . .	3
1.2 Hypothesis testing . . . . .	7
1.3 Quantum thermometry . . . . .	8
1.4 Squeezing . . . . .	8
<b>2 Estimation theory and quantum measurements</b>	<b>11</b>
2.1 Bayes rule and Fisher information . . . . .	12
2.1.1 Bayesian analysis of a measurement record . . . . .	14
2.2 Monitoring an open system . . . . .	16
2.2.1 Photon counting and homodyne detection . . . . .	18
2.2.2 Precision and Fisher information . . . . .	22
2.3 Quantum Fisher information . . . . .	23
2.3.1 QFI of an open system . . . . .	25
2.4 Outlook . . . . .	27
<b>3 Photon counting</b>	<b>29</b>
3.1 Fisher information of counting signals . . . . .	30
3.2 Waiting time distributions . . . . .	33
3.3 Achieving the Cramér Rao bound . . . . .	36
3.4 Examples . . . . .	37
3.4.1 Rabi frequency estimation . . . . .	37
3.4.2 Photon counting from a laser driven $\Lambda$ -type atom . . . . .	40
3.5 Conclusion . . . . .	46
<b>4 Homodyne detection</b>	<b>47</b>
4.1 Quantum trajectories for homodyne detection . . . . .	48
4.2 Fisher information and Bayesian inference . . . . .	50

4.3	Properties of the homodyne signal . . . . .	53
4.3.1	Two-time correlations . . . . .	54
4.3.2	Fisher information from two-time correlations . . . . .	54
4.3.3	Achieving the Cramér-Rao Bound with a linear filter . . . . .	57
4.3.4	Rabi frequency estimation . . . . .	58
4.3.5	Finite detector efficiency . . . . .	60
4.4	Conclusion and outlook . . . . .	62
<b>5</b>	<b>Quantum Zeno effect in parameter estimation</b>	<b>63</b>
5.1	Fisher information of projective measurement records . . . . .	64
5.2	Zeno inhibited evolution . . . . .	67
5.3	QZE and Fisher information for a probed two-level system . . . . .	68
5.4	Examples . . . . .	69
5.4.1	Driven system with no dephasing . . . . .	69
5.4.2	Driven system with dephasing . . . . .	72
5.5	Bayesian inference . . . . .	75
5.6	Conclusion and outlook . . . . .	77
<b>6</b>	<b>Continuous measurement of a Berry curvature</b>	<b>80</b>
6.1	Topology in quantum mechanics . . . . .	82
6.1.1	A topological transition in a qubit system . . . . .	83
6.2	Continuous measurement of the Berry curvature . . . . .	85
6.2.1	Measurement backaction . . . . .	85
6.3	Including a feedback . . . . .	89
6.3.1	Numerical verification . . . . .	91
6.4	Conclusion . . . . .	92
<b>7</b>	<b>Random search for a dark resonance</b>	<b>93</b>
7.1	Atomic model and trajectory analysis . . . . .	95
7.2	Lévy statistical analysis . . . . .	97
7.2.1	Trapped proportion . . . . .	99
7.2.2	Asymptotic frequency distribution and estimation sensitivity . . . . .	99
7.3	Comparison to a systematic scan . . . . .	101
7.4	Outlook . . . . .	104
<b>8</b>	<b>Multihypothesis discrimination</b>	<b>106</b>
8.1	Optimal state discrimination . . . . .	108
8.2	Hypothesis testing with open quantum systems . . . . .	109
8.2.1	A two-sided master equation for the state overlaps . . . . .	110

8.2.2	Low dimensional representation of states of the system and its environment . . . . .	113
8.3	Examples . . . . .	114
8.3.1	Phase of a Rabi drive . . . . .	114
8.3.2	Number of atoms inside a cavity . . . . .	115
8.3.3	Relative positions of a dopant ion . . . . .	117
8.4	Conclusion and outlook . . . . .	120
<b>9</b>	<b>Continuous monitoring in hypothesis testing</b>	<b>121</b>
9.1	Bayesian analysis for hypothesis testing . . . . .	124
9.1.1	Supplementing continuous monitoring by a projective measurement . . . . .	124
9.2	Numerical investigations . . . . .	127
9.2.1	Error probabilities under different detection models	127
9.2.2	Finite detector efficiency . . . . .	129
9.3	Conclusion and outlook . . . . .	131
<b>10</b>	<b>Ancilla assisted quantum thermometry</b>	<b>134</b>
10.1	Model . . . . .	136
10.1.1	Including a meter system . . . . .	138
10.2	Quantum Fisher information . . . . .	139
10.2.1	Example: Two-level meter . . . . .	140
10.2.2	A multi-level meter system . . . . .	145
10.3	Temperature dependence in the Liouvillian spectrum . . . . .	146
10.4	Conclusion . . . . .	149
<b>11</b>	<b>Magnetic resonance with squeezed microwaves</b>	<b>150</b>
11.1	Magnetic resonance detection and experimental setup . . . . .	152
11.2	Theoretical model . . . . .	154
11.3	Experimental results . . . . .	158
11.3.1	Characterization of the squeezer . . . . .	158
11.3.2	Squeezing enhanced spin detection . . . . .	161
11.4	Discussion . . . . .	163
11.4.1	Ultimate limits to the sensitivity and squeezing affected spin dynamics . . . . .	163
11.5	Conclusion . . . . .	166
<b>12</b>	<b>Relaxation of a spin ensemble in a squeezed bath</b>	<b>167</b>
12.1	Model . . . . .	169
12.1.1	Heisenberg equations of motion . . . . .	171

12.2 Results . . . . .	174
12.2.1 Mean values and decay rates . . . . .	174
12.2.2 Second moments and Langevin noise . . . . .	178
12.3 Discussion . . . . .	182
<b>13 Conclusion and future directions</b>	<b>184</b>
<b>A Supplemental material for Chapter 6</b>	<b>189</b>
A.1 Feedback master equation and optimal parameters . . . . .	189
A.2 Finite detector efficiency and a simple correction . . . . .	192
<b>B Supplemental material for Chapter 7</b>	<b>194</b>
B.1 Effective emission rate for a laser driven $\Lambda$ -system . . . . .	194
B.2 Broad distributions and Lévy statistics . . . . .	197
B.3 Recycling time distribution . . . . .	198
B.4 Proportion of trapped trajectories . . . . .	199
B.5 Asymptotic frequency distribution . . . . .	201
<b>Bibliography</b>	<b>204</b>

# Introduction and outline

Physics is a science of high precision measurements. By offering an ever-more detailed understand of the fundamental workings of nature, it has throughout history facilitated the devising and engineering of highly accurate instruments which, also beyond the realms of pure physics, have been crucial in the advancement of human knowledge; ranging from medicine and archaeology to the disciplines of astronomy, geology and biology and to chemistry and material sciences.

This development continues, and new scientific discoveries as well as technologies are increasingly reliant on high-precision, sub-microscopic sensing tools. Quantum mechanics offers a promising platform on which to develop such tools, and within recent years, we have acquired the technical capabilities to manipulate and observe single quantum systems in many different settings. In fact, the 2012 Nobel Prize in Physics was awarded for “ground-breaking experimental methods that enable measuring and manipulation of individual quantum systems” [14]. Today, an immense number of research groups around the world routinely perform experiments with and on a wide variety of different physical systems in the quantum regime. Some of the most common platforms are photonic modes, mechanical oscillators, cold atoms, ions, superconducting circuits, vacancy centres in diamond structures and local impurities in different solid-state systems; each of them having their own strengths and weaknesses. This fast-paced development allows us to probe and take advantage of the strange and prodigious mechanisms such as superpositions and entanglement offered by the quantum nature on a fundamental level.

Some studies suggest that evolution has already long ago reached a stage where quantum effects are utilized by biological organisms [15]. For

instance, quantum coherences can benefit transfer of energy in photosynthesis [16–19], while an explanation for the extraordinary navigation skills of migratory birds has been sought in quantum enhanced magnetometry, utilizing entangled spin-pairs for magnetoreception [20]. Whether this shall prove true or not is an open question but it seems certain that, standing at the verge of an era of quantum technologies, our species shall be the first on planet Earth to consciously and deliberately recruit the quantum aspects of nature for our benefit.

In the near future, the maturing of quantum computers promises to deliver, for certain tasks, computational powers on scales unavailable today [21–24] and allow simulations of complicated physical and chemical processes which are beyond the capacity of classical computation devices [25–27]. Additionally, quantum mechanics allows secure cryptography [28] and communication channels [29, 30] and even batteries based on quantum mechanical systems are being investigated [31, 32]. At the same time, the extraordinary sensitivity of single atoms and atom-like systems such as mechanical oscillators and nano-scale superconducting circuits [33–35] to minute variations in local fields and temperatures are being exploited in quantum sensor devices with spatial resolution on the nanometre scale [36–43]. The eminent emergence of such devices will expand the range of possible inquiries and experiments in many different branches of science. A few examples where they already emerge are in biological imaging and sensing [44–46], in astronomy for gravitational wave detection [47–51] in magnetometry [52–58], in spectroscopy [59, 60], in electrometry [61], in accelerometers [62, 63] and in far-field imaging with super resolution [64–66]. Beyond that, the devices and gadgets emerging in the technology of today rely heavily on sensing capabilities. Some examples are robotic and automated systems, and in general the so-called *Internet of Things* where our items, houses and appliances are constantly reporting on their surroundings and, disturbingly, on our behaviour. Whether one likes it or not, this development is coming and it begs for smaller and more precise sensors; something which could be supplied by quantum technologies as they move out of the laboratory and into industry [67, 68].

The growing field concerned with the theoretical and experimental development of quantum systems and quantum effects for precision sensing and estimation is denoted *quantum metrology* [33, 69, 70]. Its core idea is to encode unknown quantities or parameters in the states of quantum systems. The problem of learning such parameters is then a matter of discriminating states corresponding to their different possible values. A chief goal of quantum-enhanced metrology is to go beyond the classical (shot-noise),

$1/\sqrt{N}$  ( $1/\sqrt{T}$ ) scaling of the statistical estimation error with the number of physical resources  $N$  or effective probing time  $T$ . For instance, injecting an entangled state of  $N$  photons allows an error proportional to  $1/N$  (the so-called Heisenberg limit) in interferometric measurements [34], just like the error in estimating a parameter, unitarily encoded during a time  $T$  in a closed quantum probe, scales as  $1/T$  [71]. The advantage in the latter case can be ascribed to the existence of quantum coherences in the probe system. Even so, it is complicated to prepare entangled states of many particles by non-probabilistic means and real systems are prone to decoherence due to environmental interactions; two problems which often dismiss the advantages in scaling [72–74]. See [75] for a recent review of metrology with open quantum systems. As a consequence, quantum enhanced scaling has this far only been achieved in proof-of-principle experiments with limited values of  $N$  (e.g. [76–78]) or  $T$  [79]. Instead, at the present stage of quantum technologies, it seems that a more realistic, albeit less stirring, goal for near-future applications is to seek quantum enhancement of the front-factor in the scaling; see, e.g., [72, 80]. Notice, however, that some success has been reported in restoring the advantageous Heisenberg scaling in open systems by quantum error correction [81–84] or dynamical decoupling pulses [85], and that circumstances exist where it is possible to explicitly correct errors by observing quanta emitted into the environment [86, 87]. What’s more, the Heisenberg limit in phase estimation has been demonstrated by adaptive measurements strategies, not relying on quantum entanglement [88].

During my PhD study, I have touched upon several different aspects of the field of quantum metrology, and this thesis presents a collection of my humble contributions to its advancement. Next, I shall give an outline of my research results and their appearance in the chapters.

## 1.1 Measurement backaction

Measurements hold a defining role in quantum mechanics. The theory provides statistical predictions for the outcomes of measurements performed on any quantum system, and the exclusion of simultaneous measurements of non-commuting observables limits the extractable information. However, measurements play an even more intricate role. In the Copenhagen interpretation, the quantum state represents our knowledge of a physical system, and any observation of such a system entails an update of the state consistent with the outcome. This measurement *backaction* influences

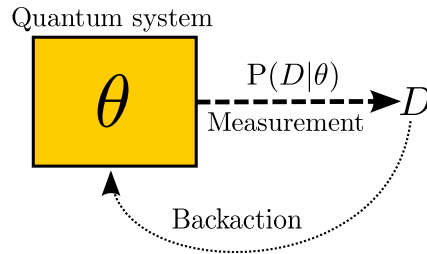


Figure 1.1: A measurement on a quantum system yields an outcome  $D$  with a probability  $P(D|\theta)$ , reflecting an unknown parameter  $\theta$ . The specific outcome causes a backaction on the system which affects the distribution  $P(D'|\theta)$  of subsequent measurement outcomes  $D'$ .

the statistics of subsequent measurements on the same system, and one may say that, in this sense, quantum measurements both extract and create information [see Fig. 1.1]. A detailed understanding of this essential quantum effect and how it may be utilized is highly beneficial in quantum metrology applications, and several of my contributions [1–6, 11] are indeed focused on this topic.

In Chapter 2, I begin by providing an introduction to some core concepts in estimation theory with a focus on measurements on quantum systems. This Chapter does not represent an original formulation from my part, but rather a brief review of my understand of these subjects, acquired during my PhD study. It will serve as a reference in the following chapters, containing my own contributions. The chapter introduces a Bayesian formulation of quantum estimation theory and the Fisher information which via the Cramér-Rao bound quantifies the ultimate precision limit. It then combines this with the notion of measurement backaction with a special focus on quantum systems subject to continuous monitoring by, e.g., a photon counter or a homodyne demodulator and provides a couple of illustrative examples.

The backaction quenches the state of a probe system subject to continuous or repeated measurements, resulting in a detection record which is correlated in time. The correlations are often advantageous for sensing or estimation [1, 2, 4, 5, 11, 89–93], but at they same time they make the evaluation of the associated Fisher information a non-trivial task. In Chapter 3 based on [1] and [2] and Chapter 4 based on [3], I show how this evaluation may be accomplished for continuous counting-type and diffusion-type measurements on a quantum probe system. The theory

is exemplified by considering the estimation of parameters governing the evolution of simple systems with two or three levels, and the effects of finite detection efficiency on the estimation precision are discussed. A similar advantage of measurement induced quenches on many-body systems for spectroscopy was recently identified [94].

Another ramification of the backaction is the possibility to realize Zeno's arrow paradox in the quantum world: The evolution of a quantum system may be frozen by the backaction of frequent, strong measurements [95, 96]. In Chapter 5 based on [3], it investigated how this quantum Zeno effect interferes with our ability to retrieve information about parameters, governing the dynamical evolution, from frequent measurements. While the quantum Zeno effect should be avoided at all costs in an isolated quantum system, a trade-off situation is identified for an open system, experiencing a dephasing with time: The quench of the state associated with the backaction rephases the system, but at the same time too frequent measurements freeze the dynamics and do not allow a dynamical encoding of the unknown parameter. This is a consequence of the fundamental relationship between distinction and disturbance of quantum systems by measurements [97, 98]

Similarly, the backaction can be problematic if one is concerned with recording the unitary evolution of a system in the absence of measurements. In Chapter 6 based on [6], we consider an example of this where the purpose is to track the state of a simple toy-model as it undergoes a topological transition by continuously observing the system. The measurement backaction inevitably alters this dynamics and hence inhibits the observation of the transition but we show that by a detailed analysis of the backaction, it is possible to implement a measurement feedback which restores the original evolution, thus allowing the transition to be observed.

The trajectories of quantum systems, evolving conditioned on the outcomes of measurements, have been observed experimentally [7, 99–101]. Studies of their statistical behaviour from a thermodynamic perspective by means of large deviation theory for both jump-type [102] and diffusion-type stochastic dynamics [103] emphasize how single and statistically rare trajectories may exhibit behaviour which is very different from the mean. This is, for instance, evident in the experiments reported in Refs. [7, 100], where a superconducting qubit, monitored by homodyne or heterodyne detection of its emission signal while it decays, evolves in a strikingly different manner than the unconditional, exponential decay. I have been involved in the theoretical modeling and supplementary simulations of the experiment reported in [7]. Just like a quantum state  $\rho(t)$  is conditioned

on measurements outcome obtained at earlier times  $t' < t$ , measurements performed at later times  $t'' > t$  also teach us about the system at the earlier time  $t$ . In general, the combined record of past and future measurements allow better predictions for the possible outcomes of a hypothetical measurement performed at the time  $t$ . This is the idea in the *Past Quantum State* formalism [104], and the experiment reported in [7] studies this mechanism for a decaying qubit, subject to continuous monitoring and a final postselection measurement. The experiment verifies the theory and simulations which show that while individual trajectories behave in a stochastic manner, the system density matrix is at all times restricted to the surface of a deterministic, time-evolving ellipsoid on the Bloch sphere, and that the same applies to the information available from future measurement outcomes, including the postselection. The trajectory mean is not contained on these surfaces which highlights the substantial deviation of individual trajectories from the ensemble average. Since their topic is one of fundamental interest rather than quantum metrology, these results shall not be explained in further detail here, but the inspired reader should examine the article [7].

As emphasized above, understanding the evolution of a quantum system on a single trajectory level rather than by an ensemble average facilitates profound advantages in sensing applications. At the same time, it allows measurement backaction to be used as a tool in quantum control. One example from my work is Ref. [12], where we show how a target state in a many-body system may be efficiently reached by a combination of unitary dynamics and tailored measurements. The protocol combines that of Ref. [105] with intelligent employment of the quantum Zeno effect to lock subsets of the Hilbert space where the populations correspond to the right target state. Quantum control is beyond the theme of this thesis and Ref. [12] will not be covered in any detail.

Another place, where the quantum trajectory picture may constitute an enlightening guide, is in the devising of non-conventional estimation and sensing protocols. An example of such a protocol is presented in Chapter 7 based on [5], where we consider the precise identification of a dark resonance in a three-level system driven by two laser fields. Conventional methods perform this task by recording the fluorescence during a systematic scan of the laser frequency over the relevant range. We propose to instead perform a random search in which the frequency of one of the lasers is shifted randomly every time a fluorescence photon is detected. At resonance, destructive interference causes the system to enter a dark state where it ceases to absorb and re-emit photons. Our analysis shows that the

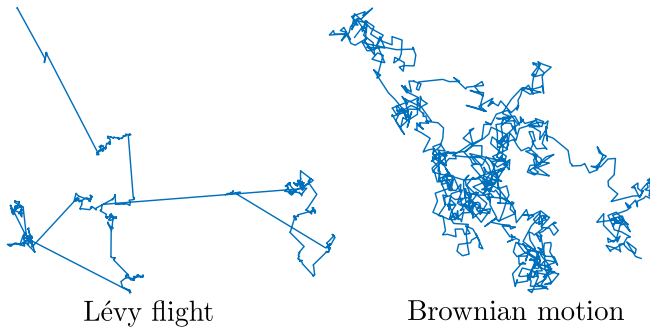


Figure 1.2: Contrary to Brownian motion, a Lévy flight is dominated by a few, very long steps.

trajectory of the system state and of the laser frequency describes a Lévy flight [see Fig. 1.2] which brings the laser frequency close to the resonance such that it composes a precise estimator. Due to the nonergodic evolution, the scaling of the precision with time does not follow from the conventional Cramér-Rao bound which relies on asymptotic normality, but a Lévy statistical analysis shows that with efficient photo detectors our protocol outperforms a systematic scan.

## 1.2 Hypothesis testing

Helstrom [106] formulated one of the founding question in the field of quantum information as he considered the ultimate distinguishability of distinct quantum states. This is among many places important for quantum communication channels [29, 107] and in metrology, quantum hypothesis testing is formally a problem of discriminating states evolved under different candidate Hamiltonians. If the probe is an open system, the ultimate discrimination capability is defined by *full* state of a system and its environment. In Chapter 8 based on [10], we show how this capability may be evaluated for any number of distinct Hamiltonian candidates by numerically efficient means. The results are illustrated by three realistic examples of multihypothesis testing with open quantum systems.

The optimal measurement observable, associated with the lower bound on the probability in assigning a false hypothesis based on the outcome, corresponds in general to a highly non-local measurement on a system and its environment and is thus hard to implement in practice. Instead, one

must rely on sub-optimal but experimentally feasible schemes. In Chapter 9 based on [11], we show how one may operate in the vicinity of the bound by combining fluorescence detection with an optimal local measurement on the probe system, designed according the conditional state of the probe which takes the backaction of the fluorescence detection into account. Alternative studies on the application of continuous measurements to hypothesis testing and state discrimination are investigated in Refs. [91, 93, 107].

### 1.3 Quantum thermometry

One of the subfields of quantum metrology which may deliver the most significant impact in other sciences and technology is, arguably, quantum thermometry. Nano-scale quantum devices such as quantum-dots and nitrogen vacancy centres in diamond [36–41], spin systems or mechanical oscillators [42, 43] allow non-invasive temperature readings in the millikelvin range, and experiments have been reported which apply such devices in, e.g., living cells [37, 38]. As a consequence, the field is very active and in recent years a substantial interest has been committed to analysing the properties and design of quantum thermometer devices [108–116]. Still, apart from a few exceptions (e.g. [113]) many of the proposed devices and schemes rely on an incoherent coupling of a quantum probe to the thermal reservoir of interest, see e.g., [108–112]. The unknown temperature is thus encoded in the populations of the probe and not in its quantum coherences, resulting in thermometer devices which are in this sense *classical* and fail to deliver a quantum advantage. In Chapter 10 based on [13], we show how coupling a quantum sensor to an external meter system via a suitable Hamiltonian interaction allows the intrinsically incoherent information on a bath temperature to be mapped from the sensor to coherences in the meter. Apart from delivering an immense gain in sensitivity, this protocol has the advantage that the read-out measurement is performed on the meter which may be situated outside a delicate sample.

### 1.4 Squeezing

The contributions mentioned above and covered in Chapters 2-10 of this thesis are predominantly concerned with the measurement process and the encoding of an unknown quantity in the state of a quantum probe. They focus on the possibility of taking into account and utilizing the quantum nature of measurements, and they show how this nature may constitute an

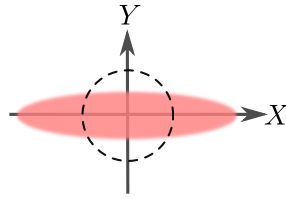


Figure 1.3: A squeezed vacuum state (red ellipse) with fluctuations in the  $Y$  quadrature reduced below vacuum level (dashed circle) at the cost of increased fluctuations in the  $X$  quadrature.

advantage or a downside in different scenarios. A main theme is the role of continuous monitoring of a field interacting with the probe system, and while optimized monitoring and efficient estimation methods allow a high precision to be achieved, the sensitivity is ultimately limited by quantum fluctuations in the field. In particular, two quadratures  $X$  and  $Y$  of a field have uncertainties which are mutually lower bounded by the Heisenberg uncertainty relation,  $\Delta X \Delta Y \geq 1/2$ .

A key idea in the toolbox of quantum metrology is to engineer a state with a reduced or *squeezed* uncertainty in one physical observable, say  $Y$ , at the cost of a corresponding increase in that of the complementary observable  $X$ ; see Fig. 1.3. By encoding the signal of interest in the  $Y$  quadrature, one can hence attain lower uncertainty while the correspondingly larger fluctuations in  $X$  are inconsequential. Squeezing is probably one of the most versatile and promising quantum tools for sensing and metrology. It has been successfully applied for phase measurements in interferometers [117], for spectroscopy [118, 119] and even for biological particle tracking [44]. Furthermore, squeezing is currently active in gravitational wave detectors which rely on an unprecedented sensitivity [47–50].

In Chapter 11 based on [8] we study its use for improved electron spin resonance (ESR) detection. The chapter reports on an experiment performed by Audrey Bienfait *et. al.* at CEA Saclay in France of which I have been involved in the theoretical modelling. A spin ensemble in a microwave resonator undergoes a Hahn echo sequence [120], and a microwave field with squeezed fluctuations shined on one input port allows a 1.2 dB noise reduction in the output signal which contains the spin echo. This allows the detection of as few as a few thousands of spins. Even though the noise reduction is modest, the experiment represents a proof-of-principle of the application of microwave-squeezing for magnetic

resonance detection.

From a theoretical perspective, the success of the scheme depends on two things: i) Injection of a squeezed input should lead to squeezed uncertainties in the output after interacting with the spin ensemble inside the resonator, and ii) The mean output echo signal must remain to a large degree unaltered by the squeezing such that the signal-to-noise ratio increases. We address these issues by performing an input-output analysis of the experiment in the Heisenberg picture [121, 122]. This analysis further allows the assessment of fundamental limitations to the squeezing-induced gain in sensitivity posed by decoherence channels and squeezing-enhanced collective behaviour of the spin-ensemble. The chapter covers my contribution, the theoretical modelling, while only the main points and results of the experiment are explained. The reader is referred to the full manuscript [8] for extended experimental details.

Our theoretical model applies the Holstein-Primakoff approximation [123] to describe the large ensemble of weakly excited spins by an oscillator mode which allows an analytic treatment. Such an approximation is valid for this experiment but it breaks down when considering only a few spins. In the present context of a number of spins embedded in a squeezed reservoir, this becomes apparent in their dynamical evolution. Chapter 12 based on [9] derives a formalism which allows the effect of a broadband squeezed reservoir, collectively coupled to any of number of spins, to be studied. As pointed out by Gardiner [124], the relaxation of the individual components of a single spin are different depending on the degree of squeezing. A large ensemble (for which the Holstein-Primakoff approximation is justified), on the other hand, experiences symmetric transverse relaxation independent of the squeezing. Conversely, for a large ensemble the squeezing of the reservoir is inherited by the second moments and steady-state fluctuations in the transverse spin components while a single spin fluctuates independently of the squeezing. Our theory allows a formal study of the transition between these two regimes as more spins are added, and identifies the difference to be rooted in the relative contributions of vacuum fluctuations and radiation reaction in the effective coupling of the spins to the squeezed environment.

The final Chapter 13 concludes the thesis and discusses a few further directions which could be interesting to pursue from the research presented here.

# Estimation theory and quantum measurements

*Apart from a few new paragraphs, Subsections 2.1.1 and 2.2.1 are reproduced from Ref. [11] with minor changes. The second paragraph of Subsection 2.2.2 is composed of formulations from [3] while the remaining paragraphs in this subsection are new. Figures 2.2 and 2.4, including their captions, are taken from Refs. [3] and [4], respectively.*

---

When analysing state of the art experiments or designing high precision technologies such as field sensors and nanoprobe, an optimal statistical treatment of the recorded measurement data is of the utmost importance. Nevertheless, many applications rely on somewhat rudimentary methods, focusing for instance on mean signals or spectral components, while ignoring the information held by higher moments and temporal correlations. This is detrimental to the precision, as emphasized by a number of enquiries on their importance in quantum metrology and sensing [1, 2, 4, 5, 11, 89–93, 125].

A proper treatment, taking all available information in a given signal into account, is offered by the method of Bayesian inference which may be applied to *any* signal. This chapter introduces the Bayesian method in the context of quantum parameter and the Fisher information which quantifies its asymptotic estimation precision. The focus will be on quantum probes

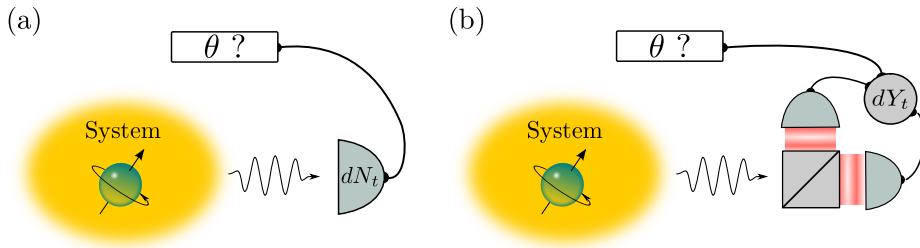


Figure 2.1: (a) The radiation emitted by a probe system for a time  $T$  is monitored by (a) a photon counter or (b) a homodyne demodulator, and the most likely value of the unknown parameter  $\theta$  is inferred from the recorded signal.

subject to a sequence of measurements or continuous monitoring; see Fig. 2.1.

In such settings, the backaction associated with quantum measurements induces a (conditional) transient evolution, and a sophisticated analysis is crucial to collect the information held by the corresponding correlations in the signal recording. One example is photon counting where long time averages over the number of fluorescence photons from an atom are identical for two strong laser driving fields. Yet, the distribution of time-intervals between subsequent emission events exhibits distinct oscillations for each field intensity [126], thus allowing their discrimination.

Recent experiments with superconducting qubits [7, 99, 100, 127] and optomechanical systems [128] have observed the conditioned evolution of quantum systems subject to continuous monitoring. At the same time, several works have been devoted to the formulation of data-processing methods which take quantum backaction into account in different measurement settings and with probe systems of various nature [1–4, 56, 89, 90, 92, 129, 130].

## 2.1 Bayes rule and Fisher information

Measurements on physical systems yield probabilistic outcomes, and the estimation of physical parameters, describing a system or governing its evolution, is a problem of statistical inference. The source of statistical errors can be related to imperfections in the experiment or read-out measurements, or it can be more fundamental, dictated by, e.g., Heisenberg's uncertainty relations in a quantum setup. The value of an unknown parameter  $\theta$  is thus assigned a probability distribution  $P(\theta)$ , which upon

performing a measurement on the system and recording a result  $D$  is updated according to Bayes rule,

$$P(\theta|D) = \frac{P(D|\theta)P(\theta)}{P(D)}, \quad (2.1)$$

where  $P(D|\theta)$  is the probability of obtaining the outcome  $D$  conditioned on the value of the unknown parameter, and  $P(D) = \int d\theta P(D|\theta)P(\theta)$  is a normalizing factor. From the updated probability density  $P(\theta|D)$ , an estimator  $S_\theta(D)$  for  $\theta$  is constructed.

The efficiency of any measurement protocol hence depends on the degree to which the distribution  $P(D|\theta)$  of the outcome  $D$  is affected by the unknown physical parameter  $\theta$ . The sensitivity of this distribution to infinitesimal variations in the value of  $\theta$  is quantified by the (classical) Fisher information [131],

$$\mathcal{I}(\theta) = \mathbb{E} \left[ \left( \frac{\partial \ln P(D|\theta)}{\partial \theta} \right)^2 \right], \quad (2.2)$$

where  $\mathbb{E}[\cdot]$  denotes the expectation value with respect to independent realizations of the detection record  $D$ .

By the Cramér-Rao bound (CRB) [132], the Fisher information defines a lower bound on the variance  $[\Delta S_\theta(D)]^2$  on any unbiased estimator,

$$[\Delta S_\theta(D)]^2 \geq \frac{1}{K\mathcal{I}(\theta)}, \quad (2.3)$$

where  $K$  is the number of independent repetitions of the measurement. The most probable value of  $\theta$ , conditioned on the measurement outcome  $D$ , constitutes an optimal estimator,  $S_\theta(D) = \max_\theta [P(\theta|D)]$  which saturates the CRB if the prior probability density  $P(\theta)$  is uniform [131]. Bayes rule (2.1) thereby provides an optimal data analysis in any parameter estimation problem.

In the general case,  $\theta \equiv \{\theta_n\}_n$  may represent a set of several unknown parameters  $\theta_n$ . The Fisher information is then a matrix with elements  $\mathcal{I}_{nm}(\theta) = \mathbb{E} \left[ \frac{\partial \ln P(D|\theta)}{\partial \theta_n} \frac{\partial \ln P(D|\theta)}{\partial \theta_m} \right]$ , and the CRB represents a lower bound on the covariance in estimating pairs of parameters,  $\text{cov}[S_{\theta_n}(D), S_{\theta_m}(D)] \geq 1/[K\mathcal{I}_{nm}(\theta)]$ . For sake of lighter notation and simpler presentation, results in Chapters 3, 4 and 5 of this thesis are formulated for cases with single unknown parameters but note that the analyses are readily generalized to the multi-parameter case.

In quantum mechanics, a physical system is described by its quantum state, represented in general by a density matrix  $\rho$ , and any measurement on a quantum system is associated with a set of measurement operators  $\{\hat{M}_D\}_D$ , which define a positive-operator valued measure (POVM) such that the sum (integral) over all possible outcomes is the identity  $\sum_D \hat{M}_D^\dagger \hat{M}_D = \mathbb{I}$ . In metrology applications, the probe system is allowed to interact with, e.g., the field of interest such that the unknown parameters  $\theta$  are encoded in its state  $\rho_\theta$ . Upon performing a read-out measurement, the corresponding probability factors, assigned the different outcomes  $D$  in Bayes rule (2.1), are given by the Born rule,

$$P(D|\theta) = \text{Tr} \left( \hat{M}_D \rho_\theta \hat{M}_D^\dagger \right). \quad (2.4)$$

The POVM formalism encompasses projective measurements where the  $\hat{M}_D$  denote projection operators as well as more general measurements which can for example be realized by measuring an ancillary system that has interacted with the main system. A very common example of the latter case is monitoring of the quantized electromagnetic field emitted by a quantum probe system [see Fig. 2.1]. The application of measurements of this kind for quantum metrology is a main theme of this thesis and in Sec. 2.2 it is presented in detail.

The probabilistic outcomes of quantum measurements reflect the intrinsic uncertainty which is at the essence of the quantum description of our world. When a measurement is performed and an outcome recorded, our characterization of the quantum system by its state  $\rho_\theta$  is adjusted to be consistent with the observation. This collapse or quantum jump of the quantum state is formalised by the update rule:

$$\rho_\theta \rightarrow \frac{\hat{M}_D \rho_\theta \hat{M}_D^\dagger}{P(D|\theta)}, \quad (2.5)$$

applied to the state upon obtaining a result  $D$ .

### 2.1.1 Bayesian analysis of a measurement record

If for metrology purposes a number of identical copies of a probe system is to be measured once, the measurement *backaction* (2.5) is inconsequential. However, if each copy is not discarded but rather subject to later measurements or continuous monitoring, it is crucial to take the backaction into account as it influences the state and hence via Eq. (2.4) the probability distribution of later outcomes. This section details how

the Bayesian method applies to a continuously monitored or frequently measured quantum probe. For concreteness, we imagine a setup where the undetermined parameter  $\theta$  parametrizes a Hamiltonian  $\hat{H}_\theta$ , governing the (unitary) evolution of the quantum probe.

Consider a system which is being observed from an initial time  $t = 0$  to a final time  $t = T$ . Throughout this period, a signal  $dD_t$  is recorded which, depending on the measurement setup, may take the form of a continuous current as in e.g. homodyne detection or consist of a sequence of outcomes obtained at discrete points in time. By  $D_t$  we denote the full signal obtained between times 0 and  $t$ . Meanwhile, the state of the system  $\rho_\theta^{(D_t)}(t)$  evolves under the influence of the encoding Hamiltonian  $\hat{H}_\theta$  and conditioned on the specific realization of  $D_t$  by the update rule (2.5). Assuming a specific value of the parameter  $\theta$ , any given realization of  $D_t$  has a probability  $P(D_t|\theta)$  determined by Eq. (2.4) from the conditional candidate quantum state  $\rho_\theta^{(D_t)}(t)$ . Bayes rule (2.1) yields the corresponding update of the likelihood  $P(\theta|D_t)$  assigned to each possible parameter value. The methods apply equally to hypothesis testing scenarios where  $\theta$  is restricted to take one of a discrete set of known values, and to parameter estimation where  $\theta$  lies in a continuous range. For numerical purposes, in the latter case the range is discretized on a fine  $\theta$ -grid and Bayes rule (2.1) applied to each point.

Figure 2.2 shows a simulated example of such a procedure, where a resonantly driven two-level system is projectively measured at short intervals with the purpose of discriminating three possible values  $\Omega = 0, 1, 2\Omega_0$  of the Rabi frequency in a Hamiltonian, which in a frame rotating with the driving frequency can be written

$$\hat{H}_\Omega = \frac{\Omega}{2}\hat{\sigma}_x. \quad (2.6)$$

The upper panel depicts the conditional evolution of the quantum state, and the lower panel shows how the Bayesian procedure, upon each measurement, gradually filters the three possible Rabi frequency candidates to favour the true value  $\Omega = \Omega_0$  at the final time  $t = 25\Omega_0^{-1}$ . See Chapter 5 for details.

If the state is not renormalized after application of the POVM backaction operators, we retain the evolution of an unnormalized state  $\tilde{\rho}^{(D_t)}(t)$ ,

$$\tilde{\rho}_\theta^{(D_t)}(t) \rightarrow \hat{M}(dD_t)\tilde{\rho}_\theta^{(D_t)}(t)\hat{M}^\dagger(dD_t), \quad (2.7)$$

whose reduction in norm is just the probability to obtain the signal  $dD_t$ . This implies that at the final time  $T$ , the probability  $P(D_T|\theta) =$

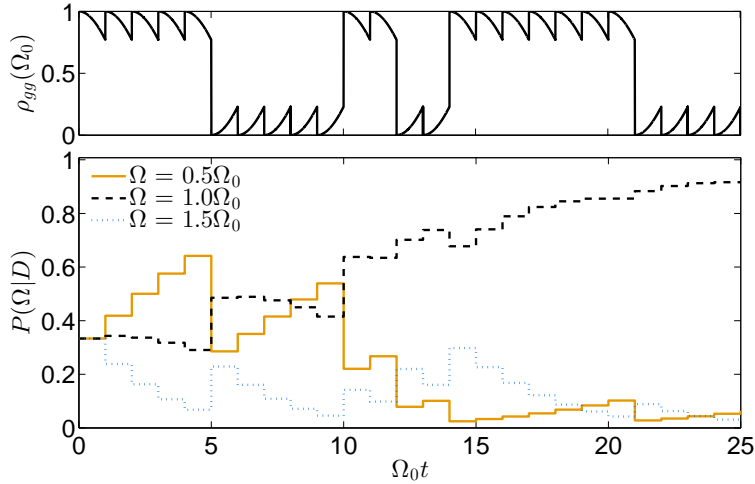


Figure 2.2: The top panel shows the ground state population  $\rho_{gg}(\Omega_0)$  resulting from a quantum trajectory simulation with the true Rabi frequency  $\Omega = \Omega_0$ . The lower panel shows the evolution of the probabilities  $P(\Omega|D)$  for three candidate values of the Rabi frequency, conditioned on the measurement record in the upper plot. Results are shown for projective population measurements performed at intervals  $\tau = \Omega_0^{-1}$ .

$P(dD_T) \cdots P(dD_{2dt})P(dD_{dt})P(dD_0)$  for the full signal  $D_T$  is given by the trace of the unnormalized state,

$$P(D_T|\theta) = \text{Tr} \left[ \tilde{\rho}_\theta^{(D_t)}(T) \right]. \quad (2.8)$$

Hence, by evolving the unnormalized state under each of the possible values of the unknown parameter conditioned on the signal *actually* recorded in a given experiment, one may by Eq. (2.1) obtain the relative likelihoods of each value as  $P(\theta|D_t) \propto \text{Tr}[\tilde{\rho}_\theta^{(D_t)}(t)]$ . Since any specific trajectory for  $D_t$  is extremely unlikely,  $\text{Tr}[\tilde{\rho}_\theta^{(D_t)}(T)]$  becomes very small even for the true value of  $\theta$  and for numerical purposes it is favourable to propagate instead the log-likelihood  $\log[P(\theta|D_t)]$ . See [92] for a detailed account of Bayesian inference with continuously monitored quantum systems.

## 2.2 Monitoring an open system

The state of a closed quantum system evolves in a unitary manner according to a Hamiltonian  $\hat{H}$ . However, in realistic settings environmental

couplings are unavoidable. Assuming that the interaction with a broadband environment validates the Born-Markov approximation, the evolution of the system density operator  $\rho$  is governed by a master equation [133, 134],

$$\frac{d\rho}{dt} = \mathcal{L}\rho, \quad (2.9)$$

where the Liouvillian superoperator may be written in Lindblad form [134] ( $\hbar = 1$ ),

$$\mathcal{L}\rho = -i[\hat{H}, \rho] + \sum_m \mathcal{D}[\hat{c}_m]\rho. \quad (2.10)$$

Here we define  $\mathcal{D}[\hat{c}_m]\rho = \hat{c}_m\rho\hat{c}_m^\dagger - \{\hat{c}_m^\dagger\hat{c}_m, \rho\}/2$  with  $\{\cdot, \cdot\}$  the anti-commutator. The operators  $\hat{c}_m$  represent different relaxation processes associated with environmental interactions. Undetermined parameters may be encoded by the Hamiltonian  $\hat{H}$  or if they relate to interactions of the probe with its environment by the  $\hat{c}_m$ . If the operators are time independent, the solution to Eq. (2.9) is formally given by exponentiation,

$$\rho(t) = e^{\mathcal{L}t}\rho(0). \quad (2.11)$$

For metrology applications, an environmental coupling is not solely a complication. In fact, opening a probe system is in many cases desirable since it allows information to be extracted from an otherwise isolated system by measuring its environment. For instance, the Purcell-enhanced emission signal from atoms or atom-like systems placed in a near-resonant cavity allows their read-out in a timely fashion [135, 136].

If the environment is unobserved, the evolution under Eq. (2.9) relaxes the system to a stationary (steady state)  $\rho^{(\text{ss})}$ , defined as the kernel of the Liouvillian,

$$\mathcal{L}\rho^{(\text{ss})} = 0. \quad (2.12)$$

When the environment is observed however, the master equation is *unravalled* to yield a stochastic evolution of the system conditioned on the specific outcomes, and rather than reaching a steady state, the system exhibits a transient evolution triggered by each detection result. On average these stochastic trajectories reproduce the master equation (2.9), and mean properties of, e.g., an emitted signal are indeed determined from the steady state (2.12). Nonetheless, each individual trajectory may be radically different from the mean (see for example [7, 102, 137]), and higher

moments and correlations in a signal contribute in many cases a much larger information than the mean alone [1, 2, 4, 11, 94]. An interesting, recent experiment monitors the two main decoherence channels of a superconducting qubit, namely decay ( $\hat{c}_m \propto \hat{\sigma}_-$ ) and dephasing ( $\hat{c}_m \propto \hat{\sigma}_z$ ), and contrary to the unconditional evolution given by Eq. (2.9), the observed trajectories reflect the incompatibility of these quantum measurements [127].

### 2.2.1 Photon counting and homodyne detection

For concreteness, we consider in this subsection the cases where the measurements are carried out continuously in time on a radiation field emitted by a quantum system of interest. The two generic setups of counting-type measurements with discrete detection events and diffusion-type measurements with continuous but infinitesimal backaction are discussed, and we outline how the master equation (2.9) and the backaction (2.7) together yield stochastic master equations, suitable for numerical propagation of  $\tilde{\rho}^{(D_t)}(t)$ . For simplicity we assume that there is only a single decay channel but the expressions may readily be generalized to multi-channel cases and alternative environmental couplings.

In Fig. 2.1(a), the fluorescence from the probe system is detected by a photon counter with quantum efficiency  $0 \leq \eta \leq 1$  and the photon counting signal  $N_t$  until time  $t$  constitutes the detection record  $D_t$ . During each short time interval  $dt$  there are two possible detection outcomes: no photon  $dN_t = 0$  or one photon  $dN_t = 1$ , where  $P(dN_t = 1) = \eta \text{Tr}[\hat{c}^\dagger \hat{c} \rho^{(N_t)}(t)] dt$  is given by the (normalized) state  $\rho^{(N_t)}(t)$  of the system. Here  $\hat{c} = \sqrt{\gamma} |g\rangle\langle e|$  denotes the quantum jump operator from an excited  $|e\rangle$  to a lower state  $|g\rangle$  at a rate  $\gamma$ . The conditional evolution of the unnormalized state, in turn, obeys a linear stochastic master equation (SME) [134, 138],

$$d\tilde{\rho}^{(N_t)} = (\mathcal{K}dt + \mathcal{B}dN_t) \tilde{\rho}^{(N_t)}, \quad (2.13)$$

where  $\mathcal{K}\rho = -i[\hat{H}, \rho] + (1 - \eta)\hat{c}\rho\hat{c}^\dagger - \frac{1}{2}\{\hat{c}^\dagger\hat{c}, \rho\}$  and  $\mathcal{B}\rho = \eta(\hat{c}\rho\hat{c}^\dagger - \rho)$ .

Figure 2.3 shows a simulated photon counting record and the associated conditional evolution given by Eq. (2.13) for our two-level example (2.6). The five detection events each resets the atom in its ground state, and we see that between these quantum jumps, the transient evolution is indeed very different from the unconditional evolution of an equivalent unmonitored system given by Eq. (2.9) which quickly approaches a steady state (2.12) with mean excitation  $\rho_{gg} \simeq 0.5$ .

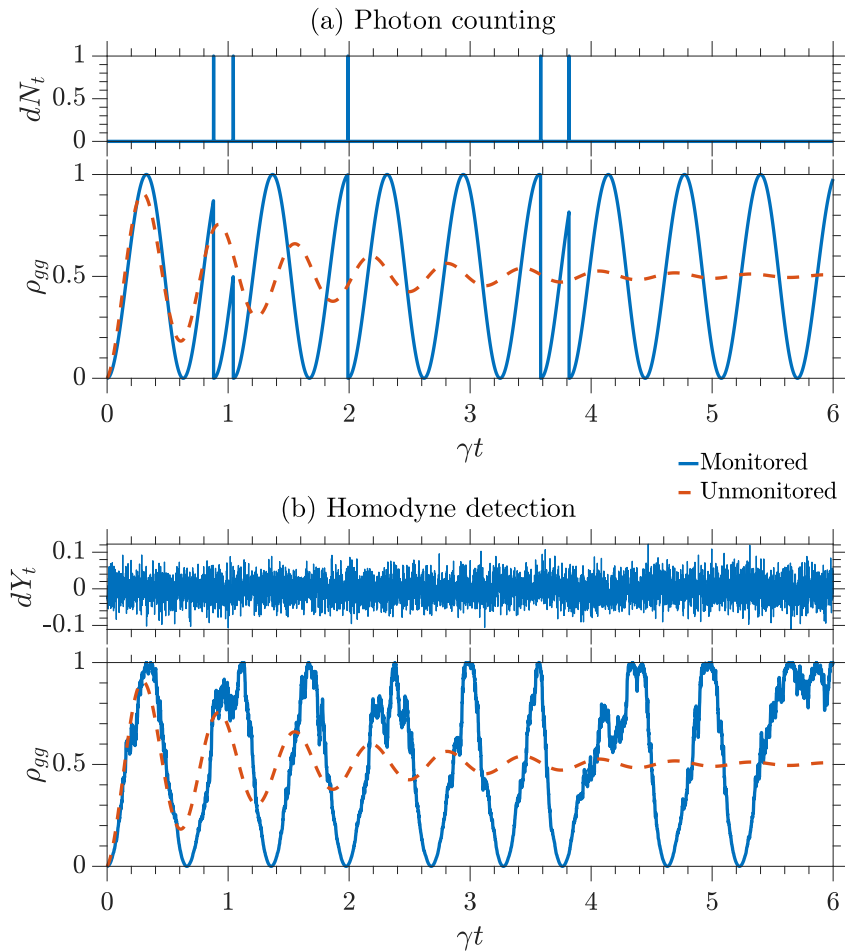


Figure 2.3: The top panels show simulated photon counting (a) and homodyne detection (b) records from a monitored, driven two-level system (2.6). Full lines in the lower panels track the ground state populations  $\rho_{gg}$  of the corresponding conditioned states, evolved according to the normalized versions of (a) Eq. (2.13) and (b) Eq. (2.16). For comparison, the evolution of an equivalent unmonitored system, governed by a master equation (2.9) is depicted as a dashed line. Results are shown for  $\eta = 1$ ,  $\Phi = \pi/2$  and  $\Omega = 10\gamma$ , where  $\gamma$  is the emission rate.

As depicted in Fig. 2.1(b), a homodyne detector mixes the fluorescence with a strong local oscillator field on a beam splitter, and the signal  $dY_t$  is obtained as the intensity difference between the two output ports. Homodyne detection is sensitive to the phase of the emitted radiation which may be favourable when probing certain dynamics of the system. The recorded signal  $dY_t$  in each short time interval  $dt$  has a mean value determined by the current state  $\rho^{(Y_t)}(t)$  of the system,

$$dY_t = \text{Tr}[\mathcal{X}_\Phi \rho^{(Y_t)}(t)]dt + dW_t \quad (2.14)$$

with  $\mathcal{X}_\Phi \rho = \sqrt{\eta} (\hat{c}e^{-i\Phi}\rho + \rho\hat{c}^\dagger e^{i\Phi})$  where  $\Phi$  is the phase of the local oscillator. Detector shot-noise is modelled by random, white-noise fluctuations around the mean and represented by infinitesimal Wiener increments  $dW_t$  which are uncorrelated, normal distributed stochastic elements with zero mean and variance  $dt$  [139],

$$\mathbb{E}[dW_t] = 0 \quad \text{and} \quad dW_t dW_{t'} = \delta(t - t')(dt)^2. \quad (2.15)$$

Since the signal depends only weakly on the state of the system, the back-action associated with homodyne detection is infinitesimal and Eq. (2.7) is equivalent to a diffusion-type linear stochastic master equation for the conditional evolution of the unnormalized state [134],

$$d\tilde{\rho}^{(Y_t)} = (\mathcal{L}dt + \mathcal{X}_\Phi dY_t)\tilde{\rho}^{(Y_t)}, \quad (2.16)$$

where the average, deterministic evolution is supplied by the Liouvillian  $\mathcal{L}\rho = -i[\hat{H}, \rho] + \mathcal{D}[\hat{c}]\rho$ , and the latter term includes the stochastic measurement backaction.

Figure 2.3(b) shows a simulated homodyne detection signal (2.14). Conditioned on this, our driven two-level system (2.6) evolves according to Eq. (2.16) as shown in the lower panel. Contrary to the case of photon counting in (a), the noisy homodyne signal imposes a continuous but weaker backaction which leads to a diffusive dynamics of the system around the underlying Rabi oscillations. Again, the measurement-quenched dynamics is very different from that of an unmonitored system.

Upon acquiring a measurement signal, the relevant stochastic master equation, (2.13) or (2.16), may be solved for each possible value of  $\theta$ , all conditioned on the signal *actually* recorded which stems from the true value of  $\theta$ . The corresponding candidate states  $\tilde{\rho}_\theta^{(D_t)}(t)$  are all initialized in the (known) initial state of the system, but normalized to the prior probabilities assigned the particular candidate,  $\text{Tr}[\tilde{\rho}_\theta^{(D_0)}(t=0)] = P(\theta)$ .

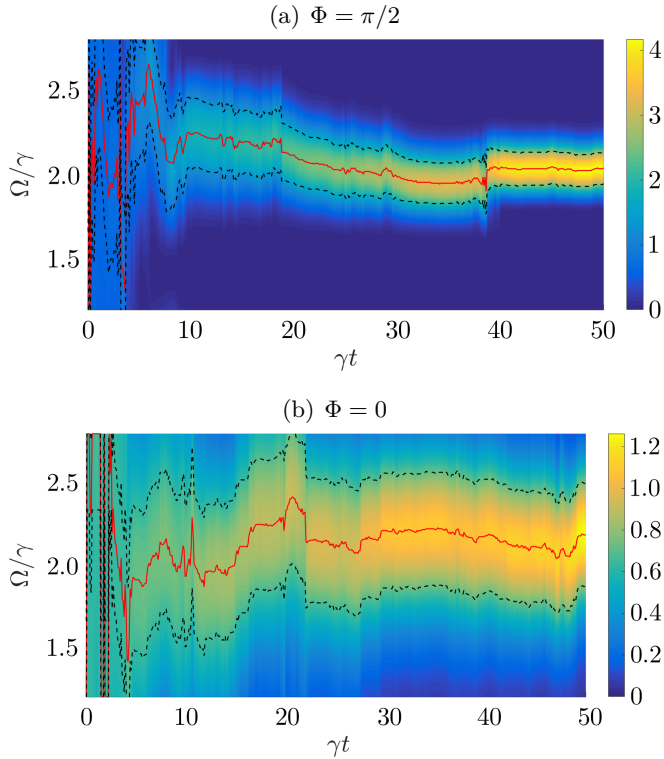


Figure 2.4: The evolution of the quasi continuous probability distribution  $P(\Omega|Y_t)$  for the Rabi frequency of a resonantly driven two-level system, conditioned on noisy homodyne measurement records  $Y_t$ . The red lines track the most likely parameter value  $S_\Omega(Y_t) = \max_\Omega [P(\Omega|Y_t)]$ , and the dashed, black lines show the FWHM of  $P(\Omega|Y_t)$ . Results are shown for two choices of the local oscillator phase, (a)  $\Phi = \pi/2$  ( $\hat{\sigma}_y$ -probing) and (b)  $\Phi = 0$ , ( $\hat{\sigma}_x$ -probing). The true value  $\Omega_0 = 2\gamma$  where  $\gamma$  is the emission rate, assumed for the Rabi frequency, is gradually identified in each simulation.

This way, the evolving likelihood distribution over the possible parameter values is directly given by the traces of the corresponding conditioned density matrices,  $\tilde{\rho}_\theta^{(D_t)}(t)$ .

Figure 2.4 illustrates this Bayesian inference protocol with continuous quantum measurements by a driven two-level system monitored by homodyne detection with the purpose of estimating the value of the Rabi driving frequency  $\Omega$  in Eq. (2.6). In both cases, the true value is gradually revealed, but it is evident that of the two local oscillator phases,  $\Phi = \pi/2$  delivers a much faster convergence of the probability density  $P(\Omega|D_t)$ . See

Chapter 4 for further details.

## 2.2.2 Precision and Fisher information

While different convergence speeds of the estimates in Fig. 2.4 (a) and (b) suggest that one strategy is favourable, what eventually matters is the precision of the final estimate  $S_\Omega(Y_t) = \max_\Omega [P(\Omega|Y_t)]$ , tracked by the red lines. It is paramount to realize that it is exactly this precision and *not* the width of the distribution  $P(\Omega|Y_t)$  [dashed black lines in Fig. 2.4] which is quantified by the Fisher information (2.2) and the Cramér-Rao bound (2.3). Hence, a rapid convergence of the Bayesian estimate does not necessarily imply a high precision. The Fisher information has been used to examine a variety of estimation setups with continuous or repeated measurements; see e.g. [1, 2, 4, 129, 140–142].

The Fisher information (2.2) normally assumes a large number of repetitions  $K$  of the experiment. For the alternative case formulated here, where a single system is interrogated a large number times  $N$ , a self-averaging occurs due to the repetitive measurements, and the relevant dependence is that of  $\mathcal{I}(\theta)$  on  $N$  (with  $K = 1$ ) or equivalently, on the total time of the probing  $T$ . Similarly, in experiments with continuous measurements, precision is acquired by monitoring a single system over time rather than by employing single measurements on many identical probe systems. For continuous probing, we may expect that the measurement precision improves with the total measurement duration  $T$ , and if measurement outcomes at different times  $(t, t')$  are uncorrelated for  $|t - t'| \geq \tau$ , the situation is comparable to that of  $N \sim T/\tau$  independent measurements. Hence, we should anticipate an estimation error scaling as  $1/\sqrt{T}$  [4, 143].

The role played by measurement backaction is a major theme of this thesis. In Chapters 3 and 4, we shall see that the backaction associated with counting photons or performing homodyne demodulation of a fluorescence signal from a quantum probe can be highly beneficial. It quenches the steady state (2.12), which would otherwise be reached, and triggers a transient evolution, inducing out-of-time correlations in the signal. These depend in many cases strongly on the unknown parameter(s) in question, and thereby allows a higher sensitivity to be achieved. We quantify this by evaluating the associated Fisher information. For the example of homodyne detection considered in Fig. 2.4, our analysis reveals that  $\Phi = \pi/2$  is indeed the optimal local oscillator phase.

On the other hand, if a system is probed too strongly or too frequently, the dynamics controlled by the parameters in question may be suppressed by

the measurement backaction. In Chapter 5 we investigate how this quantum Zeno effect undeniably deteriorates our ability to accurately estimate parameters governing the evolution of a frequently probed quantum system.

The experiment reported in Chapter 11 on squeezing enhanced magnetic resonance detection performs homodyne detection of the probe signal. Also in this case, as the limit of only a few spins is approached, the measurement backaction becomes important, implying that appreciable advantages can be achieved by a full Bayesian analysis of the measurement signal [93]. While this will hopefully become relevant in future experiments by the group at CEA Saclay, the present experiment [8] is sensitive to a minimum of  $\approx 1.3 \times 10^4$  spins, and a mean signal analysis suffices. As a closely related topic, Ref. [144] presents a blueprint for nanoscale NMR with nitrogen vacancy centres in diamond which applies a Bayesian model in the signal processing to achieve sub-micromolar sensitivity to the sample concentration.

## 2.3 Quantum Fisher information

The classical Fisher information (2.2) defines a bound on the asymptotic precision related to a *specific* measurement strategy. It is plain that different strategies extract different amounts of information. One example is seen in Fig. 2.4 where different phases of the local oscillator yield more or less sensitivity to the Rabi frequency. In general, by employing a particular measurement scheme which obtains information about a given property, the possibility to measure complementary observables in the same experiment is excluded. For a quantum mechanical system, the precision is, however, ultimately limited by the encoding of the unknown parameter  $\theta$  in the state  $\rho_\theta$  of the system. The variation of  $\rho_\theta$  with infinitesimal changes in the value of  $\theta$  thus defines an upper, *quantum* bound on the Fisher information,  $\mathcal{I}(\theta) \leq \mathcal{I}_Q(\theta)$ , where the quantum Fisher information (QFI) is given by [71, 106, 145, 146],

$$\mathcal{I}_Q(\theta) = \text{Tr} \left( L_\theta^2 \rho_\theta \right). \quad (2.17)$$

Here the symmetric logarithmic derivative  $L_\theta$  is a self-adjoint operator which relates to the variation of the state  $\rho_\theta$  with infinitesimal changes in the value of the unknown parameter  $\theta$ ,

$$\partial_\theta \rho_\theta = \frac{L_\theta \rho_\theta + \rho_\theta L_\theta}{2}. \quad (2.18)$$

This expression for the quantum Fisher information can be formally derived by maximizing the classical Fisher information (2.2) over all possible measurements [145, 147–149], and the corresponding (quantum) CRB,

$$[\Delta S_\theta(D)]^2 \geq \frac{1}{K\mathcal{I}_Q(\theta)} \quad (2.19)$$

can be asymptotically saturated for large  $K$  by measuring an optimal observable corresponding to  $L_\theta$ . It should be noted that by Eq. (2.18), this observable depends on the expected state of the probe  $\rho_\theta$ , which in turn depends on the value of the unknown parameter  $\theta$ . Hence, an optimal protocol must be approximated by an adaptive scheme which uses a small part  $J$  of the  $K$  measurements to deliver a rough prior estimate  $S_\theta(\{D_j\}_{j=1}^J)$ , defining the observable  $L_{S_\theta(\{D_j\}_{j=1}^J)}$ , used in the remaining measurements. As long as  $K$  is large enough, such a procedure is still able to saturate the quantum CRB (2.19) [69, 150], and a recent study even suggests that an intrinsic dependence of the measurement strategy on the parameter may in some cases allow even more precise quantum-enhanced estimation [151].

For different purposes, alternative forms of the QFI (2.17) are preferable. It may be explicitly expressed in terms of the eigendecomposition of the state  $\rho_\theta$  [71] or defined in a geometric picture by the change in the state as measured by Bures metric when the value of  $\theta$  changes by an infinitesimal amount [145]. For pure states  $\rho_\theta = |\psi_\theta\rangle\langle\psi_\theta|$ , the latter approach yields [152]

$$\mathcal{I}_Q(\theta) = 4\text{Re} [\partial_{\theta_1}\partial_{\theta_2} \langle\psi_{\theta_1}|\psi_{\theta_2}\rangle - \partial_{\theta_1} \langle\psi_{\theta_1}|\psi_{\theta_2}\rangle \times \partial_{\theta_2} \langle\psi_{\theta_1}|\psi_{\theta_2}\rangle]_{\theta_1=\theta_2=\theta} \quad (2.20)$$

or equivalently

$$\mathcal{I}_Q(\theta) = 4 [\partial_{\theta_1}\partial_{\theta_2} \ln (\langle\psi_{\theta_1}|\psi_{\theta_2}\rangle)]_{\theta_1=\theta_2=\theta}. \quad (2.21)$$

Finally, I would like to point out a recent form which relies on both the standard representation of the density matrix  $\rho$  and its vectorized form  $\vec{\rho}$  [153],

$$\mathcal{I}_Q[\theta] = 2\partial_\theta\vec{\rho}_\theta^\dagger (\rho_\theta^* \otimes \mathbb{I} + \mathbb{I} \otimes \rho_\theta)^{-1} \partial_\theta\vec{\rho}_\theta, \quad (2.22)$$

where  $\rho^*$  denotes complex conjugation. While such a mixed representation may seem a mess, this form is often convenient for numerical evaluation of the QFI and we shall apply it to analyse the achievements of a quantum thermometer device in Chapter 10.

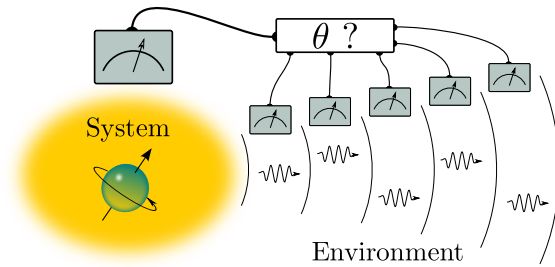


Figure 2.5: A general measurement is performed on the full state of a probe system and its environment, and the most likely value of the unknown parameter  $\theta$  is inferred from the outcome.

### 2.3.1 QFI of an open system

The density matrix  $\rho_\theta$  in the QFI (2.17) represents the full state on which a hypothetical measurement may be performed. Hence, if as illustrated in Fig. 2.1, the fluorescence from an probe system is monitored, the ultimate precision limit is determined not by the state of the probe system alone but rather by the *full* entangled state of the system and its un-measured, quantized radiative environment. This idea is illustrated in Fig. 2.5 for a general setup of a probe system coupled to an environment. The evolving pure state of a probe system and its environment,  $|\psi_\theta^{\text{SE}}\rangle$  is in many cases infinite-dimensional and hence impossible to evaluate exactly. However, the QFI (2.20) requires only knowledge of the overlaps between states pertaining to infinitesimally different values of the unknown parameter which may be evaluated by a simple master equation analysis of a system with dimensionality of the probe alone [140, 154, 155]. In particular, assuming validity of the Born-Markov approximation for the system-environment coupling, the overlap may be calculated as  $\langle \psi_{\theta_1}^{\text{SE}} | \psi_{\theta_2}^{\text{SE}} \rangle = \text{Tr}(\rho_{\theta_1, \theta_2})$ , where  $\rho_{\theta_1, \theta_2}$  operates on the system Hilbert space and solves a master equation of the form (2.9) with an effective, *two-sided* Liouvillian superoperator,

$$\begin{aligned} \mathcal{L}_{\theta_1, \theta_2} \rho = & -i \left( \hat{H}_{\theta_1} \rho - \rho \hat{H}_{\theta_2} \right) \\ & - \sum_m \left( \hat{c}_{m, \theta_1} \rho \hat{c}_{m, \theta_2}^\dagger - \left[ \hat{c}_{m, \theta_1}^\dagger \hat{c}_{m, \theta_1} \rho - \rho \hat{c}_{m, \theta_2}^\dagger \hat{c}_{m, \theta_2} \right] / 2 \right). \end{aligned} \quad (2.23)$$

See Sec. 8.2.1 in Chapter 8 for a derivation of this result. The  $\hat{c}_{m, \theta_{1(2)}}$  represent relaxation induced by the system-environment coupling which may depend on the parameter in question. Due to the action of different Hamiltonians  $\hat{H}_{\theta_{1(2)}}$  and jump-operators  $\hat{c}_{m, \theta_{1(2)}}$  from left and right, the

master equation does not preserve norm, and leads indeed to a decrease in time of  $\text{Tr}(\rho_{\theta_1, \theta_2})$ , signifying a growing distinguishability of the different values of  $\theta_1$  and  $\theta_2$ . This way the theory directly lends itself to hypothesis testing scenarios [10, 154], and in Chapter 8 it is applied to evaluate a lower bound on the probability of assigning a false value from a discrete set of possible values for an unknown parameter.

For our present purpose of parameter estimation, the derivatives needed to evaluate the associated QFI (2.20) are readily obtained by this method in a finite-difference approximation. Alternatively, the formal solution to the master equation (2.11) may be inserted in Eq. (2.21). This is especially advantageous when studying the long time limit where it allows the QFI to be expressed in terms of the eigenvalue  $\lambda_{\theta_1, \theta_2}$  of  $\mathcal{L}_{\theta_1, \theta_2}$  with the largest (least negative) real part

$$\mathcal{I}_Q(\theta) = 4t [\partial_{\theta_1} \partial_{\theta_2} \lambda_{\theta_1, \theta_2}]_{\theta_1 = \theta_2 = \theta}, \quad (2.24)$$

for large  $t$ . Reference [140] explains how the differentials in this equation may be evaluated analytically by perturbation theory rather than by numerical means, thus allowing a deeper insight and a broader applicability range. Notice that by the quantum CRB (2.19), the QFI (2.24) implies a  $1/\sqrt{t}$  scaling of the sensitivity with time  $t$ . In the vicinity of a dynamical phase transition, the Liouvillian  $\mathcal{L}_{\theta_1, \theta_2}$  has degenerate eigenvalues. Reference [155] investigates how this may allow a quadratic scaling of the QFI with time.

Even though the QFI associated with the full state of a system and its environment may be evaluated by the method explained above, it is improbable that the measurement [see Fig. 2.5] of the corresponding operator  $L_\theta$  in (2.18), which saturates the quantum CRB (2.19), can be directly implemented in an experiment. Instead one has recourse to employ conventional detection methods such as photon counting or homodyne detection on the emitted field, possibly combined with a final measurement on the probe system itself. For such applications, the QFI of the full state defines an upper bound to the retrievable information (2.2), and may thus serve as a guide to design near-optimal estimation strategies within realistic settings. When possible, the achievements of specific measurement strategies presented in this thesis are compared to the quantum bound (2.19).

For estimation of the Rabi frequency  $\Omega$  in a driven two-level system Eq. (2.6), decaying at a rate  $\gamma$  into an electromagnetic environment, the

QFI is found to scale with the total duration of the experiment  $T$  as

$$\mathcal{I}_Q(\Omega) = \frac{4T}{\gamma}, \quad (2.25)$$

implying by Eq. (2.19) a  $1/\sqrt{T}$  scaling of the estimation error with time. Interestingly, we shall see in Chapters 3 and 4 that for this specific example, the Fisher information associated with either photon counting or homodyne detection matches the upper bound (2.25), signifying that these protocols are in fact optimal as long as perfect detectors are available.

## 2.4 Outlook

The present formulation of quantum estimation theory focuses on the Bayesian approach while, of course, many alternatives exist. For instance, one may perform a spectral analysis of a measurement signal. This is sub-optimal since, contrary to Bayesian inference, the spectrum only accounts for two-time correlations in the signal<sup>1</sup>. It has the advantage though that where a Bayesian estimate is often performed in post-processing since it requires substantial computational resources, a spectral analysis can be implemented in real-time during an experiment by the fast Fourier transform (FFT) algorithm or by a spectrum analyser. This is important for the estimation of rapidly drifting parameters or if the estimate is only the first stage in an experiment [156].

Another approach, allowing a faster but sub-optimal estimate, is offered by the Baum-Welch parameter reestimation method which was recently formulated for parameter estimation with continuous quantum measurements [157]. Yet another very timely formulation applies (classical) artificial neural networks trained on continuous measurements records from quantum probes to quickly estimate unknown parameters [158]. This machine learning approach has the benefit that it requires a less comprehensive modelling of the system and the detector, and with sufficient training data it can come close to the optimality offered by the Bayesian method. Furthermore, one can imagine a commercial quantum sensor solution trained in a laboratory by a large number of experimental runs to sense, e.g., a magnetic field in field studies.

The Cramér-Rao bound as stated in Eq. (2.3) applies only to unbiased estimators but it can be generalized to apply also to estimators with an

---

<sup>1</sup>The power spectrum is the Fourier transform of the two-time correlation function [134].

explicit expression for their bias [159]. However, it was recently pointed out that for some problems estimators with more general bias may exist which allow superior precision [160]. Such cases can be analysed by means of so-called Van Trees inequalities but we shall not pursue this topic here.

For sake of completeness, let us mention finally that while the standard approach to quantum metrology taken here formulates the precision in terms of root-mean-square errors (2.3) and (2.19) bounded by the associated Fisher information (2.2) and (2.17), an interesting new approach formulates estimation as a digital problem, asking instead how many bits of an unknown parameter can be recovered in a quantum framework [161].

# Photon counting

*This chapter is reproduced from [1] and [2] with only minor changes. In particular Fig. 3.2 and Section 3.4.1 are taken from [1] while the remaining parts come from [2] with a few paragraphs and sentences added in from [1].*

---

The expression for the Fisher information (2.2) makes reference to the variation of the likelihood function over the set of possible measurement records  $D$ . The weighted summation (integral) over all data records makes the direct evaluation of Eq. (2.2) a formidable task. In [1] we present an analysis based on a specific property of the quantum trajectories associated with photon counting from a two-level emitter: The signal is a discrete set of detection times, and after each detection the system is projected in the ground state from which the evolution is reset. This implies that the detection record is fully represented by the distribution of delay times between detector clicks, and allows for a simple evaluation of the Fisher information for photon counting records. In [2] we extend to analysis to the case of multi-level systems with distinguishable emission processes and branching of the decay towards different final states. This situation is exemplified by the  $\Lambda$ -system depicted in Fig. 3.1, with an excited state from which spontaneous decay occurs towards two different ground states.

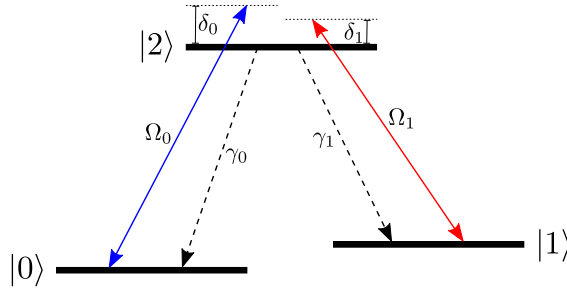


Figure 3.1: (a): A quantum  $\Lambda$ -system with laser driven  $|0\rangle \leftrightarrow |2\rangle$  and  $|1\rangle \leftrightarrow |2\rangle$  transitions with Rabi frequencies  $\Omega_0$  and  $\Omega_1$ , detunings  $\delta_0$  and  $\delta_1$  and excited state decay rates  $\gamma_0$  and  $\gamma_1$ .

### 3.1 Fisher information of counting signals

A photon counting detection record contains the discrete times of detection events  $D = \{t_k\}$  and, if the emitter always jumps to the same state when a photon is detected, measurement intervals  $\tau_k = t_{k+1} - t_k$  between detector clicks are independent and identically distributed stochastic variables. A data record with  $N + 1$  count events, thus yields  $N$  independent samples of the waiting time probability distribution  $w(\tau)$ . Each registered waiting time  $\tau_k$  falls within a short interval  $[\tau^{[i]} - \Delta\tau/2, \tau^{[i]} + \Delta\tau/2]$  with probability  $w_i = w(\tau^{[i]})\Delta\tau$ , and the data record  $D$ , fully represented by the set of numbers  $n_i$  of registered waiting times in all intervals, is statistically governed by a multinomial distribution,  $(\sum_i n_i)! \prod_i w_i^{n_i} / \prod_i n_i!$ .

In Fig. 3.2 we show the distribution of 10 000 time intervals between simulated quantum jumps in a driven two-level system Eq. (2.6) (blue dots). The comparison with the theoretical waiting time distribution (red curve) constitutes the basis of the parameter estimation since a higher or smaller value of the Rabi frequency would change the oscillation period in the distribution of waiting times.

For a given total probing time  $T$ , the total number of registered intervals,  $N = \sum_i n_i$  is itself a stochastic variable, governed by a probability distribution  $P_N$ , and hence the probability for the data record  $D = \{n_i\}$  is

$$P(D|\theta) = \frac{(\sum_i n_i)! \prod_i w_i^{n_i}}{\prod_i n_i!} P_{N=\sum_i n_i}. \quad (3.1)$$

The conditional dependence on the quantity  $\theta$  stems from the  $\theta$ -dependence of the  $w_i$ 's and  $P_N$  in Eq. (3.1), and the Fisher information (2.2)

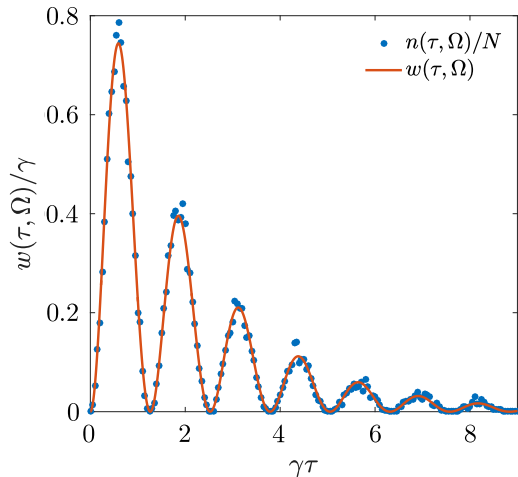


Figure 3.2: The blue noisy dots show the distribution from a simulated data record of 10 000 detection events. The red curve is the corresponding theoretical waiting time distribution  $w(\tau, \theta)$  for time intervals between detector clicks. Results are shown for  $\Omega = 5\gamma$ .

can be evaluated directly,

$$\mathcal{I}(\theta) = \overline{N} \sum_i \frac{1}{w_i} \left( \frac{\partial w_i}{\partial \theta} \right)^2 + \sum_N \frac{1}{P_N} \left( \frac{\partial P_N}{\partial \theta} \right)^2, \quad (3.2)$$

where  $\overline{N}$  denotes the mean value of  $N$ . It is convenient to rearrange the terms in Eq. (3.2) in two different contributions,

$$\mathcal{I}(\theta) = \mathcal{I}_{\text{Poisson}}(\theta) + \mathcal{I}_N(\theta). \quad (3.3)$$

The first term

$$\mathcal{I}_{\text{Poisson}}(\theta) \equiv \sum_i \frac{1}{\overline{n}_i} \left( \frac{\partial \overline{n}_i}{\partial \theta} \right)^2 = \int \frac{1}{\overline{n}(\tau)} \left( \frac{\partial \overline{n}(\tau)}{\partial \theta} \right)^2 d\tau, \quad (3.4)$$

reflects the similarity between the multinomial distribution and the Poisson distribution for each  $n_i \ll N$  with  $\overline{n}_i(\theta) = \overline{N}(\theta)w_i(\theta)$ . In the last step, we have transformed the sum over time intervals into an integral with  $\overline{n}_i(\theta) = \overline{n}(\tau)\Delta\tau$ . See, e.g., [162, 163] for similar arguments applied to high-resolution spatial measurements by scattering of coherent light or to probing of the motion of a Bose condensate.

Equation (3.4) is, indeed, the Fisher information for uncorrelated Poisson distributed variables  $n_i$ , resulting in a sum,  $N = \sum_i n_i$ , which is also Poisson distributed. The total number of photons emitted from quantum light sources may, however, show sub- or super-Poissonian counting statistics [164], and the second term in (3.3),

$$\mathcal{I}_N(\theta) \equiv \sum_N \frac{1}{P_N(\theta)} \left( \frac{\partial P_N(\theta)}{\partial \theta} \right)^2 - \frac{1}{\bar{N}(\theta)} \left( \frac{\partial \bar{N}(\theta)}{\partial \theta} \right)^2 \quad (3.5)$$

accounts for the deviation of the information held by the true statistics  $P_N$  from that of a Poisson distribution. The two expressions (3.2) and (3.3) are easily proven to be identical (note that a term with mixed derivatives vanishes because of the independence on  $\theta$  of the integral of  $w(\tau)$  over time).

The waiting times are identically distributed random variables, and the stochastic counting process is a renewal process [165]. We are interested in systems with no dark steady states, i.e., the fluorescence is persistent and the waiting time distribution does not have long tails. In the asymptotic limit of large  $T$ , where the CRB applies, a central limit theorem for such renewal processes ensures that the distribution  $P_N$  converges asymptotically to a normal distribution with a mean value  $\bar{N}$  and a variance  $V \equiv \text{Var}(N)$  which are both proportional to  $T$  [166]. In this limit we can thus evaluate Eq. (3.5),

$$\mathcal{I}_N(\theta) = \left( \frac{1}{V(\theta)} - \frac{1}{\bar{N}(\theta)} \right) \left( \frac{\partial \bar{N}(\theta)}{\partial \theta} \right)^2. \quad (3.6)$$

As easily understood, the correction (3.6) to the Fisher information is positive(negative) if the total number  $N$  fluctuates less(more) than the Poisson distribution.

Since  $\bar{N}$ ,  $V$  and  $\bar{n}(\tau, \theta)$  are all proportional to the probing time  $T$ , also the Fisher information is proportional to  $T$ , and we conclude from Eq. (2.3) that the estimation error decreases asymptotically as  $\sim 1/\sqrt{T}$  as anticipated from the discussion in Sec. 2.2.2 of the previous chapter.

Let us now turn to the more general case of signals from quantum emitters observed by photon counters that distinguish between different decay channels, e.g., by making use of the polarization or frequency of the emitted photons. For generality, we assume that there are  $M$  such channels (for the  $\Lambda$  system in Fig. 3.1,  $M = 2$ ). Our analysis is restricted to the case for which detection of a photon in channel  $m$  accompanies a

jump of the emitter into a definite state  $|\phi_m\rangle$ , which is the initial state for the subsequent evolution of the system. This is not a requirement for the Bayesian analysis, but our calculation of the Fisher information relies on definite waiting time distributions after detection in each channel. These waiting time distributions until the next detection event thus depend on  $m$ , the channel of the most recently detected photon, and we can sort the detection record into lists  $\{\tau_k\}_{mm'}$  containing the duration of time intervals between detection in channel  $m$  followed by subsequent detection in channel  $m'$ . These lists, in turn, sample the corresponding waiting time distributions in an independent and uncorrelated manner, and, for our parameter estimation, they retain all the information available in the multi-channel detection record.

The combinations  $mm'$  define  $M^2$  interval types, and for each  $mm'$ , the number  $n_{mm',i}$  denotes the number of waiting times  $\tau$  registered in intervals  $[\tau^{[i]} - \Delta\tau/2, \tau^{[i]} + \Delta\tau/2]$ . The likelihood function in Eq. (2.2) now factorizes as a product of weighted multinomial distributions,

$$P(D|\theta) = \prod_{mm'} P_{mm'}(D|\theta), \quad (3.7)$$

where the likelihood for each type,  $P_{mm'}(D|\theta)$ , is as given in Eq. (3.1), and the single channel result (3.3) is readily generalized. In particular,

$$\mathcal{I}_{\text{Poisson}}(\theta) = \sum_{mm'} \int \frac{1}{\bar{n}_{mm'}(\tau)} \left( \frac{\partial \bar{n}_{mm'}(\tau)}{\partial \theta} \right)^2 d\tau, \quad (3.8)$$

where  $\bar{n}_{mm'}(\tau, \theta)$  is the theoretically expected distribution of intervals of type  $mm'$  and duration  $\tau$ . The correction due to the count statistics with mean value  $\bar{N}_m$  but a non-Poissonian variance  $V_m$  in each channel, is in the asymptotic limit given by

$$\mathcal{I}_N(\theta) = \sum_m \left( \frac{1}{V_m} - \frac{1}{\bar{N}_m} \right) \left( \frac{\partial \bar{N}_m}{\partial \theta} \right)^2. \quad (3.9)$$

## 3.2 Waiting time distributions

We obtain the distribution functions and  $\bar{n}_{mm'}(\tau)$  by solving effective master equations where the unknown quantity  $\theta$  is one of the Hamiltonian or damping parameters. With the understanding that our results may be finally evaluated and varied with respect to the parameter of interest, we suppress, in this section, the variable  $\theta$  from the equations.

The average behaviour of an atomic quantum system decaying by spontaneous emission of photons into broad-band photon reservoirs is governed by a Liouvillian of the form (2.10), where the operators  $\hat{c}_m$  represent jump processes in the atom associated with decay and emission of different, distinguishable kinds of radiation. While decay processes may preserve, e.g., coherences between excited Zeeman states in the ground state after the emission of light of linear or circular polarization, we emphasize that our analysis of the Fisher information is restricted to the case in which a jump  $\hat{c}_m$  puts the system in a definite final state  $|\phi_m\rangle$ , from which the dynamics proceeds. This is for example the case for the three level atom, shown in Fig. 3.1, where the two operators,  $\hat{c}_0 = \sqrt{\gamma_0}|0\rangle\langle 2|$  and  $\hat{c}_1 = \sqrt{\gamma_1}|1\rangle\langle 2|$  describe decay into the ground states  $|0\rangle$  and  $|1\rangle$  with rates  $\gamma_0$  and  $\gamma_1$ , respectively.

The jumps into state  $|\phi_m\rangle$  are governed by the rate  $\langle \hat{c}_m^\dagger \hat{c}_m \rangle$  where the expectation value is calculated as function of time for a given evolving wave function. On average, the stochastic trajectories of a system evolving conditioned on the outcomes of continuous probing of its emitted radiation, as describe by Eq. (2.13), reproduce the corresponding master equation (2.9). Therefore the average number of these jumps equals the value obtained by the density matrix describing the unobserved quantum system. For probing over long times  $T$ , we thus get the average number of jumps into state  $|\phi_m\rangle$ ,  $\bar{N}_m = \text{Tr}(\hat{c}_m^\dagger \hat{c}_m \rho^{(\text{ss})})T$ , where  $\rho^{(\text{ss})}$  is the steady state density matrix solution (2.12) to the master equation (2.9).

For the distributions of intervals between detector clicks we have  $\bar{n}_{mm'}(\tau) = \bar{N}_m w_{mm'}(\tau)$ , where  $w_{mm'}(\tau)d\tau$  is the probability that after a jump into  $|\phi_m\rangle$ , the next emission event is detected in channel  $m'$  in  $[\tau, \tau + d\tau]$ . To determine the function  $w_{mm'}(\tau)$ , we note that the terms  $\sum_m \hat{c}_m \rho \hat{c}_m^\dagger$  in Eq. (2.9) account for the feeding of the system ground states associated with the emission process, i.e., they describe terms in the reduced system density matrix, correlated with single-photon excited states of the modes of the radiation field. If the system has just been put into the state  $|\phi_m\rangle$  due to detection of a photon in channel  $m$ , the probability that no photon is detected until a certain later time  $\tau$  is equal to the population of the zero-photon component of the combined state of the system and the environment at that time. This is, in turn, given by the trace of the unnormalized density matrix,  $\tilde{\rho}$ , which evolves from the initial state  $\tilde{\rho}|_m(\tau = 0) = |\phi_m\rangle\langle \phi_m|$ , omitting the ground state feeding term of

the master equation,

$$\frac{d\tilde{\rho}}{dt} = -i[\hat{H}_0, \tilde{\rho}] - \frac{1}{2} \sum_m \{\hat{c}_m^\dagger \hat{c}_m, \tilde{\rho}\}. \quad (3.10)$$

The resulting  $\tilde{\rho}|_m(\tau)$  is equivalent to the so-called no-jump wave function [138] evolving from the state  $|\phi_m\rangle$  by the non-hermitian Hamiltonian  $\hat{H}_{\text{eff}} = \hat{H}_0 - \frac{i}{2} \sum_m \hat{c}_m^\dagger \hat{c}_m$ . The probability  $w_{mm'}(\tau)d\tau$  that after a detector click at time  $t$  of type  $m$ , the next click is of type  $m'$  and occurs in the time interval  $[t + \tau, t + \tau + d\tau]$ , is now given by

$$w_{mm'}(\tau)d\tau = \text{Tr}[\hat{c}_{m'}^\dagger \hat{c}_{m'} \tilde{\rho}(\tau)]d\tau. \quad (3.11)$$

It follows from the master equation that these waiting time distributions are normalized according to

$$\sum_{m'} \int_0^\infty w_{mm'}(\tau)d\tau = 1. \quad (3.12)$$

If photons are detected with only finite efficiency  $\eta$ , this is equivalent to a fraction  $1-\eta$  of the quantum jumps passing unnoticed. The corresponding un-normalized state  $\tilde{\rho}$  conditioned on no detection events is then found by including a ground state feeding term,  $(1-\eta)\hat{c}\tilde{\rho}\hat{c}^\dagger$ , in the no-jump master equation to account for the unobserved emission [1]. In the multi-channel case, if different channels are monitored with detector efficiencies  $\eta_m$ , we obtain the no-detected-jump master equation

$$\frac{d\tilde{\rho}}{dt} = -i[\hat{H}_0, \tilde{\rho}] + \sum_m \left( (1-\eta_m)\hat{c}_m \tilde{\rho} \hat{c}_m^\dagger - \frac{1}{2} \{\hat{c}_m^\dagger \hat{c}_m, \tilde{\rho}\} \right). \quad (3.13)$$

The solutions of this equation for initial states  $\tilde{\rho}|_m(\tau=0) = |\phi_m\rangle\langle\phi_m|$  yield the waiting time distributions between the detections,

$$w_{mm'}(\tau)d\tau = \eta_{m'} \text{Tr} \left[ \hat{c}_{m'}^\dagger \hat{c}_{m'} \tilde{\rho}|_m(\tau) \right] d\tau, \quad (3.14)$$

which are normalized as in Eq. (3.12). The average number of detected events in channel  $m$  during probing for time  $T$  is  $\bar{N}_m = \eta_m \text{Tr}(\hat{c}_m^\dagger \hat{c}_m \rho^{(\text{ss})})T$ , and with the resulting  $\bar{n}_{mm'}(\tau) = \bar{N}_m w_{mm'}(\tau)d\tau$ , we can calculate the Fisher information according to (3.8).

The Fisher information (3.3) also depends on the moments of the total count statistics (3.9), and in [2] we derive

$$V_m = \frac{\text{Var}(\tau)_m}{\bar{\tau}_m^2} \bar{N}_m, \quad (3.15)$$

clearly identifying whether  $N_m$  follows sub- or super-Poissonian statistics. Here the  $k$ 'th moment of  $\tau$  pertaining to the channel  $m$  is given in terms of the waiting time distribution functions as

$$(\overline{\tau^k})_m = \int \tau^k w_{mm}(\tau) d\tau, \quad (3.16)$$

where  $w_{mm}(\tau)$  is the distribution function for waiting times between photo detection events in the channel  $m$ , and is obtained by solving Eq. (3.13) with efficiencies  $\eta_m$  and  $\eta_{m' \neq m} = 0$ .

### 3.3 Achieving the Cramér Rao bound

As proven by Fisher [131] and explained in Chapter 2, a Bayesian analysis saturates the Cramér-Rao Bound and allows parameter estimation with a precision given by the Fisher information. See Refs. [1, 92] for an illustration of Bayesian parameter estimation in the case of photon counting experiments. If asymptotically the parameter value has been identified to a small vicinity  $\delta\theta$  around a value  $\theta_0$ , the CRB may, however, equivalently be saturated by applying a linear filter to the data available for the estimation process. As derived in [2], the linear estimator in terms of the expected and the actually measured distribution of time intervals between the detector clicks, reads

$$\begin{aligned} S_{\delta\theta}(n_{mm'}(\tau)) = & \frac{1}{\mathcal{I}(\theta)} \left[ \sum_{mm'} \int \frac{\partial \bar{n}_{mm'}(\tau, \theta)}{\partial \theta} \Big|_{\theta=0} \left( \frac{n_{mm'}(\tau)}{\bar{n}_{mm'}(\tau, \theta)} - 1 \right) d\tau \right. \\ & \left. + \sum_m \frac{\partial \bar{N}_m(\tau, \theta)}{\partial \theta} \Big|_{\theta=0} \left( N_m - \bar{N}_m(\theta) \right) \left( \frac{1}{V_m(\theta)} - \frac{1}{\bar{N}_m(\theta)} \right) \right]. \end{aligned} \quad (3.17)$$

This expression represents a first order correction to the initial estimate  $\theta_0$  according to the dissimilarity between the expected and the recorded signal, and by normalizing the estimate by the Fisher information per time, it ensures that larger uncertainties allow larger adjustments. The linear filter is valid in the asymptotic limit where  $\delta\theta$  is small; see also Ref. [150].

The Fisher information is given in Eq. (3.3), and Eq. (3.17) constitutes a linear estimator that exhausts the information in the multi-channel photon counting data record and, hence, achieves the Cramér-Rao Bound asymptotically.

## 3.4 Examples

### 3.4.1 Rabi frequency estimation

As a first example let us consider Rabi frequency estimation in a resonantly driven two-level system, Eq. (2.6). For perfect photo detectors and the system in the ground state at  $\tau = 0$ , Eq. (3.10) yields for the no-jump excited state amplitude:

$$\tilde{\rho}_{ee}(\tau) = \left(\frac{\Omega}{2\lambda}\right)^2 \sin^2(\lambda\tau)e^{-\gamma\tau/2}, \quad (3.18)$$

where  $\lambda = \sqrt{\Omega^2 - (\gamma/2)^2}/2$ . The delay function given by  $w(\tau) = \gamma\tilde{\rho}_{ee}(\tau)$  is presented as the red curve in Fig. 3.2 together with the simulated series of delay times with the same laser-atom parameters.

With a delay function on this form, the integral in Eq. (3.4) can be performed analytically and it produces the following simple expression for the Fisher information:

$$\mathcal{I}(\Omega) = \bar{N} \left( \frac{8}{\gamma^2} + \frac{4}{\Omega^2} \right) = \frac{4T}{\gamma}, \quad (3.19)$$

where  $T$  is the data acquisition time, and we have used that, asymptotically,  $\bar{N}/T$  is given by the mean photon scattering rate,  $\gamma\rho_{ee}^{(ss)} = \frac{\gamma\Omega^2/4}{\Omega^2/2 + \gamma^2/4}$  (on resonance). It is remarkable that we obtain such a simple expression, which readily confirms that while the mean scattering rate saturates for strong driving,  $\Omega \gg \gamma$ , the sensitivity per detected photon becomes constant, and we can resolve large Rabi frequencies as accurately as intermediate ones. The expression for the Fisher information per detected photon diverges for small Rabi frequencies. The scattering rate, however, depends quadratically on small values of  $\Omega$ , so per time the accumulated Fisher information is finite. Furthermore, the result (3.19) reveals that the Fisher information of this concrete measurement protocol reaches the quantum Fisher information (2.17) independently of the actual Rabi frequency when the two-level system is driven on resonance and the detector is perfect.

To illustrate the achievements of the linear filter (3.17) and consistency with the Cramér-Rao bound Eq. (2.3), we show in Fig. 3.3 a Rabi frequency estimate (solid, blue curve) as a function of the number of detection events with unit detector efficiency. The estimate fluctuates around the actual value  $\Omega_0 = 5\gamma$  (dotted, red horizontal line). The dashed, red lines in the figure represent  $\Omega_0 \pm \mathcal{I}(\Omega)^{-1/2}$  and show that the deviations of the

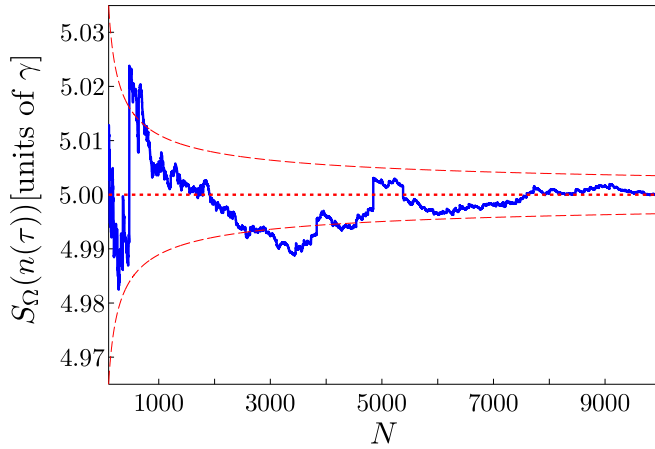


Figure 3.3: The solid, blue line shows the estimate of the Rabi frequency as a function of the number of simulated photo detection events included in the estimate. The dashed, red lines indicate the CRB sensitivity bound, enclosing the actual value (dotted, red line). Results are shown for  $100 < N \leq 10000$ . The true Rabi frequency in the simulation is  $\Omega_0 = 5\gamma$ .

estimate from the true value are, indeed, compatible with the CRB in the asymptotic limit.

We turn now the case of finite detector efficiency  $\eta$ . Some characteristic results for the waiting time distribution are summarized in Fig. 3.4. All curves show probability densities and are normalized to unity, but the time scale for the first detection increases when the detector efficiency is reduced. Due to the possibility of missed earlier events, the exact nodes in the waiting time distribution for perfect detection disappear, and while a detection within the first few  $1/\gamma$  is likely to report the first actual emission event, a later detection is almost certainly preceded by unobserved emission of photons by the atom. This explains why the modulation in the waiting time distribution is maintained for short times and gradually replaced by a smooth exponential curve for long times. In fact, in the limit of infinitesimal detector efficiency ( $\eta \ll 1$ ) the no-detected-jump master equation (3.13) approaches the unconditional master equation (2.9), and at the first detector click the no-jump master equation has very likely reached the steady state (2.12). This implies a distribution of waiting times  $w(\tau, \Omega) \simeq \eta\gamma\rho_{ee}^{(ss)} e^{-\eta\gamma\rho_{ee}^{(ss)}\tau}$ , which through Eq. (3.3) leads to the

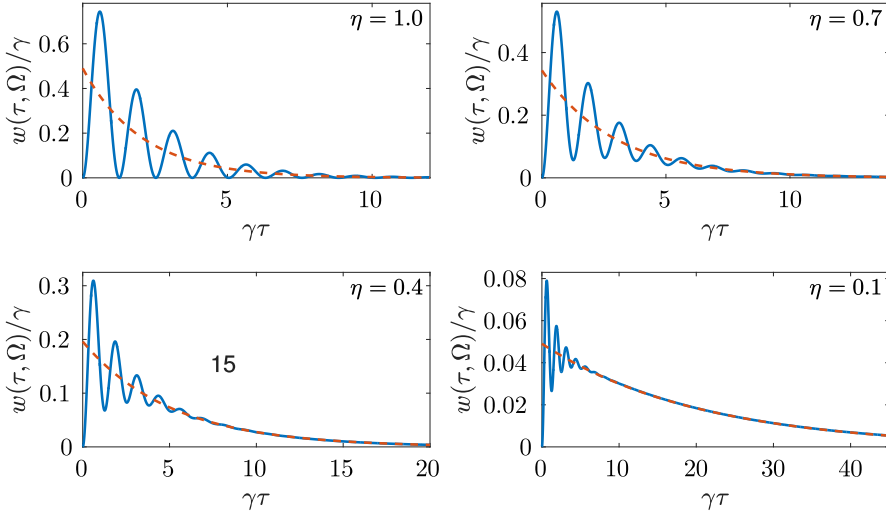


Figure 3.4: The blue curves show the delay function (3.14) for the two-level atom, and for different values,  $\eta = 1.0, 0.7, 0.4,$  and  $0.1$  of the detector efficiency. The waiting time distributions approach exponential functions for long times (dashed, red curves), when the detector is imperfect. Notice that due to the missed detection events, the waiting time distribution extends over longer time when  $\eta$  decreases. The Rabi frequency is  $\Omega = 5\gamma$ .

Fisher information,

$$\mathcal{I}(\Omega) = \bar{N} \left( \frac{\partial \rho_{ee}^{(ss)} / \partial \Omega}{\rho_{ee}^{(ss)}} \right)^2. \quad (3.20)$$

This is consistent with the uncertainty in estimates obtained from the total count  $N$  alone, assuming Poissonian counting statistics.

In Fig. 3.5 we show the Fisher information per time Eq. (3.3) as a function of the *actual* Rabi frequency for different values of the detector efficiency. Notice that since even small but finite  $\eta$  yields a finite fraction of the detection events at short times where the delay function is strongly modulated in time by the Rabi frequency, the sensitivity to the value of  $\Omega$  is still significantly improved by considering the actual waiting times rather than only the total count (dashed lines). For  $\eta < 1$  the information decreases with the value of  $\Omega$  and saturates at large Rabi frequencies.

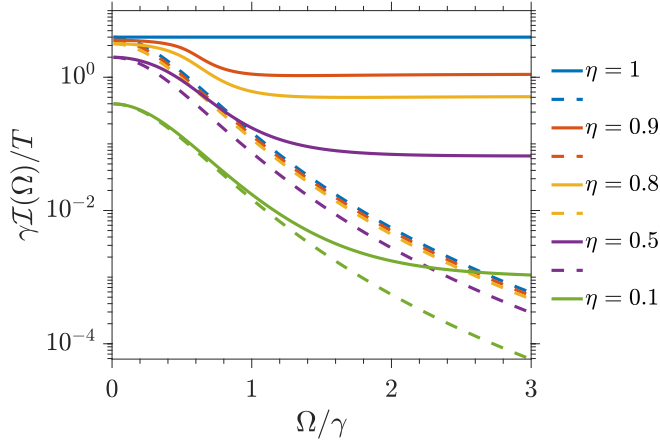


Figure 3.5: The Fisher information (3.3) (full lines) for estimating a Rabi frequency  $\Omega$  of a driven two-level system from a photon counting record of its emission signal is compared to the information from the total count alone Eq. (3.20) (dashed lines). Results are shown for different values of the detector efficiency  $\eta$  and as a function of  $\Omega$ . The full ( $\eta = 1$ )-curve has a constant value of  $\gamma \mathcal{I}(\Omega)/T = 4$ , equal to the corresponding QFI (2.17).

### 3.4.2 Photon counting from a laser driven $\Lambda$ -type atom

As an example of multichannel counting, we apply the formalism to a  $\Lambda$ -type system coupled to two laser fields, as shown in Fig. 3.1. The couplings are described by Rabi frequencies  $\Omega_0$  and  $\Omega_1$  and laser-atom detunings  $\delta_0$  and  $\delta_1$  as indicated in the figure. We assume no direct coupling between  $|0\rangle$  and  $|1\rangle$ , and that the decay into these two ground states is distinguishable, either by the polarization or by well-separated frequencies of the emitted photons.

In the rotating wave approximation, the Hamiltonian of the system can be written as ( $\hbar = 1$ ),

$$\hat{H} = \delta_0 |0\rangle \langle 0| + \delta_1 |1\rangle \langle 1| + \frac{\Omega_0}{2} (|0\rangle \langle 2| + |2\rangle \langle 0|) + \frac{\Omega_1}{2} (|1\rangle \langle 2| + |2\rangle \langle 1|). \quad (3.21)$$

The decay from  $|2\rangle$  to  $|0\rangle$  with rate  $\gamma_0$  and from  $|2\rangle$  to  $|1\rangle$  with rate  $\gamma_1$  [Fig. 3.1] leads to a measurement record of photo detection events, and the intervals between the associated quantum jumps can be sorted according to the corresponding four different types ( $mm'$ ):

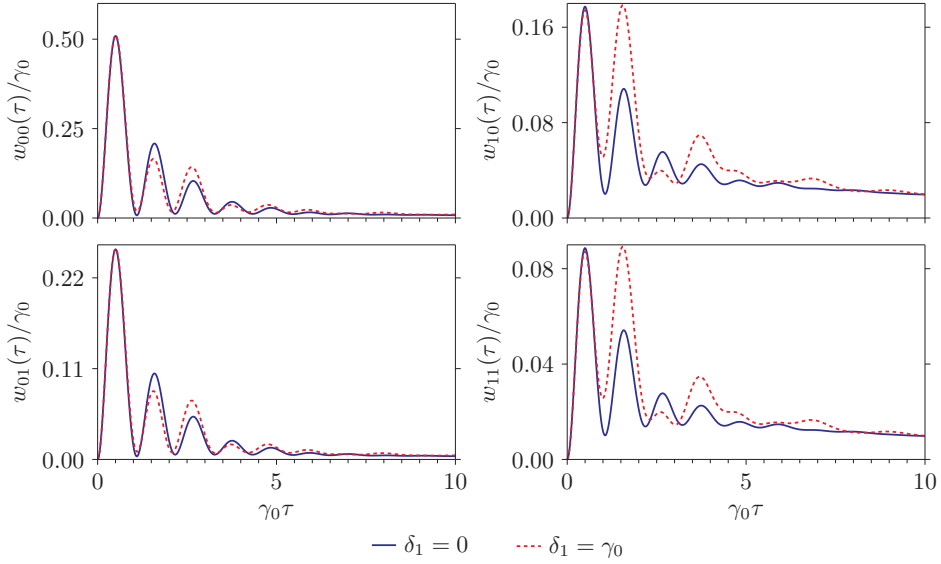


Figure 3.6: Delay functions for each of the relevant interval types in a  $\Lambda$ -type system, calculated for  $\Omega_0 = 5\gamma_0$ ,  $\Omega_1 = 3\gamma_0$ ,  $\delta_0 = 0$ ,  $\gamma_1 = 0.5\gamma_0$ , and a ground state dephasing rate  $\gamma_D = 0.1\gamma_0$ . The blue, solid lines are for the resonant case  $\delta_1 = 0$ , and the red, dotted lines are for the detuned case,  $\delta_1 = \gamma_0$ .

$$\begin{aligned}
 (00): & \quad |2\rangle \rightarrow |0\rangle \text{ after } |2\rangle \rightarrow |0\rangle & (01): & \quad |2\rangle \rightarrow |1\rangle \text{ after } |2\rangle \rightarrow |0\rangle \\
 (10): & \quad |2\rangle \rightarrow |0\rangle \text{ after } |2\rangle \rightarrow |1\rangle & (11): & \quad |2\rangle \rightarrow |1\rangle \text{ after } |2\rangle \rightarrow |1\rangle
 \end{aligned}$$

Most physical systems are prone to dephasing, e.g., due to fluctuating magnetic fields, and we model this by introducing a decoherence term in the master equations (2.9), (3.10), and (3.13) corresponding to the operator  $\hat{c}_D = \sqrt{\gamma_D}(|0\rangle\langle 0| - |1\rangle\langle 1| + |2\rangle\langle 2|)$ . The effect of this is to flip the sign of the  $|1\rangle$  amplitude relative to those of the two other states with a rate  $\gamma_D$ .

In Fig. 3.6, we show two examples of the four delay functions  $w_{mm'}(\tau)$  for the  $\Lambda$ -system, assuming perfect detection in both channels (physical parameters are given in the figure caption).

For resonant coupling on both transitions (blue, solid lines) all four waiting time distributions resemble those of a two level system in Fig. 3.2. For finite detuning (red, dashed lines) of the  $|1\rangle \leftrightarrow |2\rangle$  transition, the waiting time distribution functions after decay into  $|0\rangle$  largely maintain the same form, while after decay into  $|1\rangle$  the distributions reflect the off-resonant  $|1\rangle \rightarrow |2\rangle$  excitation process.

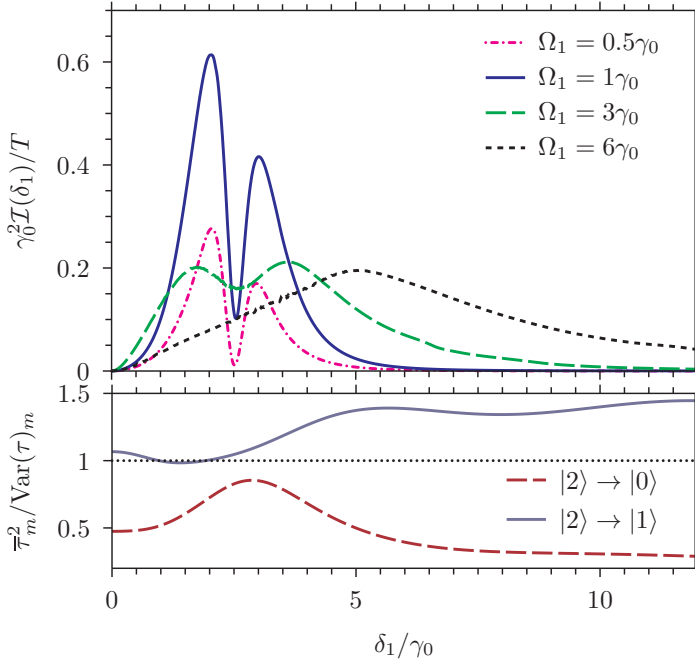


Figure 3.7: Upper panel: The Fisher information per unit time for estimation of the laser-atom detuning  $\delta_1$  by photon counting. Results are shown for different values of the Rabi frequency, from weak  $\Omega_1 = 0.5\gamma_0$  to strong  $\Omega_1 = 6\gamma_0$ , and the other parameters are  $\Omega_0 = 5\gamma_0$ ,  $\delta_0 = 0$ ,  $\gamma_1 = 0.5\gamma_0$ , and  $\gamma_D = 0.1\gamma_0$ . For  $\delta_0 = 0$ , all statistical properties of the counting signal, and hence the Fisher information, are even functions of  $\delta_1$ . Lower panel: The ratio  $\bar{\tau}_m^2 / \text{Var}(\tau)_m$  for the waiting times in the two channels as function of  $\delta_1$ . We assume  $\Omega_1 = 3\gamma_0$ , while the remaining parameters are as in the upper panel.

In Fig. 3.7 we show in the upper panel the Fisher information divided by the probing time for the estimation of the detuning  $\theta = \delta_1$  for different values of the laser Rabi frequency  $\Omega_1$ . For  $\delta_0 = 0$ , all statistical properties of the counting signal are even functions of  $\delta_1$  and, as witnessed by the vanishing Fisher information, we are not able to distinguish values of  $\delta_1$  close to  $\delta_1 = 0$ . At finite detuning, we obtain the highest Fisher information for  $\Omega_1 \simeq \gamma_0$ . For weak driving ( $\Omega_1 = 0.5\gamma_0$ ), the  $|2\rangle \leftrightarrow |1\rangle$  laser is a small perturbation in the Hamiltonian (3.21), and the absorption spectrum is characterized by resonances at  $\delta_1 = \pm\Omega_0/2$ , AC-Stark shifted by the strong  $|2\rangle \leftrightarrow |0\rangle$  coupling laser. At resonances, the gradient of  $\bar{n}_{mm'}(\tau, \delta_1)$  vanishes and, as seen from the distinct dip in the Fisher information, our

ability to discern different values of the detuning here vanishes in the limit  $\Omega_1 \rightarrow 0$ .

In the lower panel of Fig. 3.7 we show the ratio  $\bar{\tau}_m^2/\text{Var}(\tau)_m$  for the two channels as function of  $\delta_1$  and for  $\Omega_1 = 3\gamma_0$ . According to Eq. (3.15) the distribution of  $N_m$  is sub-Possionian for values of this ratio larger than unity which occur for counts in the  $|2\rangle \rightarrow |1\rangle$ -channel for almost all values of  $\delta_1$ , and super-Possionian for values smaller than unity which occur in the  $|2\rangle \rightarrow |0\rangle$ -channel for all values of  $\delta_1$ , given the remaining parameters used in this example.

Let us also investigate the parameter estimation sensitivity for a system with multiple decay channels of which only one is being observed. This situation occurs, e.g., in solid state emitters, which may relax both optically and by non-radiative coupling to the host material, and in the case of atoms which decay by emission of light in very different wavelength regions. To describe this situation, we introduce hypothetical observers, Alice and Bob, holding only partial detection records. Alice has a perfect detector that monitors only the  $|2\rangle \rightarrow |0\rangle$  channel. Her record of waiting times must then be matched to the distribution  $w_{00}(\tau)$  found from Eq. (3.13), solved for the initial state  $|0\rangle$  with  $\eta_0 = 1$  and with  $\eta_1 = 0$ . Bob, on the other hand, monitors the  $|2\rangle \rightarrow |1\rangle$  channel only, and his record of waiting times must be matched to the distribution  $w_{11}(\tau)$  found from Eq. (3.13) solved for the initial state  $|1\rangle$  with  $\eta_0 = 0$  and  $\eta_1 = 1$ . The middle time-line in Fig. 3.8(a) illustrates a full detection record while the upper (lower) line shows the detection record of Alice (Bob).

In Fig. 3.8(b), we show the waiting time distributions for two values of the detuning  $\delta_1$  (the remaining physical parameters are given in the figure caption). The achievements of optimal frequency estimation strategies based on the individual records of Alice and Bob are given by the Fisher information Eqs. (3.8) and (3.9), where the sum only has one term,  $(mm') = (00)$  for Alice and  $(mm') = (11)$  for Bob. Combining their records of waiting times, however, Alice and Bob may achieve a higher level of sensitivity. The Fisher information is then the sum of the individual Fisher informations according to Eqs. (3.8) and (3.9). We show in Fig. 3.9 the Fisher information per time for estimation of  $\delta_1$  by the separate records of Alice and Bob and by combining their registered distribution of waiting times. In Fig. 3.8(b), we observe that the delay function connected to the channel  $|2\rangle \rightarrow |0\rangle$  is less sensitive to changes in detuning than the one pertaining to the  $|2\rangle \rightarrow |1\rangle$  channel. This explains why Bob outperforms Alice at estimating the value of  $\delta_1$ .

The Fisher information for the full detection record (dash-dotted line

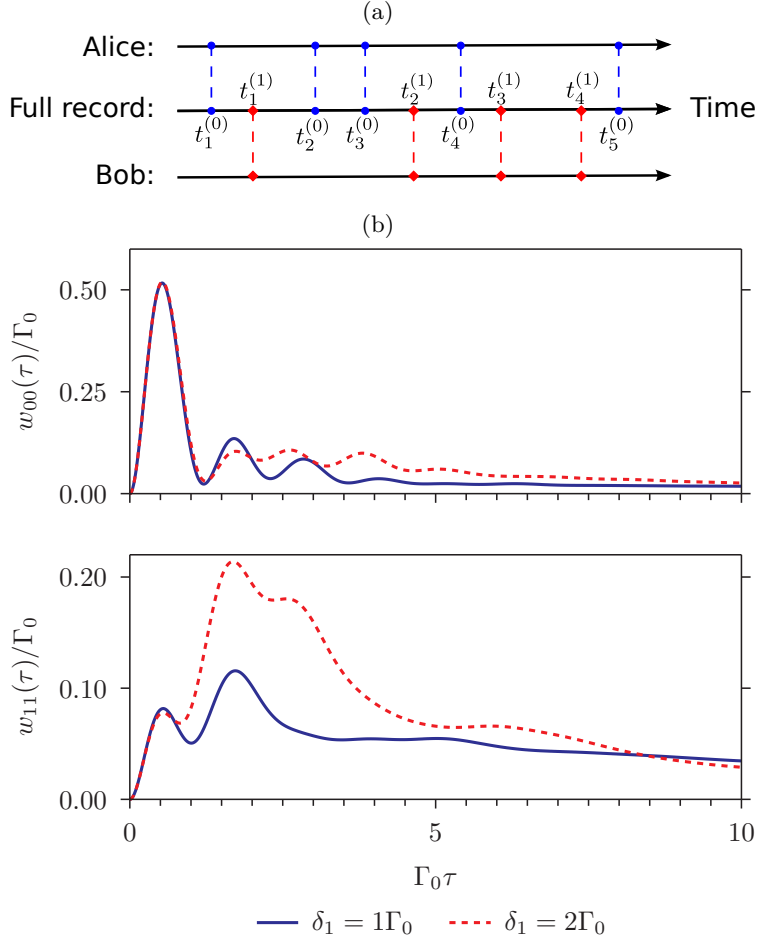


Figure 3.8: (a) Schematic illustration of the detection records of Alice and Bob (see text) and a full detection record. The blue dots at times  $t_i^{(0)}$  are emissions in the channel  $|2\rangle \rightarrow |0\rangle$  monitored by Alice. The red diamonds at times  $t_i^{(1)}$  are emissions in the channel  $|2\rangle \rightarrow |1\rangle$  monitored by Bob. The observers do not see photons from the other channel. The full record holds information on all emission events. (b) Waiting time distributions for the measurement records obtained by Alice (upper panel), monitoring only the channel  $|2\rangle \rightarrow |0\rangle$ , and by Bob (lower panel), monitoring only the channel  $|2\rangle \rightarrow |1\rangle$ . These are calculated for the parameter values  $\Omega_0 = 5\Gamma_0$ ,  $\Omega_1 = 2\Gamma_0$ ,  $\delta_0 = 0$ ,  $\Gamma_1 = \Gamma_0$ , and  $\gamma = 0.1\Gamma_0$  and shown for  $\delta_1 = \Gamma_0$  (blue, solid lines) and  $\delta_1 = 2\Gamma_0$  (red, dashed lines) respectively.

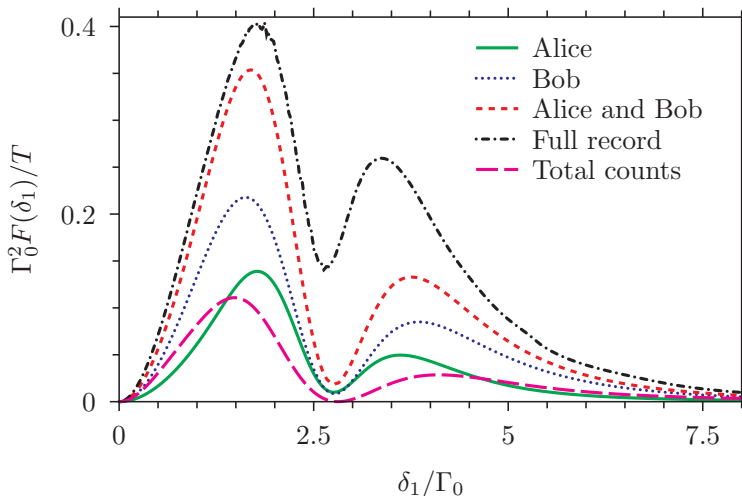


Figure 3.9: The Fisher information per time for estimation of the laser-atom detuning  $\delta_1$  in a  $\Lambda$ -type system by photon counting by Alice (green, solid line) and Bob (blue, dotted line), and by use of their combined records of waiting times (red, short-dashed line). The Fisher information from the complete detection record of both channels is shown as the dashed-dotted black curve, while the sensitivity obtained by only utilizing the total photon count [Eq. (3.22)] is shown by the purple, dashed curve. The results are calculated for the parameters  $\Omega_0 = 5\Gamma_0$ ,  $\Omega_1 = 2\Gamma_0$ ,  $\delta_0 = 0$ ,  $\Gamma_1 = 1$ , and  $\gamma = 0.1\Gamma_0$ .

in Fig. 3.9) is higher than that of Alice and Bob, even when they combine their waiting time records. This is because it makes use of all detection events and for example recognizes the first interval in Alice's record in Fig. 3.8(a) as two subsequent  $(mm') = (01)$  and  $(10)$  intervals rather than a single  $(00)$  interval.

Consider, finally, an observer who has only access to the total, accumulated photon count. For a general multi-channel emitter the mean photo current in the asymptotic limit is  $\bar{N}/T = \sum_m \text{Tr}(\hat{c}_m^\dagger \hat{c}_m \rho^{(\text{ss})})$ . For general counting statistics, we have  $\Delta N = \sqrt{V}$ . This implies an uncertainty on  $\theta$  given by  $\Delta\theta = (\partial N/\partial\theta)^{-1} \sqrt{V}$ , i.e., for detuning estimation in our  $\Lambda$ -atom,

$$\frac{(\Delta\delta_1)^{-2}}{T} = \frac{(\gamma_0 + \gamma_1)^2}{\gamma_0 \frac{\text{Var}(\tau)_0}{\bar{\tau}_0^2} + \gamma_1 \frac{\text{Var}(\tau)_1}{\bar{\tau}_1^2}} \frac{(\partial\rho_{22}^{(\text{ss})}/\partial\delta_1)^2}{\rho_{22}^{(\text{ss})}}, \quad (3.22)$$

where we have used Eq. (3.15) and  $V = V_0 + V_1$ . By Eq. (2.3) this can be directly compared to the Fisher information per time, and the result

of Eq. (3.22) is included as the purple, long-dashed curve in Fig. 3.9. As expected, parameter estimates obtained from the full record and from the combined waiting time records of Alice and Bob achieve higher sensitivity on the whole detuning range.

### 3.5 Conclusion

The full photo detection record of a quantum emitter contains more information about its dynamics than the mean signal. In this chapter, we have formulated a theory that quantifies this by calculating the Cramér-Rao sensitivity limit for multi-channel quantum light emitters: The information in the full photo detection record may be represented as waiting time distributions which may be readily calculated using the theory presented here, and which, by Eq. (3.3), supply the fundamental sensitivity limit (2.3). This optimal limit may be achieved via the linear estimator Eq. (3.17) or by a maximum likelihood estimate [92, 131]. We exemplified the theory by the estimation of a detuning parameter in a driven  $\Lambda$ -type system with two distinct decay channels and discussed the effect of finite detection efficiency in Rabi frequency estimation.

Our theory assumes an ergodic emitter, i.e., the system has a steady state which does not depend on the initial state of the system and which is not a dark state, such that the amount of accumulated data grows linearly with time. We also assumed that the decay of the system always feeds the same discrete set of final states, so that the data record can be analysed by a finite number of waiting time functions. Both the ergodicity assumption and the restriction to a finite number of final states are technical conditions for our method to apply, while the underlying Bayesian description is readily applied and several of the concepts introduced in this chapter can be modified to account for the sensitivity limit in more general cases.

# Homodyne detection

*This chapter is reproduced from Ref. [4] with only minor modifications and a few paragraphs omitted due to their overlap with Chapter 2.*

---

The previous chapter shows how a full, time-resolved photon counting record yields a larger sensitivity to unknown parameters than the mean fluorescence signal. The reason is that, unlike the mean fluorescence intensity, which is given by the steady state excitation of the atom and saturates for strong driving, the transient evolution triggered by a photon count and accompanying quantum jump shows oscillations at the Rabi driving frequency which leads to a better resolution of large Rabi frequencies and other interaction parameters

In this chapter, we investigate the alternative situation of continuous homodyne detection of the field emitted by a quantum system; see Fig. 4.1. It is theoretically interesting to study the achievements of homodyne detection for precision measurements since, as illustrated in Fig. 2.3, the character of the signal and the measurement backaction are very different from those of photon counting. Such a study is further motivated by the extensive use of homodyne detection in optics where it often offers high efficiency and practical advantages over photon counting and in probing of microwave fields; e.g., in circuit QED [167, 168], where photon counters are not available.

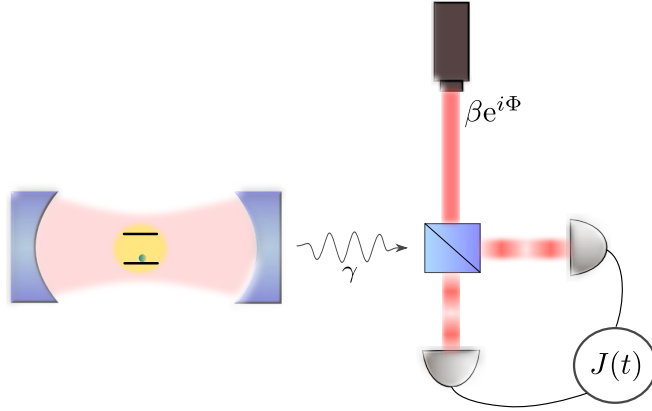


Figure 4.1: Schematic experimental setup for balanced homodyne detection. The emission from the probed quantum system (here a two-level system in a cavity) is mixed with a strong local oscillator field with relative phase  $\Phi$  in a 50/50 beamsplitter. The output ports are monitored by photo detectors and the homodyne current  $J(t)$  is the difference between the two signals.

## 4.1 Quantum trajectories for homodyne detection

Homodyne detection performs an amplitude measurement of the radiation emitted from a quantum probe by mixing it with a strong local oscillator; see Fig. 4.1. As outlined in Sec. 2.2, the homodyne current varies according to the current state  $\rho^{(J)}(t)$  of the system and random, shot-noise, fluctuations,

$$J(t) = \text{Tr} \left[ \mathcal{X}_\Phi \rho^{(J)}(t) \right] + \frac{dW_t}{dt}, \quad (4.1)$$

where the measurement operator  $\mathcal{X}_\Phi \rho = \sqrt{\eta}(\hat{c}e^{-i\Phi} \rho + \rho \hat{c}^\dagger e^{i\Phi})$  is given by the atomic dipole lowering operator  $\hat{c}$ ,  $\Phi$  is the phase of the local oscillator, and  $\eta$  is the efficiency of the photo detectors. Notice that compared to Sec. 2.2, I have in this chapter chosen a different normalization of the homodyne current,  $J(t) = dY_t/dt$  with  $dY_t$  given in Eq. (2.14). The evolution of the system is, in turn, conditioned on the measurement results [134],

$$d\rho^{(J)} = \mathcal{L}\rho^{(J)} dt + dW_t \left[ \mathcal{X}_\Phi - \text{Tr} \left( \mathcal{X}_\Phi \rho^{(J)} \right) \right] \rho^{(J)}, \quad (4.2)$$

which is the normalized version of the stochastic master equation (2.16).

While our formalism and general analysis are valid for any quantum system, we shall again exemplify the results and methods by considering

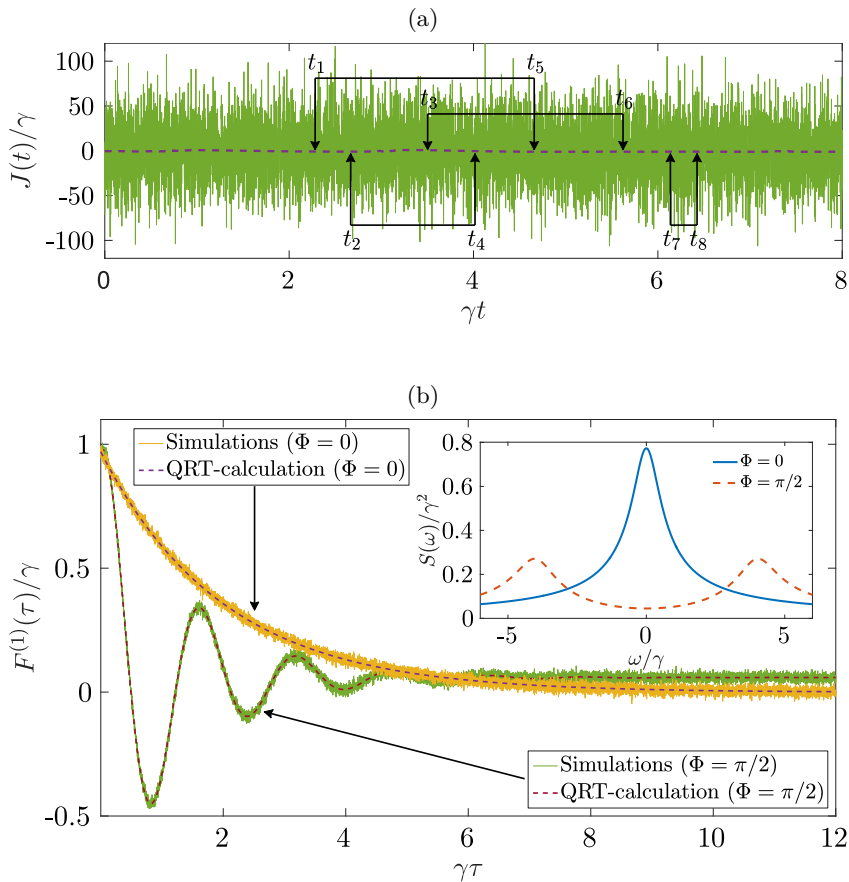


Figure 4.2: (a) An example of a homodyne current obtained by simulating the monitoring of a two-level system according to Eqs. (4.1) and (4.2) is shown as the noisy green curve. The mean signal is indicated by the dashed purple line. The signal shows non-trivial temporal correlations, e.g., between the different times connected with arrows in the figure. (b) The two-time homodyne current correlations Eq. (4.9) averaged over 5000 independent realizations of  $J(t)$ . The quantum regression theorem Eq. (4.10) yields the theoretical results shown with purple and red, dashed curves. The inset shows the power spectrum of the homodyne current Eq. (4.11) for a Rabi frequency of  $\Omega = 4\gamma$  for two choices of the local oscillator phase,  $\Phi = 0$  ( $\hat{\sigma}_x$ -probing) and  $\Phi = \pi/2$  ( $\hat{\sigma}_y$ -probing).

estimation of the Rabi frequency  $\Omega$  of monochromatic laser driving of a single atomic system for which the Hamiltonian is given in Eq. (2.6). If the system decays from the excited to the ground state at a rate  $\gamma$ , we have  $\hat{c} = \sqrt{\gamma}\sigma_-$ . By adjusting the local oscillator phase  $\Phi$ , one may choose which spin component  $\hat{\sigma}_\Phi = \cos \Phi \hat{\sigma}_x - \sin \Phi \hat{\sigma}_y$  is effectively probed. For  $\Phi = 0(\pi/2)$  in particular, the  $\hat{\sigma}_x(\hat{\sigma}_y)$ -component of the spin is measured. It follows from Eq. (4.1) that the measurement backaction in Eq. (4.2), corresponding to a particular phase  $\Phi$ , causes a rotation of the spin towards the axis defined by  $\hat{\sigma}_\Phi$ .

## 4.2 Fisher information and Bayesian inference

In a continuous homodyne measurement, the output data is the stochastic measurement current,  $D_t = \{J(t') | 0 \leq t' \leq t\}$ , and the Bayesian procedure, presented in Chapter 2, allows a full analysis of such a continuous measurement record which takes all the available information into account. Figure 2.4 in Chapter 2 presents a simulation of this procedure where the probability density for the unknown Rabi frequency  $\Omega$  is updated according to a homodyne current (4.1), simulated from the true value  $\Omega_0 = 2\gamma$ . The red lines track the best estimate  $S_\theta(D_t) = \max_\theta [P(\theta|D_t)]$ , while the dashed, black lines indicate the width of the probability distribution. For probing of  $\hat{\sigma}_y$  in Fig. 2.4(a), the distribution quickly becomes normal as demanded by the central limit theorem, and we observe a smooth convergence of the most likely value around the true  $\Omega_0 = 2\gamma$  used to simulate the measurement record  $J(t)$ . For probing of  $\hat{\sigma}_x$ , shown in panel Fig. 2.4(b), the convergence is much slower, and as reflected by the broader distribution at  $\gamma t = 50$ , less information is gained per time. This is due to the fact that the Hamiltonian Eq. (2.6) commutes with the  $\hat{\sigma}_x$ -operator, and as we shall discuss below, the finite information stems from higher order temporal correlations in the signal decaying with a  $\Omega$ -dependent rate.

The uncertainties in the estimates are provided by the CRB (2.3), and by Eq. (2.8), the Fisher information (2.2) of the full signal may be expressed as

$$\mathcal{I}(\theta) = \mathbb{E} \left[ \frac{1}{\text{Tr}(\tilde{\rho}^{(J)})^2} \left( \frac{\partial \text{Tr}(\tilde{\rho}^{(J)})}{\partial \theta} \right)^2 \right]. \quad (4.3)$$

By defining  $\zeta = \frac{1}{\text{Tr}(\tilde{\rho}^{(J)})} \frac{\partial \tilde{\rho}^{(J)}}{\partial \theta_i}$ , the Fisher score is  $\text{Tr}(\zeta)$  [169], and the equation of evolution derived from Eq. (2.16),

$$d\zeta = \left( \mathcal{L}\zeta + \frac{\partial \mathcal{L}}{\partial \theta} \rho^{(J)} \right) dt + dW_t \left( \mathcal{X}_\Phi \zeta + \frac{\partial \mathcal{X}_\Phi}{\partial \theta} \rho^{(J)} - \text{Tr}(\mathcal{X}_\Phi \rho^{(J)}) \zeta \right), \quad (4.4)$$

allows calculation of the classical Fisher information,  $\mathcal{I}(\theta) = \mathbb{E} \left[ \text{Tr}(\zeta)^2 \right]$  without numerical evaluation of derivatives of noisy quantities [92]. Note that we must simultaneously solve Eq. (4.2) for the accompanying normalized state  $\rho^{(J)}(t)$ . Unlike operator expectation values for which the average over trajectories is equivalent to results obtained by the unconditioned density matrix, we do not have a deterministic theory for the average of a nonlinear expression such as  $\mathbb{E} \left[ \text{Tr}(\zeta)^2 \right]$ . Equation (4.4) may, however, be simulated in a trajectory analysis and the Fisher information Eq. (4.3) obtained by averaging over many trajectories. In Fig. 4.3(a), we show an example of such a calculation with 100 000 trajectories for the Fisher information  $\mathcal{I}_\Phi(\Omega)$  as a function of the local oscillator phase. We find that asymptotically, the Fisher information grows linearly with time  $T$ , and the figure shows the value of the scaled quantity  $\gamma \mathcal{I}_\Phi(\Omega)/T$ . As anticipated from the Bayesian studies in Fig. 2.4, the Fisher information takes its largest values when  $\Phi \simeq \pi/2$ . Our numerical simulations of the two level system dynamics for  $\Phi = \pi/2$ , show that, for all values of the Rabi frequency  $\Omega$ , homodyne detection indeed reaches a Fisher information of  $\mathcal{I}_{\pi/2}(\Omega) = 4T/\gamma$ , and just as for photon counting, it is for this example identical to the QFI (2.25)! This result is illustrated in Fig. 4.4.

To gain analytical insight in the results, we consider the case of weak driving ( $\Omega \ll \gamma$ ), where we can use the Holstein-Primakoff approximation [123] and replace the two-level system by a driven oscillator ( $\hat{\sigma}_- \rightarrow \hat{a}$ , with  $\hat{\sigma}_x = \hat{\sigma}_- + \hat{\sigma}_+$  in Eq. (2.6), where  $\hat{a}$  is a bosonic annihilation operator). Thanks to the simple algebra of oscillator observables, Eq. (2.16) may be solved exactly [170],

$$\begin{aligned} \tilde{\rho}^{(J)}(t) &= e^{(\mathcal{L} - \frac{1}{2} \mathcal{X}_\Phi^2)t} e^{\int_0^t dt' J(t') \tilde{\mathcal{X}}_\Phi(t')} \\ &\times e^{\frac{\Omega\sqrt{\gamma}}{\delta^2 + (\gamma/2)^2} \int_0^t dt' J(t') e^{-\gamma/2t'} \left[ \delta \cos(\delta t' + \Phi) + \frac{\gamma}{2} \sin(\delta t' + \Phi) \right]} \rho(t=0), \end{aligned} \quad (4.5)$$

where  $\tilde{\mathcal{X}}_\Phi(t)\rho = \left( e^{-i(\delta t + \Phi)} \hat{c}\rho + \rho \hat{c}^\dagger e^{i(\delta t + \Phi)} \right) e^{-\frac{\gamma}{2}t}$  and we allow for a finite laser-atom detuning  $\delta$ . Picking the initial state  $\rho(t=0)$  as the coherent steady state  $|-i\frac{\Omega}{\gamma}\rangle$ , the Fisher information Eq. (4.3) is readily obtained and it yields the result  $\mathcal{I}_{\pi/2}(\Omega) = 4T/\gamma$ , as expected.

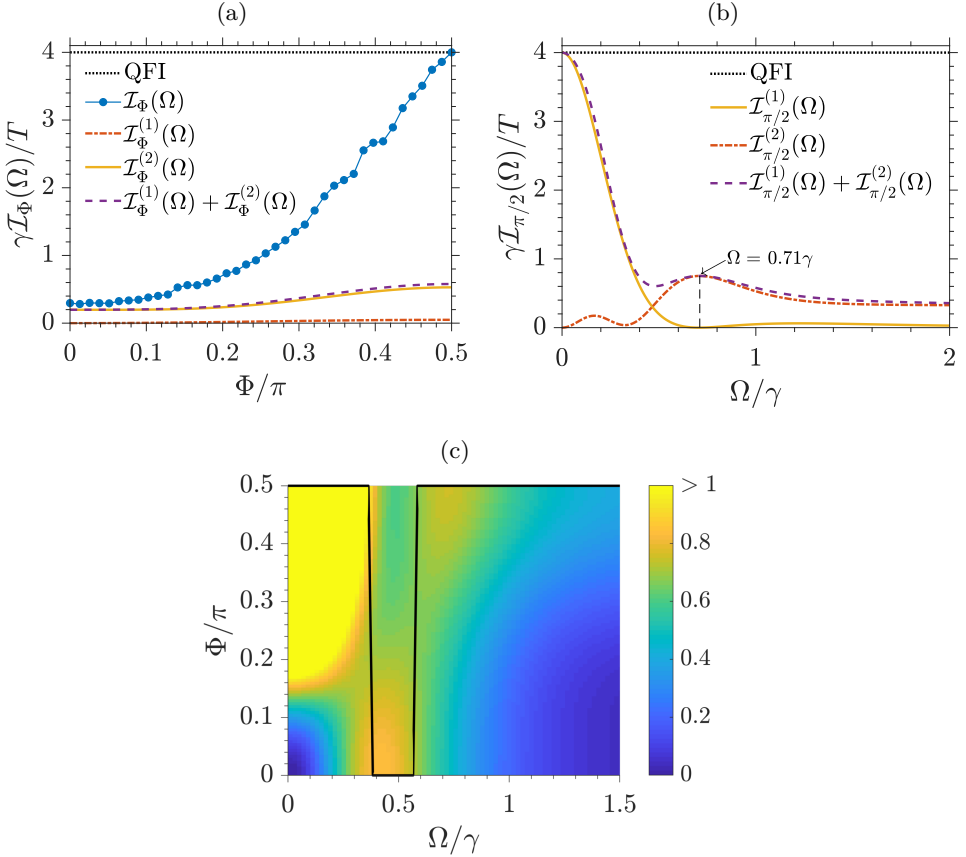


Figure 4.3: Contributions to the Fisher information  $\mathcal{I}_\Phi(\Omega)$  per time  $T$  for Rabi frequency estimation in a resonantly driven two-level system. The Fisher information is upper bounded by the value  $4T/\gamma$  of the QFI, which is independent of the Rabi frequency, and it is lower bounded by the information retrieved by the integrated (mean) signal  $\mathcal{I}_\Phi^{(1)}(\Omega)$ .  $\mathcal{I}_\Phi^{(2)}(\Omega)$  describes the information provided by the two-time correlations in the homodyne current. Results are shown in (a) as a function of the local oscillator phase  $\Phi$  for  $\Omega = \gamma$  and in (b) as a function of the Rabi frequency  $\Omega$  for  $\Phi = \pi/2$ . In (c), the value of  $\mathcal{I}_\Phi^{(1)}(\Omega) + \mathcal{I}_\Phi^{(2)}(\Omega)$  per time  $T$  is indicated by the color scheme as a function of  $\Phi$  and  $\Omega$ , and the maximum value is tracked by the black line.

### 4.3 Properties of the homodyne signal

It is remarkable that at resonant driving the Bayesian analysis of the homodyne detection signal has the same sensitivity for all values of the Rabi frequency, and that it completely exhausts the information about the Rabi frequency present in the quantized multi-mode radiation field. This ability springs from the fact that we are not only using the integrated signal but also the temporal correlations established by the measurement backaction during the continuous probing of the system, see Fig. 4.2. We refer the reader to Ref. [140] for an analysis of the case of finite laser-atom detuning.

The instantaneous homodyne current (4.1) is dominated by noise, and it provides useful information only when it is integrated over a finite time. We define the average signal from the time  $t = 0$  until time  $t = T$ ,

$$Y \equiv \lim_{T \rightarrow \infty} \frac{1}{T} \int_0^T dt J(t), \quad (4.6)$$

with the mean value

$$I = \mathbb{E}[Y] = \text{Tr} \left( \mathcal{X}_\Phi \rho^{(\text{ss})} \right). \quad (4.7)$$

Note that due to Eq. (4.1),  $J(t) - \mathbb{E}[J(t)] = \frac{dW_t}{dt}$ . Hence, the variance on the integrated current stems from white noise, Eq. (2.15), and we find

$$\text{var}(Y) = \frac{1}{T}. \quad (4.8)$$

The integrated signal thus allows extraction of the average system properties with a relative error decreasing as  $1/\sqrt{T}$ , and the same temporal scaling applies to the estimation error for any system parameter. Due to saturation, however, the steady state properties of the signal may depend only very weakly on the Rabi driving frequency. This is where correlations within the signal may hold further important information due to the transients triggered by the backaction of the continuous homodyne measurement. We shall here specifically address the two-time correlation function of the homodyne current to study the information gained by including two-time correlations together with the integrated signal in the analysis. While we choose to consider this restriction for matter of analysis, we note that experimental hardware may provide a data record that has been reduced to provide only the two-time correlation function, equivalent to the power spectrum of the homodyne current which can be directly sampled by a spectrum analyzer.

### 4.3.1 Two-time correlations

Two-time correlations in the signal are extracted as the average value

$$C(\tau) \equiv \lim_{T \rightarrow \infty} \frac{1}{T - \tau} \int_0^{T-\tau} dt J(t + \tau) J(t), \quad (4.9)$$

where, in the limit of long probing times, the initial state may be taken as the steady state, and  $C(\tau)$  depends only on the time-difference  $\tau$ .

Repeating the experiment (or repeating the quantum trajectory simulation) yields  $N$  independent samples of the current  $J(t)$  and thereby  $N$  independent realizations of the integrated signal Eq. (4.6) and the auto-correlation function Eq. (4.9). In Fig. 4.2(b), the two-time correlations Eq. (4.9) are averaged over 5000 such simulated homodyne currents. Note the oscillatory behavior for  $\hat{\sigma}_y$ -probing while  $\hat{\sigma}_x$ -probing merely triggers an exponentially decaying transient.

The average over many independent samples of the homodyne current  $J(t)$  can be calculated deterministically by the quantum regression theorem (QRT),

$$F^{(1)}(\tau) \equiv \mathbb{E}[C(\tau)] = \text{Tr} \left( \mathcal{X}_\Phi e^{\mathcal{L}\tau} \mathcal{X}_\Phi \rho^{(\text{ss})} \right) + \delta(\tau), \quad (4.10)$$

and it perfectly matches the simulated data in Fig. 4.2(b).

The Fourier transform of the two-time correlation function is the power spectrum  $S_\Phi(\omega)$  of the homodyne signal,

$$S(\omega) = \int_{-\infty}^{\infty} d\tau F^{(1)}(\tau) e^{-i\omega\tau}. \quad (4.11)$$

As seen in the inset of Fig. 4.2(b),  $\hat{\sigma}_x$ -probing yields a single frequency peak at the atomic resonance frequency, while  $\hat{\sigma}_y$ -probing gives a signal with frequency components at  $\pm\Omega$  and hence yields much more information on the Rabi frequency. The widths of the peaks and equivalently the decay rates of the two-time correlation functions in Fig. 4.2(b), however, depend weakly on the Rabi frequency. This is what allows information to be obtained also by  $\hat{\sigma}_x$ -probing and constitutes the basis for the slow convergence of the Bayesian estimate in Fig. 2.4(b). Together the spectra reflect the three peaks of the well-known Mollow triplet of fluorescence from a driven two-level emitter [171].

### 4.3.2 Fisher information from two-time correlations

We shall now evaluate the Fisher information associated with the integrated signal and the two-time correlations in the homodyne signal current, as if

only those quantities are made available for the estimation of the unknown parameter  $\theta$ . Burgarth *et al.* [143] considers parameter estimation by discrete, sequential measurements on a quantum system, and shows that as the number  $N$  of measurement data increases, the probability distribution of functionals of the data (e.g., mean values and multi-time correlations) become asymptotically normal.

Homodyne detection is a continuous measurement, and to apply the results of Ref. [143] to our problem, we consider initially the current  $J(t_i)$  at  $N$  discrete times  $t_i$ , where  $t_{i+1} - t_i = \Delta t = T/N$ . Then

$$\begin{aligned} Y &= \frac{1}{N} \sum_{i=1}^N J(t_i), \\ C_l &= \frac{1}{N-l} \sum_{i=1}^{N-l} J(t_i) J(t_i + t_l), \end{aligned} \quad (4.12)$$

approximate Eqs. (4.6) and (4.9), and Ref. [143] assures that  $\mathbf{X} = (I, C_1, \dots, C_L)^T$  is a multivariate Gaussian random variable, i.e., the probability  $P(\mathbf{X})$  becomes asymptotically normal for large  $N$ ,

$$P(\mathbf{X}) \propto e^{\frac{1}{2}(\mathbf{X} - \mathbb{E}[\mathbf{X}])^T \boldsymbol{\Sigma}^{-1} (\mathbf{X} - \mathbb{E}[\mathbf{X}])}. \quad (4.13)$$

Here the covariance matrix  $\boldsymbol{\Sigma}$  of  $\mathbf{X}$  has elements

$$\Sigma_{ij} = \mathbb{E}[(X_i - \mathbb{E}[X_i])(X_j - \mathbb{E}[X_j])]. \quad (4.14)$$

The first diagonal element of the covariance matrix is given simply by Eq. (4.8),  $\Sigma_{00} = 1/T$ , while the evaluation of the covariances between the sampled autocorrelations with different time delays  $\tau$  involves up to four-time correlations in the measurement signal,

$$\begin{aligned} \Sigma(\tau, \tau') &= \lim_{T \rightarrow \infty} \frac{1}{(T - \tau)^2} \int_0^{T-\tau} dt \int_0^{T-\tau} dt' \\ &\quad \mathbb{E} \left[ \left( J(t + \tau) J(t) - F_{\Phi}^{(1)}(\tau) \right) \left( J(t' + \tau') J(t') - F_{\Phi}^{(1)}(\tau') \right) \right]. \end{aligned} \quad (4.15)$$

The four-time correlations, and more general multi-time correlation functions, are quantified by products of the current readout at multiple times with definite separation intervals, and when averaged over the time argument of the first readout and over many independent realizations, they

read

$$F_{\Phi}^{(n/2)}(\{\tau_j\}) \equiv \left\langle \prod_{i=1}^n J\left(\sum_{1 \leq j \leq i} \tau_j\right) \right\rangle = \text{Tr} \left( \prod_{i=1}^n \left( \mathcal{X}_{\Phi} e^{\mathcal{L}\tau_i} \right) \mathcal{X}_{\Phi} \rho_{\text{st}} \right) \quad (4.16)$$

for  $\tau_i > 0$ , where  $\langle \cdot \rangle$  denotes an average over the time  $\tau_1$ . The covariance matrix elements thus follow from time-ordered integration of four-time correlation functions given in Eq. (4.16). Notice, however, that this seemingly complicated task becomes remarkably simple due to the noise properties of the homodyne signal, see Fig. 4.2(a). In fact, the leading contribution to the integrand stems from the noise terms in Eq. (4.1) when the time arguments match two by two in Eq. (4.15), i.e., to leading order in  $1/dt$  we obtain,

$$\begin{aligned} \Sigma(\tau, \tau') &\simeq \lim_{T \rightarrow \infty} \frac{1}{(T - \tau)^2} \int_0^{T-\tau} dt \int_0^{T-\tau} dt' \mathbb{E} \left[ \frac{dW_t}{dt} \frac{dW_{t+\tau}}{dt} \frac{dW'_t}{dt} \frac{dW'_{t+\tau'}}{dt} \right] \\ &= \lim_{T \rightarrow \infty} \frac{1}{(T - \tau)^2} \int_0^{T-\tau} dt \int_0^{T-\tau} dt' \delta(t - t') \delta(\tau - \tau') \\ &= \frac{\delta(\tau - \tau')}{T}, \end{aligned} \quad (4.17)$$

where we applied Eq. (2.15) at the second step.

Equation (4.17) implies  $\Sigma_{ij} = \frac{\delta_{ij}}{T\Delta t}$  for  $i, j > 0$ . Remarkably, the covariance matrix is diagonal, and to leading order in  $1/T$  there is no covariance between the autocorrelations at different times. We have verified this numerically by the covariances between the simulated data shown in Fig. 4.2(b). The variance increases as the numerical  $C_I$ -grid is made finer, leading to a convergence of the information as  $\Delta t$  is decreased.

As seen in Fig. 4.2(b) the two-time correlation function Eq. (4.10) approaches  $I^2$  for large correlation times  $\tau$  and suggests that the mean current and the asymptotic correlation are correlated. To avoid the trivial covariance between  $Y$  and  $C(\tau)$  we therefore subtract the expected integrated signal contribution from the correlations,

$$C(\tau) \rightarrow C(\tau) - I^2 \quad \text{and} \quad F_{\Phi}^{(1)}(\tau) \rightarrow F_{\Phi}^{(1)}(\tau) - I^2. \quad (4.18)$$

Without omitting any contributions to the total information acquired from the experiments, this ensures that  $\Sigma_{0l} = \Sigma_{l0} = 0$ .

The Fisher information matrix of a multivariate normal distribution is well-known,

$$\mathcal{I}_{\text{MV}}(\theta) = \frac{\partial \mathbb{E}[\mathbf{X}]^T}{\partial \theta} \Sigma^{-1} \frac{\partial \mathbb{E}[\mathbf{X}]}{\partial \theta} + \frac{1}{2} \text{Tr} \left( \Sigma^{-1} \frac{\partial \Sigma}{\partial \theta} \Sigma^{-1} \frac{\partial \Sigma}{\partial \theta} \right). \quad (4.19)$$

The inverted covariance matrix is proportional to the total time of probing, and since the latter term in Eq. (4.19) does not scale with  $T$  and hence becomes asymptotically negligible, we find  $\mathcal{I}_{\text{MV}}(\theta) = \mathcal{I}^{(1)}(\theta) + \mathcal{I}^{(2)}(\theta)$ , where

$$\mathcal{I}^{(1)}(\theta) = T \left( \frac{\partial I}{\partial \theta} \right)^2 \quad (4.20)$$

$$\mathcal{I}^{(2)}(\theta) = T \sum_i \left( \frac{\partial \mathbf{F}}{\partial \theta} \right)_i^2 \Delta\tau. \quad (4.21)$$

Equation (4.20) yields the contribution to the Fisher information from the integrated signal, and we may finally take the continuum limit  $\Delta\tau \rightarrow d\tau$  to find the contribution from two-time signal correlations,

$$\mathcal{I}^{(2)}(\theta) = T \int_{\tau_{\min}}^{\tau_{\max}} d\tau \left( \frac{\partial F^{(1)}(\tau)}{\partial \theta} \right)^2. \quad (4.22)$$

By Eq. (4.11), a spectral analysis yields the same information as a direct analysis of the two-time correlated time series. In fact, we may apply Plancherel's theorem (unitarity of the Fourier transform) in Eq. (4.22) to obtain the expected Fisher information from the spectrum,

$$\mathcal{I}^{(2)}(\theta) = T \int_{-\infty}^{\infty} d\omega \left( \frac{\partial S(\omega)}{\partial \theta} \right)^2. \quad (4.23)$$

### 4.3.3 Achieving the Cramér-Rao Bound with a linear filter

As proven by Fisher [131], a Bayesian analysis saturates the Cramér-Rao bound and allows parameter estimation with a precision given by the Fisher information. Like in the case of photon counting, the CRB may, however, equivalently be saturated by applying a linear filter to the data available for the estimation process.

The Fisher information associated with the integrated signal  $Y$  and two-time correlations  $C(\tau)$  takes a simple form Eqs. (4.20) and (4.22), and for a given experimental realization of  $Y$  and  $C(\tau)$ , an unbiased estimator  $S_\theta(D_t)$ , for which the variance is minimized and the CRB reached, exists. Suppose that asymptotically the parameter value has been identified to a small vicinity  $\delta\theta$  around a value  $\theta_0$ . With the Fisher information

$\mathcal{I}^{(1)}(\theta_0) + \mathcal{I}^{(2)}(\theta_0)$  this estimator is given explicitly by the linear filter,

$$S_{\delta\theta}(D_T) = \frac{T}{\mathcal{I}^{(1)}(\theta_0) + \mathcal{I}^{(2)}(\theta_0)} \left[ \frac{\partial I(\theta)}{\partial \theta} \Big|_{\theta=\theta_0} (Y - I(\theta_0)) + \int d\tau \frac{F^{(1)}(\tau, \theta)}{\partial \theta} \Big|_{\theta=\theta_0} (C(\tau) - F^{(1)}(\tau, \theta_0)) \right]. \quad (4.24)$$

This expression represents a first order correction to the initial estimate  $\theta_0$  according to the dissimilarity between the expected and the recorded signal, and by normalizing the estimate by the Fisher information per time, it ensures that larger uncertainties allow larger adjustments. The linear filter is valid in the asymptotic limit where  $\delta\theta$  is small.

#### 4.3.4 Rabi frequency estimation

We turn now to the example of Rabi frequency estimation in a resonantly driven two-level system Eq. (2.6) where all calculations are straightforward. We consider first perfect detection ( $\eta = 1$ ).

The Fisher information from the mean signal Eq. (4.20) is

$$\frac{\mathcal{I}_{\Phi}^{(1)}(\Omega)}{T} = 4\gamma^3 \left[ \frac{2\Omega^2 - \gamma^2}{(2\Omega^2 + \gamma^2)} \right] \sin^2 \Phi. \quad (4.25)$$

For  $\Phi = 0$ ,  $F_{\Phi}^{(1)}(\tau)$  may be evaluated analytically,

$$F_0^{(1)}(\tau) = \frac{2\Omega^2 \gamma e^{-\gamma\tau/2}}{2\Omega^2 + \gamma^2}, \quad (4.26)$$

leading to a Fisher information,

$$\frac{\mathcal{I}_0^{(2)}(\Omega)}{T} = \frac{16\Omega^2 \gamma^6}{(2\Omega^2 + \gamma^2)^4}. \quad (4.27)$$

The general expression for  $F_{\pi/2}^{(1)}$  is more complicated. An example is shown in Fig. 4.2(b).

In Fig. 4.3(a), we compare  $\mathcal{I}_{\Phi}^{(1)}(\Omega)$ ,  $\mathcal{I}_{\Phi}^{(2)}(\Omega)$  and the total contribution for at most two-time correlations in the signal  $\mathcal{I}_{\Phi}^{(1)}(\Omega) + \mathcal{I}_{\Phi}^{(2)}(\Omega)$  to the QFI and the Fisher information of the full signal Eq. (4.3). Results are shown as a function of  $\Phi$  for  $\Omega = \gamma$ . Because the steady state solution in Eq. (4.7) has no  $\hat{\sigma}_x$ -component, the information  $\mathcal{I}_{\Phi}^{(1)}$  from the integrated signal is

maximized for  $\Phi = \pi/2$ , while it vanishes for  $\Phi = 0$ . As discussed after Eq. (4.11) two-time correlations, on the other hand, are able to extract information from  $\hat{\sigma}_x$ -probing.

The information in the full signal  $\mathcal{I}_\Phi(\Omega)$  in Fig. 4.3(a) is much higher than the contributions from the integrated signal  $\mathcal{I}_\Phi^{(1)}(\Omega)$  and two-time correlations  $\mathcal{I}_\Phi^{(2)}(\Omega)$ , reflecting that higher order correlations in the signal are responsible for the bulk of the information extracted by the Bayesian protocol. For  $\Phi = 0$ , however, the main part of the information stems from just two-time correlations.

In Fig. 4.3(c), we show in colors the dependence of the Fisher information  $\mathcal{I}_\Phi^{(1)}(\Omega) + \mathcal{I}_\Phi^{(2)}(\Omega)$  on the phase  $\Phi$  of the local oscillator and on the applied Rabi frequency  $\Omega$ . While the information from two-time correlations is maximal close to  $\Omega \simeq 0.5\gamma$  for all  $\Phi$ , the integrated signal favours  $\Omega = 0$  and  $\Phi = 0$ . This leads to a combined Fisher information with three distinct maxima, and we track by the black line, the optimal local oscillator phase for different values of the Rabi frequency. Surprisingly, in the vicinity of  $\Omega = 0.5\gamma$ ,  $\Phi = 0$  is the optimal choice while in general  $\Phi = \pi/2$  is optimal. There is no range, where an intermediate value of the phase  $0 < \Phi < \pi/2$  is favourable.

In Fig. 4.3(b) the comparison is performed as a function of the actual value of the Rabi frequency for  $\Phi = \pi/2$ . The information is upper bounded by the QFI and, as evidenced by the large discrepancy between the QFI (2.25) and  $\mathcal{I}_{\pi/2}^{(1)}(\Omega) + \mathcal{I}_{\pi/2}^{(2)}(\Omega)$ , the main part of the full information comes from higher order correlations.

Below saturation ( $\Omega < \gamma/2$ ) the main part of  $\mathcal{I}_{\pi/2}^{(1)}(\Omega) + \mathcal{I}_{\pi/2}^{(2)}(\Omega)$  comes from the integrated signal. In fact, for  $\Omega = 0$  we find from Eq. (4.25) that  $\mathcal{I}_{\pi/2}^{(1)}(\Omega)/T = 4/\gamma$  which even matches the QFI (2.25). Considering two-time correlations we find for  $\Omega \ll \gamma$ ,  $F_{\pi/2}^{(1)}(\tau) \simeq -2\Omega^2 e^{-\gamma t/2}/\gamma$ , so by Eq. (4.22), the Fisher information is

$$\frac{\mathcal{I}_{\pi/2}^{(2)}(\Omega)}{T} \simeq \frac{16\Omega^2}{\gamma^3}. \quad (4.28)$$

The Fisher information, Eq. (4.22) involves the square of the derivative of the correlation functions with respect to the sought parameter, so Eq. (4.28) hints, that the  $n$ -time correlation functions scale as  $\Omega^n$ , leading to contributions to the total classical Fisher information scaling as  $\Omega^{2n-2}$ . To prove this relationship, we Taylor expand  $e^{\mathcal{L}\tau}$  and  $\rho^{(\text{ss})}$  to lowest non-vanishing order in  $\Omega/\gamma$ . Via Eq. (4.16) this reveals that for  $\Omega/\gamma \ll 1$ , we

indeed have  $F_{\pi/2}^{(n/2)}(\{\tau_j\}) \propto \Omega^n$ . Hence, we obtain for small  $\Omega$  a series expansion,

$$\mathcal{I}_{\pi/2}(\Omega) = a_0 + \Omega^2 a_2 + \Omega^4 a_4 + \dots, \quad (4.29)$$

where the  $a_i$  are  $\Omega$ -independent. This emphasizes that higher order correlations are less important at weak driving, but they, indeed, account for most of the information as the Rabi frequency is increased. This is illustrated in the high  $\Omega$  regime of Fig. 4.3(b), where the information in  $\mathcal{I}_{\pi/2}^{(2)}(\Omega)$  far from exhausts the QFI.

We find for  $\Omega \gg \gamma$  that  $F_{\pi/2}^{(1)}(\tau) \simeq \gamma \cos(\Omega\tau)e^{-3\gamma\tau/4}$ , and by Eq. (2.2) this leads to a Fisher information valid at strong driving,

$$\frac{\mathcal{I}_{\pi/2}^{(2)}(\Omega)}{T} = \frac{256\Omega^2 (243\gamma^4 + 216\gamma^2\Omega^2 + 128\Omega^4)}{27\gamma (9\gamma^2 + 16\Omega^2)^3}, \quad (4.30)$$

where taking the limit leads to

$$\frac{\mathcal{I}_{\pi/2}^{(2)}(\Omega)}{T} = \frac{8}{27\gamma} \quad \text{for } \Omega \rightarrow \infty. \quad (4.31)$$

This is independent of  $\Omega$ , showing that once the transition is fully saturated, increasing the driving strength further does not alter the information available from the two-time correlation function. This can be readily understood since exactly the same information is available from the power spectrum Eq. (4.23). Beyond saturation, the spectrum  $S_{\Phi}(\omega)$  in Fig. 4.2(b) consists of two side-peaks of unchanged shapes and separated by  $2\Omega$ . The Rabi frequency  $\Omega$  can hence be determined with the same precision for all large values. Conversely, the integrated signal holds negligible information beyond saturation, where the steady state does not depend on the actual value of  $\Omega$ .

Note at last that  $\mathcal{I}_{\pi/2}^{(2)}(\Omega)$  is maximized at  $\Omega = 0.71\gamma$ , where  $\mathcal{I}_{\pi/2}^{(1)}(\Omega)$  is zero, so here including at least two-time correlations in the data record is essential.

### 4.3.5 Finite detector efficiency

Finally, we address the distribution of information when the detector is imperfect ( $\eta < 1$ ). While under perfect detection, the conditional system state in Eq. (4.2), remains pure, this is not the case when  $\eta < 1$ . This is a consequence of our inability to trace the state exactly when some

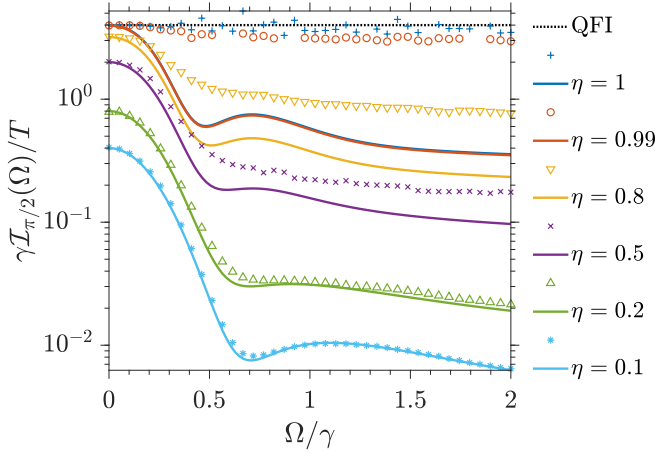


Figure 4.4: The full classical Fisher information for homodyne detection (markers) is shown for different values of the detector efficiency  $\eta$  and compared to the combined information from the integrated signal and two-time correlations  $\mathcal{I}_{\pi/2}^{(1)}(\Omega) + \mathcal{I}_{\pi/2}^{(2)}(\Omega)$  (lines in the same order). The results are shown as functions of the actual Rabi frequency  $\Omega$  for probing with a local oscillator phase  $\Phi = \pi/2$ .

photo emission events are missed by the detectors, and inevitably leads to a decreased information in the signal.

The integrated current Eq. (4.6) scales as  $\sqrt{\eta}$  which by Eq. (4.20) is reflected as an  $\eta$ -scaling in the information from this part. In general, it follows from Eq. (4.1) and Eq. (4.16) that  $F_{\Phi}^{(n/2)}(\{\tau_j\}) \propto \eta^{n/2}$ , so that

$$\mathcal{I}_{\Phi}^{(n)}(\theta) \propto \eta^n. \quad (4.32)$$

Hence, higher order correlations in the signal are less important as the detection efficiency decreases and correspondingly by Eq. (4.32), the information in the signal is fully contained in the lowest order temporal correlations, i.e., for low  $\eta$  we expect  $\mathcal{I}_{\Phi}(\theta) \simeq \mathcal{I}_{\Phi}^{(1)}(\theta) + \mathcal{I}_{\Phi}^{(2)}(\theta)$ . As seen in Fig. 4.4, where we compare  $\mathcal{I}_{\pi/2}^{(1)}(\theta) + \mathcal{I}_{\pi/2}^{(2)}(\theta)$  to the Fisher information of the full homodyne current Eq. (4.3) for different values of  $\eta$  as a function of the Rabi frequency, this is indeed the case. In particular, for realistic detection efficiency  $\eta \lesssim 0.5$  the full information is largely contained in the lowest order time-correlations of the signal, and with low efficiency detection  $\eta \lesssim 0.1$  higher order correlations hold only negligible information as seen by the light blue data in the figure.

## 4.4 Conclusion and outlook

We have calculated the classical Fisher information for homodyne detection of the radiative emission from a resonantly driven two-level system and demonstrated that a Bayesian signal analysis reaches the corresponding Cramér-Rao sensitivity bound on the applied Rabi drive strength. The classical Fisher information of homodyne detection is upper bounded by the quantum Fisher information associated with the quantum state of the (unmeasured) field emitted by the system, and lower bounded by the information retrieved by the mean value of the homodyne signal.

The emitter system is subject to measurement backaction due to the noisy measurement data, and the signal thus acquires non-trivial temporal correlations, which are at the heart of the performance of the Bayesian analysis. In the case of photon counting, the waiting time distribution between subsequent detection events, and hence the two-time intensity-intensity correlation function accounts for the full data record, and suffices to compute the Fisher information and explain its dependence on the physical parameters. Here we have investigated the information contained within the two-time correlation function or, equivalently, the power spectrum of the homodyne detection current. Due to the weaker measurement backaction, homodyne detection outcomes may be correlated for a larger number of different measurement times and, in particular for strong driving, we have observed that most of the information about the Rabi frequency is hidden in multi-time correlations in the current and can be retrieved efficiently only by the Bayesian analysis.

Our methods of analysis are general and apply to detection of signals from any quantum system and for the estimation of any physical parameter governing the evolution of that system. There have been theories suggesting that a sufficiently weak measurement backaction might lead to an asymptotic resolution scaling better than  $1/\sqrt{T}$  [172], and that more complex systems will offer similar improvement [155, 173]. Our two-level example system does not offer long memory times and, despite the weak homodyne probing, it is subject to the ergodicity arguments given in Sec. 2.2.2 of Chapter 2, implying a  $1/\sqrt{T}$  scaling of sensitivity. Our theory for the classical Fisher information related to diffusion-type quantum measurements, however, constitute a good starting point for a general investigation of the parameter resolution limit offered by quantum systems subjected to such realistic monitoring.

# Quantum Zeno effect in parameter estimation

*This chapter is reproduced from Ref. [3] with only minor modifications and a few paragraphs omitted due to their overlap with Chapter 2.*

---

In the two previous chapters we have seen how the backaction associated with detection of fluorescence from single quantum systems is favourable as it randomly quenches the system and thus triggers a transient evolution with temporal signal correlations that depend more strongly than the steady state on the desired physical properties [1, 2]. For too strong or too frequent measurements, however, the backaction may completely dominate the evolution. This is manifested in the quantum Zeno effect (QZE) [174], named after Zeno's arrow paradox, which inhibits population transfer between discrete states in a quantum system due to frequent observations. The effect was first demonstrated in ion trap experiments [95] and has since been used to account for experiments on many other systems, e.g. [175, 176].

The intuition behind the quantum Zeno effect has stimulated proposals for application in quantum information processing [96], e.g. for entanglement protection [177], preservation of systems in decoherence free subspaces [175, 178], error suppression in quantum computing [179], and quantum control [12]. In many of these studies the measurement backaction is actually not unambiguously identified as the crucial element, but

experiments and calculations have clearly established the intuition behind the quantum Zeno effect as a useful and inspirational source for new ideas and proposals.

In this chapter, we focus on information retrieved directly by the measurements and, closer to the original Zeno paradox, we ask to what extent frequent measurements on a quantum system prevent the observation, through the same measurements, of its dynamical evolution. In order to perform such an analysis we shall first derive theoretical expressions for the Fisher information (2.2) associated with a sequence of projective measurements on a single quantum system.

Once again, our main example concerns estimation of an unknown Rabi frequency  $\Omega$  in a two-level Hamiltonian (2.6), and we shall focus on projective measurements of the excitation performed at regular intervals spaced by  $\tau$ . Looking at Fig. 5.1, it is intuitively clear that the Rabi oscillation dynamics is prevented as the interval  $\tau$  between measurements decreases, and if we measure too often, the signal holds no information about  $\Omega$ . If, on the other hand, we measure too rarely we may obtain very little data in any finite probing time  $T$ . So, what is the optimal value of  $\tau$  for the purpose of parameter estimation? Our expression for the Fisher information provides the  $\tau$ , maximizing the information in any record obtained in a finite time, and by employing the Bayesian inference protocol of Chapter 2 to the measurement outcomes we discuss further the convergence of parameter estimation based on such optimal probing intervals.

## 5.1 Fisher information of projective measurement records

A realistic approach to continuous or frequent measurements performed directly on a system should take the finite bandwidth and noise properties of the measurement device into account (see, e.g., [180]), but we shall restrict our attention to the ideal case of instantaneous, accurate measurements, repeated at regular intervals  $\tau$  with  $N$  measurements occurring during an experiment of total duration  $T = N\tau$ . The continuous regime, approximated by the limit  $\tau \rightarrow 0$ , thus assumes a corresponding high bandwidth of detection.

While as outlined in Chapter 2, measurement theory can be formulated more generally in the POVM formalism, for simplicity we restrict in the present study our analysis to projective measurements. Each measurement

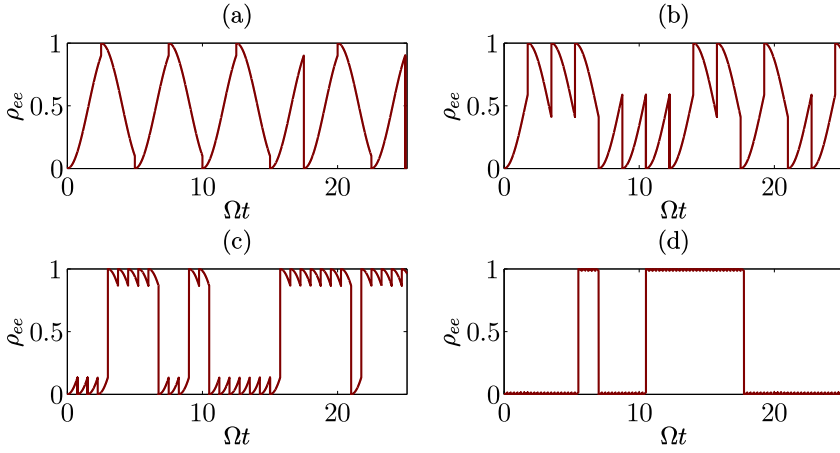


Figure 5.1: Illustration showing the excited state population as a function of time for a two-level system driven on resonance, and randomly projected at regular intervals according to measurements in the eigenstate basis. The measurement intervals are different in the different panels, (a):  $\tau = 2.5\Omega^{-1}$ , (b):  $\tau = 1.75\Omega^{-1}$ , (c):  $\tau = 0.75\Omega^{-1}$  and (d):  $\tau = 0.25\Omega^{-1}$ , and show the quantum Zeno suppression of the coherent Rabi oscillations.

outcome is thus an eigenvalue  $\lambda$  of a given operator  $\hat{\Lambda}$ , occurring with the probability

$$P(\lambda) = \text{Tr}[\hat{\Pi}_\lambda \rho(t)] \equiv \rho_{\lambda\lambda}(t), \quad (5.1)$$

where  $\hat{\Pi}_\lambda = |\lambda\rangle\langle\lambda|$  is a projector on the corresponding eigenstate. The projection postulate (2.5) states that the conditional state after a measurement performed on the state  $\rho(t)$  at time  $t$  is,

$$\rho_\lambda(t) = \frac{\hat{\Pi}_\lambda \rho(t) \hat{\Pi}_\lambda}{P(\lambda)}, \quad (5.2)$$

Retaining our focus in this thesis on parameter estimation with open quantum systems, we assume that in between measurements the evolution is generated by a Liouvillian-superoperator  $\mathcal{L}$  of the form (2.10) which encodes the parameter in the state of the probe system. Additionally, to study the Zeno effect, we center our attention on cases where  $\mathcal{L}$  is time independent such that the state is propagated from a time  $t$  to a time  $t'$  according to Eq. (2.11),

$$\rho(t') = e^{\mathcal{L}(t'-t)} \rho(t). \quad (5.3)$$

A data record of  $N = T/\tau$  projective measurement outcomes obtained at times  $t_j = j\tau$ ,  $D = \{\lambda_j\}_{j=1}^N$ , occurs then with the probability

$$\begin{aligned} P(D|\theta) &= \prod_j \text{Tr} \left( |\lambda_j\rangle \langle \lambda_j| e^{\mathcal{L}\tau} \rho(t_{j-1}) \right) \\ &= \prod_j \text{Tr} \left( |\lambda_j\rangle \langle \lambda_j| e^{\mathcal{L}\tau} [|\lambda_{j-1}\rangle \langle \lambda_{j-1}|] \right), \end{aligned} \quad (5.4)$$

assuming that the initial state is one of the eigenstates,  $\rho(0) = |\lambda_0\rangle \langle \lambda_0|$ .

To quantify the precision of the best possible estimate under this specific measurement protocol, we turn to the Cramér-Rao bound (2.3). As explained in Sec. 2.2.2, the interesting property is the dependence of the Fisher information (2.2) on  $N$  or, equivalently, on the total time of the probing  $T$ . Since by Eq. (5.2) the system is always projected (reset) in one of the eigenstates upon detection, the probability for an entire data record factors into a product of conditional probabilities

$$P(\lambda_j|\lambda_{j-1}, \theta) = \text{Tr} \left( |\lambda_j\rangle \langle \lambda_j| e^{\mathcal{L}\tau} [|\lambda_{j-1}\rangle \langle \lambda_{j-1}|] \right), \quad (5.5)$$

where we recall that the Liouvillian (2.9) and hence the time evolution operator (2.11) depends on  $\theta$ . The data record is fully represented by the set of numbers  $n_{lm}$ , counting the occurrences of subsequent detections in states  $(\lambda_{j-1}, \lambda_j) = (\lambda_m, \lambda_l)$ . The mean number of such events during a total of  $N$  measurements is  $\mathbb{E}[n_{lm}] = NP(\lambda_m|\lambda_l, \theta)P(\lambda_l|\theta)$ , where the probability that the average measurement will yield  $\lambda_l$  may be calculated as  $P(\lambda_l|\theta) = \rho_{\lambda_l, \lambda_l}^{(\text{ss})}$  with  $\rho^{(\text{ss})}$  the stationary (steady state) solution (2.12) of the non-selective evolution in Eq. (2.9), where the average measurement backaction is included as a dephasing of the atomic coherence at a rate  $\propto \tau^{-1}$ ; see Sec. 5.4.2 below.

The conditional probability for subsequent measurements,  $P(\lambda_j = \lambda_m|\lambda_{j-1} = \lambda_l, \theta)$  does not depend on  $j$ , and with a total number of measurements  $N = \sum_{lm} n_{lm}$ , the probability in Eqs. (2.1) and (2.2) for the data record  $D = \{n_{lm}\}$  is a multinomial distribution,

$$P(D|\theta) = \prod_{lm} P(\lambda_m|\lambda_l, \theta)^{n_{lm}}. \quad (5.6)$$

Utilizing  $\sum_m P(\lambda_m|\lambda_l, \theta) = 1$ , we readily obtain the Fisher information for a sequence of  $N$  projective measurements, which we can represent as

$$\frac{\mathcal{I}_\tau(\theta)}{N} = \sum_{lm} \frac{(\partial_\theta P(\lambda_m|\lambda_l, \theta))^2}{P(\lambda_m|\lambda_l, \theta)} P(\lambda_l|\theta). \quad (5.7)$$

The result Eq. (5.7) applies to any parameter estimate from a record of projective measurements performed at constant intervals  $\tau$ .

The quantity of relevance in this article is the Fisher information obtained for a given, long interrogation time,  $T = N\tau$ , and to address the asymptotic precision as well as the optimal value of  $\tau$ , we shall consider the Fisher information per time  $\mathcal{I}_\tau(\theta)/T = \mathcal{I}_\tau(\theta)/N\tau$ .

## 5.2 Zeno inhibited evolution

Following Peres [181], we give now a simple account of the quantum Zeno effect. Let  $\rho_0$  denote a pure state of a quantum system subject to evolution by the master equation Eq. (2.9). The probability that the system will be found in its initial state after a short time  $\tau$  is

$$P_0 \simeq 1 + a\tau + b\tau^2, \quad (5.8)$$

where  $a = \text{Tr}(\rho_0 \mathcal{L}[\rho_0])$  and  $b = \frac{1}{2} \text{Tr}(\rho_0 \mathcal{L}^2[\rho_0])$ . In cases where  $a \neq 0$ , the dominating contribution to  $P_0$  is linear in  $\tau$ , and the survival probability in the initial state after  $N$  time steps and projective measurements is

$$P_0^{\text{linear}}(N) \simeq \left[ 1 + a \frac{T}{N} \right]^N, \quad (5.9)$$

yielding an exponential decay law  $P_0^{\text{linear}}(N \rightarrow \infty) = \exp(aT)$  for large  $N$ .

In a number of cases,  $a = 0$  (see Sec. 5.3 below). Then, if the measurement is performed  $N$  times at intervals  $\tau = T/N$ , the probability that all measurements yield the initial state reads

$$P_0^{\text{quadratic}}(N) \simeq \left[ 1 + b \left( \frac{T}{N} \right)^2 \right]^N, \quad (5.10)$$

In the limit  $N \rightarrow \infty$ ,  $P_0^{\text{quadratic}}(N)$  tends to 1: The QZE freezes the system dynamics.

At small but finite  $\tau$ , it is instructive to set  $(T/N)^2 = \tau(T/N)$  in Eq. (5.10) and keep  $\tau$  constant. Then, taking the limit  $P_0^{\text{quadratic}}(N \rightarrow \infty) = \exp(\tau b T)$ . The probability to find the system in its initial state thus decays on the Zeno time scale  $\tau_Z$ , given by  $\tau_Z^{-1} \equiv -\tau b$ . For closed system dynamics governed by a Hamiltonian  $\hat{H}$ ,  $a$  vanishes, but we obtain  $\tau_Z^{-1} = \tau(\langle \hat{H}^2 \rangle - \langle \hat{H} \rangle^2)$  [181].

### 5.3 QZE and Fisher information for a probed two-level system

We shall now investigate how the Zeno effect affects precision probing by considering a two-level system with ground  $|g\rangle$  and excited state  $|e\rangle$  driven by a laser field. In a frame rotating with the frequency of the laser field, the Hamiltonian reads

$$\hat{H} = -\delta |e\rangle \langle e| + \frac{\Omega}{2} (|e\rangle \langle g| + |g\rangle \langle e|), \quad (5.11)$$

where  $\Omega$  is the laser-Rabi frequency and we include this time a possibility for an atom-laser detuning  $\delta$ .

Following the previous discussion, projective measurements in the atomic eigenstate basis,  $\hat{\Pi}_g = |g\rangle \langle g|$  and  $\hat{\Pi}_e = |e\rangle \langle e|$ , are performed at intervals  $\tau$ . The conditional, stochastic evolution is exemplified in Fig. 5.1 for different durations of the interval  $\tau$  between measurement during which the evolution given by Eq. (5.3) is unitary in the absence of environmental couplings. Decreasing  $\tau$  gradually inhibits the coherent dynamics, and eventually leads to quantum jumps occurring at the rate  $\tau_Z^{-1} = \tau\Omega^2/4$ .

To determine the Fisher information in Eq. (5.7), we note that the  $\lambda_j$  take only two values corresponding to measuring the ground ( $\lambda_j = g$ ) or excited ( $\lambda_j = e$ ) state, respectively. In this case,

$$\frac{\mathcal{I}_\tau(\theta)}{N} = \frac{P(g|\theta)(\partial_\theta P(g|g, \theta))^2}{P(g|g, \theta)(1 - P(g|g, \theta))} + \frac{P(e|\theta)(\partial_\theta P(e|e, \theta))^2}{P(e|e, \theta)(1 - P(e|e, \theta))}, \quad (5.12)$$

where  $P(g|\theta)$  and  $P(e|\theta)$  are the populations of the ground and excited state, in the unconditional steady state of the system. Absent energy relaxing processes these are both 1/2.

Due to the symmetry of the problem, the only relevant information in the measurement record concerns how often consecutive measurements yield identical or different results, and we have

$$\frac{\mathcal{I}_\tau(\theta)}{N} = \frac{(\partial_\theta P(g|g, \theta))^2}{P(g|g, \theta)(1 - P(g|g, \theta))}, \quad (5.13)$$

which can be recognized as the Fisher information for binomially distributed data.

For very short durations between measurements,  $P(g|g, \theta)$  is on the form of Eq. (5.8) with  $\rho_0 = |g\rangle \langle g|$ , and from Eq. (5.13) the Fisher information

is

$$\frac{\mathcal{I}_\tau(\theta)}{N} \simeq \frac{(\partial_\theta a)^2 \tau^2 + 2(\partial_\theta a)(\partial_\theta b) \tau^3 + (\partial_\theta b)^2 \tau^4}{a\tau + (a^2 + b)\tau^2}. \quad (5.14)$$

If  $a = 0$  the QZE freezes out the system dynamics in the limit of  $\tau \rightarrow 0$ , and  $\mathcal{I}_\tau(\theta)/T \simeq \tau(\partial_\theta b)^2/b \rightarrow 0$ , so despite the growing number of measurements,  $N = T/\tau \rightarrow \infty$  the data holds vanishing information on  $\theta$ . If, on the other hand,  $a \neq 0$ , we find a constant Fisher information per time in the limit of  $\tau \rightarrow 0$ ,  $\mathcal{I}_\tau(\theta)/T \simeq (\partial_\theta a)^2/a$ . Note, that if  $a$  is independent of  $\theta$  the Fisher information may still vanish even though the dynamics is not frozen out for  $\tau \rightarrow 0$ .

For simplicity, we restricted this discussion to the case of a two-level system, but the relation between a vanishing linear term in the survival probability Eq. (5.8) and quantum Zeno inhibited parameter estimation equally applies to the general case of Eq. (5.7).

## 5.4 Examples

In this section, we exemplify the Zeno inhibited Fisher information by considering Rabi-frequency estimation. We first discuss the case of unitary dynamics between measurements, and then turn to a model including dephasing.

### 5.4.1 Driven system with no dephasing

For the two-level system with Hamiltonian Eq. (5.11) the time evolution may be solved analytically,

$$P(g|g, \Omega) = \frac{1}{2} \left[ 1 + \frac{\delta^2 + \Omega^2 \cos \chi\tau}{\chi^2} \right], \quad (5.15)$$

where  $\chi = (\Omega^2 + \delta^2)^{1/2}$  is the generalized Rabi-frequency. By Eq. (5.13) the corresponding Fisher information per measurement for Rabi-frequency estimation is

$$\frac{\mathcal{I}_\tau(\Omega)}{N} = \frac{(\Omega^2 \chi\tau \cos \frac{\chi\tau}{2} + 2\delta^2 \sin \frac{\chi\tau}{2})^2}{\chi^4(\delta^2 + \Omega^2 \cos^2 \frac{\chi\tau}{2})}. \quad (5.16)$$

In the upper panel of Fig. 5.2, we show how the Fisher information grows as a function of the total interrogation time  $T = N\tau$  for different

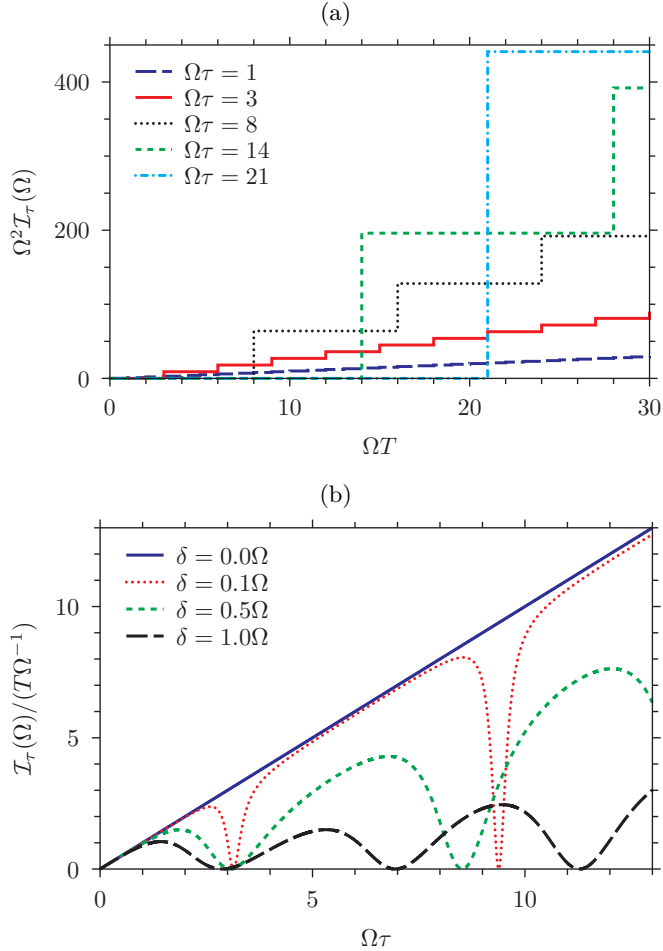


Figure 5.2: (a) Fisher information  $\mathcal{I}_\tau(\Omega) = \tau T$  for Rabi frequency estimation in a resonantly driven two-level system as a function of the total probing time. Results are shown for different durations of the intervals between measurements. (b) Fisher information Eq. (5.16) per time for Rabi frequency estimation as a function of the duration of the intervals between measurements assuming  $\tau \ll T$ . Results are shown for different detunings.

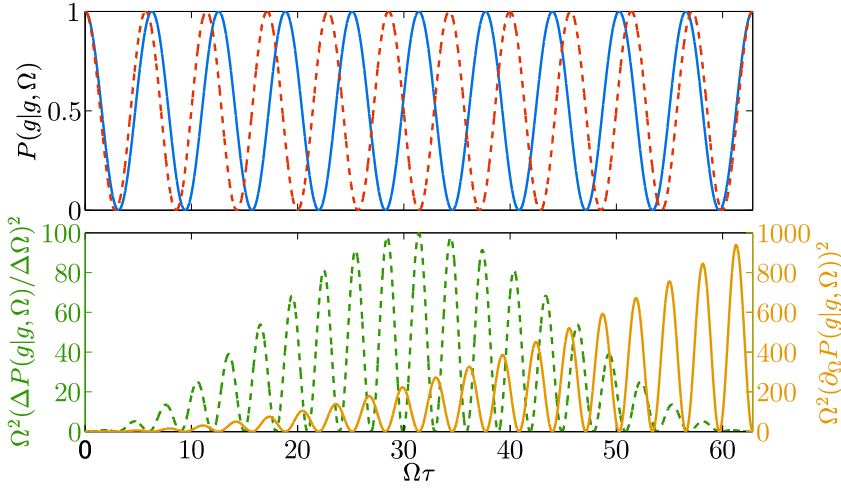


Figure 5.3: Upper panel: The probability of finding a two-level system driven on resonance in the ground state as a function of time for  $\Omega_1 = \Omega$  (blue curve) and  $\Omega_2 = 1.1\Omega$  (dashed, red curve). Lower panel: The dashed, green curve shows the squared difference quotient,  $[P(g|g, \Omega_2) - P(g|g, \Omega_1)] / [\Omega_2 - \Omega_1]$ , between the probabilities in the upper panel while the orange curve shows the squared differential quotient,  $\partial_\Omega P(g|g, \Omega)$ , corresponding to the limit of infinitesimally close Rabi frequencies.

values of  $\tau$ . Information is only obtained when measurement outcomes are acquired, and the Fisher information therefore grows in steps. While the frequency of the steps increases when the durations between measurements are decreased, the figure clearly shows a reduction of both the height of the individual steps and the effective slope of the Fisher information as function of time  $T$ . In the lower panel of Fig. 5.2, the slope  $\mathcal{I}_\tau/T$  is shown as a function of  $\tau$  for different values of the laser detuning and  $\tau \ll T$ . On resonance ( $\delta = 0$ ) Eq. (5.16) reduces to the Fisher information per measurement,  $\mathcal{I}_\tau(\Omega)/N = \tau^2$ , independent of the actual value of  $\Omega$  (equivalent to a linear relationship between  $\mathcal{I}_\tau(\Omega)/(T\Omega^{-1})$  and  $\Omega\tau$ ). For a fixed total time, the Rabi oscillation dynamics is frozen out and as anticipated by the discussion following Eq. (5.14) any  $\Omega$ -estimate is inhibited by the QZE in the limit  $\tau \rightarrow 0$ .

To understand the behaviour for large  $\tau$ , we consider the numerator in Eq. (5.13). In the upper panel of Fig. 5.3,  $P(g|g, \Omega)$  is shown for two slightly different values of  $\Omega$ . The two candidate values lead to solutions

evolving at different frequencies acquiring the same phase after a certain time. This effect contributes the envelope to the difference quotient seen in the lower plot (dashed, orange curve). The smaller the difference between the Rabi frequencies, the later the peak appears in the envelope function, and in the limit of infinitesimally close Rabi frequencies, their Rabi oscillations will only come back in phase after an infinitely long time. As the Fisher information relates to infinitesimally different hypotheses, a single measurement at time  $\tau = T$  provides the optimal distinction, and the limiting procedure of preparation of an initial state followed by a single read out at the final time is favoured. Indeed, the quadratic dependence on  $\tau$ , causing the Zeno suppression for short measurement intervals, is responsible for the advantageous Heisenberg scaling when  $\tau = T$  [172].

#### 5.4.2 Driven system with dephasing

Real physical systems experience dephasing due to, e.g., magnetic noise, off-resonant light scattering and collisions with background gas [95, 175]. To study how such effects affect parameter estimation, we introduce a transversal dephasing of the atomic coherence at a rate  $\gamma$  with the Lindblad operator  $\sqrt{\gamma}\hat{\sigma}_z$  in Eq. (2.10). The ground and excited states are eigenstates of  $\hat{\sigma}_z$ , and  $\text{Tr}(\rho_0\mathcal{L}\rho_0)$  still vanishes so that by Eq. (5.10) the QZE is present in the system.

The system evolution may be solved analytically, and on resonance one finds

$$P(g|g, \Omega) = \begin{cases} \frac{1}{2} + \frac{e^{-\gamma\tau}}{2} \left( \frac{\gamma}{\omega} \sin \omega\tau + \cos \omega\tau \right) & \Omega \neq \gamma \\ \frac{1}{2} + \frac{e^{-\Omega\tau}}{2} (\Omega\tau + 1) & \Omega = \gamma, \end{cases} \quad (5.17)$$

where  $\omega = \sqrt{\Omega^2 - \gamma^2}$ .

Results are shown in Fig. 5.4 which depicts the time evolution of  $P(g|g, \Omega)$  for different values of  $\gamma$ . Due to the dephasing, the oscillations are damped over time, and it is intuitively clear that it is no longer optimal to wait as long as possible between measurements.

Using Eq. (5.13) we determine the Fisher information per measurement

$$\frac{\mathcal{I}_\tau(\Omega)}{N} = \frac{-2\Omega^2 (\gamma\omega\tau \cos \omega\tau - (\gamma + \omega^2\tau) \sin \omega\tau)^2}{\omega^4(\Omega^2 - 2\omega^2 e^{2\gamma\tau} + (\omega^2 - \gamma^2) \cos 2\omega\tau + 2\gamma\omega \sin 2\omega\tau)}, \quad (5.18)$$

valid for  $\Omega \neq \gamma$  as well as in the limit  $\Omega \rightarrow \gamma$ . In the six upper panels of Fig. 5.5, the Fisher information per time for different dephasing rates is

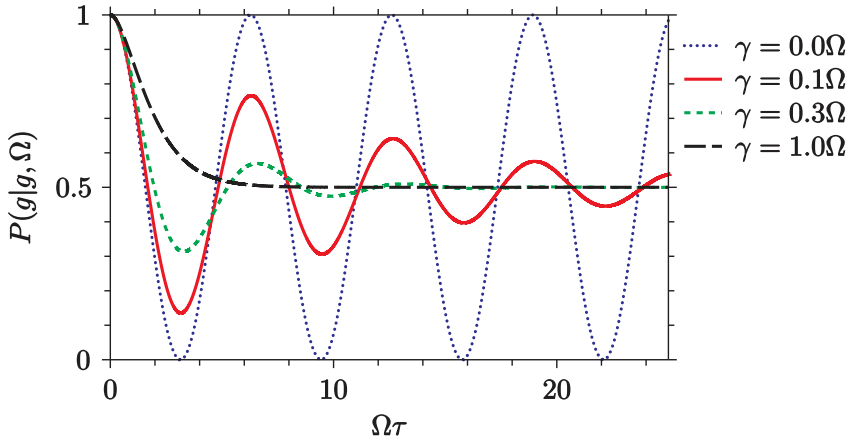


Figure 5.4: The time evolution of  $P(g|g, \Omega)$  for a two-level system driven on resonance. Results are shown for values of  $\gamma$  ranging from no dephasing ( $\gamma = 0$ ) to critical damping of the Rabi oscillations ( $\gamma = \Omega$ ).

depicted. Note the oscillatory behaviour, and that it is indeed peaked for finite measurement intervals.

From Eq. (5.18) one finds, in the strong driving regime,

$$\frac{\mathcal{I}_\tau(\theta)}{T} = \tau e^{-2\gamma\tau} \frac{\sin^2 \omega\tau}{1 - e^{-2\gamma\tau} \cos^2 \omega\tau} \quad \text{for } \Omega \gg \gamma. \quad (5.19)$$

For small  $\tau$  the envelope  $\tau e^{-2\gamma\tau}$  yields the same linear dependence as in the undamped case caused by the quantum Zeno effect, while for larger  $\tau$  dephasing suppresses the information.

The lower panel of Fig. 5.5 shows in color the Fisher information as a function of  $\gamma$  and  $\tau$ , and the black curve indicates the values of  $\tau$  that maximize the information for any given  $\gamma$ . For high  $\gamma$ , phase information is only significantly maintained during the first  $\pi/2$  of the rotation and quite frequent measurements are optimal. As  $\gamma$  decreases, additional  $\pi$  rotations are favourable between measurements, and since the sensitivity to  $\Omega$  by population measurements is highest when both populations are close to  $\frac{1}{2}$ , the optima occur around  $\omega\tau = \pi(n + \frac{1}{2})$  where  $n$  is an integer. The optimal measurement intervals change in steps as the dephasing rate becomes smaller and smaller.

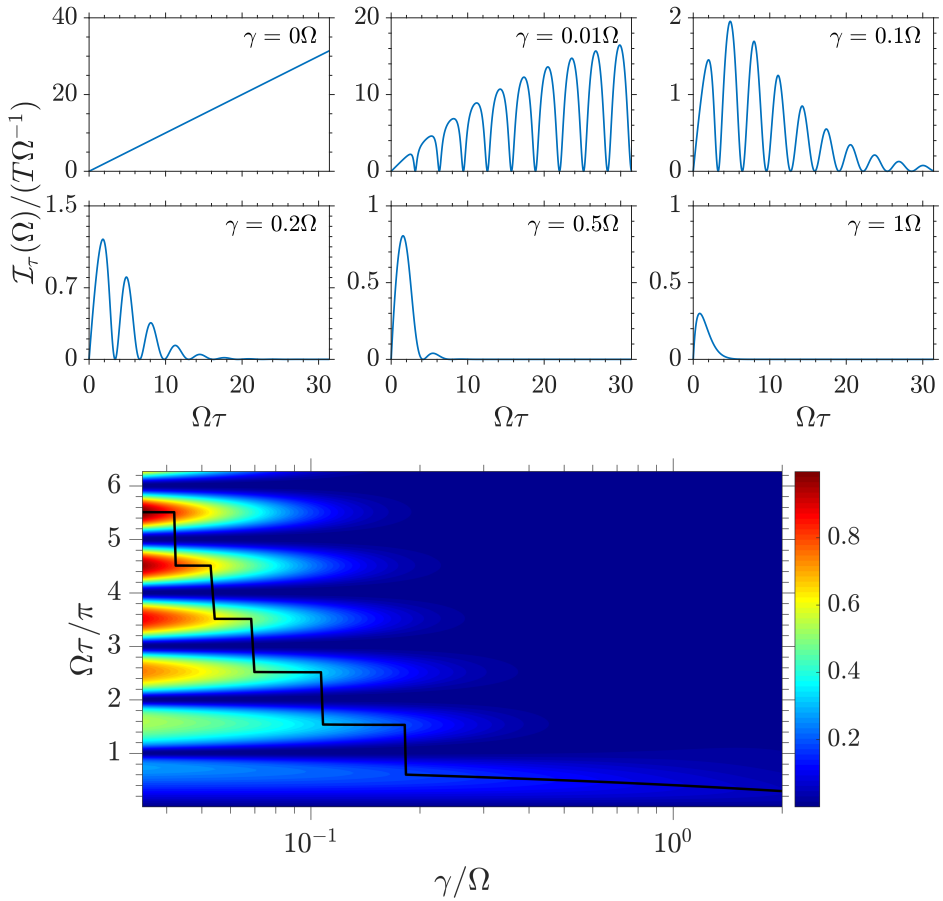


Figure 5.5: The Fisher information Eq. (5.13) per time for Rabi frequency estimation in a two-level system driven on resonance. In the six upper panels, results are shown as a function of the duration of the intervals between measurements and values of  $\gamma$  ranging from no dephasing ( $\gamma = 0$ ) to critical damping of the Rabi oscillations ( $\gamma = \Omega$ ). The color plot pictures the Fisher information as a function of both  $\tau$  and  $\gamma$ . The color scale is in units relative to the maximum value. The black curve in the plot tracks the value of  $\tau$  maximizing the Fisher information for any given value of  $\gamma$ . For weak damping, the maxima occur close to  $\omega\tau = \pi(n + \frac{1}{2})$ , where  $n$  is an integer.

## 5.5 Bayesian inference

In the sections above we investigated the theoretical optimal sensitivity based on projective measurements. We shall now address the attainability of this sensitivity by the explicit estimation strategy offered by Bayesian inference as formulated in Chapter 2. Given the outcome at the time  $t_j = j\tau$ , Bayes rule (2.1) yields an update for the probability  $P(\theta)$  assigned to different values of the unknown parameter  $\theta$  prior to the time  $t_j$ .

We illustrate this principle in the lower panel of Fig. 2.2 in Chapter 2 by propagating probabilities based on three candidate values of the Rabi frequency used to generate the trajectory in the upper panel. The trajectory is dominated by intervals of projections to the same state in consecutive measurements (the QZE), consistent with a vanishing Rabi frequency and hence causing an increase in the probability for the lowest value of  $\Omega$ . Due to the finite value of  $\tau$ , however, the system performs quantum jump like dynamics between the eigenstates at a rate  $\sim \tau_Z^{-1}$ , favoring the higher values of  $\Omega$  in the filtering process. Eventually, after a long sequence of measurements, the full record is only consistent with the true value of  $\Omega$ .

Figure 5.6 shows the results of applying the same procedure for a wider range of candidate values of the Rabi frequency on a fine grid and for a longer time. To distinguish infinitesimally different hypotheses (parameter values) the probing intervals should be chosen to maximize the Fisher information, and with a finite dephasing  $\gamma = 0.1\Omega_0$ , this happens for  $\Omega_0\tau = 4.83$  [see Fig. 5.5]. However, as seen in (a), the procedure is not able to filter away other candidate values  $\Omega$  fulfilling

$$\sqrt{\Omega^2 + \gamma^2}\tau = 2n\pi \pm \sqrt{\Omega_0^2 + \gamma^2}\tau, \quad (5.20)$$

with  $n$  an integer. If  $\Omega \gg \gamma$ , these Rabi frequencies lead to the same ground (excited) state populations at the time  $\tau$ , and thus yield identical probabilities for the measurement outcomes.

A solution to this problem is analyzed in Fig. 5.6(b), where shorter time intervals with  $\Omega_0\tau = 0.3$  are used to distinguish the discrete frequencies in Eq. (5.20). As observed in the upper panel, however, we are here far in the Zeno regime, and even though the distribution centers around the true value in the lower panel, it is broader than the individual peaks in (a).

An optimized strategy applies a combination of  $q$  measurements with sub-optimal evolution times to distinguish the discrete frequencies in Eq. (5.20), i.e., to select the correct branch in Fig. 5.6(b), followed by

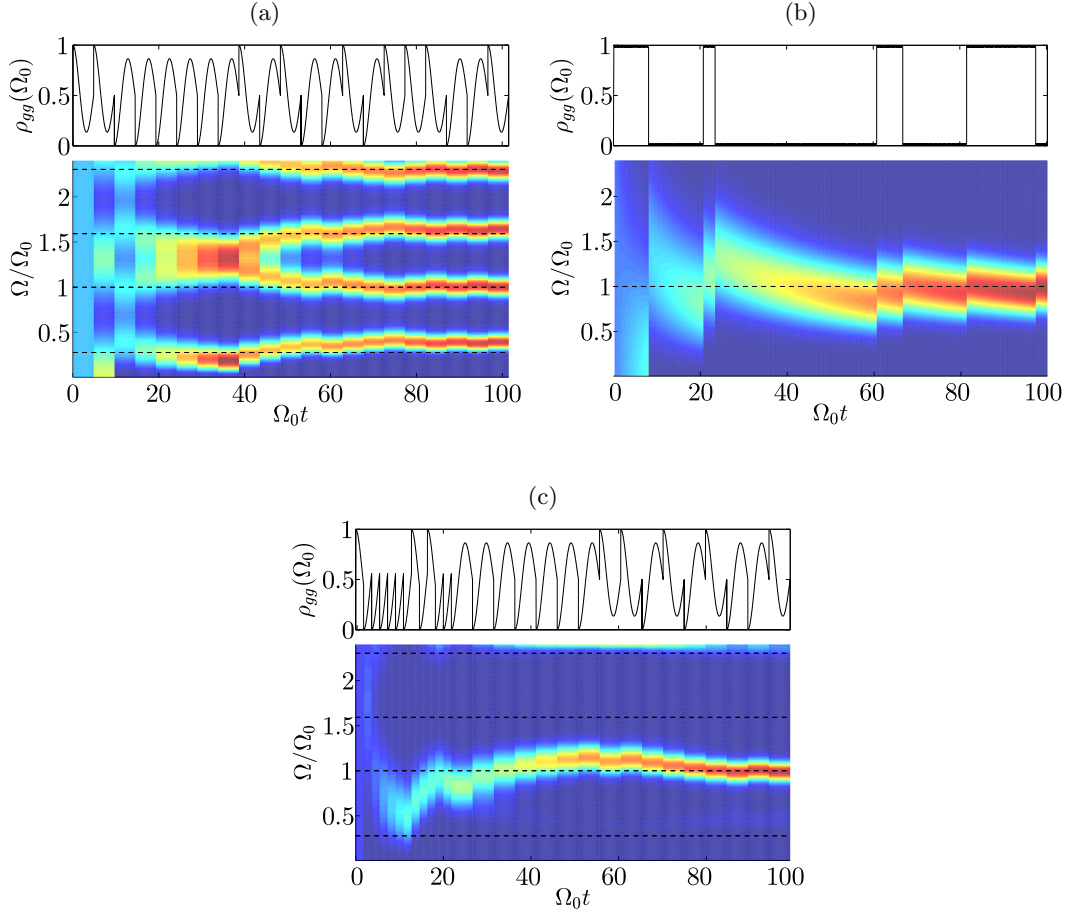


Figure 5.6: The upper panels show the ground state population during a simulation with  $\Omega = \Omega_0$ ,  $\delta = 0$  and  $\gamma = 0.1\Omega_0$ . The lower panels show the evolution of the quasi continuous probability distribution  $P(\Omega|D)$  for the Rabi frequency, conditioned on the measurement records in the upper plots. Results are shown for (a)  $\Omega_0\tau = 4.83$  and (b)  $\Omega_0\tau = 0.3$ . In (c) the measurement is optimized (see text) with 12 measurements with a separation given by  $\Omega_0\tau = 1.82$  followed by 16 measurements with a separation given by  $\Omega_0\tau = 4.83$ . The dashed, black lines represent values of  $\Omega$  fulfilling the condition in Eq. (5.20). Note, that  $\Omega$  is assumed to lie between 0 and  $2.5\Omega_0$ .

$N - q$  measurements with the optimal evolution intervals  $\tau_{\text{optimal}}$ , maximizing the Fisher information. From Eq. (5.20) all problematic candidates are ruled out by setting  $\tau_s < (2\pi - \eta)/(\sqrt{\Omega_{\text{max}}^2 + \gamma^2} + \sqrt{\Omega_0^2 + \gamma^2})$ , where  $\Omega_{\text{max}}$  is the maximal candidate and  $\eta$  is a small positive number.

This procedure is equivalent to one used in state estimation, where an asymptotically insignificant fraction  $q = N^{1-\epsilon}$  of the measurements is applied to identify an estimate for the state within a neighbourhood of size  $N^{-1/2+\epsilon}$  around the true state  $\rho_0$  [150]. The state  $\rho_\Omega(\tau)$  at time  $\tau$  corresponds to a particular value of  $\Omega$ , and with a distance from the true state given by

$$L \equiv \|\rho_\Omega(\tau_s) - \rho_0(\tau_s)\|_1, \quad (5.21)$$

where  $\|\mu\|_1 = \text{Tr}(\sqrt{\mu^\dagger \mu})$ , efficient distinction of  $\Omega$  from  $\Omega_0$  by the first  $q$  measurements, dictates a lower bound for  $\epsilon$ ,

$$\epsilon \geq \frac{1}{2} + \frac{\ln L}{\ln N}. \quad (5.22)$$

We pick  $L$  to be small enough to discern values of the Rabi frequency that would lead to opposite measurement probabilities, i.e., for  $\Omega \gg \gamma$ , we set in Eq. (5.21)  $\sqrt{\Omega^2 + \gamma^2}\tau_s = \pi - \sqrt{\Omega_0^2 + \gamma^2}\tau_s$  so that  $P(g|g, \Omega) = 1 - P(g|g, \Omega_0)$ . Note, that  $L$  can be rewritten as twice the difference in ground state populations. Finally, we obtain the optimal parameters for  $N$ ,  $q$  and  $\tau_s$  numerically subject to the total time constraint  $T = q\tau_s + (N - q)\tau_{\text{optimal}}$ .

This scheme is implemented in Fig. 5.6(c). The optimized measurement parameters are given in the figure caption. The measurements in the first  $t \sim 22\Omega^{-1}$  efficiently filter away the problematic candidates of Eq. (5.20), and the subsequent optimal measurements provide a narrow peak around the correct Rabi frequency. Hence, the hybrid method proves successful. Note that while we presented the scheme as if the first measurements are needed to initially identify the approximate range of  $\Omega$ , it was recently demonstrated how adaptive measurements relying on real time Bayesian updating can be applied for optimized sensing with a single electron spin [182].

## 5.6 Conclusion and outlook

In this chapter, we have presented an analysis of the Fisher information for the determination of parameters that govern the dynamics of a quantum

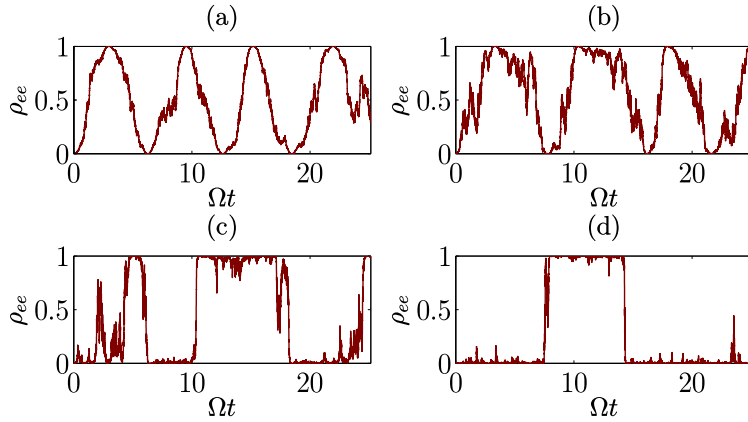


Figure 5.7: Illustration of the quantum Zeno effect for a two-level system driven on resonance subject to continuous dispersive probing with strength  $\Gamma$  of the eigenstate populations. (a):  $\Gamma = 0.05\Omega$ , (b):  $\Gamma = 0.2\Omega$ , (c):  $\Gamma = \Omega$  and (d):  $\Gamma = 3\Omega$ . Note, the resemblance with the plots in Fig. 5.1.

system subject to projective measurements at a given frequency. We identified and analyzed the inhibition of precise parameter estimation caused by the quantum Zeno effect. Our results directly relate the Zeno inhibited evolution of a quantum system to a vanishing information acquired in any given time from the measurements causing the inhibition. Our exemplification through the monitored Rabi oscillations of a two-level system shows that, in the Zeno limit of frequent probing, the parameter sensitivity approaches zero, and that the interval of propagation between measurements should be made as large as possible. In the presence of dephasing, finite intervals are favourable for optimal estimation purposes, while the Zeno effect still excludes frequent probing.

We emphasize that in the absence of a Zeno effect, where the linear term in the survival probability Eq. (5.8) is non-zero, the Fisher information per time may still vanish in the limit  $\tau \rightarrow 0$  if this term is independent of  $\theta$ . As an example, consider the inclusion of spontaneous decay at a rate  $\gamma_{\text{spont}}$  in our two-level model. With an initial excited state this yields  $\text{Tr}(\rho_0 \mathcal{L} \rho_0) = \gamma_{\text{spont}} \neq 0$ , and the Fisher information for estimating Hamiltonian parameters indeed vanishes, while the information for estimating  $\gamma_{\text{spont}}$  remains finite in the limit  $\tau \rightarrow 0$ .

The Fisher information and the Cramér Rao bound quantify the optimal asymptotic sensitivity, but to reach unambiguous sensing at that limit, we must employ a strategy that distinguishes among remote candidate

parameter values. We discussed and demonstrated a Bayesian estimation protocol, that spends a small fraction of the total probing time to establish a rough estimate, from which the asymptotic results are valid. The problem of parameter estimation from periodic probability distributions is elaborated in [142].

For simplicity, and for the possibility to establish analytical results, our model focused on projective (strong) measurements performed at discrete times, and we introduced the Zeno effect as the limit of very frequent measurements. We believe, however, that our results are also valid for the interpretation of different measurement scenarios, such as continuous, dispersive probing. In such experiments, a system is interrogated by a laser or microwave field, which undergoes a phase shift that depends on the state of the system, and by adjusting the intensity of the probe field, both weak and strong (projective) measurements may be implemented on the time scale of the system dynamics. The probe strength  $\Gamma$  thus plays a role equivalent to the frequency  $1/\tau$  of projective measurements in the present work [cf., the similarity of the conditional dynamics in Fig. 5.7 for continuous probing, simulated according to [183, 184] by a diffusion-type master equation on the form (2.16) with  $\hat{c} = \sqrt{\Gamma}\hat{\sigma}_z$ , and Fig. 5.1 for the frequent projective measurements].

# Continuous measurement of a Berry curvature

*This chapter is reproduced from Ref. [5] with minor adjustments and rearrangements of the structure.*

---

The research presented in the preceding chapters have been concerned with the usage of quantum measurement to learn *classical* parameters encoded in states of quantum probes. Another, complementary, aspect of quantum metrology is the tracking of quantum states and their evolution. This may have different purposes, often with the eventual objective of mapping a complex classical property. In this chapter, we consider the observation of a quantum system as it undergoes a topological transition [185–187]. Apart from their fundamental interest, quantum systems with topological invariants may be a key to achieve protection of quantum bits from environmental noise [188].

The starting point of our investigations is the simplest toy-model of a quantum system with distinct topological phases: A qubit system subjected to a quasi-adiabatic quench of a field [189, 190]. The Bloch spheres inserted in Fig. 6.1 show trajectories traced by the qubit Bloch vector for different quench times and for different sweeps of the field parameters causing a flip of the spin (left insert) and a return to the initial state (right insert), respectively. As explained below, the time trace of the  $\sigma_y$  component defines in this way a topological phase. By combining the outcomes of repeated projective measurements of  $\sigma_y$  after different partial sweeps of

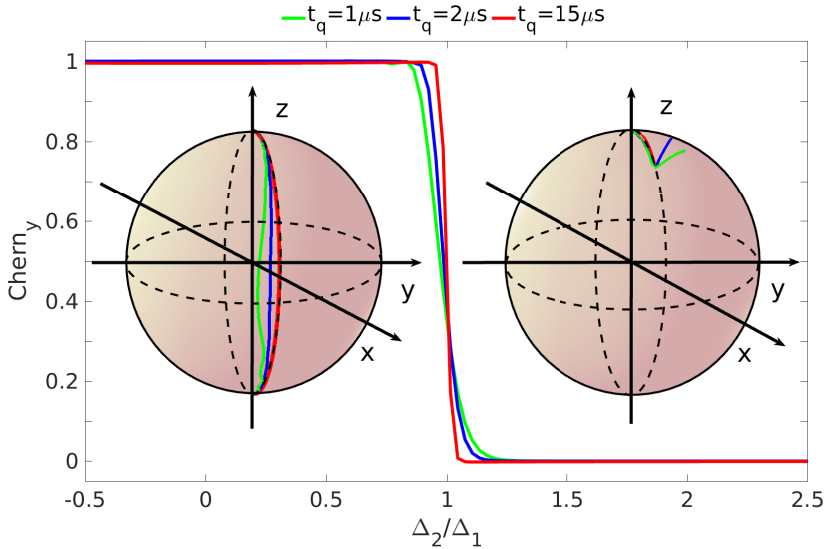


Figure 6.1: The plotted curves show the dependence of the integral Eq. (6.3) or Eq. (6.8) on  $\Delta_2/\Delta_1$  for different quench times  $t_q = 1\mu s$  (green, lower curve),  $2\mu s$  (blue, middle curve), and  $15\mu s$  (red, upper curve). We assume  $\phi = 0$ ,  $\Omega_1/2\pi = \frac{1}{3}\Delta_1/2\pi = 10$  MHz. The Bloch sphere on the left (right) shows the evolution of the quantum state during the quench for  $\Delta_2 = \frac{1}{3}\Delta_1$  ( $\Delta_2 = 1.1\Delta_1$ ).

the Hamiltonian parameters, the experiment in Ref. [190] indeed revealed a transition between different topologies represented by the Chern number in Fig. 6.1. Rather than performing a sequence of partial sweeps, it is an attractive possibility to experimentally extract the topological properties by continuously monitoring the system during a full quench of the Hamiltonian. In this chapter, we shall analyze a protocol that allows such measurement.

As an alternative to projective measurements, we apply a weak dispersive probe which in the qubit example provides a signal with a mean value proportional to the time-dependent expectation value of  $\sigma_y$ . Contrary to parameter estimation where as seen in Chapters 3 and 4 it may provide an advantage, the measurement backaction is problematic when we are interested in observing the undisturbed evolution of a quantum system. For sufficiently weak probing, we can disregard the backaction on the system, but the signal will be dominated by detector shot noise. Stronger probing offers a better signal-to-noise ratio, but backaction will then mod-

ify the state and hence the future evolution of the system, reflecting the well-known and fundamental relationship between distinguishability and disturbance of quantum states by measurements [97, 98].

To cancel the backaction of the strong continuous measurement, we propose to apply a simple continuous feedback on the qubit. As we are not aiming to determine an unknown quantum state but rather to probe a (classical) property of the Hamiltonian governing the system dynamics, there is no fundamental impediment against such a strategy, and we shall demonstrate its achievements with theoretical arguments and simulations.

## 6.1 Topology in quantum mechanics

Since the pioneering work on topological phases of matter by Kosterlitz, Thouless and Haldane [185–187], quantum states with nontrivial topological properties have constituted a very active research field. Topological invariants, such as the Chern number [191], characterize how the system ground state (or an excited state) varies when the system Hamiltonian explores a closed two-dimensional manifold of parameter values. States with nontrivial topology in extended quantum systems are associated with, e.g., the variation of Bloch wave functions over a two-dimensional Brillouin zone [192], while the ground state of a single spin under variation of the direction of an external magnetic field constitutes a simple example where a topological transition may be witnessed by a discrete change in the Chern number [189].

Topological properties are not derived from a single state but depend on how the eigenstates of different, continuously varied Hamiltonians are connected. This is quantified by the Berry phase [193], associated with the evolution of a quantum system under adiabatic variation of the Hamiltonian. In addition to a dynamical phase,  $-\int dt' E_n(t')/\hbar$ , governed by the energy eigenvalue, the  $n$ th eigenstate of the system acquires a geometric (Berry) phase,  $i \int \langle \phi_n | \nabla_R | \phi_n \rangle dR$ , along the curve explored by the Hamiltonian in parameter space. By parametrizing  $R = (\mu, \nu)$ , one can define the Berry connection

$$A_\mu = \langle \phi_n | i \partial_\mu | \phi_n \rangle, \quad (6.1)$$

and the Berry curvature,

$$F_{\mu\nu} = \partial_\mu A_\nu - \partial_\nu A_\mu, \quad (6.2)$$

whose integral over any surface in parameter space by Stokes theorem yields the Berry phase for the closed boundary curve. When the surface

integral is extended to a closed manifold (no boundary), it must yield  $2\pi$  times an integer  $C$ , which in the classical Gauss-Bonnet theorem [194] is identified with the genus of the manifold and which in the quantum case defines the topological Chern number,

$$C = \frac{1}{2\pi} \int_S dS_{\mu\nu} F_{\mu\nu}, \quad (6.3)$$

where  $dS_{\mu\nu}$  is a surface element in the parameter space. The restriction of Chern numbers to discrete values is associated with the topological properties of the system and explains the robustness of physical phenomena such as the integer quantum Hall effect [195–197]. The inherent robustness implies reduced sensitivity to small perturbations and decoherence, suggesting quantum systems with nontrivial topology as promising building blocks in a quantum computer [188].

In this work, we focus on the Berry curvature and Chern number associated with a particular system eigenstate  $|\phi_0\rangle$ <sup>1</sup>. Due to the dependence of the eigenstates on a manifold of different Hamiltonians, the Chern number is not directly related to an experimental observable. Recently, however, Gritsev and Polkovnikov [189] have shown that the slowly quenched dynamics of a quantum system permits identification of the Berry curvature as the expectation value of the gradient of the Hamiltonian: If the quantum system is subject to a slow quench of the Hamiltonian parameter  $\nu$  with a rate of change  $v$ , the operator  $f_\mu \equiv -\partial_\mu H$  has the expectation value

$$\langle f_\mu \rangle = \langle \phi_0 | f_\mu | \phi_0 \rangle + v F_{\mu\nu} + O(v^2). \quad (6.4)$$

The Berry curvature and the Chern number can hence be inferred from an experiment by measuring the physical observable  $f_\mu$  and extracting its linear dependence on  $v$ .

### 6.1.1 A topological transition in a qubit system

The protocol suggested in Ref. [189] has recently been demonstrated by the evolution of a superconducting qubit subject to a time-dependent microwave field [190] whose detuning and Rabi frequency act in a manner equivalent to  $z$  and  $x$  magnetic field components on a spin-1/2 particle. Perfect adiabatic evolution accomplishes a Bloch vector rotation in the  $xz$  plane. The gradient of the Hamiltonian along the azimuthal direction

---

<sup>1</sup>We study the case of a spin-1/2 qubit in an effective magnetic field for which the two eigenstate manifolds yield equivalent results.

is then proportional to the spin component  $\sigma_y$  which, indeed, acquires a finite expectation value proportional to  $v$  under a quasiadiabatic sweep. The shorter quench times yield the larger nonadiabatic deviation of the quantum states in Fig. 6.1 and the larger expectation values of  $\sigma_y$ .

We adopt the model of Ref. [190] as we consider a qubit with two levels  $|g\rangle$ ,  $|e\rangle$  and transition frequency  $\omega_q$ . In a frame rotating at the frequency of the applied microwave drive  $\omega_d$ , the Hamiltonian can be expressed as ( $\hbar = 1$ )

$$\hat{H} = \frac{1}{2}[\Delta\hat{\sigma}_z + \Omega\hat{\sigma}_x \cos \phi + \Omega\hat{\sigma}_y \sin \phi]. \quad (6.5)$$

Here,  $\hat{\sigma}_x$ ,  $\hat{\sigma}_y$ , and  $\hat{\sigma}_z$  are the Pauli operators,  $\Delta = \omega_q - \omega_d$  is the detuning,  $\Omega$  is the product of the microwave field amplitude and the qubit transition dipole moment, and  $\phi$  is the phase of the microwave field. We parametrize the dynamical quench of the detuning and Rabi frequency by a time-dependent polar angle variable  $\theta(t) = vt$ ,

$$\Delta = \Delta_1 \cos \theta + \Delta_2, \quad \Omega = \Omega_1 \sin \theta. \quad (6.6)$$

The quench speed  $v = \pi/t_q$ , appearing in Eq. (6.4), is determined by the quench time  $t_q$ .

The Bloch vector components  $(x, y, z)$  of a two-level system are defined by the expansion of the density matrix on Pauli spin matrices,

$$\rho = \frac{1}{2}(\mathbb{I} + x\hat{\sigma}_x + y\hat{\sigma}_y + z\hat{\sigma}_z), \quad (6.7)$$

i.e.,  $u_\rho = \text{Tr}(\hat{\sigma}_u \rho_t)$  for  $u = x, y, z$ . As shown by the left inset in Fig. 6.1, if  $\Delta_2/\Delta_1 < 1$  (assuming both are positive), the microwave frequency performs a chirp across the qubit resonance and the adiabatic qubit Bloch vector  $(\Omega \cos \phi, \Omega \sin \phi, \Delta)/\sqrt{\Omega^2 + \Delta^2}$  passes from the north to the south pole, while if  $\Delta_2/\Delta_1 > 1$ , both the initial and final states of the adiabatic evolution are represented by the north pole of the Bloch sphere (right inset).

A rapid quench of the parameter  $\theta$ , i.e., a small value of  $t_q$ , causes deviations from the adiabatically evolved state, as clearly illustrated in Fig. 1. Equations (6.3) and (6.4) now yield the expression for the Chern number,

$$C_y = - \int_0^\pi \frac{\Omega_1}{2v} \langle \sigma_y \rangle \sin \theta d\theta, \quad (6.8)$$

where we have used the independence of the Berry connection and Berry curvature on the azimuthal angle  $\phi$  to reduce Eq. (6.3) to a one-dimensional integral along the  $\phi = 0$  longitude.

## 6.2 Continuous measurement of the Berry curvature

A continuous measurement of the  $\hat{\sigma}_y$  observable is performed by injecting a probe field which interacts dispersively with the qubit, and the reflected signal is amplified and demodulated to yield an output voltage signal  $V(t)$  [Fig. 6.2(a)]; see, e.g., Refs. [198–200]. In dimensionless units,  $V(t)$  has the form

$$V(t) = \text{Tr} [\hat{\sigma}_y \rho(t)] + \frac{dW_t}{2\sqrt{\eta\kappa}dt}, \quad (6.9)$$

with a mean value given by the desired qubit expectation value and with random, shot-noise fluctuations represented by Wiener increments  $dW_t$ . The noise term dominates the readout if the probe field strength  $\kappa$  is weak or if the detector efficiency  $\eta$  is low.

The different normalization of  $V(t)$  compared to  $dY_t$  in Eq. (2.14) has the advantage that the Chern number  $C_V$  is deduced from the probe signal by performing the integral (6.8) with the signal  $V(t)$  directly in place of the expectation value  $\langle \hat{\sigma}_y \rangle$ . Due to the Gaussian fluctuations in the signal, the estimated Chern number samples a normal distribution with mean  $C_y$ , while the white-noise component in the signal Eq. (6.9) yields a statistical error in the estimation of  $C_y$  from a single quench experiment of magnitude

$$\Delta C_V^{(1)} = \Omega_1 \sqrt{\frac{t_q}{32\eta\kappa}}. \quad (6.10)$$

Upon  $N$  repetitions of the experimental sequence, this is reduced to  $\Delta C_V^{(N)} = \Delta C_V^{(1)}/\sqrt{N}$ . As we need the uncertainty to be well below unity to discern the integer values of  $C_y$ , we demand  $\sqrt{\eta\kappa v N} \simeq \Omega_1$  which for small  $N$  brings us in conflict with either the near adiabaticity or the assumption of negligible measurement backaction.

### 6.2.1 Measurement backaction

As discussed in Sec. 2.2, the measurement backaction related to continuous monitoring of the  $\sigma_y$  observable, leads to a conditional evolution of the density matrix  $\rho(t)$  of the probed qubit. The explicit, normalized version of the stochastic master equation (2.16) is in this case [134, 201],

$$d\rho = -i[\hat{H}(t), \rho]dt + \kappa \mathcal{D}[\hat{\sigma}_y]\rho dt + \sqrt{\eta\kappa} \mathcal{H}[\hat{\sigma}_y]\rho dW_t. \quad (6.11)$$

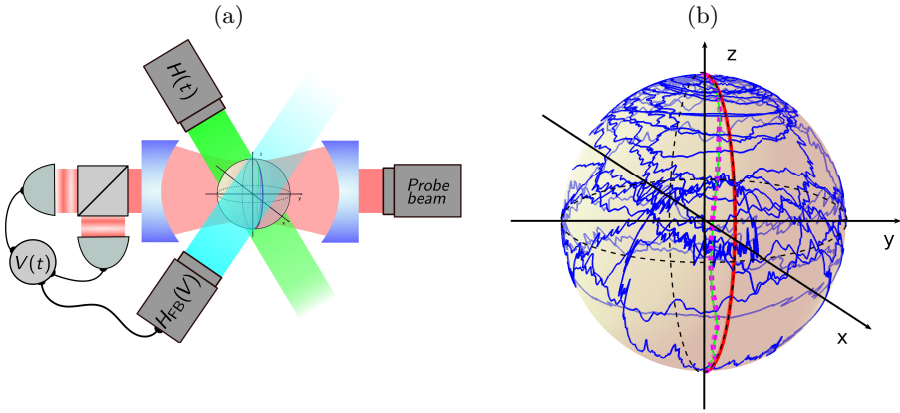


Figure 6.2: (a) A two-level system driven by a time-dependent Hamiltonian is monitored by homodyne detection of a transmitted microwave field. The stochastic homodyne current can be used to control a feedback microwave field applied to the qubit. (b) The dynamical evolution of the quantum state is calculated with  $\Omega_1 = \Delta_2 = \frac{1}{3}\Delta_1 = 10$  MHz. Results are shown for adiabatic evolution with  $t_q = 15 \mu\text{s}$  (red, in  $xz$  plane) and for quasiadiabatic evolution with  $t_q = 1 \mu\text{s}$  (green, blue, and dotted magenta). The dotted magenta curve depicts the evolution absent probing, the blue curve shows the evolution with high measurement strength ( $\kappa/2\pi = 0.37$  MHz), and the green curve (matching the dotted magenta curve) indicates the evolution under a strong measurement employing the feedback described in the text.

The first term represents the evolution absent probing as described by the Schrödinger equation and depicted in the insets of Fig. 6.1. Because of the interaction with the probe field, this evolution is supplemented by the latter two terms, where we define the superoperators

$$\mathcal{D}[a]\rho = a\rho a^\dagger - \frac{1}{2} \{a^\dagger a, \rho\}, \quad (6.12)$$

$$\mathcal{H}[a]\rho = a\rho + \rho a^\dagger - \text{Tr}(a\rho + \rho a^\dagger)\rho, \quad (6.13)$$

responsible for deterministic decoherence and stochastic measurement backaction, respectively.

Under perfect detection ( $\eta = 1$ ), the conditional state remains pure and the system lives on the surface of the sphere, while with imperfect detection ( $0 \leq \eta < 1$ ) our inability to trace the state leads to a mixed state *inside* the Bloch sphere. Henriët *et al.* [202] have investigated the behavior of the mixed state Bloch vector components and the resulting

value of the integral (6.8) in the case of a qubit coupled to a reservoir of bath degrees of freedom. That study, for not too strong bath coupling, justifies the determination of the Chern number by our procedure, and for clarity we restrict our attention to the  $\eta = 1$  case. See Appendix A.2 for a discussion of the implications of finite detection efficiency.

In the case of a strong probing, the signal will be less noisy but the system will be attracted to one of the eigenstates of the monitored observable,  $\sigma_y$ . At this point, both of the last terms in Eq. (6.11) vanish; i.e., in the limit of very large  $\kappa$ , the theory describes a projective measurement. In this case, as exemplified by the simulated blue curve in Fig. 6.2(b), the evolution deviates strongly from the unprobed dynamics and integration of the measurement signal will not yield the Chern number.

This fact can be addressed further by considering the estimate for the Chern number obtained by averaging over a large number  $N \gg 1$  of experimental runs. The ensemble average or *unconditional* evolution of the system follows from the master equation (2.9), corresponding to (6.11), but without the last term, which because of the white-noise increment averages to zero. The second term describes the average measurement-induced decoherence, which introduces an error in the Chern number as defined in Eq. (6.8). The dashed lower curves in Fig. 6.3(d) show the Chern number calculated from the solution of the unconditional master equation (2.9) during a single sweep of the parameter  $\theta$ . Results are shown for a range of detunings and we assume different values of the measurement strength. The figure confirms our expectations: For (very) weak probing, the procedure yields a result which is compatible with the correct value of the Chern number, but by Eq. (6.10) distinguishing this value requires a large number of experimental repetitions,  $N \gtrsim \Omega_1^2/\eta\kappa v$ . For stronger probing, the noise is reduced, but the average measurement backaction disturbs the evolution and we do not obtain a good candidate value for the Chern number. This conclusion is supported by the blue upper curve in Fig. 6.3(c), showing the error in the Chern number at  $\Delta_2/\Delta_1 = 0$  as a function of the probe strength  $\kappa$ . For small  $\kappa$ , the error is  $\propto \kappa$ , reflecting a system evolution which is maintained only when subject to very weak probing. As seen from the inset at  $\Delta_2/\Delta_1 = 2$  where the Chern number should be 0, the effect of the probing is three orders of magnitude lower than at  $\Delta_2 = 0$ .

Since the statistical error bars are reduced by a factor  $1/\sqrt{N}$  if the quench protocol is repeated  $N$  times, we can obtain the Chern number by repeated probing with a weak probing strength, but we shall now turn to an alternative approach depicted schematically in Fig. 6.2(a).

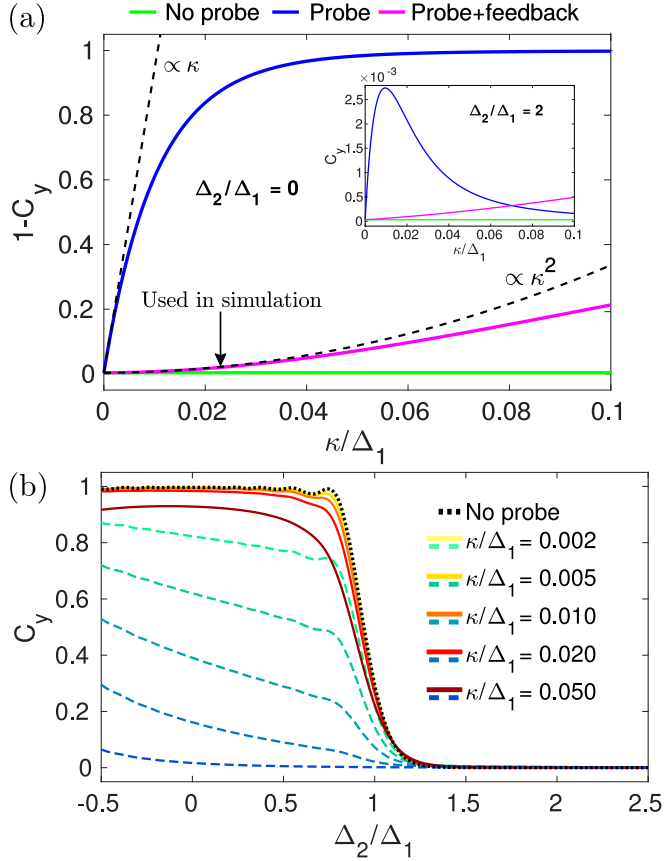


Figure 6.3: (a) The deviation in the Chern number (integral in Eq. (6.8) calculated from the unconditional evolution) from the expected integer value, introduced by measurement backaction. Curves are displayed as a function of the probing strength  $\kappa$  for the cases of no probing (green, lower line), probing (blue, upper line), and probing with feedback (magenta, middle line). Results are shown for  $\Delta_2 = 0$ , where in the absence of probing,  $C_y = 1$ , and the inset refers to  $\Delta_2 = 2\Delta_1$ , where we expect  $C_y = 0$ . (b) The value of  $C_y$  for different detuning ratios  $\Delta_2/\Delta_1$  and different values of the probing strength. We use  $\Omega_1 = \frac{1}{3}\Delta_1$  and the remaining parameters are set to optimize the measurement proposal (see text);  $\Delta_1/2\pi = 16.1$  MHz and  $t_q = 0.96 \mu\text{s}$ . Lower, dashed curves (cool colors) depict the case of probing without feedback and the upper, full curves (warm colors) show the case with feedback. The dotted black curve shows  $C_y$  without probing.

### 6.3 Including a feedback

As the stochastic master equation (6.11) provides the evolution of the qubit state, conditioned on the measurement signal, if the state remains pure (which is the case if the measurement is performed with unit efficiency), we can compensate for the measurement backaction by a unitary qubit rotation.

Such an approach has been proposed [203, 204] and recently applied in experiments to stabilize an arbitrary state [205] and to sustain Rabi oscillations [206] of a superconducting qubit long after the system would have decayed by spontaneous emission. These works apply feedback based on quadrature detection of the resonance fluorescence from a two-level system. Here we derive a similar capability for a dispersive readout of the  $\sigma_y$  component, and we show that it can be used to measure an unknown small deviation of the quantum state from the adiabatic evolution without severely affecting the state.

Figure 6.2(a) illustrates how the probe signal is directly applied to control the drive strength and detuning parameters of a feedback microwave signal, acting on the qubit by the Hamiltonian,

$$\hat{H}_V(t) = \kappa(\alpha\hat{\sigma}_x + \beta\hat{\sigma}_z)V(t). \quad (6.14)$$

As detailed in Appendix A.1, if we assume the values

$$\alpha = 2z, \quad \beta = -2x, \quad (6.15)$$

all the stochastic terms, linear in  $dW_t$ , cancel. There are, however, corrections which are linear in  $dt$  due to correlations between the  $dW_t$  terms in the master equation and in the feedback. Adding a second state-dependent Hamiltonian term,

$$\hat{H}_D(t) = \kappa(a\hat{\sigma}_x + b\hat{\sigma}_z), \quad (6.16)$$

with

$$a = -yz, \quad b = xy, \quad (6.17)$$

ensures that the system evolves according to the quench Hamiltonian only.

While this feedback may perfectly cancel the measurement backaction, it assumes knowledge of the quantum state and hence of the very observable that we want to measure. However, since our scheme assumes only a small deviation of the quantum state from the analytically known eigenstate

of the time-dependent Hamiltonian, we may approximate our feedback operation with the one that we would have applied to restore the adiabatic state if that had been subject to the measurement; i.e., we approximate the values  $x, y, z$  in (6.15) and (6.17) by the analytically known (time-dependent) Bloch vector components  $(\Omega, 0, \Delta)/\sqrt{\Omega^2 + \Delta^2}$ , and obtain a recipe that may be applied in real time during an experiment.

In the case of a quasiadiabatic sweep, the state only deviates slightly from the adiabatic eigenstate, and the feedback error is expected to be small. To assess the effect of this discrepancy, we turn again to the average evolution over many experimental runs, now with the feedback turned on. The unconditional master equation for a system subject to the feedback, Eqs. (6.14) and (6.16), is given in Appendix A.1, and from the solution of this equation during a full sweep of  $\theta$ , Eq. (6.8) yields a Chern number candidate. The purple (middle) curve in Fig. 6.3(c) shows that the feedback indeed effectively removes the effect of the backaction and that the slight deviation from the adiabatic state used in the feedback parameters yields an error in the Chern number scaling as  $\propto \kappa^2$ . This allows much larger values of the measurement strength to be used and hence a significant noise reduction [cf. Eq. (6.10)] without severely affecting the estimate. However, once the probing strength is increased beyond  $\kappa \simeq 0.03\Delta_1$  the evolution is strongly affected by the feedback, which effectively pulls the state toward the adiabatic eigenstate for which the  $\sigma_y$  component and hence  $C_y$  is zero. In other words, the imperfect feedback sets an upper limit to the probing strength and hence the achievable noise reduction.

In our choice of the experimental parameters  $\Omega_1$ ,  $t_q$ , and  $\kappa$ , we are hence presented with a tradeoff, leading to a simple optimization problem: The noise Eq. (6.10) must be minimized under the constraint that the error in the mean Chern number  $C_y$  calculated from Eq. (6.8) is small. As an example, we here perform the optimization at a representative ratio of the detuning parameters. We use  $\Delta_2 = 0$  and require  $C_y > 0.98$ . The resulting dependence of the integral (6.8) on the ratio of the detuning parameters is compared to the unprobed results by the upper curves in Fig. 6.3(d) and the optimal parameters are given in the figure caption. It is evident that by employing the feedback, we can use much stronger probing and still obtain the expected variation of the Chern number with the detuning parameter.

The achievable noise reduction subject to the constraint imposed by the error tolerance does not allow a full determination of the Chern number from a single physical measurement and one has recourse to perform a number of repetitions. If, for instance, one wishes to distinguish a

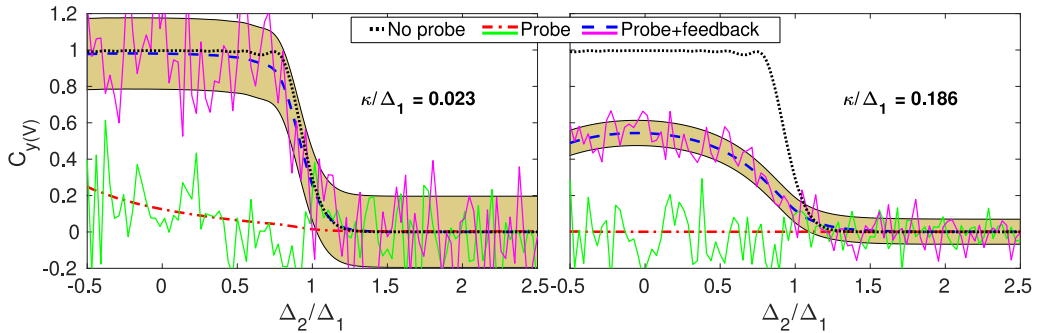


Figure 6.4: The Chern number for different detuning ratios  $\Delta_2/\Delta_1$  with the optimized measurement strength  $\kappa/2\pi = 0.37$  MHz (left panel) and with a much larger strength  $\kappa/2\pi = 3.0$  MHz (right panel). Shaded areas illustrate error bars with  $N = 383$  experimental repetitions. Noisy, magenta (upper) and green (lower) curves, consistent with the error bars and ensemble average signals  $C_y$ , illustrate the results for  $C_V$  from simulations of the measurement and feedback procedure.

Chern number of  $C_V > 0.98$  from  $C_V = 0$  to five- $\sigma$  accuracy (that is, a probability to assign a wrong Chern number of 0.00003%), one must require  $\Delta C_V^{(N)} \leq 0.196$ . This implies that  $N \simeq 383$  repetitions are needed. The corresponding error bars are illustrated along with the mean value over a range of detuning parameters in the left panel of Fig. 6.4. For comparison, we show in the right panel also the value of  $C_y$  for much stronger probing  $\kappa/2\pi = 3$  MHz with error bars corresponding to the same  $N$ . Notice how the mean Chern number is reduced from  $> 0.98$  to around 0.5, but that the same number of repetitions produces much smaller error bars, according to Eq. (6.10).

### 6.3.1 Numerical verification

We have implemented the feedback scheme in numerical simulations of the quench and measurement procedure by solving the feedback SME given in Appendix A.1. In Fig. 6.2(b), the dotted magenta curve shows how the evolution of the Bloch vector during a single quench is virtually indistinguishable from the green curve representing the evolution in the absence of measurements. This confirms that with these optimized parameters, the feedback succeeds in canceling the measurement backaction while maintaining a quasi-adiabatic evolution, allowing a dynamical phase

transition to be observed.

In Figs. 6.4, we plot results for the Chern number  $C_V$  obtained from the simulated measurement records. In the left panel, we use the optimized sweep parameters and measurement strength and in the right panel we use a much stronger measurement strength. The lines are guides to the eye and their fluctuations are representative of the estimation error on the Chern number from the signal recorded in  $N \simeq 383$  sweeps. The simulations are consistent with the mean value obtained from the unconditional evolution and the shaded areas, illustrating the analytic noise estimate Eq. (6.10).

## 6.4 Conclusion

In summary, we have proposed to measure the topological Chern number by continuously probing a physical observable during a full quench of the system Hamiltonian. Our results show that relatively few experimental repetitions are required to obtain an acceptable signal-to-noise ratio. While it may also be possible to employ interference protocols to determine geometric phases of a qubit degree of freedom [207, 208], the arguments and more complicated examples offered in Ref. [189] encourage efforts to experimentally extract the Berry curvature and Chern number by direct measurement of a physical observable. Whether more complex physical systems also permit an explicit feedback scheme and noninvasive measurements depends on the specific system and on practical experimental capabilities.

Let us finally comment that our continuous, non-invasive measurement may be applied to evaluate the integrated effect of any weak perturbation acting on a system, e.g., a small variation in a Hamiltonian strength parameter. For many measurements, a longer probing time  $T$  will yield an improved scaling of the resolution with  $1/\sqrt{T}$ . Such improvement does not occur for the measurement of the Chern number where the mean signal,  $\langle \sigma_y \rangle$ , vanishes, while the integrated noise increases in the adiabatic limit of long quench times.

# Random search for a dark resonance

*This chapter is reproduced from Ref. [5] with only minor adjustments.*

---

When quantum systems act as sensitive probes and field sensors, the precision by which the value of a physical parameter can be determined follows from a statistical analysis, and as described in Chapter 2, conventional problems, heeding normal statistics, produces an estimation error which obeys the Cramér-Rao bound (2.3). This fact was utilized to analyse the metrological achievements of quantum probes subject continuous fluorescence detection in Chapters 3 and 4 and to rapidly repeated projective measurements in Chapter 5.

In this chapter, we propose and analyse an estimation protocol which is beyond the validity of the CRB. We consider the special case where the fluorescence rate of an atomic system vanishes when it is excited by a laser field on exact resonance. Such dark resonances occur in connection with the phenomenon of electromagnetically induced transparency [209, 210], and due to their narrow linewidths, they are sensitive probes of perturbations on the system; see, e.g., [211–213]. As an alternative to a systematic scanning and accumulation of signal at different, discrete laser frequencies, we investigate a random search protocol in which the probe laser frequency may come arbitrarily close to the dark resonance. That event is witnessed by the complete absence of signal and suggests application of the following

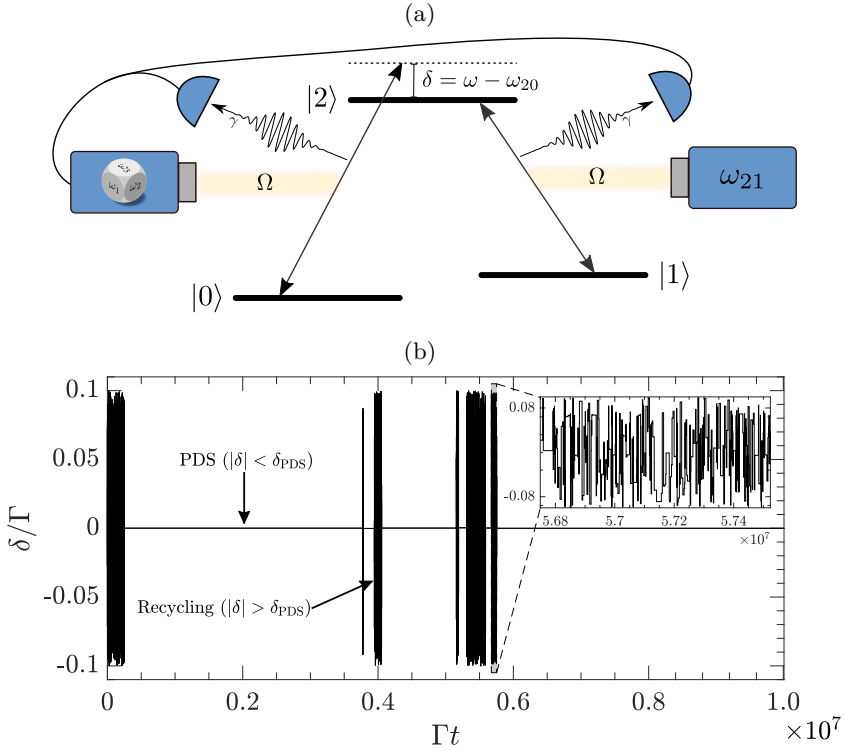


Figure 7.1: (a)  $\Lambda$ -type system driven by laser fields with Rabi frequency  $\Omega$ . The  $|1\rangle \leftrightarrow |2\rangle$  coupling laser is kept on resonance while the  $|0\rangle \leftrightarrow |1\rangle$  coupling laser is detuned by an amount  $\delta = \omega - \omega_{20}$ , where  $\omega_{20}$  is the atomic resonance frequency. Both emission channels are monitored by photo detectors, and upon detection in either channel  $\delta$  is shifted randomly on a uniform interval with  $\delta \in [-\delta_{\max}, \delta_{\max}]$ . (b) Quantum Monte Carlo simulated trajectory for the detuning  $\delta$  as a function of time  $t$ . The simulation is made with  $\Omega = 0.1\Gamma/\sqrt{2}$  and  $\delta_{\max} = 0.1\Gamma$  where  $\Gamma^{-1}$  is the excited state lifetime.

adaptive protocol for the duration  $T$  of the experiment: The system is excited at a frequency picked uniformly within a fixed interval, including the resonance. Whenever a photon is detected, a new random laser frequency is chosen and the system is excited until the next photodetection, where the frequency is again shifted. The protocol is illustrated for a driven  $\Lambda$ -type system in Fig. 7.1(a).

When driven far from the dark resonance, the high scattering rate implies a high probability for an early photon detection and a shift to a

different frequency, while for frequencies close to resonance, the photon emission rate is very small, and these frequencies are hence maintained for a long time before the next emission event. We thus expect that the longer we probe the atom, the more likely are occurrences of long intervals with laser frequencies close to the dark resonance. The instantaneous, stochastically tuned laser frequency thus constitutes a good estimate of the atomic transition frequency. Due to the distribution of short, long, and very long time intervals, however, the dynamics is not ergodic, and the Cramér-Rao bound which relies on asymptotic normality can neither be used to assess the quantitative achievements of the protocol nor to estimate how the error scales with the duration of the experiment.

We show here that the problem is tractable by methods of generalized statistics [214, 215] that have been developed to analyze non-ergodic dynamics in, e.g., animal foraging behavior [216, 217], human travel patterns [218], earthquake occurrences [219] and financial systems [220, 221]. In quantum physics they have found applications in analysis of anomalous transport properties of quantum arrays [222], and our approach is inspired by and closely follows Bardou *et. al.* [223], who apply Lévy statistics to subrecoil laser cooling mediated by a dark state mechanism. While we provide quantitative results and simulations for a specific model, the analysis is general, and we shall return to wider consequences and applications of our results in the final section of this chapter.

## 7.1 Atomic model and trajectory analysis

Figure 7.1(a) depicts the situation of a  $\Lambda$ -type three-level quantum system interacting with two laser fields with equal coupling strengths. Assume that one field is fixed on resonance, while the other is scanned with a detuning  $\delta = \omega - \omega_{20}$  from the exact resonance in the system. The upper level is unstable and decays with equal probabilities into the two low-lying states, which can both be expanded on the dark state  $|\psi_{-}\rangle = (|0\rangle - |1\rangle)/\sqrt{2}$  and the bright state  $|\psi_{+}\rangle = (|0\rangle + |1\rangle)/\sqrt{2}$ . The bright state is coupled to the excited state, and after a short time, the system starting in state  $|0\rangle$  or  $|1\rangle$  has either undergone excitation and emitted a photon or been effectively projected into the dark state [138]. The dark state has a vanishing excitation rate but for a finite detuning, the phase difference between the laser and the dark state atomic components evolves, and leads to an effective photon emission rate  $R(\delta)$ . This rate is derived in Appendix B.1 and shown as a function of the detuning  $\delta$  in Fig. 7.2. If the

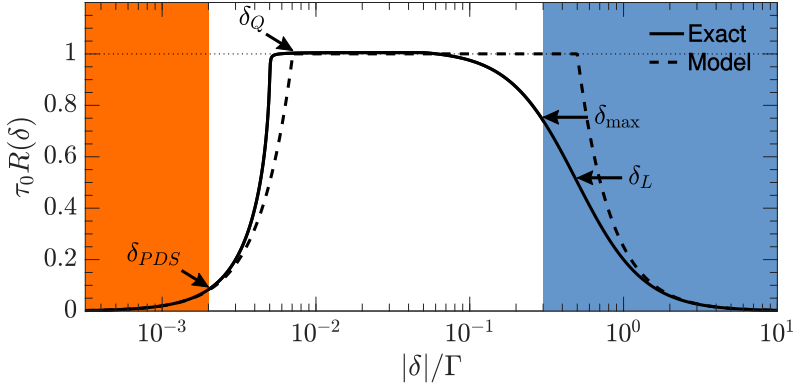


Figure 7.2: Effective frequency dependent photo emission rate from the dark state  $|\psi_{-}\rangle$  shown for  $\Omega/\Gamma = 0.1\Gamma/\sqrt{2}$ . The full line shows the exact rate and the dashed line our simplified model Eq. (7.1). Characteristic detunings (see main text) are annotated. The rate is an even function of  $\delta$ . The red (left) shaded area is the trapping region and the blue (right) shaded area marks the frequency range not included in the stochastic scan.

coupling laser is tuned slightly away from resonance, the effective photo emission rate depends quadratically on the detuning  $\delta$ , and for a range  $|\delta| < \delta_{PDS}$ , the system will be trapped for a long time in a pseudo-dark state (PDS). At higher detunings the excitation rate levels off and decreases when the detuning exceeds  $\delta_L \simeq \Gamma$ , the excited state linewidth.

A characteristic waiting time between subsequent emissions is  $\tau(\delta) = 1/R(\delta)$ . Ergodicity relies on the ability to average single trajectories over long times compared to any intrinsic time scale, but since  $R(\delta) \rightarrow 0$  we have  $\tau(\delta) \rightarrow \infty$  for  $\delta \rightarrow 0$ , so even a very long time  $T$  may be dominated by a single waiting time with  $|\delta| < \delta_T$ , where  $R(\delta_T)T = 1$ .

We shall restrict the choice of frequencies to an interval  $|\delta| < \delta_{\max}$ , containing the resonance, but avoiding the wings of the absorption profile,  $\delta_{\max} < \delta_L$ . To verify the intuition behind the scheme, we show in Fig. 7.1(b) the evolution of the detuning as a function of time as obtained from a Monte Carlo wave function simulation of the continuous measurements and random frequency jumps [138]. The total duration  $T$  is, indeed, dominated by a few long intervals with small detuning, interrupted by brief periods with larger, fluctuating values of  $\delta$ . The value of the laser frequency at any random time is likely to be very close to the atomic resonance frequency.

To obtain analytic predictions for the generic behavior of our estimation protocol, we shall focus in the following section on the most significant

features and abandon less important details. The variation of the fluorescence rate  $R(\delta)$  by an atom occupying the pseudo dark state  $|\psi_{-}\rangle$  will thus be approximated by the function

$$R(\delta) = \begin{cases} \tau_0^{-1}(\delta/\delta_Q)^2, & |\delta| < \delta_Q \\ \tau_0^{-1}, & \delta_Q < |\delta| < \delta_L \\ \tau_0^{-1}(\delta_L/\delta)^2, & \delta_L < |\delta|. \end{cases} \quad (7.1)$$

This simple form of  $R(\delta)$ , illustrated by the dashed curve in Fig. 7.2, is adequate to represent the very long and very short waiting times attained for  $\delta \simeq 0$  and for larger  $\delta$ , respectively. The parameters, yielding the best agreement with the actual rate for the  $\Lambda$ -system illustrated by the solid curve in Fig. 7.2, are derived in Appendix B.1.

## 7.2 Lévy statistical analysis

While the simulation illustrates the apparent success of such an estimation strategy, a quantitative analysis of its precision and its scaling with  $T$  is hampered by the fact that the probability distribution  $P(\tau)$  of dwell times  $\tau$  between detection events has a very long tail, and its mean and variance formally diverge in the interesting regime where  $\delta \rightarrow 0$ . For such problems, e.g., the sum of  $N$  waiting times  $T_N = \sum_{i=1}^N \tau^{(i)}$  does not obey the central limit theorem (CLT) and will not converge to a Gaussian distributed variable with a mean value proportional to  $N$ . Instead, the increasing probability that a single term attains a very large value and dominates the sum may cause it to scale as a higher power of  $N$ . This is the characteristic property of Lévy flights, and  $P(T_N)$  is a Lévy distribution [215].

In Fig. 7.1(b), we see how the evolution is comprised of two different time scales: In a narrow interval  $|\delta| \leq \delta_{\text{PDS}} \leq \delta_Q$ , the system occupies the PDS for which the waiting times are of the order  $\tau \propto \delta^{-2}$ . A single detector click here will with overwhelming probability cause a jump to a detuning  $|\delta| \geq \delta_{\text{PDS}}$  where the waiting times are short and many jumps occur before the system returns to the narrow PDS detuning interval. A trajectory thus consists of a number of trapping intervals  $\tau_t^{(1)}, \tau_t^{(2)}, \dots$  interspersed by recycling periods of duration  $\tau_r^{(1)}, \tau_r^{(2)}, \dots$  each containing many detection events. The competition between trapping and recycling periods is at the core of our statistical analysis, and the probability distributions  $P_t(\tau_t)$  of trapping times  $\tau_t$  and  $P_r(\tau_r)$  of recycling intervals  $\tau_r$  will suffice to analyze the asymptotic behavior of our estimation scheme as  $T \rightarrow \infty$ .

For  $P_t(\tau_t)$  we note that since each detuning in the PDS interval is reached with equal probability, the density of trajectories just returned to the PDS is  $\rho(\delta) = \frac{1}{2}\delta_{\text{PDS}}^{-1}$ . Upon return with a given  $\delta$ , the probability of a trapping time  $\tau_t$  is ascribed by the delay function  $w(\tau_t|\delta)$  which can be calculated by a master equation analysis as described in Chapter 3, [1, 126]. In the limit of predominantly long waiting times,  $w(\tau_t|\delta)$  is well approximated by a single exponential function,  $w(\tau_t|\delta) = R(\delta)^{-1} \exp(-\tau_t R(\delta))$ , where the frequency-dependent emission rate  $R(\delta)$  vanishes at  $\delta = 0$ ; cf. Eq. (7.1).

The distribution  $P_t(\tau_t)$  of trapping intervals is given by integrating  $w(\tau_t|\delta)$  over the PDS region with weight  $\rho(\delta)$ , and for long  $\tau_t$  we find

$$P_t(\tau_t) \underset{\text{large } \tau_t}{\simeq} \frac{\mu\tau_b^\mu}{\tau_t^{1+\mu}}, \quad (7.2)$$

where  $\mu = 1/2$ , and  $\tau_b = \tau_0\pi(\delta_Q/\delta_{\text{PDS}})^2/16$ . As anticipated by the arguments above,  $P_t(\tau_t)$  decreases very slowly (as  $1/\tau_t^{3/2}$ ) for large values of  $\tau$ , and we are in the regime where standard Gaussian statistics must be replaced by Lévy statistics.

For a distribution with power-law tails such as Eq. (7.2), all moments  $\langle \tau^n \rangle$  for which  $n \geq \mu$  diverge. A well-known example is a Cauchy distribution, which has  $\mu = 1$ . The central limit theorem of Gaussian statistics states that for  $\mu > 1$  the total time spent in the trapping region  $T_N^{(\text{PDS})} = \sum_{i=1}^N \tau_t^{(i)}$  is proportional to  $N$ , while for  $\mu < 1$  any sequence is dominated by rare events and the generalized CLT dictates that asymptotically  $T_N^{(\text{PDS})} \propto N^{1/\mu}$ . See Appendix B.2 for a brief introduction to broad distributions and the generalized CLT.

The behavior of  $R(\delta)$  for large  $\delta$  determines  $P_r(\tau_r)$ . When setting up the protocol, we have a choice in the maximum and minimum values allowed in the random selection of  $\delta$  after each detection event. We assume that a rough prior estimate restricts the search interval  $\delta \in [-\delta_{\text{max}}, \delta_{\text{max}}]$  around  $\omega = \omega_{20}$ . The symmetry is not of importance since we assume  $\delta_{\text{max}} \gg \delta_{\text{PDS}}$ . The properties of  $P_r(\tau_r)$  depend on the value of  $\delta_{\text{max}}$  compared to the characteristic detunings  $\delta_Q$  and  $\delta_L$ . If  $\delta_Q \ll \delta_{\text{max}} < \delta_L$ , the high- $\delta$  rate is given by the plateau in Fig. 7.2, and as derived in Appendix B.3 we obtain a finite mean value  $\langle \tau_r \rangle = \tau_0(\delta_{\text{max}}/\delta_{\text{PDS}})$ , implying that  $T_N^{(\text{REC})} = \sum_{i=1}^N \tau_r^{(i)}$  grows linearly with  $N$ . For simplicity, we restrict our attention to this case and defer discussion of the case with  $\delta_{\text{max}} > \delta_L$  to Section 7.4.

### 7.2.1 Trapped proportion

The results for the trapping times and recycling intervals already provide qualitative insight regarding the asymptotic achievements of our estimation scheme at large times  $T$  (large  $N$ ). For  $\delta_{\max} < \delta_L$ ,  $T_N^{(\text{PDS})} \propto N^2$  dominates over  $T_N^{(\text{REC})} \propto N$ , and we expect trajectories to spend most of the time occupying the PDS. In fact, the time averaged proportion of time in the PDS is given by  $f_T(T) = T_N^{(\text{PDS})} / (T_N^{(\text{PDS})} + T_N^{(\text{REC})})$ , which by applying the generalized CLT [see Appendix B.2] for long times  $T$  can be written  $f_T(T) = 1 - \xi(\langle \tau_r \rangle / \tau_b) T^{(\mu-1)}$ . This reveals a time-averaged non-PDS proportion decreasing as  $1/\sqrt{T}$ , but contrary to ergodic processes with Gaussian statistics it continues to fluctuate, via the Lévy increment  $\xi$ , even in the high- $T$  limit.

The ensemble averaged proportion of trajectories that will asymptotically be trapped in the PDS is derived in Appendix B.4,

$$f_E(T) \simeq 1 - \frac{\sin(\pi\mu)}{\pi} \frac{\langle \tau_r \rangle}{\tau_b^\mu T^{1-\mu}}, \quad (7.3)$$

where we see the same scaling with time  $T$ , but without fluctuations. Equation (7.3) expresses the probability as a function of time that the laser frequency is within  $\delta_{\text{PDS}}$  of the true resonance frequency, while with a probability  $1 - f_E(T)$  the frequency resides, at the time  $T$ , in the recycling region, and it will not be a good estimator of the resonance frequency. The convergence of  $f_E(T)$  to unity for large  $T$  hence signifies that the random search is a successful estimation scheme. In Fig. 7.3 we show how  $f_E(T)$  matches the ensemble average of trajectories such as the one in Fig. 7.1(b) for large times,  $T \gtrsim 10^6 \Gamma^{-1}$ .

### 7.2.2 Asymptotic frequency distribution and estimation sensitivity

To address the sensitivity of the random search we consider the distribution  $\mathcal{P}(\delta, T)$  of trajectories with  $|\delta| < \delta_{\text{PDS}}$ . The Lévy statistical analysis in Appendix B.5, reveals that  $\mathcal{P}(\delta, T)$  can be factorized as  $\mathcal{P}(\delta, T) = h(T)G(q)$ , where  $h(T)$  is the time-dependent height of the distribution, and  $G(q)$ , where  $q = \delta/\delta_T$ , is a form factor. It is a signature of the broken ergodicity that  $\mathcal{P}(\delta, T)$  depends explicitly on  $T$  and does not approach a stationary form even for very long times. We find  $h(T) = (\tau_{\text{PDS}}/\tau_b)^\mu \sin(\pi\mu) / (\pi\mu\delta_T)$ , where  $\tau_{\text{PDS}} = 1/R(\delta_{\text{PDS}})$ . A general expression for the form factor is given in Appendix B.5. It depends only

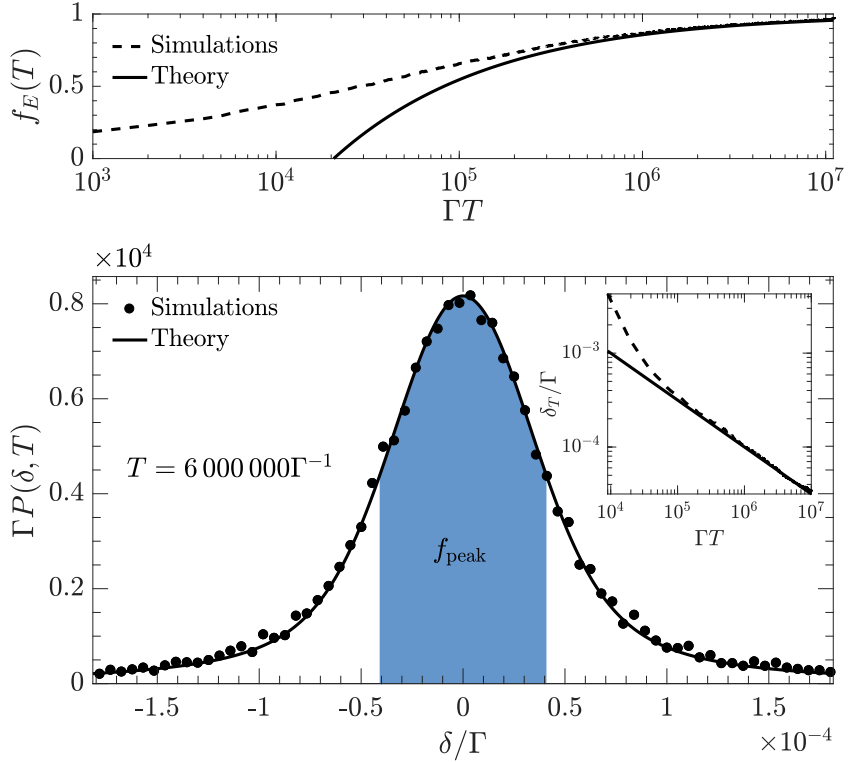


Figure 7.3: Top: Proportion of trapped trajectories Eq. (7.3) (with  $\delta_{\text{PDS}} = 0.01\Gamma$ ) as a function of time. The dashed line depicts a quantum jump simulation of 20 000 trajectories with the same parameters as in Fig. 7.1(b). It matches the statistical model (full line) for (very) large times. Bottom: Distribution of the detuning  $\delta$  after a long time  $T = 6 \times 10^6\Gamma^{-1}$ . The dots show simulated data, the full line the theoretical result of our statistical analysis and the shaded area marks the fraction with  $|\delta| \leq \delta_T$ . The inset shows how the characteristic width  $\delta_T$  of the distribution scales as  $T^{-1/2}$  and matches the model for times larger than  $\sim 10^5\Gamma^{-1}$ .

on the value of  $\mu$ , and for  $\mu = 1/2$  it may be expressed as  $G(q) = D(q)/q$ , where  $D(q)$  is the Dawson function. The tails of  $G(q)$  are Lorentzian  $\sim 1/2q^2$  and much wider than those of a Gaussian while its maximum is flat compared to a Lorentzian.

The important detuning scale is, as anticipated, given by  $\delta_T = \delta_Q(\tau_0/T)^\mu$ . This implies that  $h(T) \propto T^\mu$ , and the full width at half-maximum (FWHM) of  $G(q)$  is  $q_w \delta_T \propto T^{-\mu}$ , where for  $\mu = 1/2$  we find numerically  $q_w \simeq 2.13$ . Since the distribution has long tails, we define the fraction  $f_{\text{peak}} = \int_{-\delta_T}^{\delta_T} d\delta \mathcal{P}(\delta, T)$  of occurrences of final detunings in the characteristic range  $|\delta| < \delta_T$ , as a measure for the parameter estimation sensitivity and we find  $f_{\text{peak}} \simeq 0.59$  independently of  $T$ . This shows that asymptotically a constant part of the trajectories are within  $\delta_T \propto T^{-\mu}$  of the true resonance frequency. Note that the sensitivity does not depend on the values of  $\delta_{\text{max}}$  and  $\delta_{\text{PDS}}$  as long as  $\delta_{\text{PDS}} \ll \delta_{\text{max}} < \delta_L$ . For the  $\Lambda$ -system with  $\mu = 1/2$  we hence find a  $1/\sqrt{T}$  scaling of the sensitivity in our estimation protocol. We note that 59% of the distribution within  $\delta_T$  corresponds to an  $\simeq 0.82\sigma$  confidence level if  $\mathcal{P}(\delta, T)$  was a normal distribution.

In Fig. 7.3 we show how the ensemble obtained from simulations until  $T = 6 \times 10^6 \Gamma^{-1}$  is well represented by  $\mathcal{P}(\delta, T)$ . The inset shows the consistency of the theoretical result for  $\delta_T$  with numerical results obtained directly from the sampled  $\mathcal{P}(\delta, T)$  as a function of time.

### 7.3 Comparison to a systematic scan

We have shown that under certain restrictions our estimation scheme is successful, but it remains to be seen if it outperforms standard spectroscopy methods in the same settings. A typical way to determine a resonance frequency is by observing fluorescence as the laser frequency is systematically scanned over the relevant frequencies with equal time at each point. The spectrum is reconstructed from the integrated fluorescence signal at each frequency. Such a scheme lends it self to a standard analysis relying on the Cramér-Rao bound (2.3) in a manner similar to the one performed in Chapter 3 for a photon counting record or to the one in Ref. [163] for position measurements of a dark matter-wave soliton. In this section, we perform such an analysis and compare the performance of a systematic scan to our stochastic protocol.

Assume first that a scan of total duration  $T$  consists in observing the fluorescence for a time  $t = T/N$  at each of a set of  $N$  discrete, equally spaced frequencies  $\{\delta_k\}_{k=1}^N$  on the search interval  $[-\delta_{\text{max}}, \delta_{\text{max}}]$ . A data

record  $D = [n_1, n_2, \dots, n_N]^T$  obtained in a time  $T$  then contains the total photocount  $n_k$  at each discrete frequency. These are independently sampled, and we assume that for large  $T$  they are normally distributed with means  $\bar{n}_k$  and variances  $v_k$ . The full data record  $D$  then samples a multivariate normal distribution  $P(D|\theta) = \mathcal{N}(\boldsymbol{\mu}, \boldsymbol{\Sigma})$  with mean value vector  $\boldsymbol{\mu} = [\bar{n}_1, \bar{n}_2, \dots, \bar{n}_N]^T$  and a diagonal covariance matrix with elements  $\Sigma_{kk} = v_k$ .

The Fisher information for estimating a parameter  $\theta$  from such a distribution is well-known,

$$\mathcal{I}(\theta) = \frac{\partial \boldsymbol{\mu}^T}{\partial \theta} \boldsymbol{\Sigma}^{-1} \frac{\partial \boldsymbol{\mu}}{\partial \theta} + \frac{1}{2} \text{Tr} \left( \boldsymbol{\Sigma}^{-1} \frac{\partial \boldsymbol{\Sigma}}{\partial \theta} \boldsymbol{\Sigma}^{-1} \frac{\partial \boldsymbol{\Sigma}}{\partial \theta} \right), \quad (7.4)$$

yielding in this case

$$\mathcal{I}(\theta) = \sum_k \frac{1}{v_k} \left( \frac{\partial \bar{n}_k}{\partial \theta} \right)^2 + \frac{1}{2} \sum_k \left( \frac{1}{v_k} \frac{\partial v_k}{\partial \theta} \right)^2. \quad (7.5)$$

The mean and variance of the photocount at each discrete frequency follow from the master equation (2.9). The mean fluorescence is  $\bar{n}_k = \frac{T}{N} \tilde{R}(\delta)$ . The photocount variance stems from temporal signal fluctuations, and it can be expressed as

$$v_k = \bar{n}_k + 2T \sum_i \int_0^\infty d\tau \tilde{G}_i^{(2)}(\tau), \quad (7.6)$$

where the sum runs over the distinct emission channels, and  $\tilde{G}_i^{(2)}(\tau) = G_i^{(2)}(\tau) - \text{Tr} \left( \hat{c}_i^\dagger \hat{c}_i \rho^{(\text{ss})} \right)^2$ . The last term in Eq. (7.6) determines the deviation from Poissonian counting statistics.

From Eq. (7.6), we notice that the second term in Eq. (7.5) does not scale with  $T$  and is hence negligible at large times. Taking the limit of a continuum of frequencies,  $N \rightarrow \infty$ , we transform the sum in Eq. (7.5) to an integral and obtain our final expression for the Fisher information of estimating a parameter  $\theta$  by systematically scanning a laser frequency across a resonance,

$$\mathcal{I}(\theta) = \frac{T}{2\delta_{\text{max}}} \int_{-\delta_{\text{max}}}^{\delta_{\text{max}}} d\delta \frac{1}{V(\delta)} \left[ \frac{\partial \tilde{R}(\delta)}{\partial \theta} \right]^2, \quad (7.7)$$

where

$$V(\delta) = \tilde{R}(\delta) + 2 \sum_i \int_0^\infty d\tau \tilde{G}_i^{(2)}(\tau) \quad (7.8)$$

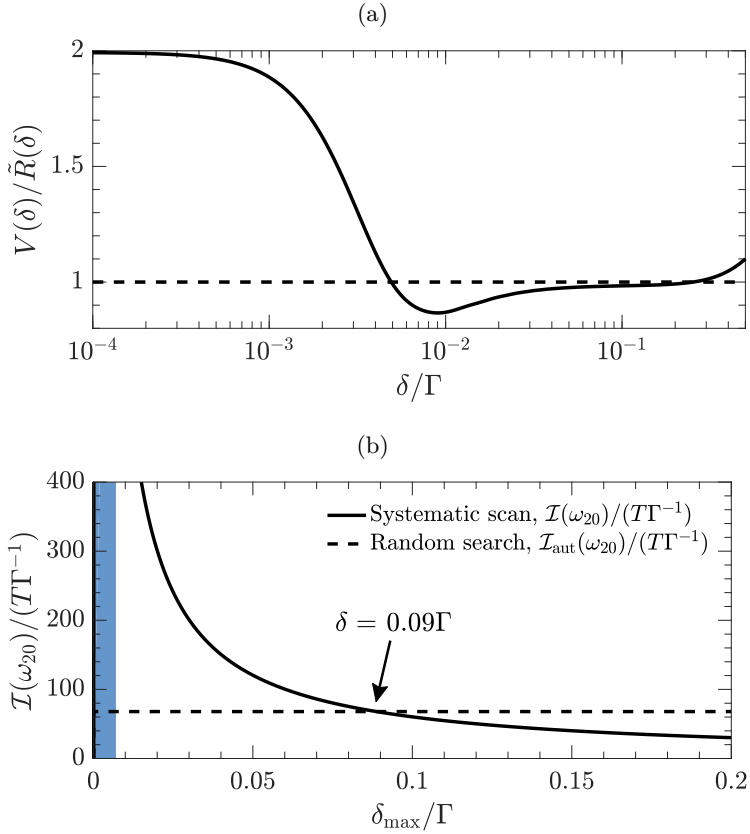


Figure 7.4: (a) Dependence on the detuning  $\delta$  of the photocount variance per time  $V(\delta)$  divided by the rate  $\tilde{R}(\delta)$ . The dashed line marks the Poissonian case where  $V(\delta) = \tilde{R}(\delta)$ . (b) Information measures for estimating  $\omega_{20}$  in the  $\Lambda$ -system by a systematic scan and the random search protocol, respectively. In both cases the search is restricted to an interval  $[-\delta_{\max}, \delta_{\max}]$  around the dark resonance. The shaded area is the region where  $\delta_{\max} < \delta_Q$  and our statistical model of the recycling process requires modifications. Results are shown for  $\Omega = 0.1\Gamma/\sqrt{2}$ .

is the frequency dependent photocount variance per time. The Fisher information (7.7) reveals via the Crámer Rao bound an uncertainty  $\sigma(\theta) = [\mathcal{I}(\theta)]^{-1/2}$ , scaling as  $1/\sqrt{T}$  with time.

In Fig. 7.4(a) we show  $V(\delta)/\tilde{R}(\delta)$  as a function of the detuning  $\delta$  for the  $\Lambda$ -system considered in the main text. Notice how the photo current exhibits photon bunching and super-Poissonian counting statistics close to the dark resonance, while it is sub-Poissonian for intermediate values and again super-Poissonian away from the resonance.

To compare with the autonomous search protocol presented in the main text, we show in Fig. 7.4(b) the Fisher information Eq. (7.7) for estimating  $\omega_{20}$  by a systematic scan along with the equivalent information measure  $\mathcal{I}_{\text{aut}}(\omega_{20}) = (\delta_T/0.82)^2$  of our random search for different widths of the search interval as determined by  $\delta_{\text{max}}$ . The comparison shows that for the parameters used in Fig. 7.1(b), our random search proves superior to the frequency scan if we search an interval  $[-\delta_{\text{max}}, \delta_{\text{max}}]$  with  $\delta_{\text{max}} > 0.09\Gamma$ , i.e., as long as the resonance is not a-priori known to very high precision.

## 7.4 Outlook

While we presented the scheme for a driven  $\Lambda$ -system and restricted our attention to a rate  $R(\delta)$  with a quadratic dip around  $\delta = 0$  and a flat plateau for large  $\delta \simeq \delta_{\text{max}}$ , the arguments are general, and the statistical methods apply equally well to other systems. For example, different forms of  $R(\delta) \propto \delta^\alpha$  for  $\delta \simeq 0$  will lead to different values of  $\mu = 1/\alpha$  which, in turn, imply different scaling with time of the sensitivity as quantified by  $\delta_T \propto T^{-\mu}$ . For instance, a variant of the presented scheme may apply Raman pulses rather than continuous illumination. It can be shown that, e.g., a sequence of Blackman pulses [224] yields an excitation probability characterized by  $\mu = 1/4$ , while square pulses lead to  $\mu = 1/2$  [225]. Although these examples do not yield a faster convergence of the random walk in frequency space towards the atomic resonance frequency than the example studied here, they illustrate the usefulness of the general formalism. This formalism will allow better than  $1/\sqrt{T}$  scaling of the error in estimating a general unknown parameter  $\theta$  if a process is found for which the rate depends on  $\theta$  as  $R(\theta) \propto \theta^\alpha$  with  $0 < \alpha < 2$ .

If  $\omega_{20}$  is only known to a precision of  $\lesssim \Gamma$ ,  $\delta_{\text{max}}$  must be chosen bigger than  $\delta_L$ . In this case, the rate decreases as  $1/\delta^2$  in the recycling region, leading to recycling times of order  $\sim \delta^2$ , and there is a risk that trajectories will be trapped far away from the resonance. The return times

are then also described by anomalous statistics, and  $P_r(\tau_r)$  is of the form Eq. (7.2) with  $\mu_r < 1$ . The actual value of  $\mu_r$  depends on the detailed frequency-shifting protocol. If  $\delta$  is restricted to jump to a vicinity of the current value, one finds  $\mu_r = 1/4$  [226] and  $T_N^{(REC)} \propto N^4$ . Our scheme then fails asymptotically as  $f_E(T) \rightarrow 0$  for large  $T$ . If, instead, the laser frequency is shifted uniformly on the search interval, the exact zero of  $R(\delta)$  at  $\delta = 0$  dominates the asymptotic zero as  $|\delta| \rightarrow \infty$ , and the trajectories will converge (albeit more slowly) to the PDS.

In this work, we have proposed to locate the absorption zero of a dark resonance by a random frequency search protocol. Due to the non-ergodic behavior of the system, methods from Lévy statistics were employed to assess the asymptotic spectroscopic sensitivity of the scheme. For the example of a driven  $\Lambda$ -type system, our method compares favourably with the Cramér-Rao bound of a conventional frequency scan. Metrology protocols have been proposed that feature similar feedback and adaptive elements, and which show convergence faster than  $1/\sqrt{T}$  or  $1/\sqrt{N}$ , where  $N$  quantifies the amount of physical resources; see e.g. [33, 88, 173, 227]. Since adaptive schemes may generally induce non-ergodic dynamics, we believe that elements of our theoretical analysis will be relevant in the characterization of a number of such protocols where standard statistical analyses are inadequate.

# Multihypothesis discrimination

*This chapter is reproduced from Ref. [10] with only a few adjustments.*

---

The first part of this thesis has been concerned chiefly with Hamiltonian parameter estimation where a continuum of candidate parameter values are filtered by their different action on the state of a quantum probe. I shall now turn my attention to *hypothesis testing*, which considers complementary scenarios with a discrete set of hypotheses,  $m = 1, 2, \dots, N$  for the Hamiltonian acting on the probe. In both cases, our ability to determine the true candidate hypothesis or physical parameter is ultimately limited by our ability to discern the corresponding signals obtained by measurements on the probe system; Fig. 8.1(a).

Our focus shall remain on experiments with an open probe system whose interaction with a broadband environment validates the Born-Markov approximation. As emphasized in Chapter 2, if the environment is left unmonitored, the interaction leads to decoherence of the system and to a loss of distinguishability, while a combined measurement on the probe system and its environment may yield much more information about the Hamiltonian governing the dynamics; see Fig. 8.1(b). Assuming that such a measurement is implementable, the ultimate precision is concerned not with the discrimination of reduced density-matrix candidates  $\{\rho_m\}_{m=1}^N$  for the small system but rather with the discrimination of the, possibly,

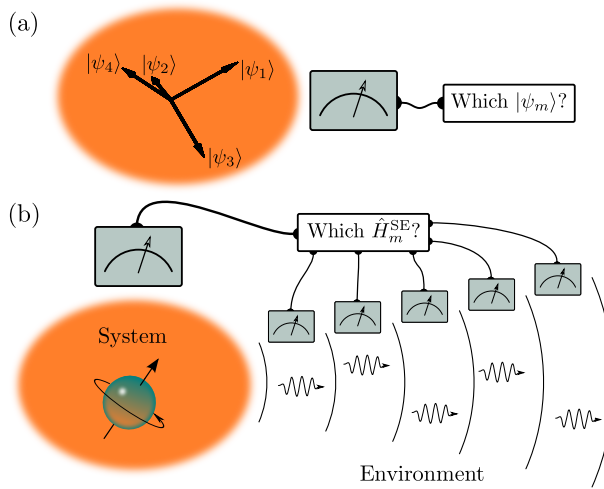


Figure 8.1: (a) In state discrimination, a measurement is performed to distinguish between a set of  $N$  candidate states  $\{|\psi_m\rangle_{m=1}^N$ . (b) In hypothesis discrimination with an open quantum probe, a combined measurement on the system and its environment is performed to determine the true candidate from a set of  $N$  possible Hamiltonians  $\{\hat{H}_m^{\text{SE}}\}_{m=1}^N$  of the system or the combined system and environment.

pure quantum states of the system and its environment  $\{|\psi_m^{\text{SE}}\rangle_{m=1}^N$ . For parameter estimation, the associated precision is bounded by the quantum Fisher information [Sec. 2.3]. In this chapter we show how discrimination between an arbitrary number of (non-orthogonal) states of a quantum system may be employed to determine an upper bound for our ability to distinguish among a discrete set of different hypotheses concerning the evolution of a Markovian open quantum system.

For two candidate states  $|\psi_1\rangle$  and  $|\psi_2\rangle$  prepared with prior probabilities  $P_1$  and  $P_2$ , Helstrom derived in 1969 a general expression for the minimum error probability in discriminating them by a single measurement [106],

$$Q_e^{(\text{Helstrom})} = \frac{1}{2} \left( 1 - \sqrt{1 - 4P_1P_2|\langle\psi_1|\psi_2\rangle|^2} \right). \quad (8.1)$$

Recent works, e.g., Refs. [228, 229], have made progress towards deriving a general framework for cases with multiple hypotheses, but no closed form expression has been found except in cases where the candidate density operators commute [230]. As pointed out by Helstrom [106] it is, however, clear that even for multiple hypotheses, the error probability

$Q_e$  depends only on the pairwise overlaps between the candidate states and their prior probabilities. In this chapter we outline how the error probability in discriminating  $N$  arbitrary quantum states can be phrased as a semidefinite-programming problem for which numerically efficient algorithms exist.

The full states of a system and a Markovian environment occupy in general a very large Hilbert space and the candidate states of the combined system and their overlaps  $\langle \psi_n^{\text{SE}} | \psi_m^{\text{SE}} \rangle$  are at a first glance intractable. To solve this issue, we rederive the main results of Ref. [154] for evaluating  $\langle \psi_n^{\text{SE}} | \psi_m^{\text{SE}} \rangle$  by propagating a so-called two-sided master equation for an effective density matrix which lives in the much smaller Hilbert space of the system alone. We further show how the pairwise state overlaps among  $N$  candidate states can be applied to embed these states in a reduced Hilbert space of dimension  $N$ . Distinguishing  $N$  hypotheses for the evolution of the open quantum system is equivalent to a multistate discrimination problem on this Hilbert space. We illustrate our theory by three realistic examples.

## 8.1 Optimal state discrimination

One may specify different goals and hence measures of the quality of a state discrimination process, depending on the number of copies of the quantum system available [231] and depending on the cost and reward for making wrong and correct estimates [232]. In the limit where measurements on asymptotically many copies  $M$  of the quantum probe system are available, the probability of making an erroneous assignment decreases exponentially with  $M$ . The exponent obeys the quantum Chernoff bound [233], which was recently generalized to cases with multiple candidate states [234].

In the present study we are interested in the information obtainable by performing a measurement on a single quantum system. We assume that the system is prepared with probability  $P_m$  in one of  $N$  different, mixed quantum states  $\{\rho_m\}_{m=1}^N$ , and that we can perform measurements on the system with outcomes that we combine into our assignment  $\lambda = 1, 2, \dots, N$  of the most likely state. We quantify a given measurement strategy by the *error probability* of assigning a false state (hypothesis) based on the outcome  $\lambda$  of a measurement performed on the system,

$$Q_e = \sum_{m=1}^N P_m \sum_{\substack{n=1 \\ n \neq m}}^N P(\lambda = n | \rho_m). \quad (8.2)$$

To be able to assign  $N$  possible states, the measurement must have  $N$  possible outcomes, so for a Hilbert space of dimension  $d < N$ , we have recourse to generalized (non-projective) measurements with fundamentally ambiguous outcomes. Such measurements are defined by a positive-operator valued measure (POVM) with effects  $\{\hat{E}_m\}_{m=1}^N$  which are positive semidefinite ( $\hat{E}_m \geq 0$ ) and sum to identity  $\sum \hat{E}_m = \mathbb{I}$ , [134]. The probability to obtain an outcome  $n$  if the *true* state is  $\rho_m$  is then  $P(\lambda = n|\rho_m) = \text{Tr}(\hat{E}_n \rho_m)$ , so by applying  $\sum \hat{E}_m = \mathbb{I}$  and  $\sum P_m = 1$  we may rewrite Eq. (8.2),

$$Q_e(\{\hat{E}_m\}_{m=1}^N) = 1 - \sum_{m=1}^N P_m \text{Tr}(\hat{E}_m \rho_m). \quad (8.3)$$

The task of obtaining the optimal POVM, which minimizes the error probability for a given set of candidate states  $\{\rho_m\}_{m=1}^N$  with (prior) probabilities  $\{P_m\}_{m=1}^N$  defines a semidefinite programming problem [235]:

$$\begin{aligned} & \text{minimize} && Q_e(\{\hat{E}_m\}_{m=1}^N) \\ & \text{subject to} && \hat{E}_m \geq 0 \quad \forall m \in \{1, \dots, N\} \\ & \text{and} && \sum_{m=1}^N \hat{E}_m = \mathbb{I}. \end{aligned} \quad (8.4)$$

Recent studies provide analytic solutions for this problem in the case of discriminating three qubit states ( $N = 3$ ,  $d = 2$ ) with arbitrary prior probabilities [228] or any number of *a priori* equally probable qubit states [236]. Furthermore, it was recently realized that any  $N$ -outcome measurement can be decomposed into sequences of nested two-outcome measurements which allow straightforward numerical optimization [229]. A detailed discussion of the state discrimination problem as a convex optimization task and a general solution by semidefinite programming was provided in Ref. [237]. In the present study we apply the CVX package for specifying and solving convex programs in Matlab [238, 239].

## 8.2 Hypothesis testing with open quantum systems

Hypothesis testing is the task of discriminating the evolution of a probe system subject to one of a discrete set of candidate Hamiltonians. To distinguish different hypotheses, a system may be subject to continuous monitoring by a probe beam or information may be obtained by, e.g., homodyne detection or photon counting of the radiation emitted by the

system [7, 99, 107]. The achievements of such concrete procedures shall be to the topic of the next chapter.

As argued in [129, 140, 154], the Markovian nature of the system-environment interaction implies that the discernibility of the (unmeasured) quantum states of the system and environment provides a theoretical upper bound for our practical ability to distinguish the different hypotheses by, e.g., continuous monitoring of the environment degrees of freedom as in Ref. [93] and in Chapter 9 of this thesis. Each individual hypothesis  $m$  thus leads to a particular unmeasured quantum state  $|\psi_m^{\text{SE}}\rangle$  of the system and the environment at a given time  $t$  and hypothesis testing is equivalent to the problem of discriminating the states  $\{|\psi_m^{\text{SE}}(t)\rangle\}_{m=1}^N$ . Due to the large Hilbert space dimension of the environment, these states are generally not accessible. Nevertheless, following the idea of Ref. [154], we show in this section that in situations where the Born-Markov approximation applies to the system-environment interaction, the overlaps between any two candidate states can be evaluated by solving a two-sided master equation for an effective density operator on the small system Hilbert space alone. We subsequently show how the overlaps between all pairs of states can be used to construct a low-dimensional representation of the problem to which the technique (8.4) of Sec. 8.1 applies.

### 8.2.1 A two-sided master equation for the state overlaps

The distinct hypotheses can be formally mapped to the states  $|m\rangle$  of an  $N$ -level ancillary system such that the evolution of the system and environment is conditioned on the state of the ancilla via the Hamiltonian

$$\hat{H}^{\text{ASE}} = \sum_{m=1}^N |m\rangle \langle m| \otimes \hat{H}_m^{\text{SE}}, \quad (8.5)$$

where the candidates,  $\hat{H}_m^{\text{SE}}(t) = \hat{H}_m + \hat{V}_m^{\text{SE}}$  for the system-environment Hamiltonian in the interaction picture may be separated into candidates for the part acting on the system alone  $\hat{H}_m$  and candidates  $\hat{V}_m^{\text{SE}}$  for the system-environment interaction.

While the ancilla, system, and environment are initially prepared in a separable pure state  $|\psi(t=0)\rangle = \frac{1}{\sqrt{N}} \sum_{m=1}^N |m\rangle \otimes |\psi^{\text{SE}}(t=0)\rangle$ , evolution under the Hamiltonian (8.5) yields, after a time  $t$ , an entangled state,

$$|\psi(t)\rangle = \frac{1}{\sqrt{N}} \sum_{m=1}^N |m\rangle \otimes |\psi_m^{\text{SE}}(t)\rangle. \quad (8.6)$$

Instead of the explicit separation in ancilla (A) and system-environment (SE) components in Eq. (8.6), we shall separate the complete system in ancilla-system (AS) and environment degrees of freedom. Assuming a weak coupling to a memoryless environment, the state  $\rho^{\text{AS}}$  of the ancilla-system obeys a Born-Markov master equation in the interaction frame [133, 134] ( $\hbar = 1$ ),

$$\dot{\rho}^{\text{AS}} = -i[\hat{H}^{\text{AS}}, \rho^{\text{AS}}] - \int_0^\infty dt' \text{Tr}_{\text{E}} \left( [\hat{V}^{\text{ASE}}(t), [\hat{V}^{\text{ASE}}(t'), \rho^{\text{AS}}(t') \otimes \rho^{\text{E}}(0)]] \right). \quad (8.7)$$

In Eq. (8.7), the unitary part of the evolution is governed by a Hamiltonian

$$\hat{H}^{\text{AS}} = \sum_{m=1}^N |m\rangle \langle m| \otimes \hat{H}_m, \quad (8.8)$$

and the interaction with the environment described by

$$\hat{V}^{\text{ASE}}(t) = \sum_{m=1}^N |m\rangle \langle m| \otimes \hat{V}_m^{\text{SE}}(t). \quad (8.9)$$

The ancilla-system state can be put on the form of a block matrix,

$$\rho^{\text{AS}}(t) = \frac{1}{N} \sum_{n,m=1}^N \rho_{nm}(t) |n\rangle \langle m|, \quad (8.10)$$

where the operators  $\rho_{nm}(t)$  on the system Hilbert space are all equal to the projection operator on the initial state of the system at time  $t = 0$ .

As seen from Eq. (8.6), the overlap between the  $n$ th and  $m$ th system-environment candidate states can be obtained as the expectation value of  $|n\rangle \langle m|$ ,

$$\begin{aligned} \langle \psi_n^{\text{SE}} | \psi_m^{\text{SE}} \rangle &= N \langle \psi(t) | n\rangle \langle m| \psi(t) \rangle \\ &= N \text{Tr}_{\text{AS}} \left[ |n\rangle \langle m| \rho^{\text{AS}}(t) \right] \\ &= \text{Tr}_{\text{S}} [\rho_{mn}(t)]. \end{aligned} \quad (8.11)$$

Inserting Eq. (8.10) as an Ansatz into Eq. (8.7) produces a set of equations,

$$\begin{aligned} \dot{\rho}_{nm} &= -i \left( \hat{H}_n \rho_{nm} - \rho_{nm} \hat{H}_m \right) - \int_0^\infty dt' \text{Tr}_{\text{E}} \left( \hat{V}_n^{\text{SE}}(t) \hat{V}_n^{\text{SE}}(t') \rho_{nm}(t) \otimes \rho^{\text{E}}(0) \right. \\ &\quad + \rho_{nm}(t) \otimes \rho^{\text{E}}(0) \hat{V}_m^{\text{SE}}(t') \hat{V}_m^{\text{SE}}(t) - \hat{V}_n^{\text{SE}}(t) \rho_{nm}(t) \otimes \rho^{\text{E}}(0) \hat{V}_m^{\text{SE}}(t') \\ &\quad \left. - \hat{V}_n^{\text{SE}}(t') \rho_{nm}(t) \otimes \rho^{\text{E}}(0) \hat{V}_m^{\text{SE}}(t) \right). \end{aligned} \quad (8.12)$$

We refer to these as *two-sided* master equations because the matrix argument  $\rho_{nm}(t)$  is acted upon by the different candidate Hamiltonians from the left and right hand sides.

Suppose now that in the rotating-wave approximation, the system-environment interaction can be written on a Jaynes-Cummings form,

$$\hat{V}_m^{\text{SE}} = \sum_k \left( g_m^{(k)} \hat{a}_k \hat{S}_m^\dagger e^{-i\delta_k t} + (g_m^{(k)})^* \hat{a}_k^\dagger \hat{S}_m e^{i\delta_k t} \right), \quad (8.13)$$

where the sum runs over the bosonic bath modes with annihilation (creation) operators  $\hat{a}_k$  ( $\hat{a}_k^\dagger$ ), detuned by  $\delta_k$  from the system resonance. Hypotheses for the interaction with the environment are represented by the system operators  $\hat{S}_m$  and complex coupling coefficients  $g_m^{(k)} = |g_m^{(k)}| e^{i\phi_m^{(k)}}$  to the individual modes.

If we assume the environment to be in the vacuum state  $\rho^{\text{E}}(0) = \sum_k |0_k\rangle \langle 0_k|$ , performing the partial trace over the environment in Eq. (8.12) yields a two-sided master equation,

$$\dot{\rho}_{nm} = -i \left( \hat{H}_n \rho_{nm} - \rho_{nm} \hat{H}_m \right) + \hat{c}_n \rho_{nm}(t) \hat{c}_m^\dagger - \frac{1}{2} \left( \hat{c}_n^\dagger \hat{c}_n \rho_{nm} - \rho_{nm} \hat{c}_m^\dagger \hat{c}_m \right), \quad (8.14)$$

where the candidate dissipation operators are defined as  $\hat{c}_m = \sqrt{\gamma_m} \hat{S}_m e^{-i\phi_m}$ . Here the damping rates  $\gamma_m$  and phases  $\phi_m$  are obtained from the integrated correlation functions of the environment,

$$\Gamma_{ab}(t) = \int_0^\infty dt' \sum_k (g_a^{(k)})^* g_b^{(k)} e^{-i\delta_k(t-t')}. \quad (8.15)$$

Consistent with Fermi's golden rule, due to the time-integral, one obtains  $\Gamma_{ab}(t) = 2\pi (g_a^{(k_s)})^* g_b^{(k_s)}$  with  $\delta_{k_s} = 0$ , such that  $\gamma_m = 2\pi |g_m^{(k_s)}|^2$  and  $\phi_m = \phi_m^{(k_s)}$ . Note that, for simplicity, we included only a single environment and a single transition operator. In the case of hypotheses concerning multiple environmental couplings, a corresponding sum over dissipation operators,  $\hat{c}_m \rightarrow \{\hat{c}_{j,m}\}_{j=1}^J$ , is employed in the master equation (8.14).

The solution of the uncoupled equations (8.14) yields by Eq. (8.11) the temporal dynamics of the overlap between any pair of the *full* states of the system and environment pertaining to the different hypotheses for the effective system Hamiltonians  $\hat{H}_m$  and relaxation operators  $\hat{c}_m$ . Hence, the numerically intractable problem of evolving the full states in the very large system and environment Hilbert space is reduced to the much simpler task of evolving  $(N^2 - N)/2$  matrices with the dimension of the smaller probe system.

### 8.2.2 Low dimensional representation of states of the system and its environment

Although the full state of a system and its environment lives in a formally infinite-dimensional Hilbert space, the discrete nature of the hypothesis testing problem implies that at any time we have at most  $N$  different possible states to distinguish. These span a (time-dependent) subspace of dimension  $N$  which is sufficient to fully characterize the discrimination problem. To apply the semidefinite programming methods of Sec. 8.1, let us define an orthogonal basis  $\{|\phi\rangle_n\}_{n=1}^N$  for this subspace such that each candidate state can be expressed as a linear combination,

$$|\psi_m^{\text{SE}}\rangle = \sum_{n=1}^m C_n^{(m)} |\phi_n\rangle,$$

where the  $C_n^{(m)}$  are complex expansion coefficients.

We shall now outline how one may in general define a basis and obtain the  $C_n^{(m)}$ : let the first basis state be the first candidate state  $|\phi_1\rangle = |\psi_1\rangle$ , i.e.,  $C_n^{(1)} = \delta_{n1}$ . The second state is then used to define the second basis state,  $\text{span}(|\psi_1^{\text{SE}}\rangle, |\psi_2^{\text{SE}}\rangle) = \text{span}(|\phi_1\rangle, |\phi_2\rangle)$ , such that  $C_n^{(2)} = 0$  for  $n > 2$ . Since any of the basis states may be multiplied by an arbitrary complex phase factor, we may further use the convention that  $C_2^{(2)}$  is positive which together with the overlap  $\langle\psi_1^{\text{SE}}|\psi_2^{\text{SE}}\rangle$  and the normalization criterion completely determines  $|\phi_2\rangle$ . Similarly the third candidate defines the third basis state and we set  $C_3^{(3)} \in \mathbb{R}_{\geq 0}$ . By continuing in this manner, we represent the states of the system and the environment as a sequence of  $N$ -dimensional vectors

$$\begin{array}{ccccccc} \mathbf{C}^{(1)} & & \mathbf{C}^{(2)} & & \mathbf{C}^{(3)} & \dots & \mathbf{C}^{(N)} \\ \parallel & & \parallel & & \parallel & & \parallel \\ \begin{pmatrix} 1 \\ 0 \\ \vdots \\ \vdots \\ 0 \end{pmatrix} & & \begin{pmatrix} C_1^{(2)} \\ C_2^{(2)} \\ 0 \\ \vdots \\ 0 \end{pmatrix} & & \begin{pmatrix} C_1^{(3)} \\ C_2^{(3)} \\ C_3^{(3)} \\ \vdots \\ 0 \end{pmatrix} & & \begin{pmatrix} C_1^{(N)} \\ C_2^{(N)} \\ \vdots \\ \vdots \\ C_N^{(N)} \end{pmatrix} \end{array} \quad (8.16)$$

where all state amplitudes are given by a recursive procedure:

$$C_n^{(m)} = \frac{1}{C_n^{(n)}} \left( \langle\psi_n|\psi_m\rangle - \sum_{k=1}^{n-1} C_k^{(n)*} C_k^{(m)} \right) \quad (8.17)$$

for  $1 \leq n \leq m - 1$  and

$$C_m^{(m)} = \sqrt{1 - \sum_{k=1}^{m-1} |C_k^{(m)}|^2}. \quad (8.18)$$

It may in a given hypothesis testing scenario occur that two or several candidate states become identical. The number of POVM elements is then reduced and for some outcomes of our protocol we have recourse to select the one of the corresponding hypotheses with the largest prior probability.

## 8.3 Examples

The ideas and methods presented in Secs. 8.1 and 8.2 allow us to evaluate the minimum error probability in the assignment of one of *any* number of distinct hypotheses for the evolution of an open quantum system as a function of the duration  $t$  of an experiment. Here we provide three examples which illustrate different aspects of our theory and its application.

### 8.3.1 Phase of a Rabi drive

We first examine a two-level system driven resonantly with a known Rabi frequency  $\Omega$  but with an unknown complex phase  $\phi_m$ . In a frame rotating with the resonance frequency, the candidate Hamiltonians can be written as,

$$\hat{H}_m = \Omega [\cos(\phi_m)\hat{\sigma}_x + \sin(\phi_m)\hat{\sigma}_y] / 2. \quad (8.19)$$

In this example we consider the phases  $\phi_m = \pi(m - 1)/2$  as illustrated in the inset of Fig. 8.2, and we assume that the atomic excitation decays into the environment at a known rate  $\gamma$  such that  $\hat{c} = \sqrt{\gamma}\hat{\sigma}_-$ . The Rayleigh component of the emitted radiation is in phase with the driving field and homodyne detection should thus gradually reveal the value of  $\phi_m$ . In contrast, photon counting tracks the intensity of the emitted radiation and hence maps the excitation of the system which is independent of  $\phi_m$ .

The full curve in Fig. 8.2 shows the minimum error probability  $Q_e(t)$  calculated from our theory as a function of the duration  $t$  of the experiment. Initially  $Q_e(t = 0) = 75\%$ , reflecting that each of the four hypotheses are *a priori* equally probable ( $P_m = 1/4$ ), while for large times they may be unambiguously discriminated. Interestingly, however,  $Q_e(t)$  is not a monotonous function of  $t$ . For instance, it reaches a minimum around

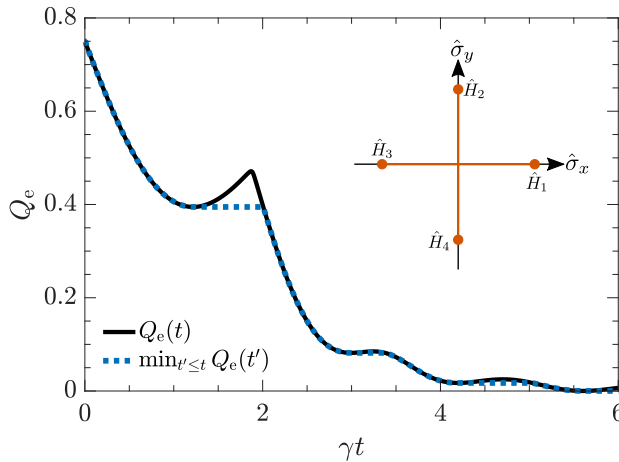


Figure 8.2: Phase of a Rabi drive on a two-level system Eq. (8.19) is determined by performing a combined measurement on the atom and the emitted field. Inset: the four hypotheses are  $\hat{H}_1 = \Omega\hat{\sigma}_x/2$ ,  $\hat{H}_2 = \Omega\hat{\sigma}_y/2$ ,  $\hat{H}_3 = -\Omega\hat{\sigma}_x/2$ , and  $\hat{H}_4 = -\Omega\hat{\sigma}_y/2$ . Main figure: the probability of assigning a wrong hypothesis is shown for  $\Omega = 2\gamma$  and an atom initialized in its ground state. The dotted curve shows the smallest error probability reachable by any given time  $t$ .

$\gamma t \simeq 1.25$  and if for some reason the experiment lasts a little longer,  $\gamma t \lesssim 2$ , the ability to discriminate the four cases deteriorates. The reason is that, irrespective of the excitation phase, the atomic Bloch vector approaches the vertical direction around  $\Omega t \simeq \pi$ , and only the emitted radiation provides any information until the Bloch vector candidates evolve further. It is thus sometimes favorable to perform a measurement on the atom and the field at an earlier time and keep the result rather than wait for more data to accumulate. The dotted curves track the minimum error probability obtainable by performing a measurement before any given time  $t$  and hence represent the lowest error achievable in an experiment of duration  $t$ .

### 8.3.2 Number of atoms inside a cavity

Here we imagine a cavity field driven by a (classical) field of strength  $u$  and interacting with an unknown but small number of atoms. Due to an out-coupling at a rate  $\kappa$  from the cavity, the emitted radiation from the spins can be monitored and we further assume that the experimental setup allows direct measurements on the atomic ensemble. The atoms

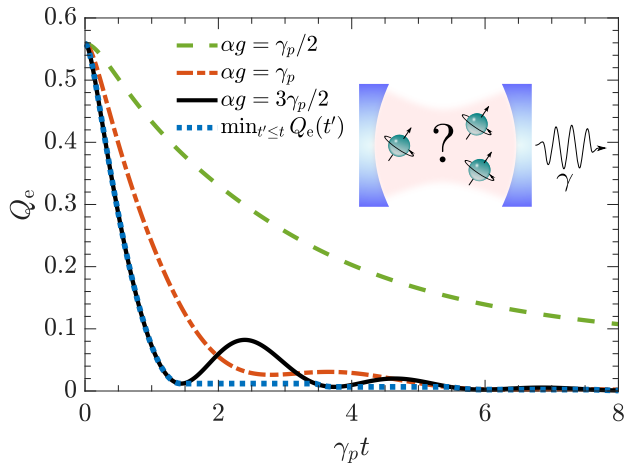


Figure 8.3: Inset: an unknown number of atoms are coupled to a driven cavity. The number is estimated by performing a combined measurement on the atomic spins and the field emitted from the cavity. The hypotheses are  $m = 1, 2, 3$  and 4 atoms and the system evolves according to the Hamiltonian (8.20). Main figure: The probability of assigning a false hypothesis is shown for weak driving  $\alpha g = \gamma_p/2$ , for moderate driving  $\alpha g = \gamma_p$  and for strong driving  $\alpha g = 3\gamma_p/2$ . The dotted curve shows the smallest error probability reached before any given time  $t$  for the underdamped cases where local minima occur in  $Q_e(t)$ .

are modeled as  $N$  two-level systems of which  $m$  are coupled linearly with strength  $g$  to a single cavity mode and  $N - m$  are uncoupled. Assuming the bad cavity limit, the field may be adiabatically eliminated leading to an effective Hamiltonian and relaxation of the atoms. The different hypotheses concerning the number of spins inside the cavity are hence characterized by  $N$  sets of Hamiltonians and relaxation operators,

$$\begin{aligned}\hat{H}_m &= g \left( \alpha \hat{S}_+^{(m)} + \alpha^* \hat{S}_-^{(m)} \right) \\ \hat{c}_m &= \sqrt{\gamma_p} \hat{S}_-^{(m)},\end{aligned}\tag{8.20}$$

where  $\hat{S}_\pm^{(m)} = \sum_{i=1}^m \hat{\sigma}_\pm^{(i)}$ ,  $\alpha = 2u/\kappa$  and  $\gamma_p = 4g^2/\kappa$  is the Purcell-enhanced decay rate. We assume that the number of atoms coupled to the cavity is Poisson distributed with mean value  $\mu = 1.5$ . The probabilities prior to the experiment are hence  $P_m \propto \mu^m/m!$ .

Fig. 8.3 shows the evolution of the minimum error probability in distinguishing the cases of  $m = 1, 2, 3$  and 4 atoms inside the cavity.

Results are shown for a weakly, a moderately, and a strongly driven cavity, respectively. While it is never favorable to drive the cavity very weakly since this does not lead to a fluorescence signal with much structure, it is evident that the moderate driving case outperforms the strong driving case for a brief period around  $\gamma_p t \simeq 2.5$ . However, the dotted curves, tracking the minimum error probability obtainable by performing a measurement at an optimal time before  $t$ , shows that the stronger driving is always favorable.

### 8.3.3 Relative positions of a dopant ion

Our final example concerns testing of the relative positions between two impurity dipoles in a lattice structure. Rare-earth-ion dopants in inorganic crystals have permanent electric dipole moments which are different depending on whether each ion is excited or not and may hence be used for controlled gates in a quantum computation [240, 241]. Such systems are produced by low random doping during crystal growth and, for applications in a quantum sensor or computer, one may want to assess the relative positions of the individual ions (qubits) by probing their interactions. A generic version of this kind of setup in a cubic lattice structure with lattice constant  $a$  is illustrated in Fig. 8.4(a). We assume dilute doping such that a read-out (sensor) ion couples only to a single qubit ion and we introduce a simple model of each ion as a two-level system. We let the sensor ion relax radiatively at a rate  $\gamma$  and assume the qubit ion states to be long lived. To obtain a fluorescence signal, the sensor is driven by a laser field with Rabi frequency  $\Omega_s$  and detuned by  $\delta_s$  from the bare transition frequency. We assume also the possibility to resonantly drive the qubit ion with a Rabi frequency  $\Omega_q$  in order to optimize the sensing capabilities. The candidate Hamiltonians may hence be written,

$$\hat{H}_m = \frac{\Omega_s}{2} \hat{\sigma}_x^{(s)} + \frac{\Omega_q}{2} \hat{\sigma}_x^{(q)} - \delta_s |e_s\rangle \langle e_s| + \Delta_m |e_q\rangle \langle e_q| \otimes |e_s\rangle \langle e_s|, \quad (8.21)$$

where the latter term accounts for the state dependent shift in frequency of the sensor ion due to the dipole-dipole interaction with the qubit ion [242],

$$\Delta_m = \left( \frac{\epsilon + 2}{3\epsilon} \right)^2 \frac{\mu_s \mu_q}{4\pi\epsilon_0 r_m^3} [\hat{\boldsymbol{\mu}}_s \cdot \hat{\boldsymbol{\mu}}_q - 3(\hat{\boldsymbol{\mu}}_s \cdot \hat{\mathbf{r}}_m)(\hat{\boldsymbol{\mu}}_q \cdot \hat{\mathbf{r}}_m)]. \quad (8.22)$$

Here  $\boldsymbol{\mu}_{s(q)} = \mu_{s(q)} \hat{\boldsymbol{\mu}}_{s(q)}$  is the difference in permanent electric dipole moment between the excited and ground state of the sensor (qubit) ion and

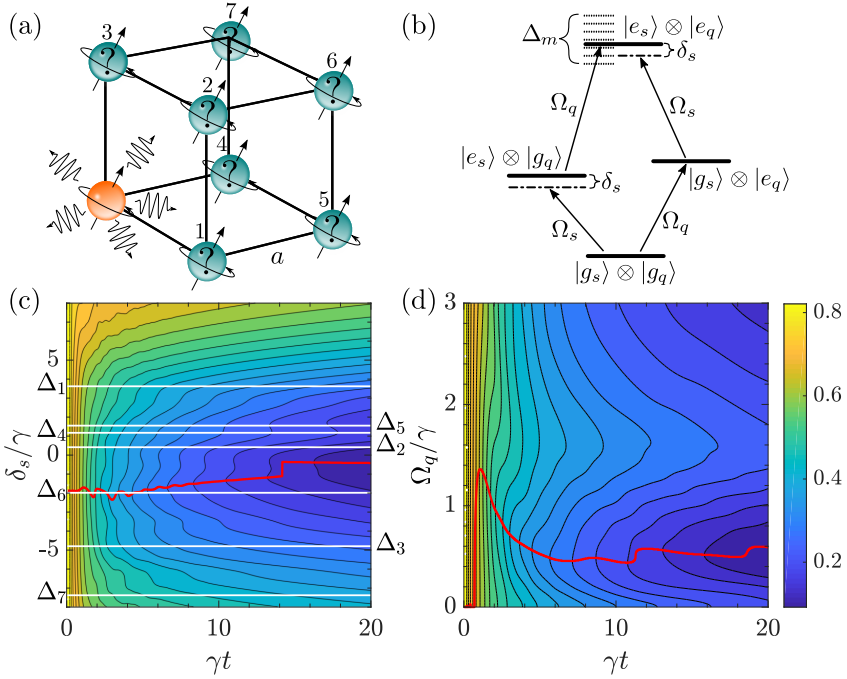


Figure 8.4: (a) Position of a qubit ion (green spin) in a cubic lattice structure with lattice constant  $a$  affects the fluorescence signal emitted by a sensor ion (orange spin) of a different species at a nearby lattice position and the internal state of the two ions. In our example  $\boldsymbol{\mu}_s = \boldsymbol{\mu}_q = (0.5, 0.3, 0.8)^T$  such that each of the seven possible marked positions yield a distinct energy shift of the sensor ion as given by Eq. (8.22). (b) The level structure of the Hamiltonian (8.21) of the two ions. The qubit ion is resonantly driven with a Rabi frequency  $\Omega_q$  and the sensor ion is driven with a Rabi frequency  $\Omega_s$  and a detuning  $\delta_s$  from resonance. The sensor excited state is shifted by  $\Delta_m$  due to the excited qubit ion. (c) Contour plot showing the probability  $Q_e$  of assigning a wrong lattice position to the qubit ion as a function of time and the (constant) detuning  $\delta_s$  of the sensor ion drive. The red line tracks the constant value of  $\delta_s$  which minimizes  $Q_e(t)$  at any given time. The white lines mark the energy shifts  $\Delta_m/\gamma$  associated with each of the seven possible positions in (a). (d) Contour plot showing the probability  $Q_e$  of assigning a wrong lattice position as a function of time and the (constant) strength of the qubit drive  $\Omega_q$  with  $\delta_s = 0$ . The red line tracks the constant value of  $\Omega_q$  which minimizes  $Q_e(t)$  for any given probing time. Results in (c) and (d) are shown for  $\Omega_s = 3\gamma$ ,  $(\frac{\epsilon+2}{3\epsilon})^2 \frac{\mu_s \mu_q}{4\pi\epsilon_0} = 5\gamma a^3$ , and equal priors  $P_m = 1/7$ .

$\mathbf{r}_m = r_m \hat{\mathbf{r}}_m$  is the vector between the sensor and the qubit with which the hypothesis testing is concerned. The prefactor, where  $\epsilon$  is the relative permittivity at zero frequency, accounts for local field corrections due to the crystal host material. One example is  $\text{Eu}^{3+}$  or  $\text{Pr}^{3+}$  ions doped in an  $\text{YAlO}_3$  or an  $\text{Y}_2\text{SiO}_5$  crystal [243]. A suitable sensor ion could be  $\text{Ce}^{3+}$ , which has a large difference  $\mu_s$  in static dipole moment [244]. A level diagram for the Hamiltonian (8.21) is shown in Fig. 8.4(b) and the level shift as well as the driven transitions are indicated.

Imagine first that we prepare the qubit ion in the excited state and then turn off the qubit drive ( $\Omega_q = 0$ ). As illustrated in Fig. 8.4(b) the resonance frequency of the excited state is then shifted by  $\Delta_m$  in a manner depending on the position of the qubit ion. It is intuitively clear that a higher sensitivity can be obtained if the system is driven at the actual resonance, i.e., by detuning the sensor ion driving laser such that  $\delta_s$  matches the true  $\Delta_m$ . In Fig. 8.4(c), the contour plot shows the error probability as a function of time and the (constant) value of  $\delta_s$ . The red curve tracks the optimum which is seen to be located near the mean value of the  $\Delta_m$ . Based on this understanding, one could imagine an optimized scheme where  $\delta_s$  is cycled though the different  $\Delta_m$  candidates with an appropriate portion of the total experimental time allocated to each.

By preparing an excited qubit the last term in Eq. (8.21) remains fully active at all times while driving the qubit yields a transient evolution of the system which might depend more strongly on  $\Delta_m$ . To investigate this, we show in Fig. 8.4(d) a contour plot of the error probability as a function of time and the qubit drive strength. The red line tracks the (constant) values of  $\Omega_q$  which minimizes  $Q_e(t)$  at any given time. Interestingly, for short times a relatively strong drive is favourable. This can be explained by the same mechanisms as in the previous example: when the system is strongly driven, it undergoes oscillations which are more pronounced at short times and whose frequency is modulated by  $\Delta_m$ . For longer times it becomes favorable to maintain the excited state for longer durations and with the parameters used here the optimal value lies around  $\Omega_q \simeq 0.5\gamma$ .

We presented this example for dopant ions but the general idea may be relevant in a number of similar setups. For example, the dipole-dipole potential between neutral atoms similarly yields an energy shift of the form Eq. (8.22) which is responsible for, e.g., the Rydberg Blockade mechanism [245]. Hence, our formalism could be fitted to the determination of the relative positions of Rydberg atoms in an optical lattice structure. Another platform is the sensing of a remote nuclear spin  $\hat{I}$  by an electron spin  $\hat{S}$ . Here the frequency shift is due to the hyperfine coupling [246–248].

For instance, the electron spin of an NV center can be used to sense the position of a  $^{13}\text{C}$  impurity in a vapor deposited (CVD) diamond which has a  $^{13}\text{C}$  abundance of less than 0.01% [249].

## 8.4 Conclusion and outlook

This chapter has evoked how optimal discrimination between an arbitrary number of quantum states may be phrased as a semidefinite programming problem for which efficient numerical solutions are available. The theory utilises that distinguishing a set of  $N$  hypotheses for the evolution of a Markovian open quantum system is equivalent to the discrimination of a set of time-dependent states of the full system and its environment. We show how their overlaps may be calculated in a straightforward manner and used to construct a lower-dimensional representation which is suitable for numerical treatment. This allows us to evaluate a lower (quantum) bound to the probability of assigning a false hypothesis, and the three examples presented in this chapter serves to illustrate some insights that may be obtained by such an analysis.

For the example in Sec. 8.3.3, it was shown how different but constant values of the qubit ion Rabi frequency and the detuning in the driving frequency of the sensor ion lead to different error probabilities. In optimal control, the bound could be further optimized by allowing time-dependent parameters  $\Omega_q(t)$  and  $\delta_s(t)$ . More generally, by following this line of thought our formalism is suitable for systematic optimization of the sensing capabilities in a given quantum setup by, e.g., controlling auxillary Hamiltonian parameters or environmental coupling strengths.

We would like to thank Frank Verstraete and Andreas Walther for helpful discussions regarding the example in Sec. 8.3.3.

# Continuous monitoring in hypothesis testing

*This chapter is reproduced from Ref. [11] with only a few adjustments. Notably, a large part of Sec. II of Ref. [11] is not included since it is instead presented in Chapter 2.*

---

The quantum bound to hypothesis discrimination with open quantum systems, derived in the previous chapter, may pertain to a highly nonlocal measurement performed on the full state of the system and its environment. This kind of measurement is in general infeasible to implement and in real experimental situations one has recourse to perform a more conventional measurement of the environment. The ability to distinguish a discrete set of models that describe a system observed by such measurement protocols is the topic of this chapter.

While the theory presented in Chapter 8 allows multiple unknown hypotheses, we shall for clarity of presentation now restrict our investigations to the discrimination of just two,  $h_0$  and  $h_1$ . When an experimentalist assigns a hypothesis ( $m$ ), the average error probability, i.e., the probability that the assignment,  $m = 0$  or  $1$  is wrong, is given by Eq. (8.2),

$$Q_e = P(m = 1|h_0)P(h_0) + P(m = 0|h_1)P(h_1), \quad (9.1)$$

where  $P(m = 0 \text{ or } 1|h = h_0 \text{ or } h_1)$  denotes the conditional probability to make the guess  $m = 0$  or  $1$ , when the data is obtained under the hypothesis

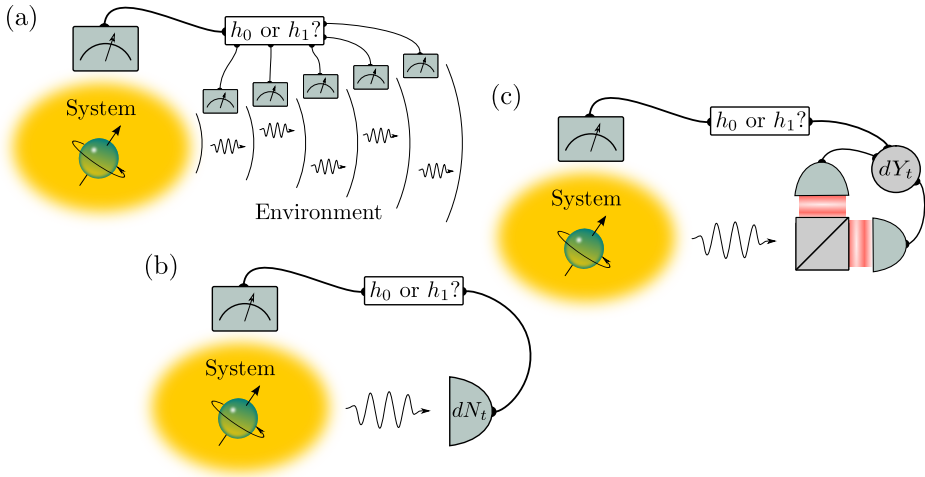


Figure 9.1: (a) A projective measurement on a system and its environment is performed after they have interacted for a time  $T$ . Based on the outcome, one of two hypotheses  $h_0$  and  $h_1$  about their evolution is judged to be more likely than the other. An experimentally more realistic approach monitors the radiation emitted by the probe system for a time  $T$  by (b) photon counting or (c) homodyne detection. The conditional state of the emitter defines the optimal system projection to be performed at the final time  $T$  and the most likely hypothesis is inferred from the combined monitoring signal and projection outcome.

$h = h_0$  or  $h_1$ , and  $P(h_0)$  and  $P(h_1)$  are the prior probabilities of the two hypotheses.

As emphasized in the previous chapter, distinguishing two different Hamiltonians  $\hat{H}_0$  and  $\hat{H}_1$ , governing the evolution of a closed quantum system, is achieved by discriminating the two quantum states  $\rho_0(t) = |\psi_0(t)\rangle\langle\psi_0(t)|$  (hypothesis  $h_0$ ) and  $\rho_1(t) = |\psi_1(t)\rangle\langle\psi_1(t)|$  (hypothesis  $h_1$ ), resulting from time evolution under each candidate Hamiltonian from a common initial state of the system. Only orthogonal states can be discriminated unambiguously while, in general, the overlap between the candidate states defines a minimum error probability for any measurement protocol,  $Q_e \geq Q_e^{(\text{Helstrom})}$  with  $Q_e^{(\text{Helstrom})}$  given in Eq. (8.1).

As derived by Helstrom [106], this bound can be saturated by performing a projective measurement of the operator,

$$\hat{A} = P(h_0)\rho_0 - P(h_1)\rho_1, \quad (9.2)$$

and assigning hypothesis  $h_0(h_1)$  if the outcome is one of the positive(negative) eigenvalues of  $\hat{A}$ . However, with an open quantum system,  $|\psi_i(t)\rangle$  in Eq. (9.2) denotes the combined states of the system and its environment. For the main (and experimentally very common) example of this thesis where a quantum system is coupled to a broadband radiation reservoir, a driven system and the quantized radiation field evolves into entangled states in an infinite dimensional Hilbert space. While these states may differ significantly for different Hamiltonians the, potentially, highly non-local projective measurement (9.2) of combined system and environment observables [see Fig. 9.1(a)] becomes difficult to achieve in practice. Instead, as illustrated in Fig. 9.1, one often has recourse to perform photon counting (b) or field quadrature measurements [e.g., homodyne detection (c)] on the environment.

In this study, we investigate to what extent supplementing continuous monitoring of the emitted radiation from the initial time  $t = 0$  to a final time  $t = T$  by a final projective measurement on the emitter system, allows better distinction between different hypotheses governing the system dynamics. Due to the measurement backaction associated with continuous monitoring of the environment, the state of the emitter evolves in a conditional manner according to the stochastic measurement signal as described in Sec. 2.2. In any particular realization of the measurement sequence, the optimal final measurement on the system (9.2) is thus conditioned on the detection record  $D_T$  obtained up until the final time  $T$ ,

$$\hat{A}_T^D = P(h_0|D_T)\rho_0^{(D_T)}(T) - P(h_1|D_T)\rho_1^{(D_T)}(T). \quad (9.3)$$

Here the information extracted from the environment is incorporated in the conditional candidate states  $\rho_i^{(D_T)}(T)$  and their probabilities updated by Bayes rule (2.1),  $P(h_i) \rightarrow P(h_i|D_T)$ .

The continuous monitoring and conditioned evolution of quantum states have for instance been realized in experiments with superconducting qubits [7, 99, 100] and optomechanical systems [128]. After homodyne or heterodyne detection of the radiation signal has been performed until time  $T$  on for example a superconducting qubit, a final system projection can be achieved in these experiments by applying a strong, dispersively coupled probe field [99, 137].

## 9.1 Bayesian analysis for hypothesis testing

Just as for optimal parameter estimation, optimal hypothesis discrimination from a continuous measurement record is provided by the Bayesian formalism presented in Chapter 2. To illustrate its application, we apply the formalism of Sec. 2.1.1 to simulate perfect monitoring of a two-level system with the purpose of discriminating two hypotheses for the resonant driving with a Rabi frequency of either  $\Omega_0$  or  $\Omega_1$ . That is, we test the two Hamiltonian hypotheses:  $\hat{H}_0 = \frac{\hbar\Omega_0}{2}\hat{\sigma}_x$  and  $\hat{H}_1 = \frac{\hbar\Omega_1}{2}\hat{\sigma}_x$ . The results are shown in Fig. 9.2. The signals,  $dN_t$  from photon counting and  $dY_t$  from homodyne detection, in the upper panels of (a) and (b) are sampled from the true hypothesis which we assume to be  $h_0$ . Conditioned on these signals, the (unnormalized) candidate states  $\tilde{\rho}_i^{(D_t)}(t)$  with  $D_t = N_t, Y_t$  evolve according to Eqs. (2.13) and (2.16), respectively. Their traces and the condition  $P(h_0|D_t) + P(h_1|D_t) = 1$  yield the time evolution of the inferred probabilities for each hypothesis as shown in the lower panels of Figs. 9.2(a) and 9.2(b). We assume equal priors  $P(h_0) = P(h_1) = 1/2$ .

For photon counting in Fig. 9.2(a) the probability updates are dominated by three photo detection events while periods with no detections lead to a less pronounced, continuous update. The noisy homodyne signal in Fig. 9.2(b), on the other hand, holds only very little information in each individual time-bin and here the probabilities continuously converge to reveal the true hypothesis. In both cases, at the final time  $t = 5\gamma^{-1}$  the accumulated signals are seen to favor the true hypothesis ( $h_0$ ) with almost unit probability. A figure of merit for a particular measurement strategy is the speed at which we arrive at perfect distinction.

### 9.1.1 Supplementing continuous monitoring by a projective measurement

If the hypotheses are not sufficiently discriminated at the end of the probing at time  $T$ , it may be possible to extract further information by a direct measurement on the emitter system. Due to the continuous monitoring, the emitter is assigned the conditional candidate states  $\rho_i^{(D_T)}(T)$ , while the probabilities that we ascribe to these states,  $P(h_i|D_T)$  are given by the traces of the unnormalized density matrices.

The optimal projective measurement we can perform on the system then concerns the system observable  $\hat{A}_T^{D_T}$  defined in Eq. (9.3). For a two-level system, the projective measurement of any observable  $\hat{A}$  is equivalent to the measurement of a Pauli spin component along a specific unit vector

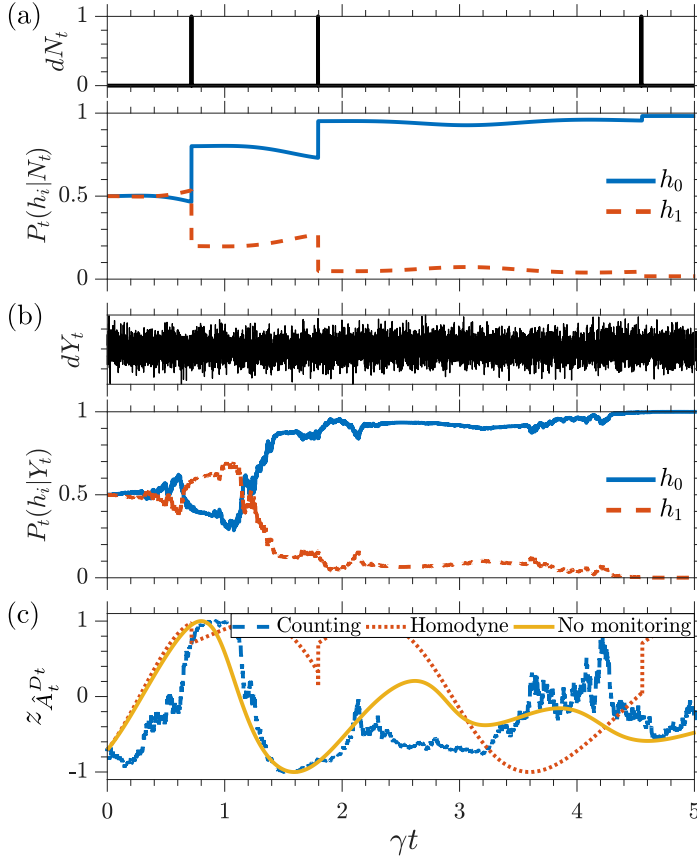


Figure 9.2: Simulated monitoring of a driven two-level system by (a) photon counting and (b) homodyne detection with the purpose of discriminating two hypotheses  $h_0$  ( $\Omega_0 = 2\gamma$ ) and  $h_1$  ( $\Omega_1 = 4\gamma$ ) for the Rabi frequency. The simulations are made assuming  $h_0$  to be the true hypothesis and with a detector efficiency  $\eta = 1$  and in (b) a local oscillator phase  $\Phi = -\pi/2$ . The second and fourth panels show the evolution of the probabilities  $P(h_i|D_t)$  for the two hypotheses conditioned on (a) the photon counting signal and (b) the noisy homodyne current shown in the first and third panels. The lower panel (c), shows the  $z$ -component  $z_{\hat{A}_t^{D_t}} \propto \text{Tr}(\hat{\sigma}_z \hat{A}_t^{D_t})$  of the optimal Pauli measurement observable (clarified in the main text) if monitoring is stopped at any given time. We observe that this optimal system measurement differs for the three cases of counting, homodyne detection and unobserved, dissipative emitter dynamics.

$(x_A, y_A, z_A)$  with  $u_A \propto \text{Tr}(\hat{\sigma}_u A)$ . In Fig. 9.2(c) we visualize the optimum observable  $\hat{A}_T^{DT}$  if the continuous monitoring, yielding the signals in the upper panels of (a) and (b), is terminated at the corresponding point in time. In this example the unit vector, designating the direction of the spin measurement, is confined to the  $(y, z)$  plane and we show its  $z$  component

During each experimental realization,  $\hat{A}_t^{Dt}$  assumes a stochastic value, which is different from the one that optimally discriminates the states of an unobserved system governed by the corresponding Lindblad master equation (2.9). With homodyne detection the measurement observable, represented by the blue noisy trace in Fig. 9.2(c), is seen to fluctuate around the full, yellow curve, pertaining to the unmonitored system, while with photon counting, large deviations arise accompanying the quantum jumps of the system state.

The possible eigenvalues  $\lambda$  of the measurement observable  $\hat{A}_T^{DT}$  occur under hypothesis  $h_i$  with probability  $P(\lambda|h_i) = \text{Tr}(\Pi_\lambda \rho_i(t))$ , where  $\Pi_\lambda$  is the projector on the affiliated eigenstate of the operator  $\hat{A}_T^{DT}$ . According to Bayes rule (2.1) the combined information from the monitoring and from the system projection hence leads to an update of the probabilities assigned to each hypothesis

$$P(h_i|D_T, \lambda) = \frac{P(\lambda|h_i)P(h_i|D_T)}{P(\lambda)}. \quad (9.4)$$

The hypothesis  $h_m$  with the largest likelihood  $P(h_m|D_T, \lambda)$  is the preferred one, and averaged over many independent realizations of the final projective measurement, the fraction of erroneous assignments based on that choice will be given by the generalization of Eq. (8.1) to mixed states,

$$Q_e = \frac{1}{2} \left[ 1 - \left| P(h_0|D_T)\rho_0^{(DT)}(T) - P(h_1|D_T)\rho_1^{(DT)}(T) \right| \right], \quad (9.5)$$

where  $|O| \equiv \text{Tr}(\sqrt{O^\dagger O})$ . To obtain the error probability of a given measurement scheme, we however still need to numerically evaluate the conditional states and probabilities and average Eq. (9.5) over the random outcomes of the continuous monitoring.

Note that Eq. (9.5) can also be applied to the distinction of mixed states or of the (unconditioned) candidate density matrices of a system evolving under different Hamiltonian hypotheses and leaking into an unmonitored environment. A recent comparison of probing by measurements on a system alone and on both a system and its environment shows the ability of the latter to better exploit (initial) entanglement among its sub-components [250].

## 9.2 Numerical investigations

### 9.2.1 Error probabilities under different detection models

To address the performance of the different monitoring schemes, we turn to the associated error probability  $Q_e$ . We consider both the case where the probability update is based solely on the detection signal, and the case where the signal is combined with a final optimized projective measurement on the system, Eq. (9.4).

The probabilities pertain to the average over many independent experimental realizations. However, they are non-linear functionals of the conditional states so there is no deterministic theory which allows their evaluation. Instead we have recourse to perform a large number  $M$  of simulations of the full measurement sequence and Bayesian inference. We repeated the simulations assuming each of the two hypotheses  $h_0$  and  $h_1$  to be true. In testing based on the detection signal  $D_T$  alone, hypothesis  $h_i$  is assigned if  $P(h_i|D_T) > 1/2$ . The probability in Eq. (9.1) to discard a true hypothesis  $h_j$  is then estimated by  $P(m = i|h_j) = n_i^{(j)}/M$ , where  $n_i^{(j)}$  is the number of samples assigning  $h_i$  when  $h_j$  is true. When a final system projection with outcome  $\lambda$  is included in the procedure, the assignment is dictated by  $P(h_i|D_T, \lambda) > 1/2$  and the error probability is given directly by Eq. (9.5).

The resulting error probabilities for our two-level example are compared to the quantum bound derived in Chapter 8 and to that of a projective measurement on the open system alone in Fig. 9.3. Curves are shown for three pairs of Rabi frequency candidates. They are all separated by  $\Omega_1 - \Omega_0 = 4\gamma$ , and therefore the error probabilities have the same quantum lower bound [154], but their particular offsets make either counting or homodyne detection more advantageous. All protocols yield larger error probabilities than the quantum bound, implying that none of the measurement strategies are optimal in the sense that they are able to extract all information from the full state of the system and its environment.

A photon counting signal is sensitive to the intensity of the emitted radiation and hence reflects the excitation of the two-level system. As seen in Fig. 9.3(a) this makes it near ideal to distinguish  $\Omega_0 = 0$ , which leads to no photon emissions, from a strong drive  $\Omega_1 = 4\gamma$ . The counting signal alone generates a much smaller error probability than the homodyne signal and approaches zero on a timescale similar to that of the quantum bound. When combining the counting signal with a final system projection, the error probability follows the quantum bound closely at short times

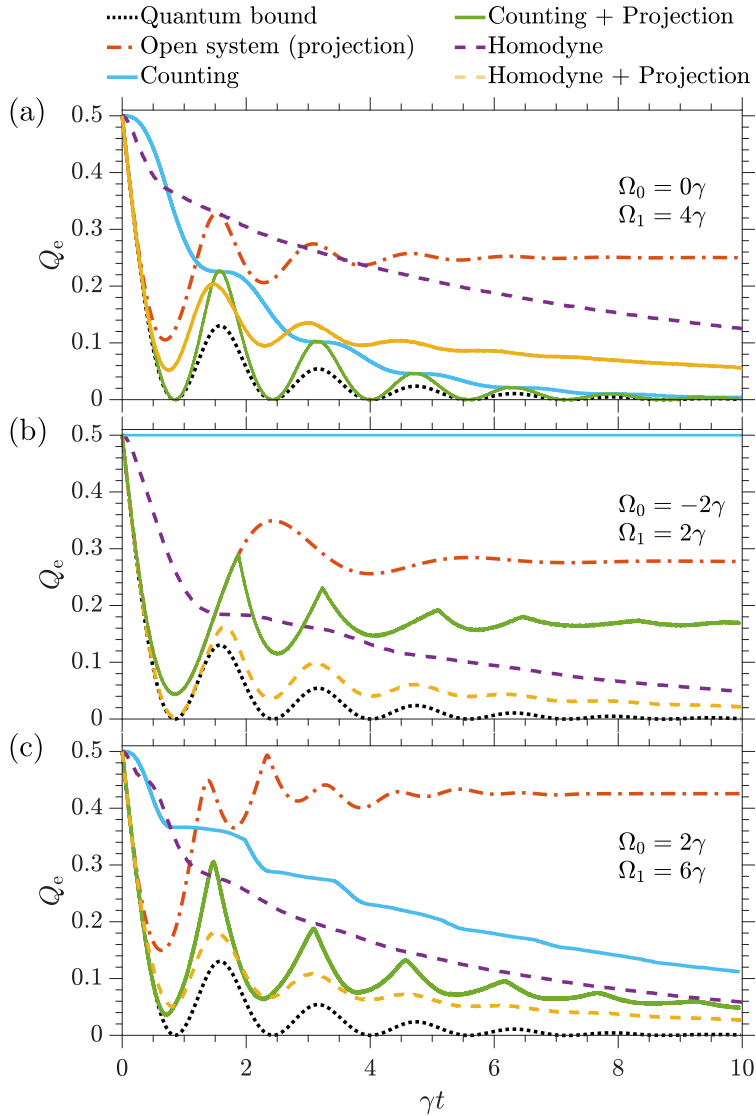


Figure 9.3: Temporal evolution of the error probability in assigning one of two hypotheses  $\Omega_0$  and  $\Omega_1$  for the Rabi driving frequency of a two-level system. The three plots correspond to different pairs of Rabi frequency candidates as annotated in the figure windows and the system is prepared in the ground state at  $t = 0$ . Results are shown for each of the different measurement schemes discussed in this paper. The error probabilities pertaining to monitoring protocols with perfect detection  $\eta = 1$  are sampled from  $M = 100\,000$  simulations (see main text).

and it shows that we may at specific finite probing times distinguish the hypotheses with certainty. These are points in time where the non-zero Rabi frequency  $\Omega_1$  assures an atomic or a photonic excitation.

The photon count is, however, insensitive to the phase of the emitted radiation and to the coherences in the two-level system. As a consequence, the two candidates  $\Omega_0 = -2\gamma$  and  $\Omega_1 = 2\gamma$  in (b) can not be discriminated by the photon counting signal alone; i.e.,  $Q_e(t) = 1/2$  for all times. Homodyne detection is, on the other hand, highly sensitive to the phase of the emitted radiation and when combined with a final system projection, the associated error matches the quantum bound for  $\gamma t \lesssim 1.5$  after which it remains close to the bound.

Since for the case studied in (b) the photon count alone holds no discriminatory power, one might expect that supplementing a counting signal with a final system projection yields an error probability identical to that pertaining to a projective measurement on the mixed state of an unmonitored system. Nevertheless, it is seen than for  $\gamma t \gtrsim 1.75$ , counting the photo emissions reduces the final error probability by around 10%. This illustrates an additional advantage of monitoring the environment. Subject to backaction, the system state remains pure and experiences a transient behavior which generally depends more strongly on the particular hypothesis than the mixed state of the unmonitored system. This allows more information to be extracted from the final system measurement. Previous works identify similar mechanisms at play in parameter estimation with monitored systems [1, 2, 4, 92, 250].

The candidate values  $\Omega_0 = 2\gamma$ ,  $\Omega_1 = 6\gamma$  in Fig. 9.3(c) can be distinguished both by the excitation and the coherence of the system. It is evident that while homodyne detection is slightly better than counting for these particular values, they both perform well and reach within 5 – 10% of the quantum bound.

### 9.2.2 Finite detector efficiency

While the simulations in Figs. 9.2 and 9.3 assume perfect monitoring, any real experiment suffers from finite detection efficiency  $\eta < 1$ . If the environment is monitored with perfect efficiency  $\eta = 1$ , the system state remains pure but if, e.g., some photo emissions are missed by the detector we are unable to perfectly track the state of the system and the conditional state  $\rho^{(D_t)}(t)$  evolves to a statistical mixture. Consequently, in addition to the direct decrease in information available from the monitoring signal, the

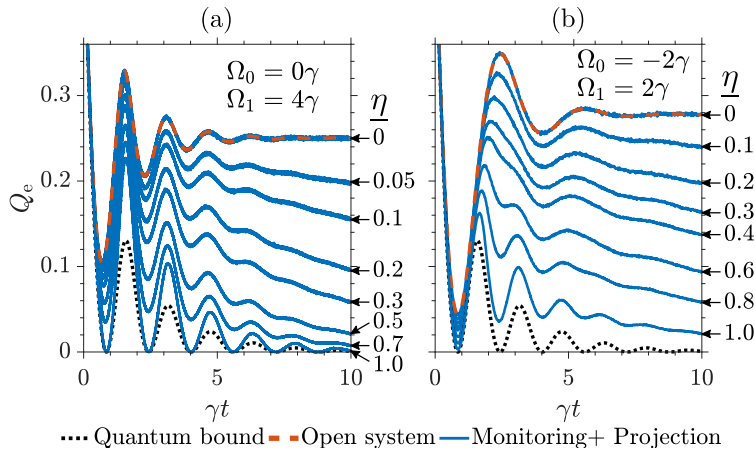


Figure 9.4: Temporal evolution of the error probability in assigning one of two hypotheses  $\Omega_0$  and  $\Omega_1$  for the Rabi driving frequency of a two-level system. The candidate values are annotated in the figure windows and the system is prepared in the ground state at  $t = 0$ . The full, blue curves, concerning monitoring by photo detection (a) and by homodyne detection (b) combined with a final system projection, are sampled from  $M = 100\,000$  simulations (see main text) with different values of the detection efficiency  $\eta$  as indicated on the right hand side of each plot. For comparison, we show also the quantum bound (dotted curve) and error probability associated with a projective measurement on an open system (dashed, red curve).

final system measurement is performed on a mixed state with, in general, less discriminatory power.

To probe these effects, we show in Fig. 9.4 the (sampled) error probability for different values of  $\eta$ . For Fig. 9.4(a) photon counting we focus on the candidates  $\Omega_0 = 0$ ,  $\Omega_1 = 4\gamma$  and for Fig. 9.4(b) homodyne detection  $\Omega_0 = -2\gamma$ ,  $\Omega_1 = 2\gamma$  where each of the two methods work particularly well. As  $\eta$  decreases, the error probability  $Q_e(t)$  undergoes a smooth transition from the perfect detection case studied in Fig. 9.3 to the case of a projection measurement performed on the mixed state of the system alone in the limit  $\eta \rightarrow 0$ . For the parameters used in this example, the photon counting protocol in Fig. 9.4(a) is surprisingly robust to detector imperfections. This is due to the fact, that as explained in Sec. 9.2.1, even a single photo detection completely rules out the hypothesis  $\Omega_0 = 0$ . While the homodyne example in Fig. 9.4(b) shows a more linear increase in the error probability as the detector efficiency deteriorates, both plots demonstrate that even with fairly large imperfections, monitoring the

environment severely improves the hypothesis testing capabilities of an open quantum system. This is due to the fact that the monitoring induces transient evolution in the system which depends more strongly on the system parameters than the steady state.

### 9.3 Conclusion and outlook

We have investigated how hypothesis testing with an open quantum system may be improved by monitoring the radiative environment to which it is coupled. We propose to supplement the information retrieved directly from the monitoring signal with a final system measurement optimized according to the conditional state.

It was found that, while monitoring by a photon counter or a homodyne demodulator allows the extraction of much of the information leaked from the open system into the field, the error probability in these schemes does not reach the fundamental quantum bound derived in Chapter 8. This is not surprising since generally the optimal measurement is highly non-local on the full system and environment.

From the results presented in Fig. 9.3, it is clear that homodyne detection and photon counting yield different reductions in the error probability at different stages in the evolution. That is, at some points in time either homodyne detection or photon counting is more efficient than the other. Experiments have been performed that combine both detection possibilities in a single run [251, 252] by the setup illustrated in Fig. 9.5(a), which splits the radiation emitted by the system such that a fraction  $1 - \beta$  is monitored by a photon counter and the remaining  $\beta$  fraction is subject to homodyne detection. The conditional, unnormalized state  $\tilde{\rho}^{(N_t, Y_t)}(t)$  then evolves according to both monitoring signals,

$$d\tilde{\rho}^{(N_t, Y_t)} = \left( [(1 - \beta)\mathcal{K} + \beta\mathcal{L}] dt + (1 - \beta)\mathcal{B}dN_t + \sqrt{\beta}\mathcal{X}_{\Phi}dY_t \right) \tilde{\rho}^{(N_t, Y_t)}. \quad (9.6)$$

A similar scheme applies the homodyne setup, Fig. 9.1(c), but with a local oscillator of variable strength  $\xi$  [253]. Conventional homodyne detection is realized in the limit of large  $\xi$ , while with a weak local oscillator the setup effectively counts photons.

The significance of such *hybrid* schemes is more apparent in scenarios with multiple distinct hypotheses, and in Fig. 9.5(b) this is illustrated by considering the differentiation of three discrete values  $\Omega = 0, \pm 2\gamma$  of

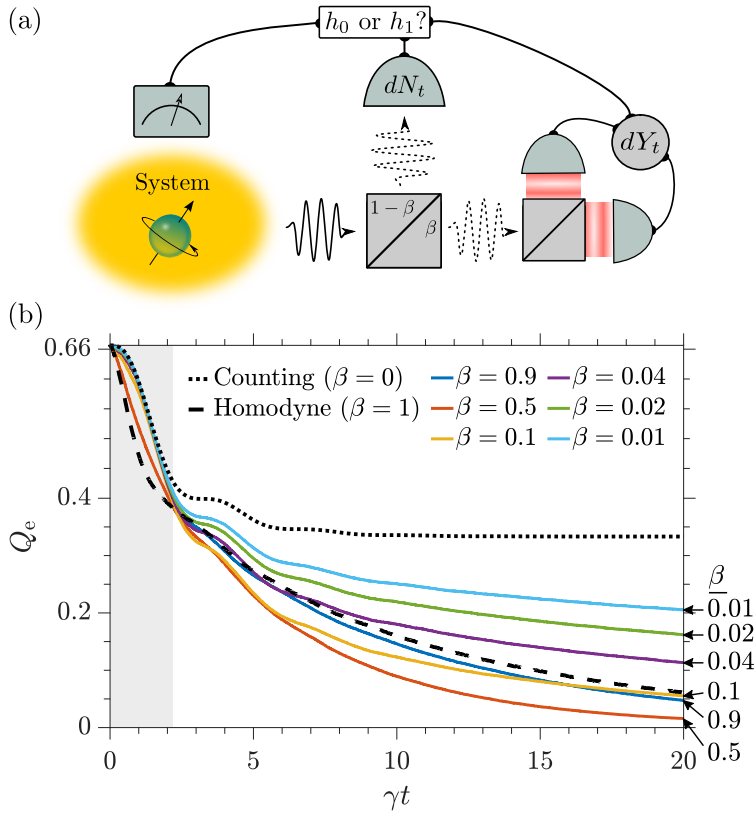


Figure 9.5: (a) A fraction  $\beta$  of the radiation emitted by a probe system is collected by a homodyne demodulator while the remaining fraction  $1 - \beta$  is directed to a photon counter. The system state, which defines the optimal system projection to perform at the final time  $T$ , is conditioned on both the photon count and the homodyne signal. (b) Temporal evolution of the error probability in assigning one of three hypotheses  $\Omega = 0, \pm 2\gamma$  for the Rabi frequency of a driven two-level system based on the two monitoring signals,  $N_t$  and  $Y_t$  of the hybrid monitoring scheme in (a). The cases of pure counting ( $\beta = 0$ ) and pure homodyne detection ( $\beta = 1$ ) are compared to different hybrid schemes with  $0 < \beta < 1$ . Pure homodyne detection is only optimal for times  $\gamma t \lesssim 2.3$  (shaded area). The error probabilities are sampled from  $M = 100\,000$  simulations.

the Rabi frequency in our two-level model. For sake of argument, we consider only monitoring without a final system projection. As discussed in Sec. 9.2.1, pure photo detection ( $\beta = 0$ ) is only sensitive to the absolute value of  $\Omega$ , and hence the error probability never reaches values lower than  $Q_e = 1/3$ , signifying perfect discrimination between  $\Omega = 0$  and the values  $\Omega = \pm 2\gamma$  which are, on the contrary, indistinguishable. When even a small fraction  $\beta > 0$  of the intensity of the emission signal is monitored by a homodyne demodulator, however, the combined signal is able to perfectly distinguish the three hypotheses if sufficient time is allotted. Interestingly, while pure homodyne detection ( $\beta = 1$ ) is optimal for times  $\gamma t \leq 2.3$  (shaded area), hybrid schemes with  $0 < \beta < 0.9$  converge faster to perfect discrimination because a photon counting signal very efficiently discriminates  $\Omega = 0$  from any non-zero values. Notice, finally, the large reduction in the error probability from the  $\beta = 0$  to the  $\beta = 0.01$  case. This is because just 1% of the intensity amounts to 10% of the amplitude, which is the relevant observable in homodyne detection, and leaves the counting signal virtually unaltered.

By using a beamsplitter with a tunable transmittance  $\beta(t)$  or by adjusting the local oscillator strength  $\xi(t)$ , the effective monitoring scheme can be updated in a time-dependent manner in order to further optimize the information extracted at each point in time. The expected performance of such a sensitivity scheduling strategy may be optimized by dynamical programming or by steepest descent gradient methods [254], while even better performance should be expected from more advanced schemes, that adaptively adjust  $\xi(t)$  as a function of the measurement record [255].

# Ancilla assisted quantum thermometry

*This chapter is reproduced from Ref. [13] with only very minor adjustments.*

---

The aim of thermometry is to estimate with high precision the temperature  $T$  of a thermal bath, and a thermometer consists of a probe system which is put in contact with the bath of interest. By monitoring the state of the probe one seeks to recover the value of  $T$ . If the probe is small, this has the advantage of inducing a negligible disturbance to the thermal equilibrium of the reservoir. The same principle applies in the quantum regime and substantial interest has recently been devoted to the design and properties of sensitive quantum thermometers [108–116].

By employing single or few-body quantum probes it has proven possible to obtain very precise temperature readings at millikelvin temperatures with spatial resolution at the nanometer scale. For instance, single quantum dots and NV-centers in nanodiamonds experience frequency shifts which depend on the temperature of their surroundings, thus allowing their implementation as sensitive fluorescent thermometers [36–41]. Other designs utilize mechanical oscillators or spin systems [42, 43]. By supplying such devices, the advancement of quantum technology and metrology paves the way for profound developments in many different branches of science, ranging from material sciences to biology and medicine [37, 38], which

would otherwise be infeasible due to current less efficient and(or) invasive measurement probes.

In a generic quantum thermometer, the temperature of the bath is encoded in the evolving quantum state  $\rho(t)$  of the probe and may hence be read out by measuring this state after a given  $t$ . If a large number  $K$  of such independent measurements are performed, the variance  $(\Delta T)^2$  of the derived temperature estimate around a rough prior estimate  $T$  obeys the quantum Cramér-Rao bound (2.19),

$$(\Delta T)^2 \geq \frac{1}{K\mathcal{I}_T[\rho(t)]}. \quad (10.1)$$

Here the quantum Fisher information  $\mathcal{I}_T[\rho(t)]$ , defined in Eq. (2.17)<sup>1</sup>, quantifies the information encoded in the state  $\rho(t)$  at time  $t$  about the temperature  $T$ . There exist in general a (possibly adaptive) measurement protocol which closes the bound (10.1) as  $K$  becomes large. A well-designed thermometer should thus aim at maximizing the value of  $\mathcal{I}_T[\rho(t)]$ ; a task which corresponds to an optimal encoding of the temperature in the state of the probe.

In conventional thermometer setups, the encoding is characterized by incoherent exchanges of energy between the probe and the bath. The temperature is thus effectively encoded in the excitation of the probe system which quickly thermalizes with the bath to reach a steady state  $\rho^{(\text{ss})}$ . At this point, the QFI saturates at the value  $\mathcal{I}_T[\rho^{(\text{ss})}]$  and no further information is encoded as time progresses. Hence, such a quantum thermometer operates as a classical sensor, utilizing only populations, while not including the advantages offered by quantum mechanics which rely on quantum coherences and entanglement [33–35]. Previous studies suggest that initial coherences in or simultaneous coherent driving of a single (qubit) probe system do not improve its thermometric properties; see e.g. [109]. To overcome this problem, it has been proposed to map thermometry to a task of optimal phase estimation which allows quantum advantages to be utilized [113].

In this chapter, we propose a thermometer consisting of two separate quantum systems: a sensor  $S$  directly coupled to the thermal bath of interest and a meter  $M$  which is not directly coupled to the bath but instead serves as an information storage that can be read out at the final

---

<sup>1</sup>In this chapter, we use a different notation for the QFI than in Eq. (2.17) in order to make explicit the state  $\rho(t)$  to which it pertains. That is,  $\mathcal{I}_T[\rho(t)] \equiv \mathcal{I}_Q(T)$  evaluated with  $\rho_T = \rho(t)$ .

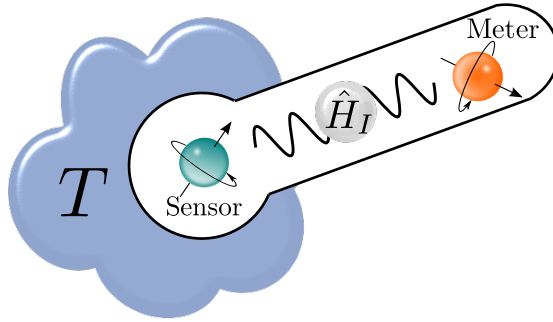


Figure 10.1: The temperature  $T$  of a thermal bath is probed by a quantum thermometer consisting of a sensor system  $S$ , directly coupled to the bath, and a meter system  $M$ , uncoupled from the bath but interacting via a Hamiltonian  $\hat{H}_I$  with  $S$ .

time  $t$ ; see Fig. 10.1. While initial entanglement between the sensor and a meter system has been found to provide thermometric advantages in discriminating two distinct temperatures [112], we shall not rely on this effect nor on the possibility of performing joint measurements on  $S$  and  $M$ . On the contrary, in our approach we assume the sensor and the meter to be initially uncorrelated but coupled through an interaction Hamiltonian term  $\hat{H}_I$  which operates in parallel with the thermalising process affecting  $S$ . The main purpose of this extra dynamical contribution is to transform the sensor into an efficient information transducer between the bath and the meter. The bath-induced excitations of the sensor affect the (local) coherence terms of the meter system, creating an off-balance configuration that effectively overcomes the before-mentioned saturation problem and thereby results in considerably larger values of the associated quantum Fisher information.

## 10.1 Model

For concreteness, we assume a bosonic bath and we consider a two-level (qubit) sensor system  $S$  with ground state  $|g\rangle_S$  and excited state  $|e\rangle_S$  whose interaction at strength  $\gamma$  with the bath validates the Born-Markov approximation such that its state  $\rho_S(t)$  evolves according to a master equation of the Lindblad form (2.9)

$$\dot{\rho}_S = \mathcal{L}_T \rho_S, \quad (10.2)$$

where the Liouvillian super-operator is of the form (2.10),

$$\mathcal{L}_T = -i\frac{\omega}{2}[\hat{\sigma}_z, \cdot] + \gamma_- \mathcal{D}[\hat{\sigma}_-] + \gamma_+ \mathcal{D}[\hat{\sigma}_+]. \quad (10.3)$$

Here  $\omega$  is the characteristic frequency of  $S$  and the temperature is mapped to the evolution of the probe via the average number of resonant thermal excitations  $N$ , as given by the Bose distribution

$$N = \frac{1}{e^{\hbar\omega/k_bT} - 1}, \quad (10.4)$$

causing a decay at a rate  $\gamma_- = (N + 1)\gamma$  and excitation at a rate  $\gamma_+ = N\gamma$ .

It was shown by Correa *et. al.* [109] that an effective two-level system exhibits maximal thermal sensitivity and the use of a small quantum sensor is further motivated by the fact that often the bath is itself a nanoscale system; e.g. a micromechanical oscillator [256]. Additionally, Ref. [109] finds that temperature is encoded with highest accuracy in a qubit prepared in its ground state. In this case, the solution to Eq. (10.2) is

$$\rho_S(t) = p_e(t) |e\rangle \langle e| + (1 - p_e(t)) |g\rangle \langle g| \quad (10.5)$$

with  $p_e(t) = \frac{N}{2N+1}(1 - e^{-(2N+1)\gamma t})$  which quickly relaxes to the Gibbs canonical ensemble at the temperature  $T$  of the bath; that is  $\rho_S(t) \rightarrow \rho_S^{(ss)} = \frac{|g\rangle \langle g| + e^{-\hbar\omega/k_bT} |e\rangle \langle e|}{1 + e^{-\hbar\omega/k_bT}}$  on a time scale set by the rate  $(2N + 1)\gamma$ .

The QFI for a measurement performed directly on the state of  $S$  can be expressed as

$$\mathcal{I}_T[\rho_S(t)] = \frac{(dp_e/dT)^2}{p_e(1 - p_e)}. \quad (10.6)$$

This function exhibits a non-monotonic behaviour [109, 110] which from the zero value attained at  $t = 0$  brings it to the asymptotic value

$$\mathcal{I}_T[\rho_S^{(ss)}] = \left(\frac{\hbar\omega}{k_b}\right)^2 \frac{e^{\hbar\omega/k_bT}}{(1 + e^{\hbar\omega/k_bT})^2 T^4} \quad (10.7)$$

as the state  $\rho_S(t)$  approaches  $\rho_S^{(ss)}$ . Although local maxima can typically be identified at finite times  $t$ , the global maximum of the function (10.6) corresponds to the maximum of (7); i.e.,  $\max_T (\mathcal{I}_T[\rho_S^{(ss)}]) \simeq 4.53(\hbar\omega/k_b)^2$  at a temperature  $k_bT \simeq 0.242\hbar\omega$ .

### 10.1.1 Including a meter system

While the time-independent value of the QFI,  $\mathcal{I}_T[\rho_S^{(\text{ss})}]$  reflects a steady state which depends only weakly on the temperature, it is well-known in quantum metrology that the Fisher information associated with a parameter  $g$  encoded in a closed quantum system by a unitary transformation  $U = e^{-ig\hat{H}t}$  is given by  $\mathcal{I}_g[\rho(t)] = 4(\langle \hat{H} \rangle^2 - \langle \hat{H} \rangle^2)t^2$  [33, 71]; i.e., it exhibits a persistent  $t^2$ -scaling with time and does not reach a constant value. This difference is due to the role of coherences in the latter case, and it is enticing to seek a protocol which maps the incoherent temperature encoding in mixed state populations to coherences.

In order to circumvent the inevitable loss of coherence in the open sensor system  $S$  due to the thermal coupling, we propose to achieve this goal by introducing a second *meter* system  $M$  which is uncoupled from the thermal bath. The temperature is encoded in  $M$  by introducing a Hamiltonian coupling between  $S$  and  $M$  of the form,

$$\hat{H}_I = \hat{M} \otimes |e\rangle\langle e|, \quad (10.8)$$

where  $\hat{M}$  is an operator on the local space of  $M$ . If, for instance,  $M$  is a qubit, one might let  $\hat{M} = \Omega\hat{\sigma}_x/2$ . Beyond the simplicity of its expression, what makes such choice for  $\hat{H}_I$  appealing is that it then describes a Rabi drive of the meter qubit conditioned on  $S$  being in its excited state. Such an interaction can be realized by utilizing the dipole-dipole coupling between two spins which leads to an energy shift (see the example studied in Sec. 8.3.3 for details). For instance, rare-earth-ion dopants in inorganic crystals have permanent electric dipole moments which are different depending on whether each ion is excited or not [240, 241]. A continuous laser illumination of a meter ion can thus be resonant when the sensor ion is in its excited state and completely off-resonant when it is in the ground state. Another well-known example is the dipole-dipole potential between neutral atoms responsible for the Rydberg Blockade mechanism [245], and yet another is the hyperfine coupling between a nuclear spin and an electron spin in, e.g., NV centers [246–248].

The state  $\rho(t)$  of the full system, consisting of  $S$  and  $M$  obeys a master equation

$$\dot{\rho} = -i[\hat{H}_I, \rho] + \mathcal{L}_T\rho, \quad (10.9)$$

where  $\mathcal{L}_T$ , defined in Eq. (10.3), operates locally on the sensor system.

The spectrum of  $\hat{H}_I$  can be seen as a sequence of effective two-level systems, uncoupled by the thermal interaction ( $\mathcal{L}_T$ ), with ground states

$|m\rangle \otimes |g\rangle$  and excited states  $|m\rangle \otimes |e\rangle$  where the  $|m\rangle$  are eigenstates of the operator  $\hat{M}$  with corresponding eigenvalues  $\lambda_m$ ,

$$\hat{M} |m\rangle = \lambda_m |m\rangle. \quad (10.10)$$

The total population difference between the upper  $\{|m\rangle \otimes |e\rangle\}_m$  and lower manifolds  $\{|m\rangle \otimes |g\rangle\}_m$  hence represents the information available from  $S$  alone, while the information encoded in  $M$  is represented by the coherences amongst the individual two-level transitions.

Following this idea, we expand  $\rho(t)$  in the eigenbasis of  $\hat{M}$ ,

$$\rho(t) = \sum_{m,m'} A_{mm'} |m\rangle \langle m'| \otimes \rho_{mm'}(t). \quad (10.11)$$

Here the  $\rho_{mm'}(t)$  operate on the sensor qubit space, and the  $A_{mm'} = \langle m'| \rho_M(t=0) |m\rangle$  are defined by the initial state  $\rho_M(t=0)$  of  $M$ . From the master equation (10.9), the equations of motion for the  $\rho_{mm'}(t)$  are seen to be,

$$\dot{\rho}_{mm'} = -i \frac{\lambda_m + \lambda_{m'}}{2} [ |e\rangle \langle e|, \rho_{mm'} ] - i \frac{\Omega_{mm'}}{2} \{ |e\rangle \langle e|, \rho_{mm'} \} + \mathcal{L} \rho_{mm'}, \quad (10.12)$$

where  $\Omega_{mm'} = \lambda_m - \lambda_{m'}$ . The commutator term does not have any effect for the case of a sensor initialized in the ground state as assumed here. The diagonal elements with  $\Omega_{mm} = 0$  hence solve Eq. (10.2); i.e., one finds  $\rho_{mm}(t) = \rho_S(t)$  as given in Eq. (10.5). The anti-commutator term is not trace preserving, and the solutions for the coherences,

$$\begin{aligned} \rho_{mm'}(t) = & \frac{e^{-[\gamma(N+1/2)+i\Omega_{mm'}/2]t}}{\alpha} \left( \gamma N [e^{\alpha t/2} - e^{-\alpha t/2}] |e\rangle \langle e| \right. \\ & \left. + \frac{1}{2} [(\gamma + i\Omega_{mm'}) (e^{\alpha t/2} - e^{-\alpha t/2}) + \alpha (e^{\alpha t/2} + e^{-\alpha t/2})] |g\rangle \langle g| \right), \end{aligned} \quad (10.13)$$

with  $\alpha(N) = \sqrt{(2N+1)\gamma^2 - \Omega_{mm'}^2 + 2i\gamma\Omega_{mm'}}$ , a complex parameter, are not normalized but rather decay to zero at long times.

## 10.2 Quantum Fisher information

As detailed above, the simple form of the Hamiltonian Eq. (10.8) allows the dynamical evolution of the full system to be solved analytically for a

general meter operator  $\hat{M}$ , and it is clear that the solution and hence the thermometric properties of our device depend only on the spectrum of the operator  $\hat{M}$ .

Tracing out  $M$ , we recover the thermalizing state of  $S$ ,  $\text{Tr}_M(\rho) = \sum_m A_{mm} \rho_{mm}(t) = \rho_S(t)$  where we used that  $\sum_m A_{mm} = 1$ . Note that in the partial trace operation all coherence terms with  $m \neq m'$  cancel. This implies that the QFI associated with a measurement on the sensor  $S$  alone is not influenced by the presence of the meter  $M$  and is indeed encoded in the total population difference between the manifolds as argued above.

The reduced state of  $M$  is given by

$$\rho_M(t) = \sum_m A_{mm} |m\rangle \langle m| + \sum_{m \neq m'} A_{mm'} \text{Tr}_S(\rho_{mm'}) |m\rangle \langle m'|, \quad (10.14)$$

where we used that the  $\rho_{mm}(t)$  obey a trace preserving master equation. Since the first sum depend only on the initial state of  $M$ , it is evident that the temperature is indeed encoded purely in its coherences. Furthermore, it is clear that the performance depends critically on the initial preparation of  $M$ . If, for instance, it is prepared in an eigenstate  $|n\rangle$ , we have  $A_{mm'} = \delta_{m'n} \delta_{nm}$ , and its state  $\rho_M(t)$  is temperature independent. The optimal initial state  $|\psi_M(t=0)\rangle = \sum_m c_m |m\rangle$ , which due to the convexity on the QFI is pure, depends in general on the spectrum of the operator  $\hat{M}$ , but we note that since any phases correspond to a unitary transformation of the meter state, to which the QFI is invariant [71], the  $c_m$  can be taken as real and positive.

### 10.2.1 Example: Two-level meter

Our main example concerns a meter system with two levels,  $|0\rangle$  and  $|1\rangle$ , and for concreteness we shall let  $\hat{M} = \Omega \hat{\sigma}_x / 2$ , corresponding to a conditional Rabi drive of  $M$  as explained above. To maximize the coherences in the eigenbasis of  $\hat{M}$ , the meter should be prepared in a state  $|0\rangle = (|+\rangle + |-\rangle) / \sqrt{2}$ , where  $|\pm\rangle$  are the eigenstates of  $\hat{\sigma}_x$ .

In Fig. 10.2, we compare the QFI associated with either of the reduced states,  $\rho_S(t)$  or  $\rho_M(t)$ , to that of the full sensor-meter state  $\rho(t)$ . Results are shown as a function of the temperature  $T$  and for different probing times in each panel. At short times,  $\gamma t = 1$ , the thermometric information is held mainly by  $S$  ( $\mathcal{I}_T[\rho_S(t)] \simeq \mathcal{I}_T[\rho(t)]$ ) but as time progresses, temperature dependent coherences build up in  $M$  and while  $S$  reaches a steady state with maximum information (10.7), the information in the meter  $M$  keeps increasing. Hence, at  $\gamma t \simeq 2.6$  we have ( $\mathcal{I}_T[\rho_M(t)] \simeq \mathcal{I}_T[\rho_S(t)]$ ), and

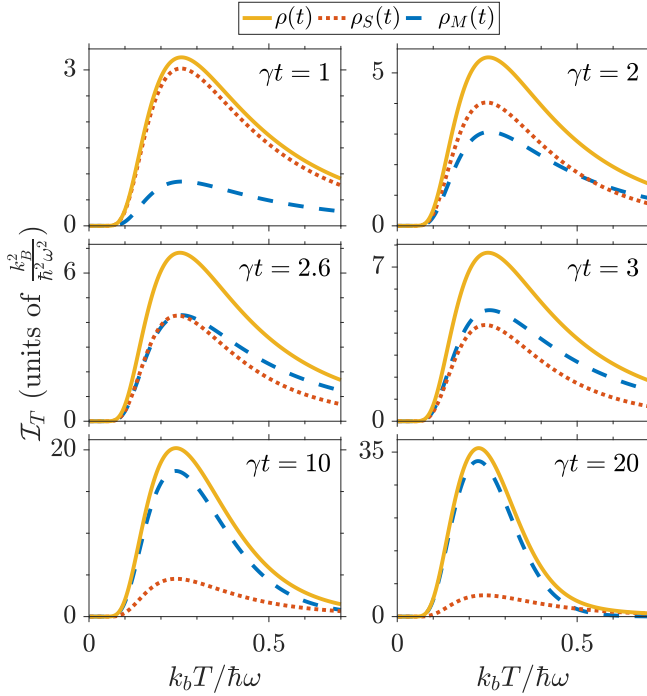


Figure 10.2: Quantum Fisher information  $\mathcal{I}_T[\cdot]$  associated with the full state  $\rho(t)$ , the sensor state  $\rho_S(t)$  or the meter state  $\rho_M(t)$ . Results are shown as a function of the temperature  $T$  and for  $\Omega = 2\gamma$ . The panels correspond to different probing times  $t$  as annotated in the figure window.

at larger times  $\gamma t = 20$  the information in the combined state is held predominantly by  $M$ . Furthermore, at this point  $\mathcal{I}_T[\rho(t)] \simeq \mathcal{I}_T[\rho_M(t)] \gg 4.53(\hbar\omega/k_B)^2 \geq \mathcal{I}_T[\rho_S(t)]$ . Evidently, the capability of the meter system to accumulate information for a much longer time allows it to reach a significantly larger thermometric sensitivity.

It is an attractive feature of our device that after some initial time, a local measurement on the meter  $M$  is able to extract almost all the information from the state. This makes the thermometer more feasible to implement, and at the same time less invasive since  $M$  may, as depicted in Fig. 10.1, be located outside, e.g., a biological sample. To characterize our quantum thermometer, we shall thus focus on the long-time behavior of the QFI, associated with the reduced state  $\rho_M(t)$  of the meter  $M$  alone.

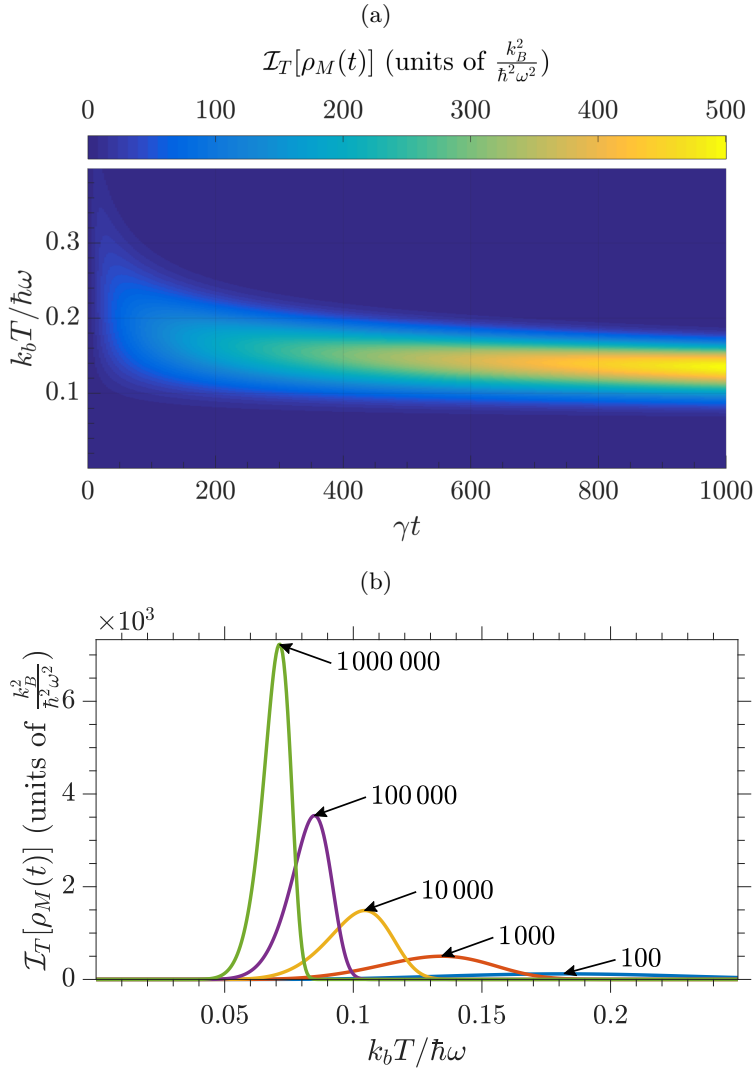


Figure 10.3: Quantum Fisher information  $\mathcal{I}_T[\rho_M(t)]$  associated with estimating the temperature  $T$  from a local measurement on a two-level meter system  $M$  coupled to the sensor  $S$  via a Hamiltonian  $\hat{H}_I = \Omega \hat{\sigma}_x / 2 \otimes |e\rangle\langle e|$  with  $\Omega = 2\gamma$ . (a) Color plot showing the dependence of  $\mathcal{I}_T[\rho_M(t)]$  on the temperature  $T$  and the probing time  $t$ . (b) Curves for  $\mathcal{I}_T[\rho_M(t)]$  as a function of  $T$  are shown for different probing times  $\gamma t = 100, 1000, 10000, 100000, 1000000$  as annotated with arrows in the figure window.

The QFI of a two-level density matrix may be expressed as [257],

$$\mathcal{I}_T[\rho_M] = 4\text{Tr} \left[ \rho_M \left( \frac{\partial \rho_M}{\partial T} \right)^2 \right] + \frac{1}{\det(\rho_M)} \left[ \frac{\partial \det(\rho_M)}{\partial T} \right]^2, \quad (10.15)$$

and the color plot in Fig. 10.3(a) shows an example of its evolution from time  $\gamma t = 0$  to  $\gamma t = 1.000$  for a relevant range of temperatures. In 3(b) we plot  $\mathcal{I}_T[\rho_M(t)]$  at specific times from  $t = 100\gamma^{-1}$  to  $t = 100\,000\gamma^{-1}$ . The sensitivity of  $M$  depends on the temperature  $T$  relative to the frequency  $\omega$  of  $S$  and reaches a maximum at a temperature  $T_{\max}(t)$  which, as seen in Fig. 10.4, decreases with time (we will come back to this point). The QFI,  $\mathcal{I}_T[\rho_M(t)]$  at and around this temperature reaches values which are much larger than the sensitivity offered by a sensor qubit alone;  $\mathcal{I}_T[\rho_S(t)] \leq 4.53217(\hbar\omega/k_b)^2$ . It should be noted that Fig. 10.3(b) shows how the temperature-range, at which  $M$  is sensitive, decreases with time, and that though it appears that the sensitivity at  $T_{\max}(t)$  increases without bounds, our treatment of the thermal coupling in the Born-Markov approximation breaks down for very low temperatures where strong correlations between the sensor  $S$  and the bath may appear.

The strength  $\Omega$  of the Hamiltonian (10.8) appears as a control parameter, and in Fig. 10.4, we show  $T_{\max}(t)$  and the corresponding QFI,  $\mathcal{I}_{T_{\max}}[\rho_M(t)]$  for different values of  $\Omega$ . For small  $\Omega \lesssim \gamma$ , the sensitivity of  $M$  can be tuned within a relatively broad interval by adjusting  $\Omega$ , while it is near independent for stronger interactions; see  $\Omega = 2, 4\gamma$  in the figure. The value of  $\mathcal{I}_{T_{\max}}[\rho_M(t)]$  is at short times larger for strong couplings while at later times it is favorable to apply a weaker laser field to the meter  $M$ . This can be understood by a competition between the two roles played by  $\hat{H}_I$ : i) to transfer information about the temperature from  $S$  to  $M$ , and ii) to mediate decoherence between the two systems. Hence, at short times it is favorable to transfer a large amount of information quickly at the cost of a faster dephasing of that information, while when longer time is available a slower transfer is compensated by a longer coherence time of  $M$ .

From Figs. (10.2) and (10.3), it is clear that the interesting regime concerns large times, and that the relevant temperature range is centered around  $k_b T / \hbar\omega \simeq 0.2$  which corresponds to small values  $N \simeq 0.007$  of the thermal bath excitation [108, 109]. Assuming then  $\Omega \gg \gamma N$  and  $\gamma t \gg 1$ , we obtain a simple approximation for the QFI,

$$\mathcal{I}_T[\rho_M(t)] \simeq \left( \frac{dN}{dT} \right)^2 \frac{\gamma^2 t^2 e^{-2\Gamma N t}}{\Omega^2 + \gamma^2} \left( \Omega^2 + 4\gamma^2 N^2 + \frac{(\Omega^2 - 2\gamma^2 N^2)^2}{(\Omega^2 + \gamma^2)(e^{2\Gamma N t} - 1)} \right), \quad (10.16)$$

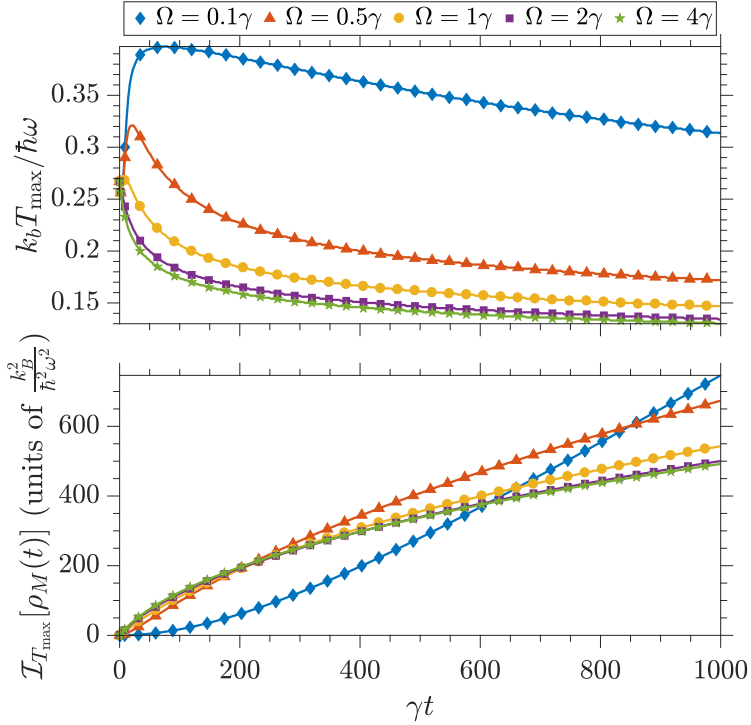


Figure 10.4: The temperature  $T_{\max}$  (upper panel) at which the QFI takes its maximum value  $\mathcal{I}_{T_{\max}}[\rho_M(t)]$  (lower panel) as a function of the probing time. Results are shown for a two-level meter system  $M$  and with  $\hat{H}_I = \Omega \hat{\sigma}_x / 2 \otimes |e\rangle\langle e|$  for different values of  $\Omega$ .

where  $dN/dT$  is the differential of the Bose distribution (10.4) with respect to temperature and we point out that the effective decay rate  $\Gamma_N = N\gamma(\Omega^2 - N\gamma^2)/(\Omega^2 + \gamma^2)$  is very small. We thus see that the QFI scales as  $\propto \gamma^2 t^2 e^{-2\Gamma_N t}$ , and for any given temperature ( $N$ ) it reaches a maximum value at the time,  $t_{\max}(T) = \Gamma_N^{-1}$  after which it decreases to zero as the coherences (10.13) decay. This time, however, appears later for smaller values of  $N$  leading to the decrease in time of  $T_{\max}(t)$  seen in Fig. 10.4. Still, we want to stress that for any temperature  $T$ , the QFI is upper bounded by  $\mathcal{I}_T[\rho_M(t_{\max}(T))]$ , and that at very large times  $t \gg t_{\max}(T)$  the coherences  $\text{Tr}_S(\rho_{\pm\mp})$  in  $M$  vanish such that, according to Eq. (10.14), it is left in a statistical mixture  $\rho_M(t) = \mathbb{I}/2$  with no information regarding the temperature of the bath.

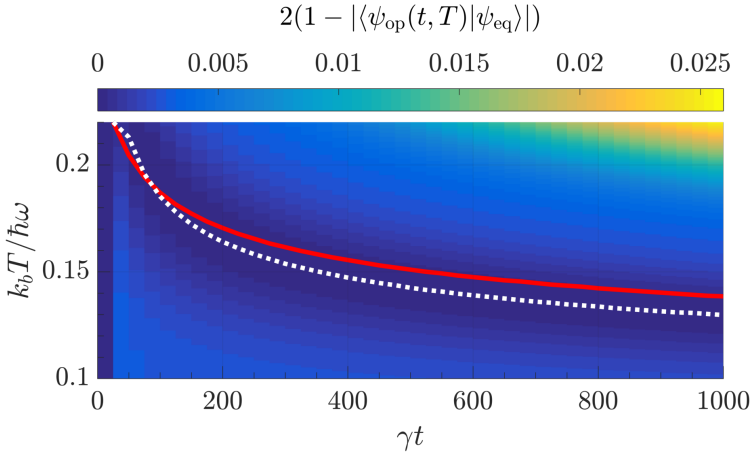


Figure 10.5: Color plot depicting for a range of temperatures  $T$  and total probing times  $t$ , the Bures distance,  $2(1 - |\langle \psi_{\text{op}}(t, T) | \psi_{\text{eq}} \rangle|)$  from an equal superposition  $|\psi_{\text{eq}}\rangle = \frac{1}{\sqrt{n}} \sum |m\rangle$  of the eigenstates of the operator  $\hat{M}$  to the initial state  $|\psi_{\text{op}}(t, T)\rangle$  of  $M$ , which maximizes the value of  $\mathcal{I}_T[\rho_M(t)]$ . The dotted, white line tracks the temperature where  $|\psi_{\text{op}}(t, T)\rangle = |\psi_{\text{eq}}\rangle$ . The full, red line tracks the temperature  $T_{\text{max}}(t)$  for which  $\mathcal{I}_T[\rho_M(t)]$ , evaluated with initial meter state  $|\psi_M\rangle = |\psi_{\text{op}}(t, T)\rangle$ , is maximal. Results are shown for a meter system with  $n = 6$  levels.

### 10.2.2 A multi-level meter system

For a meter system  $M$  of arbitrary dimension  $n$ , the quantum Fisher information constitutes a complicated expression even when an analytic expression is known for the mixed state density matrix of the system. Here we treat these cases. For this purpose we apply Eq. (2.22) to evaluate  $I_T[\rho_M]$ , and generalize the two-level example studied in Sec. 10.2.1 we focus on a meter operator  $\hat{M} = \Omega \hat{S}_x$ , where  $\hat{S}_x$  is the x-component of the spin in a spin- $(n-1)/2$  system. If  $M$  is composed of several qubits, we have  $\hat{S}_x = \sum \hat{\sigma}_x^{(i)}$  where  $\hat{\sigma}_x^{(i)}$  operates on qubit  $i$ .

While identification of the optimal initial state as an equal superposition  $|\psi_{\text{eq}}\rangle = \frac{1}{\sqrt{n}} \sum_m |m\rangle$  of the eigenstates of  $\hat{M}$  was straightforward in the two-level case, the general case is more complicated. Rather than just maximizing the initial coherences, the different values of the  $\Omega_{mm'}$  must be taken into account, and in general we have recourse to numerical maximization of the QFI over all possible initial configurations with positive coefficients  $c_m$ . The optimal state  $|\psi_{\text{op}}(t, T)\rangle$  depends on both the probing

time  $t$  and the temperature  $T$ . In Fig. 10.5 we plot the Bures distance of  $|\psi_{\text{op}}(t, T)\rangle$  from  $|\psi_{\text{eq}}\rangle$  as a function of  $t$  and  $T$  and for  $n = 6$ . It is seen that while  $|\psi_{\text{op}}(t, T)\rangle$  is in general different from  $|\psi_{\text{eq}}\rangle$ , the discrepancy is moderate and for a given time-dependent temperature (dotted, white curve) it vanishes. This temperature is close but not equal to  $T_{\text{max}}(t)$  as tracked by the red line. We find that the distance from an equal superposition shows a similar functional dependence on  $t$  and  $T$  for other values of  $n$ .

In any real thermometry task, the precise temperature is unknown so rather than defining an initial state  $|\psi_M(t = 0)\rangle$  which depends on the specific value of  $T$ , one has recourse to select a specific state regardless of the precise temperature. The results in Fig. 10.5 and the intuition regarding the role of coherences suggest that in general one can expect near optimal results by setting  $|\psi_M(t = 0)\rangle = |\psi_{\text{eq}}\rangle$  which we shall assume in the remainder of this section.

We proceed to probe the advantage of adding more levels to the meter system  $M$ . We find that  $\mathcal{I}_T[\rho_M(t)]$  is maximized around the same time dependent value  $T_{\text{max}}(t)$  (see Fig. 10.4(a)) independently of  $n$ , and in Fig. 10.6 we show the QFI at this temperature as a function of time and for different values of  $n$ . It is seen that for all times,  $\mathcal{I}_{T_{\text{max}}}[\rho_M(t)]$  increases with  $n$ , signifying that a higher dimensional meter system allows a larger sensitivity to small temperature variations. This result suggests that the optimal meter system is a harmonic oscillator with an infinite dimensional Hilbert space. Notice, however, that the gain saturates for larger  $n$  as the curves are seen to lie closer and closer. In the inset we quantify this by showing how the relative increase in the QFI as one more level is added to  $M$  is (near) time-independent and approaches zero for  $n \gtrsim 10$ .

### 10.3 Temperature dependence in the Liouvillian spectrum

By discussing the emergence of coherences, we have provided an intuitive understanding of the advantage offered by coupling the sensor  $S$  to a meter system  $M$ . In this section we explain how this advantage can be understood from the structure of the Liouvillian superoperator  $\mathcal{L} = -i[\hat{H}_I, \cdot] + \mathcal{L}_T$ , governing, via. Eq. (10.9), the encoding of the temperature in the full sensor-meter state.

In the long time limit, this super-operator will asymptotically bring the joint sensor-meter state to the stationary eigenspace associated with its null

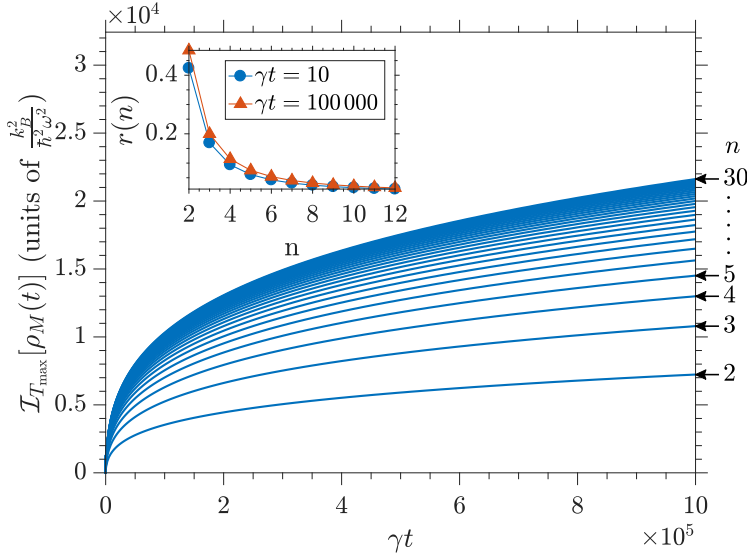


Figure 10.6: Time evolution of the quantum Fisher information  $\mathcal{I}_{T_{\max}}[\rho_M(t)]$  associated with estimating the temperature  $T_{\max}(t)$  which maximizes its value from a local measurement on an  $n$ -level meter system coupled to  $S$  via a Hamiltonian  $\hat{H}_I = \Omega \hat{S}_x \otimes |e\rangle\langle e|$  with  $\Omega = 2\gamma$ . Results are shown for  $n = 2, 3, \dots, 30$ . The inset depicts the relative scaling,  $r(n) = (\mathcal{I}_{T_{\max}}^{(n+1)} - \mathcal{I}_{T_{\max}}^{(n)})/\mathcal{I}_{T_{\max}}^{(n)}$ , of  $\mathcal{I}_{T_{\max}}^{(n)}$  with  $n$  at short times  $\gamma t = 10$  and at long times  $\gamma t = 100000$ .

eigenvalue. The convergence of this process is exponential and determined by the inverse of the smallest modulus of the real parts of its non-zero eigenvalues. (which by construction are all non-positive). Accordingly, in this regime we can write

$$\rho(t) \simeq \Pi_0 \rho(0) + \sum_j e^{\lambda_j t} \Delta_j, \quad (10.17)$$

where  $\Pi_0$  is the projector on the null eigenspace of  $\mathcal{L}$  and the summation involves those non-zero eigenvalues  $\lambda_j$  of  $\mathcal{L}$  that have the smallest (in modulus) real component with corresponding state components  $\Delta_j$ .

The quantum Fisher information (10.15) or (2.17) refers to the derivative of the state at time  $t$  with respect to the temperature, i.e., to

$$\partial_T \rho(t) = (\partial_T \Pi_0) \rho(0) + \sum_j e^{\lambda_j t} (t \partial_T \lambda_j \Delta_j + \partial_T \Delta_j). \quad (10.18)$$

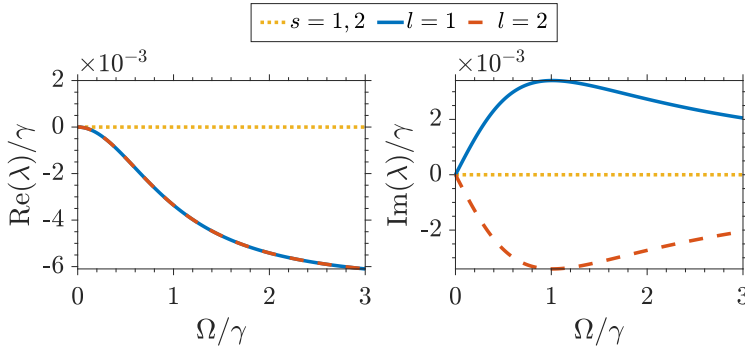


Figure 10.7: Real (left panel) and imaginary (right panel) parts of the four eigenvalues with the largest real parts of the superoperator  $\mathcal{L}$  governing the evolution of the full sensor-meter system. Results are shown as a function of the strength of the interaction Hamiltonian  $\Omega$  and for a temperature  $k_B T = 0.2\hbar\omega$ .

As  $t$  diverges only the first term survives and the related QFI derives from

$$\partial_T \rho(t) \simeq (\partial_T \Pi_0) \rho(0). \quad (10.19)$$

Hence no scaling with time remains, and the QFI is given by that of  $S$  alone, Eq. (10.7).

If, however, some eigenvalues indexed by  $l$  have real parts very close to zero, the contribution from their part of the spectrum in Eq. (10.18) persist for very long and one may indeed see terms in the QFI (2.17) scaling as  $\propto t^2$  until times  $t \gg \text{Re}(\lambda_l)^{-1}$ . In other words, allowing the temperature to be encoded in the eigenvalues and not just the projectors may provide a significant metrological advantage.

This is exactly the case for our thermometer device. For the two-level example of Sec. 10.2.1, we show in Fig. 10.7 the real and imaginary parts of the four eigenvalues with largest real parts as a function  $\Omega$  for a temperature  $k_B T = 0.2\hbar\omega$ . Without a meter ( $\Omega = 0$ ), the four eigenvalues are all zero. The effect of adding a meter ( $\Omega > 0$ ) is to lift the degeneracy of two of the eigenvalues

$$\begin{aligned} \lambda_{l=1} &= \frac{1}{2} [-(2N+1)\gamma + i\Omega - \alpha^*(N)] \\ \lambda_{l=2} &= \frac{1}{2} [-(2N+1)\gamma - i\Omega + \alpha(N)], \end{aligned} \quad (10.20)$$

while the other two ( $s=1,2$ ), corresponding to the steady state, remain zero. The very small value of  $|\text{Re}(\lambda_l)|$  combined with non-zero, temper-

ature ( $N$ ) dependent values of  $\text{Im}(\lambda_l)$  are crucial for the success of our thermometer.

## 10.4 Conclusion

We have proposed a quantum thermometer which maps the incoherent encoding of a temperature from a sensor system to coherences in a meter system by a realistic Hamiltonian interaction. The coherent encoding allows the meter state to exhibit a much larger temperature-sensitivity than the sensor state alone. While an effective two-level system has been identified as an optimal temperature sensor [109], we find that the sensitivity increases with the dimensionality of the meter system. For simplicity we focused on a bosonic bath in our presentation but calculations show that similar results are valid in the case of a fermionic reservoir.

From our examples, it is clear that the achievements and sensitivity range of our thermometer device depends in a complicated manner on the strength and the spectrum of the interaction Hamiltonian (10.8), on the initial preparation of the meter system, and on the total time  $t$  available in a given experiment. Hence, an appropriate meter should be designed for the specific task at hand, e.g taking into account the expected temperature and experimental constraints.

# Magnetic resonance with squeezed microwaves

*This chapter is based on Ref. [8]. In particular, Sections 11.2, 11.3.2 and 11.4.1 and the figure material, including their captions, are reproduced with only minor adjustments. The first two paragraphs of the introduction are taken from Ref. [9].*

---

Quantum mechanics imposes uncertainty relations on non-commuting observables and when quantum theory is applied to electromagnetic fields, even the zero-photon vacuum state is equipped with electromagnetic amplitude fluctuations. While such fluctuations appear to pose a fundamental limit to, e.g., optical measurements, the development of sources producing squeezed states of light (see, e.g., [258–261]) allows higher sensitivity probing of the squeezed field quadrature [34].

Material quantum systems have quantum degrees of freedom such as position, momentum, angular moment, and spin components with well-known uncertainty relations. Since such systems are routinely being employed in precision tests and measurements, it is an attractive possibility to squeeze the relevant degrees of freedom or to squeeze the light used to probe the system in an experiment. Examples include optomechanical devices and ensembles of atoms, molecules, and spin dopants in solids, studied for, e.g., gravitational wave detection [51], atomic clocks [60], and fundamental tests [262]. Furthermore, squeezed light has been demonstrated to provide

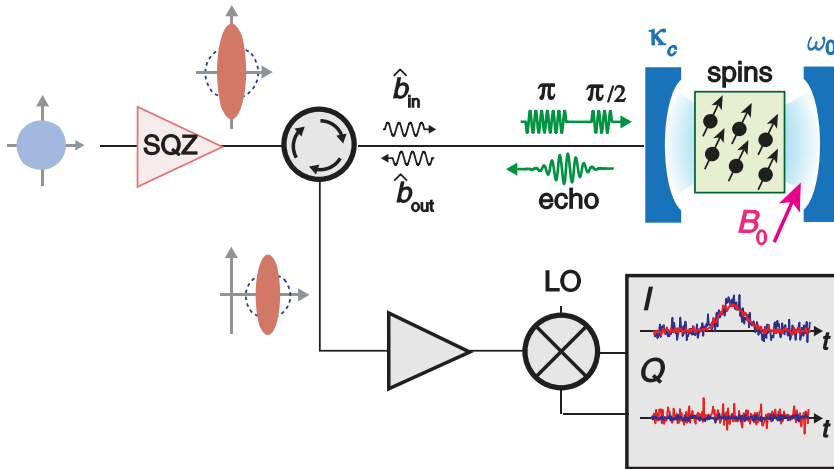


Figure 11.1: Principle of squeezing-enhanced pulsed magnetic resonance. A squeezed vacuum state is incident on an ESR cavity of frequency  $\omega_0$ . The cavity contains the spins to be detected, which are tuned into resonance at  $\omega_0$  by a dc magnetic field  $B_0$ . A Hahn echo microwave pulse sequence ( $\pi/2 - \tau - \pi - \tau$ ) is applied to the spins, leading to the emission of an echo in the detection waveguide on the  $X$  quadrature. This echo is noiselessly amplified along  $X$  before its homodyne demodulation with a local oscillator (L.O.) phase such that  $I(t)$  is proportional to  $X(t)$ . The traces in the bottom right grey box, which are not real data, depict schematically the expected difference between SQZ off (blue) and SQZ on (red) output quadrature signals when the squeezed quadrature is aligned along the echo emission quadrature  $X$ . The signal-to-noise ratio is improved on the  $I$  quadrature which contains the entire echo signal.

improved sensitivity in spectroscopy setups [118, 119] and in biological particle tracking [44]. Generally, squeezing in multi-particle and multimode optical systems entails entanglement, allowing squeezed states of both light and matter to find additional applications in quantum information protocols such as teleportation [263–265].

This chapter describes the application of a squeezed probe field to magnetic resonance detection in a proof-of-principle experiment performed by Audrey *et. al* in the Quantronics group at CEA Saclay in France [8]. The experiment builds upon a recent demonstration by the group that it is possible to apply a Hahn echo sequence [120] to detect an ensemble of spins in a microwave resonator at the nanoscale [266]. The unprecedented sensitivity reported in that experiment reaches the limit set by vacuum

fluctuations in the microwave field used to probe the ensemble. In the new experiment [8] it is shown that by squeezing fluctuations in the field quadrature holding the echo signal, it is possible to further reduce the signal to noise ratio by 1.2 dB.

The figure of merit for an experiment of this kind with an ensemble of weakly coupled spins is the *minimum* number of spins which can be detected with unit signal-to-noise ratio in a given measurement time. The proposal and experiment presented here reduce this minimum or equivalently the needed measurement time, and is thus highly relevant for ensembles with very low spin concentrations. As the limit of only a few spins is approached, the measurement backaction becomes important, and appreciable advantages can be achieved by applying a full Bayesian analysis of the measurement signal as described in Chapter 2 [93]. While this will hopefully become relevant in future experiments by the group at CEA, the present experiment requires at least  $\sim 1.3 \times 10^4$  spins, and a mean signal analysis suffices.

The experimental setup is shown and explained in the caption of Fig. 11.1. Since my contribution has been to apply the conventional methods of quantum optics in the theoretical modelling, I will only explain the main points of the experimental procedure and results while encouraging the reader to consult Ref. [8] for further details.

## 11.1 Magnetic resonance detection and experimental setup

The purpose of the experiment is to show that squeezing improves our ability to identify and characterize a small ensemble of electron spins by electron spin resonance (ESR) detection. This goal will prove useful in, e.g., chemistry, material sciences, and quantum information processing. The experiment probes an ensemble of Bismuth atoms embedded in a silicon substrate where the hyperfine levels are used as a spin-transition in the microwave regime. The experimental setup is schematically depicted in Fig. 11.1. The substrate, holding the spins, is placed in a single-port lossless microwave resonator with frequency  $\omega_0$ , and the ensemble is probed by pulsed magnetic resonance detection of the microwave signal mode,  $\hat{b}_{\text{out}}$  emitted by resonant spins to a measurement line coupled to the resonator with a rate  $\kappa_C$  [267]. The spins can be tuned out of and into resonance by a DC magnetic field  $B_0$ .

The probe signal is injected via a mode  $\hat{b}_{\text{in}}$ , and the pulsed detection is implemented by a Hahn echo sequence [120] which first brings the spins to an equal superposition of the excited and ground state by a  $\pi/2$  pulse at time  $t = 0$ . Due to their inhomogeneous frequency distribution, the spins dephase for a duration  $\tau$  until a  $\pi$  pulse inverts their evolution and leads to rephasing at the final time  $t = 2\tau$  of spins with frequency  $\omega_s$  close to  $\omega_0$ . At this time, an echo is collectively emitted in one of the field quadratures (we call this  $X$ ) of the output mode  $\hat{b}_{\text{out}}$ . The advantage of an echo scheme is that the signal is not overlaid by the reflection on the resonator of a strong excitation pulse.

The experiment then guides the signal through a quantum-limited amplifier tuned to amplify the  $X$  quadrature and finally detects it by a homodyne demodulator. The noise in the signal recording, which ultimately limits the spectroscopic sensitivity in the experiment, stems then (in the ideal case) solely from fluctuations in the cavity output mode  $\hat{b}_{\text{out}}$ . The experiment operates at cryogenic temperatures,  $T \ll \hbar\omega_s/k_B$ , so the thermal contribution to these fluctuations is negligible. Hence, the noise is inherited from the input mode  $\hat{b}_{\text{in}}$ . The core idea in this experiment is to squeeze the uncertainty  $\delta X$  in the quadrature  $X$ , where the echo is emitted, below vacuum level,  $\delta X_0 = 1/2^1$ , thus allowing a noise in the output signal which is reduced below the conventional quantum limit defined by a signal mode with vacuum fluctuations. Of course, according to Heisenberg's uncertainty relation  $\delta X^2 \delta Y^2 \geq 1/16$ , this implies an increased noise  $\delta Y$  in the complementary quadrature  $Y$ ; see Fig. 11.1. However, this is inconsequential since the experiment is tuned to not emit any spin signature in this quadrature.

As outlined in the introduction to this chapter, the production and applications of squeezed states of optical light have been reported in many experiments and settings. Yet, squeezing in experiments operating in the microwave regime [268, 269] is largely unexplored and the present experiment represents one of the first proof-of-principle demonstrations of its application to high sensitivity metrology. In addition, squeezed microwaves have in a number recent experiment proven advantageous in the readout of qubit states [270–273]

The possibility to efficiently squeeze microwave fields is provided by the recent development of state-of-the-art Josephson parametric amplifying (JPA) devices [261, 274–276], sparked by the huge interest in superconducting circuits for quantum information purposes [277]. The present experi-

---

<sup>1</sup>We define the field quadratures in dimensionless units.

ment employs JPAs, operated with different settings, to both squeeze the input field (SQZ) [269] and noiselessly amplify (AMP) the output signal.

Before describing the experimental results, we shall go through a theoretical model which shows that the idea presented above should indeed lead to an increased signal-to-noise ratio in the echo signal.

## 11.2 Theoretical model

Our physical system, illustrated in Fig. 11.1, consists of a cavity mode coupled resonantly to  $N_{\text{spins}}$  spins and to input and output microwave fields. As we are interested in both the mean amplitude and the quantum fluctuations in the output signal, we describe the whole system quantum mechanically. Inhomogeneous broadening and spatial variations of the spins within the ESR cavity lead to different transition frequencies  $\omega_j$  and coupling strengths  $g_j$  of the individual spins to the cavity mode. We will assume here that the spins are in resonance with the cavity, namely that their mean frequency  $\omega_s$  is equal to the cavity frequency  $\omega_0$ . In a frame rotating at  $\omega_0$ , the total Hamiltonian of the spins and the resonator mode is

$$\hat{H} = \hbar \sum_j \left[ g_j \left( \hat{\sigma}_-^{(j)} \hat{a}^\dagger + \hat{\sigma}_+^{(j)} \hat{a} \right) + \frac{\Delta_j}{2} \hat{\sigma}_z^{(j)} \right], \quad (11.1)$$

where  $\Delta_j = \omega_j - \omega_0$  denotes the detuning of the  $j$ th spin from the cavity resonance frequency,  $\hat{a}$  and  $\hat{a}^\dagger$  denote field annihilation and creation operators, and  $\hat{\sigma}_z^{(j)}$ ,  $\hat{\sigma}_\pm^{(j)}$  are Pauli operators describing the spin degrees of freedom.

The quantum-optical input-output formalism [278] yields the following Heisenberg equation for the cavity field operator:

$$\dot{\hat{a}} = -i \sum_j g_j \hat{\sigma}_-^{(j)} - \frac{\kappa}{2} \hat{a} + \sqrt{\kappa_L} \hat{b}_{\text{loss}}(t) + \sqrt{\kappa_C} \hat{b}_{\text{in}}(t), \quad (11.2)$$

where  $\kappa = \kappa_C + \kappa_L$  is the total cavity damping rate with contributions  $\kappa_C$  due to the out-coupling and  $\kappa_L$  due to internal cavity losses. The last two terms in Eq. 11.2 describe inputs from bath modes:  $\hat{b}_{\text{loss}}(t)$  associated with the internal cavity losses and  $\hat{b}_{\text{in}}(t)$  associated with the quantized radiation field incident on the cavity.

Rather than solving the complete excitation dynamics of the spins, we will assume that ideal  $\pi/2$  and  $\pi$  control pulses have been applied to the spins at times  $t = -\tau$  and  $t = 0$ , respectively, preparing a state where

the spin excited states have acquired phases  $\exp(i\Delta_j\tau)$  with respect to the spin ground states in a frame rotating at  $\omega_s$ . As the spins precess at different frequencies  $\Delta_j$ , they come back in phase at the later time  $t = \tau$ , and we analyze their coupling to the quantized field during the rephasing of the spins that leads to the emission of an echo of duration  $T_E$ , set by the spin spectral linewidth and the duration of the  $\pi/2$  and  $\pi$  control pulses.

To this end we apply the Holstein-Primakoff approximation [123], which assumes oscillator-like commutator relations  $[\hat{\sigma}_-^{(j)}, \hat{\sigma}_+^{(k)}] = \delta_{jk}$  for the spin lowering operators  $\hat{\sigma}_-^{(j)}$ , and we treat each spin as an oscillator prepared in a coherent state of complex amplitude  $\alpha \exp(i\Delta_j\tau)$  at  $t = 0$ . The precession about the spin z-axis due to the inhomogeneous distribution of spin excitation energies is equivalent to the rotation of the complex oscillator amplitude, while the oscillator approximation assigns a constant damping rate to the collective transverse spin components and a linear coupling of the spin and field oscillator amplitudes rather than the nonlinear, excitation-dependent one. Since the decay of the transverse spin components is very limited during the timescale of our protocol, describing it by a constant effective rate and assuming a linear oscillator-like coupling to the field is a good approximation. We solve the coupled dynamics of the field mode and the spin ensemble, and we hence need the Heisenberg equation of motion for the spin lowering operator, which incorporates the coherent state initial condition as a delta-function excitation pulse at  $t = 0$ :

$$\dot{\hat{\sigma}}_j = -(\gamma + i\Delta_j)\hat{\sigma}_-^{(j)} - ig_j\hat{a} + \alpha e^{i\Delta_j\tau}\delta(t) + \sqrt{2\gamma}\hat{F}_j(t). \quad (11.3)$$

The relaxation rate  $\gamma$  represents spin decoherence, and is accompanied by quantum Langevin noise sources  $\hat{F}_j(t)$  with non-vanishing commutators  $[\hat{F}_i(t), \hat{F}_j^\dagger(t')] = \delta(t-t')\delta_{ij}$ .

An analysis of the beam-splitter like coupling of the incident, resonator and outgoing fields [121] yields the input-output relation,

$$\hat{b}_{\text{out}}(t) = \sqrt{\kappa_C}\hat{a}(t) - \hat{b}_{\text{in}}(t). \quad (11.4)$$

Applying Fourier transforms, and solving the resulting algebraic set of equations for the coupled spin and field operators leads to the compact and general form of the output field operator,

$$\tilde{b}_{\text{out}}(\omega) = -\frac{iq(\omega)}{\sqrt{2\pi}} + t(\omega)\tilde{f}_{\text{spin}}(\omega) + l(\omega)\tilde{b}_{\text{loss}}(\omega) + r(\omega)\tilde{b}_{\text{in}}(\omega), \quad (11.5)$$

where

$$q(\omega) = \frac{2\sqrt{\kappa_C}A(\omega)}{\kappa[1 + C(\omega)] - 2i\omega}, \quad (11.6)$$

$$t(\omega) = \frac{2\sqrt{\kappa_C \kappa_L \operatorname{Re}[C(\omega)]}}{\kappa[1 + C(\omega)] - 2i\omega}, \quad (11.7)$$

$$l(\omega) = \frac{2\sqrt{\kappa_C \kappa_L \operatorname{Re}[C(\omega)]}}{\kappa[1 + C(\omega)] - 2i\omega} \quad (11.8)$$

and

$$r(\omega) = \frac{\kappa_C - \kappa_L - (\kappa_C + \kappa_L)C(\omega) + 2i\omega}{\kappa[1 + C(\omega)] - 2i\omega}, \quad (11.9)$$

are frequency-dependent complex coefficients describing, respectively, the mean field emitted by the spins and Langevin noise operator terms associated with the spins, the resonator internal loss and reflection of the microwave field on the cavity.

In Eqs. (11.5)-(11.8), the distribution of spin detunings and coupling strengths are incorporated in the frequency-dependent ensemble cooperativity,

$$C(\omega) = \sum_j \frac{2g_j^2}{\kappa(\gamma + i\Delta_j - i\omega)}, \quad (11.10)$$

and the amplitude factor,

$$A(\omega) = \sum_j \frac{g_j \alpha e^{i\Delta_j \tau}}{\gamma + i\Delta_j - i\omega}. \quad (11.11)$$

The noise operators  $\tilde{f}_{\text{spin}}(\omega) = \tilde{F}_{\text{spin}}(\omega)/\sqrt{\kappa \operatorname{Re}[C(\omega)]}$ ,  $\tilde{b}_{\text{loss}}(\omega)$  and  $\tilde{b}_{\text{in}}(\omega)$  obey standard commutator relations, e.g.,  $[\tilde{f}_{\text{spin}}(\omega), \tilde{f}_{\text{spin}}^\dagger(\omega')] = \delta(\omega - \omega')$ , and the condition  $|r(\omega)|^2 + |t(\omega)|^2 + |l(\omega)|^2 = 1$  ensures the same commutator relation applies to the output field operators  $\tilde{b}_{\text{out}}(\omega)$ . We refer to the supplemental material of Ref. [8] for details of the derivation of the general expressions and for explicit analytical results in the special case of a Lorentzian detuning distribution uncorrelated with the coupling strengths. For instance, it is interesting to note that in this case the frequency dependent cooperativity (11.10) may be expressed explicitly as

$$C_{\text{Lorentzian}}(\omega) = \frac{2g^2 N_{\text{spins}} [\Gamma/2 + \gamma + i\omega]}{\kappa[(\gamma + \Gamma/2)^2 + \omega^2]}, \quad (11.12)$$

where  $\Gamma \simeq 2T_E^{-1}$  is the spectral width of the spin Larmor frequencies.

We turn now to the definition of the modes on which the echo is emitted in order to define and estimate the measurement sensitivity. For the sake

of simplicity we assume that the bandwidth  $T_E^{-1}$  of the spin-echo signal is narrower than the bandwidth of the squeezed radiation and of the resonator. The output signal mode is defined as  $\hat{b}_{\text{mode}} = (1/\sqrt{T_E}) \int_{\tau-T_E/2}^{\tau+T_E/2} \hat{b}_{\text{out}}(t') dt'$ , its  $\hat{X}$  quadrature operator being  $\hat{X} = \frac{1}{2i}(\hat{b}_{\text{mode}} - \hat{b}_{\text{mode}}^\dagger)$ . The normalization is chosen such that  $\hat{b}_{\text{mode}}^\dagger \hat{b}_{\text{mode}}$  is the photon number (operator) in the mode. We similarly introduce  $\hat{b}_{\text{in}} = (1/\sqrt{T_E}) \int_{\tau-T_E/2}^{\tau+T_E/2} \hat{b}_{\text{in}}(t') dt'$ ,  $\hat{f}_{\text{spin}} = (1/\sqrt{T_E}) \int_{\tau-T_E/2}^{\tau+T_E/2} \hat{f}_{\text{spin}}(t') dt'$  and  $\hat{b}_{\text{loss}} = (1/\sqrt{T_E}) \int_{\tau-T_E/2}^{\tau+T_E/2} \hat{b}_{\text{loss}}(t') dt'$ , as well as their respective  $\hat{X}_{\text{in}}$ ,  $\hat{X}_{\text{bath}}$  and  $\hat{X}_{\text{loss}}$  quadrature operators. The mean integrated amplitude of the spin-echo signal is given by the mean value of the  $\hat{X}$  operator,

$$\langle \hat{X} \rangle = \frac{-iq(0)}{\sqrt{T_E}}. \quad (11.13)$$

From Eq. (11.5), one finds that its fluctuations are

$$\delta X^2 = |r(0)|^2 \delta X_{\text{in}}^2 + |l(0)|^2 \delta X_{\text{bath}}^2 + |t(0)|^2 \delta X_{\text{spin}}^2. \quad (11.14)$$

In a model where the spins are described as harmonic oscillators coupled via the  $F_j$  to an effective zero temperature bath,  $\delta X_{\text{spin}}^2 = \frac{1}{4} \langle [ \tilde{f}_{\text{spin}}, \tilde{f}_{\text{spin}}^\dagger ] \rangle + 2 \langle \tilde{f}_{\text{spin}}^\dagger \tilde{f}_{\text{spin}} \rangle$  is equal to  $1/4$ . A more realistic description of the spins, going beyond the Holstein-Primakoff approximation and taking into account a non-zero effective temperature, would yield a larger value but still of order unity. Since  $|t(0)|^2 = \frac{\kappa C}{\kappa} (1 - |r(0)|^2) \simeq 4 \frac{\kappa C}{\kappa} C(0)$ , the contribution of the spin fluctuation to the total output noise scales as the ensemble cooperativity  $C(0)$ .

In the limit where the ensemble cooperativity and the cavity losses are small ( $C(0) \ll 1$  and  $|l(0)|^2 \ll 1$ ), which is the case in our experiment as explained in the next sections, the dominant contribution to the output fluctuations therefore is the reflected input noise and Eq. (11.14) reduces to  $\delta X \approx \delta X_{\text{in}}$ . This input field originates from a squeezing source [SQZ in Fig. 11.1] that we assume to be ideal, generating a squeezed vacuum along the  $X$  quadrature with a variance  $\delta X_{\text{sq}}^2$  at its output. Due to transmission losses between SQZ and the ESR cavity, modelled by an effective loss coefficient  $\eta_{\text{loss}}$ , the squeezing properties are deteriorated and the variance in the input quadrature becomes

$$\delta X_{\text{in}}^2 = (1 - \eta_{\text{loss}}) \delta X_{\text{sq}}^2 + \eta_{\text{loss}}/4, \quad (11.15)$$

characterized by the ratio of the squeezed quadrature variance to the vacuum fluctuations  $\eta_S = \delta X_{\text{in}}^2 / (1/4)$  called the squeezing factor. The

signal-to-noise ratio of the spin-echo detection is given by  $\langle \hat{X} \rangle / \delta X$ ,  $\langle \hat{X} \rangle$  being independent of the input field fluctuations as seen from Eq. (11.13). Our analysis therefore shows that in the limit where the spin ensemble is weakly coupled to the cavity and the cavity losses are negligible, applying a squeezed vacuum to the ESR resonator should improve the spin detection sensitivity by approximately a factor  $\sqrt{\eta_S}$ .

## 11.3 Experimental results

I shall now provide a overview of the experimental implementation of this proposal while referring to the full manuscript [8] for extended details of the procedure and apparatus.

### 11.3.1 Characterization of the squeezer

The first step was the characterization of the squeezed microwave field produced by the squeezing JPA denoted SQZ in Fig. 11.1. This JPA acts on a vacuum input and performs parametric amplification [122] to produced a squeezed vacuum state with a variance of  $1/(4G^2)$  on its squeezed quadrature. Here  $G$  is the amplitude gain factor. The average photon number in this state is  $N = (G^2 + G^{-2} - 2)/4$  and the two-photon coherence  $M = \sqrt{N(N+1)}$ . By an appropriate choice of phase for the pump tone to the JPA [261], this results in an output in Eq. (11.15) from SQZ to the ESR resonator with a variance in its  $X$  quadrature squeezed according to

$$\delta X_{\text{sq}}^2 = \frac{1}{2} \left( N - M + \frac{1}{2} \right). \quad (11.16)$$

The experimental characterization of the squeezing source verifies this relation and by using the same experimental setup shown in Fig. 11.1 but with the spins tuned far from resonance by the bias magnetic field  $B_0$ , it was able to also estimate the losses from the squeezer SQZ to the resonator in Eq. (11.15) as well as those from the resonator to the homodyne demodulator where a signal  $I(t)$  is recorded.

The histograms of the statistical distributions of  $I(t)$  in Fig. 11.2 shows that the total noise in the measurement signal was reduced by 1.2 dB when the squeezer was turned from on to off, corresponding to a reduction in the variance by a factor of 0.75, i.e,

$$\delta I_{\text{on}}^2 = 0.75 \delta I_{\text{off}}^2. \quad (11.17)$$

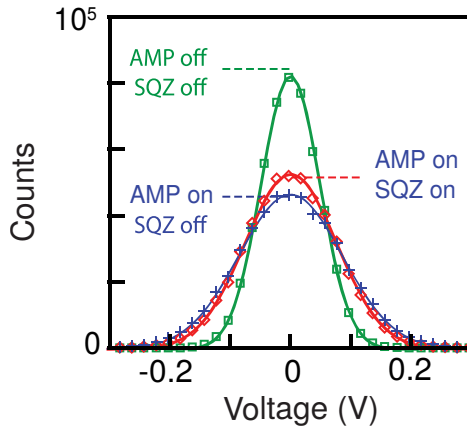


Figure 11.2: Characterization of the prepared squeezed vacuum state. Noise histograms for AMP and SQZ both off (green open squares), AMP on and SQZ off (blue crosses), and AMP and SQZ both on (red open symbols) in which case the fluctuations are reduced below the vacuum level. Gaussian fits for each are also shown (full curves).

Notice that in order to record a spin-signal in the homodyne demodulator it is crucial to turn the amplifier AMP on, so the green curve is not relevant for the purpose at hand.

For the squeezing to be in quantum regime, the noise in the signal recording  $I(t)$  must be reduced below the level of vacuum fluctuations  $\delta I_0$  which is only possible if the thermal occupation of the mode is negligible. A calibration measurement, using a superconducting qubit, was used to show that indeed only an average of  $\bar{n} = 0.1$  photons are present in the mode when the squeezer is turned off. The fluctuations in a quadrature  $X_{\text{th}}$  of a thermal state are given by  $\delta X_{\text{th}}^2 = (1 + 2\bar{n})/4$ , so in this experiment, the following set of inequalities were obeyed,

$$\delta I_0^2 < \delta I_{\text{off}}^2 < 1.2\delta I_0^2. \quad (11.18)$$

Combined with Eq. (11.17) this shows that the measured noise with the squeezer turned on was, indeed, reduced by at least 10% and at most 25% below vacuum level. See [8] for further details on the calibration of the squeezing JPA.

An ideal, lossless parametric amplifier is in principle able to produce an infinitely squeezed state [122]. However, in all practical implementations the achievable squeezing is limited by imperfections, often to a quite modest

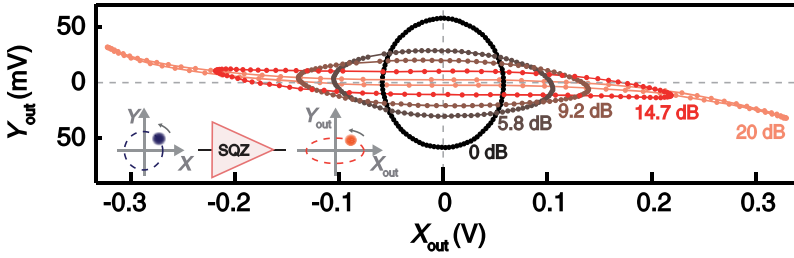


Figure 11.3: Output quadratures  $X_{\text{out}}$  and  $Y_{\text{out}}$  of a small coherent signal sent to the SQZ measured for input phases  $\phi_S$  spanning the whole interval between 0 and  $2\pi$  for five different power gains,  $G^2 = 0, 5.8, 9.2, 14.7, 20$  dB. Note that these data were obtained in a separate calibration run in which the ESR cavity was removed [279].

level. As described above and seen in Fig. 11.2, this proof-of-principle experiment delivers also only a relatively small squeezing induced noise reduction in the output signal. This is partly due to microwave losses between SQZ and the homodyne detector in Fig. 11.1, stemming from the insertion of circulators and cables and from internal losses in the components. The experiment aims to reduce these losses but still finds an effective loss coefficient in Eq. (11.15) of  $\eta_{\text{loss}} = 0.54$ .

Another, and more fundamental limitation to the squeezing is imposed by the JPA device. The ideal parametric amplifier assumes linearity in the Hamiltonian, while higher order terms in the expansion of the Josephson junction potential energy become important as the gain  $G$  is increased in order to actualize higher degrees of squeezing according to Eq. (11.16); [280, 281]. This problem is apparent in Fig. 11.3, where for small gains ( $G^2 < 6$  dB) a standard squeezing ellipse is observed in the quadrature plane while from around 10 dB, the ellipse is deformed, taking instead a banana shape. This distortion is detrimental to the reduced variance of the squeezed quadrature, and the experiment was hence performed at the saturation point of the squeezing JPA,  $G^2 = 6$  dB.

As explained in [8], the amplifier, AMP is also affected by the nonlinearities in the JPA device. It was thus necessary to limit the amplitude of the spin-echo signal in order to avoid saturation effects. Section 11.3.2 explains how this was accomplished.

### 11.3.2 Squeezing enhanced spin detection

The spins used in the experiment are provided by bismuth ( $^{209}\text{Bi}$ ) donors implanted in a silicon sample, which has been isotopically enriched in the nuclear-spin-free  $^{28}\text{Si}$ . At low magnetic fields, the strong hyperfine interaction between the  $S = 1/2$  electron and the  $I = 9/2$  nuclear spins yields multiple allowed ESR-like transitions around 7.37 GHz; this experiment works on the lowest frequency transition. More details on the characterization of this sample can be found in [282, 283].

Figure 11.4(a) shows this spin resonance line, obtained by measuring the spin-echo intensity as a function of the magnetic field  $B_0$  (with SQZ off). This shows the expected resonance around  $B_0 = 2.8\text{ mT}$  [see Fig. 11.4(a)], with the 0.1 mT linewidth primarily due to strain exerted by the aluminium wire on the underlying silicon substrate [284]. The spin linewidth is considerably broader ( $\times 30$ ) than the resonator bandwidth. As a consequence, only a narrow subset of spins is excited at each magnetic field  $B_0$  and contributes to the echo signal. With a 5- $\mu\text{s}$   $\pi/2$  excitation pulse in this experiment, the excitation bandwidth is estimated to 100 kHz, justifying the choice of a 300-kHz digitization bandwidth.

Rabi oscillations (obtained by sweeping the power of the 10  $\mu\text{s}$  rectangular refocusing pulse in the Hahn echo sequence) were used to calibrate the pulses for subsequent experiments [136]. To avoid saturation of the AMP as explained in the previous section, the field was purposely set far away from the maximum of the spin resonance line at  $B_0 = 2.6\text{ mT}$  [see Fig. 11.4(a)], and an echo sequence of the form ( $\theta - \tau - \pi - \tau - \text{echo}$ ) with  $\tau = 200\ \mu\text{s}$  was used. Here the usual  $\pi/2$  Rabi angle of the Hahn echo sequence was replaced by a lower Rabi angle  $\theta \simeq \pi/3$ , realized with a 3- $\mu\text{s}$ -rectangular pulse .

An echo was then recorded in the two following conditions: SQZ off and SQZ switched on for a time window of 200  $\mu\text{s}$  centered around the echo emission time (for reasons explained in the next section, pulsing the squeezed state generation was found to be crucial for the success of the experiment). The phases of the excitation and refocusing pulses were set in such a way that the echo signal was produced entirely on the  $I$  quadrature aligned with the squeezed vacuum. Time traces of the digitized  $I(t)$  quadrature are shown in Fig. 11.4(b), with the echo barely visible in single-shot traces. After averaging, the spin-echo amplitude appears to be identical for SQZ on and off, confirming that the saturation effects mentioned in the previous subsection were avoided. The 20- $\mu\text{s}$  echo duration is due to the excitation bandwidth. Histograms of the noise

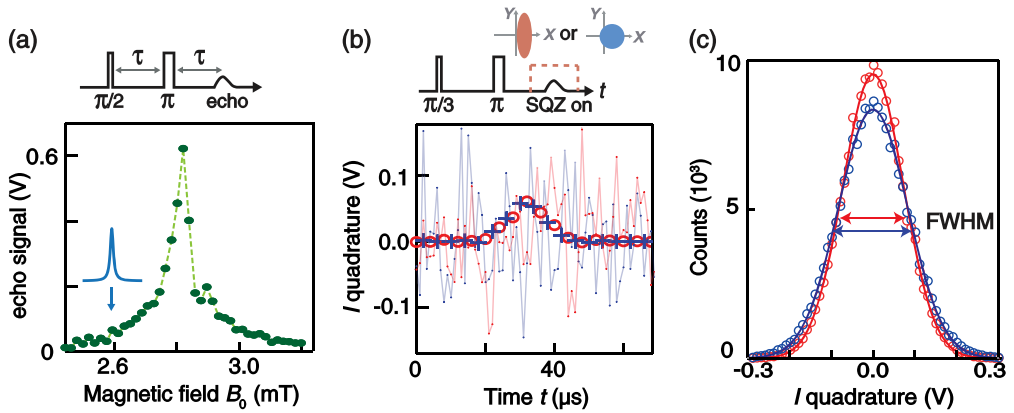


Figure 11.4: Squeezing-enhanced spin-echo detection. (a) Hahn-echo detected magnetic field sweep, showing the bismuth donor resonance line. The blue arrow indicates the field chosen in the rest of the experiment and the blue Lorentzian curve indicates the fraction of spins that are within the cavity resonance. (b) Echo signals observed with SQZ off (blue) and on (red) for a single shot (lines) and averaged over 2500 traces (symbols) confirm that the signal intensity is identical. SQZ was switched on only during a short  $\Delta t = 200 \mu\text{s}$  window around the echo emission time (dashed rectangle in the pulse sequence). The excitation pulse angle is chosen to be  $\approx \pi/3$  in order to avoid saturation effects (see main text). (c) Histograms of the noise around the average signals of panel (b) measured with 2500 single-shot traces acquired on a  $70 \mu\text{s}$ -time-window centered on the echo, with SQZ off (blue) and on (red) (see Supp. Mat. of [8]), and corresponding Gaussian fits (full curves). Standard deviations are  $0.0858 \pm 2 \cdot 10^{-4} \text{ V}$  for SQZ off and  $0.0748 \pm 2 \cdot 10^{-4} \text{ V}$  for SQZ on, confirming a reduction in the noise accompanying the spin-echo signal when SQZ is on.

during the echo emission [Fig. 11.4(c)] show that the data obtained with SQZ on exhibit less noise than with SQZ off — indeed, the similarity between these distributions and those obtained with no spin-echo signal [Fig. 11.2] confirm that quantum fluctuations are the primary noise source in the spin echo measurements. In both cases, the variance is reduced by a factor of 0.75 when SQZ is on, in agreement with the theoretical analysis presented in Sec. 11.2. As the noise reduction is obtained while maintaining constant spin-echo signal amplitude, this demonstrates that the sensitivity of magnetic resonance detection is enhanced using quantum squeezing.

## 11.4 Discussion

While the experiment was able to successfully demonstrate squeezing-enhanced magnetic resonance detection, due to the limited noise reduction of only 1.2 dB, it must be considered a proof-of-principle experiment. Some reasons for this were explored in Sec. 11.3. The first, saturation effects imposed by non-linearity of the JPAs used for SQZ and AMP, could in an optimized setup be reduced significantly by installing state-of-the-art JPAs which can operate with 30 dB higher saturation powers [285, 286]. This would already provide an additional noise reduction of  $\approx 3$  dB. Microwave losses along the path from SQZ to the detector constitute another major source of noise. An optimization of this path with better elements (shorter cables and fewer circulators) is estimated to be able to deliver an additional noise reduction of  $\approx 2$  dB. Hence, under realistic circumstances, an optimized setup could present a noise reduction below vacuum level of roughly a factor 5 while leaving the signal unchanged, thereby allowing a much smaller spin sample to be detected in the same measurement time. This will clearly find practical applications. See Ref. [8] for an extended discussion of the applicability of the scheme optimized under realistic experimental settings.

The optimizations mentioned above concern technical limitations which at this stage are issues of engineering. There are, however, still fundamental limitations to the squeezing-enhanced sensitivity imposed by quantum mechanics. These shall now be discussed.

### 11.4.1 Ultimate limits to the sensitivity and squeezing affected spin dynamics

Supposing that an ideal squeezed state of arbitrary squeezing factor could be sent onto the cavity so that the purely electromagnetic contribution to the total noise would be completely suppressed, it is interesting to investigate the other physical mechanisms that would ultimately limit the sensitivity. Those can be deduced from the theoretical expression for the noise (11.14), which shows that in the limit where  $\delta X_{\text{in}} \rightarrow 0$ , a finite variance is maintained,  $\delta X^2 = |l(0)|^2 \delta X_{\text{bath}}^2 + |t(0)|^2 \delta X_{\text{spin}}^2$ . In an ideal experiment, the cavity internal losses may be suppressed so that the first term is negligible; however, the second term describes noise emitted by the spins (as observed experimentally in [287]), and is thus unavoidable. While negligible in the present experiment, this contribution becomes relevant in the limit where the squeezing factor  $\eta_S$  becomes

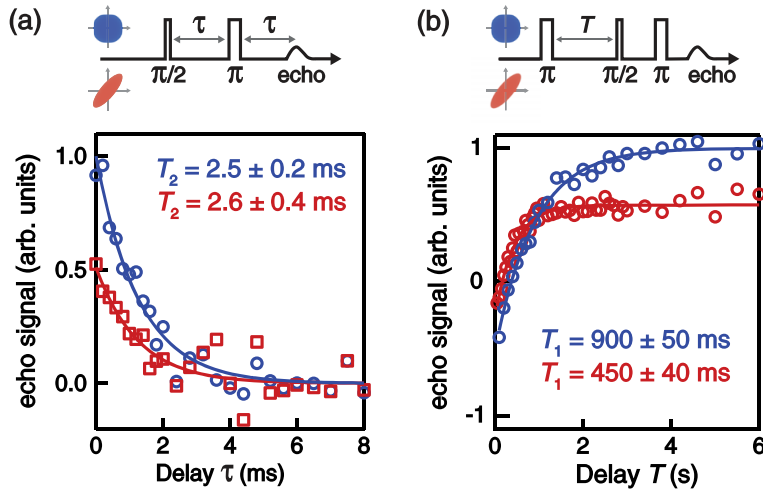


Figure 11.5: Influence of squeezing on the spin coherence times. (a) Coherence time  $T_2$  measured with a Hahn echo sequence for SQZ off (blue circles) and on (red squares). Contrary to the experiments in Fig. 5, SQZ is now switched on or off for the entire experimental sequence. The integrated echo signal is plotted as a function of the delay  $\tau$  between the  $\pi/2$  and  $\pi$  pulses. Exponential fits (solid lines) yield  $T_{2, \text{off}} = 2.5 \pm 0.2$  ms and  $T_{2, \text{on}} = 2.6 \pm 0.4$  ms. (b) Energy relaxation time  $T_1$  with SQZ on (blue circles) and off (red circles). Exponential fits (solid lines) yield  $T_1 = 900 \pm 50$  ms with SQZ off and  $T_1 = 450 \pm 40$  ms with SQZ on. Both  $T_1$  (b) and  $T_2$  (a) curves have their amplitude reduced by  $\approx 0.5$  with SQZ on, indicating reduced spin polarisation in the steady-state when the SQZ is continuously switched on.

comparable to the ensemble cooperativity  $4C(0)$  as seen in Sec. 11.2. Additional measurements (reported in the Supplemental Material of [8]) yield  $C(0) = 0.002$ , which implies that spin noise would be a limitation for 20-dB squeezing, corresponding to a maximum gain in sensitivity by a factor  $\simeq 10$ .

Another fundamental effect disregarded so far concerns the influence exerted by squeezed radiation on the spin dynamics, which may in certain cases lead to a reduction of the echo signal. Indeed, in steady-state, squeezed radiation incident on a two-level system modifies its relaxation and coherence times as well as its average polarization, as predicted in Ref. [124] and observed in recent experiments with superconducting qubits [99, 288]. Note that since this effect does not apply for a harmonic oscillator degree of freedom, it did not appear in the analysis of Sec. 11.2

where the spins are modelled as a collection of oscillators. The topic of the next chapter in this thesis is the emergence of these effects as the two limiting cases of a single and of many spins are bridged [9].

These two fundamental limitations were experimentally investigated by measuring spin coherence and relaxation times with SQZ turned off or on during the entire experimental sequence. The effective coherence time  $T_2$  is found to be unaffected by squeezing [see Fig. 11.5(a)], because decoherence occurs by nonradiative processes such as dipolar interactions [289]. Energy relaxation, on the other hand, has been shown to be caused by spontaneous emission of microwave photons through the cavity (the Purcell-effect) with a rate  $T_1^{-1} = 4g^2/\kappa$  [136],  $g$  being the coupling strength of a single spin to the radiation field as defined in Sec. 11.2. The effective lifetime  $T_1$  should thus be affected by the squeezed microwave injection. Accordingly, it was found to decrease from 0.9 to 0.45 s when squeezing is continuously switched on [see Fig. 11.5(b)], with an overall echo amplitude diminished by the same factor 2, revealing the expected reduction in spin polarisation. The reduction factor on both  $T_1$  and polarization is predicted by Gardiner to be  $2N+1$  [124], yielding  $N \approx 0.5$  in this experiment, compatible with the chosen SQZ gain  $G^2 = 6$  dB as well as the squeezed state characterisation by homodyne detection shown in Fig. 11.2.

Squeezing-induced spin depolarisation is avoided in the data shown in Figs. 11.2 and 11.4(c) because the squeezer SQZ is switched on only for a short time window  $\Delta t = 200 \mu\text{s}$  around the echo, much smaller than the depolarisation time which is of order  $\approx T_1/(1+2N) = 0.45$  s in this experiment. This strategy can be applied only if the depolarisation time is longer than the echo duration  $T_E$ , i.e., if the squeezing parameter  $\eta_S \approx 1/N > 8g^2T_E/\kappa$ .

By looking at, e.g., the expression (11.12) for the ensemble cooperativity in the Lorentzian case, it is interesting to note that  $8g^2T_E/\kappa \approx 4C(0)/N_{\text{spins}}$ , which is the *single-spin* cooperativity and is therefore much smaller than the ensemble cooperativity  $4C(0)$  as long as the ensemble contains a large number of spins  $N_{\text{spins}} \gg 1$ . Spin noise is therefore expected to limit the achievable sensitivity gain much earlier than spin depolarization, provided the squeezed state generation is pulsed as in the present experiment. For the present experimental parameters,  $T_1/T_E \approx 10^{-5}$ , so that squeezing-induced spin depolarization would not be an issue before 50-dB squeezing is achieved which is much later than the 20-dB limit imposed by spin noise.

## 11.5 Conclusion

The experiment reported in [8] and described here has proven that it is possible to increase the sensitivity in magnetic resonance detection of a weakly coupled spin ensemble by injecting a squeezed probe field. The experiment constitutes one of the first metrology applications of squeezing in the microwave regime, and while the reported noise reduction is only 1.2 dB, it is realistic to optimize the experimental platform to achieve a much larger squeezing-induced advantage. This would be highly beneficial in practical applications and eventually in technologies such as commercial ESR-spectroscopy devices.

This study opens the lid to the toolbox of quantum metrology for usage in the microwave regime and in particular for magnetic resonance detection. It would be interesting to extend the present results by considering the advantages offered by employing alternative non-classical states such as Schrödinger-cats [34, 61].

# Relaxation of a spin ensemble in a squeezed bath

*This chapter is reproduced from Ref. [9] with only minor modifications and two paragraphs from the introduction moved to Chapter 11.*

---

In the previous chapter, we saw an example of how squeezing the uncertainty in a probe field allows a higher sensitivity to be achieved in a cutting-edge sensing experiment. In that case, the advantages offered by squeezing were limited by technical restrictions imposed by the components of the experimental setup. Ideal settings would allow a much larger sensitivity gain but it would eventually be limited by more fundamental mechanisms, which are the topic of the discussion in Sec. 11.4.1 of that chapter. One of these is the influence exercised by the squeezed probe field on the internal dynamics of the spin ensemble. This did not play a role in those particular experimental settings. In this chapter, we shall consider a more general setup as we delve deeper into the physical processes, defining the workings of this mechanism in different settings and regimes.

The topic was first approached by Gardiner [124] who showed that when the fluctuations in electromagnetic field modes are altered, so are the derived relaxation dynamics of the systems interacting with the field. In particular, Gardiner's seminal result on a single two-level system in a

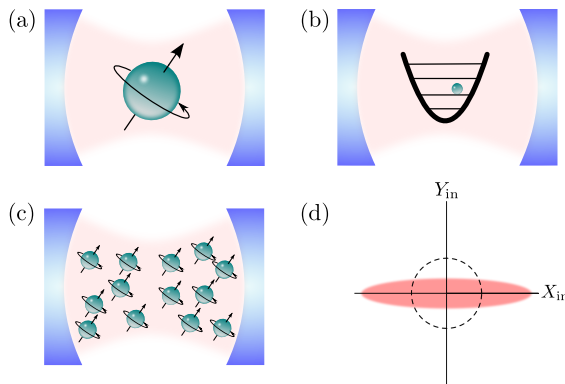


Figure 12.1: A bad cavity is coupled linearly to (a) a single spin-1/2 particle, (b) an oscillator degree of freedom, or (c) a collection of  $n$  spin-1/2 particles. (d) Quadrature representation of the squeezed vacuum input field to the cavity, Eq. (12.1) with squeezing parameters  $N = 1$  and  $M = \sqrt{2}$ , shown as the red ellipse. The fluctuations in the  $Y_{in}$  quadrature are reduced below those of a vacuum state (dashed circle) at the cost of increased fluctuations in the  $X_{in}$  quadrature.

squeezed reservoir [124] shows how the decay of the excitation and the two transverse Bloch vector components is modified by the coupling to that reservoir. This effect has recently been observed in a superconducting qubit coupled to a squeezed vacuum microwave field produced by a Josephson parametric amplifier [288, 290], and it is equivalently witnessed in the resonance fluorescence spectrum [291] and the steady-state inversion of a driven system [292]. A single two-level system can be represented as a spin-1/2 particle with a spin-up (excited) and a spin-down (ground) state. As utilized in the modelling of the experiment in Chapter 11, in the Holstein-Primakoff approximation (HPA) [123], an ensemble of weakly excited spins is equivalent to an oscillator mode. An oscillator experiences a squeezed reservoir as Langevin noise acting asymmetrically on its two quadratures but unlike a spin-1/2 system, the relaxation of the quadratures is not affected by the squeezing, which instead manifests itself directly in their variances.

The interaction of an ensemble of atoms with a broadband squeezed reservoir of field modes has been studied theoretically with the master equation formalism (see, e.g., [293]) and it has been shown that the collective interaction of two-level atoms with squeezed vacuum fields, which have minimum-uncertainty product of the field quadratures, leads to a

pure steady state for a pair [294] and for any even number of spins [295]. These steady states are spin squeezed with minimum uncertainty product of their squeezed and anti-squeezed spin components [295].

In this chapter we study the dynamics of spin systems due to their coupling to a squeezed bath. As our model system we consider a cavity subject to a squeezed vacuum input and containing either an oscillator or a system of spins to which it is linearly coupled [see Fig. 12.1]. Assuming the bad cavity limit, we eliminate the cavity mode and derive equations of motion for the first and second moments of the oscillator or collective spin components. Note that in the present study, the systems only couple collectively to the radiation field and experience no individual damping, which would make the collective system explore mixed states beyond the large spin Dicke states [296]. We reproduce the result of Gardiner for a single spin, and we show how an oscillator description of the ensemble becomes valid in the limit of many weakly excited spins. Our analysis unveils how the two limiting cases differ by the relative contributions of quantum (vacuum) fluctuation and of radiation reaction to the dynamics.

## 12.1 Model

We consider a generic model of a quantum system coupled resonantly with strength  $g$  to a single cavity mode with field annihilation operator  $\hat{a}_c$ . The cavity serves the purpose of mediating and enhancing the coupling of the system to an input field  $\hat{b}(t)$  incident on the cavity mirrors [135]. We focus on the case where the input is a broadband squeezed vacuum field defined by the properties

$$\begin{aligned}\langle \hat{b}(t) \rangle &= 0 \\ \langle \hat{b}^\dagger(t) \hat{b}(t') \rangle &= N \delta(t - t') \\ \langle \hat{b}(t) \hat{b}(t') \rangle &= M \delta(t - t'),\end{aligned}\tag{12.1}$$

where  $|M| \leq \sqrt{N(N+1)}$ . Such a field can be produced by a parametric amplifier driven in degenerate mode or by coupling of light to non-linear materials [122]. In the following we assume, without loss of generality, the phases to be aligned such that  $M$  is real and positive. As illustrated in Fig. 12.1(d), the field quadrature  $\hat{X}_{\text{in}} = \hat{b} + \hat{b}^\dagger$  has a higher variance,  $\langle \hat{X}_{\text{in}}^2 \rangle = 2N + 2M + 1$ , than the vacuum state obtained when  $N = M = 0$ , while the variance  $\langle \hat{Y}_{\text{in}}^2 \rangle = 2N - 2M + 1$  in the orthogonal quadrature,  $\hat{Y}_{\text{in}} = i(\hat{b}^\dagger - \hat{b})$  is reduced. The input field thereby fulfills Heisenberg's uncertainty

relation  $\langle \hat{X}_{\text{in}}^2 \rangle \langle \hat{Y}_{\text{in}}^2 \rangle \geq 1$  with equality for all  $N$  if  $M = \sqrt{N(N+1)}$ , which we assume in the following<sup>1</sup>. Squeezed states have been demonstrated with  $N \simeq 4.2$  corresponding to variances reduced by 12.7 dB below the vacuum level [259].

Figure 12.1(a) shows a single two-level system, represented as a spin-1/2 particle by the Pauli vector of operators  $\vec{\sigma} = (\hat{\sigma}_x, \hat{\sigma}_y, \hat{\sigma}_z)$  and the associated lowering and raising operators,  $\hat{\sigma}_- = \hat{\sigma}_x - i\hat{\sigma}_y$  and  $\hat{\sigma}_+ = \hat{\sigma}_-^\dagger$ , respectively. Figure 12.1(b) shows a harmonic oscillator described by a lowering operator  $\hat{a}$  with commutator relations  $[\hat{a}, \hat{a}^\dagger] = 1$  and oscillator quadratures  $\hat{X} = \hat{a} + \hat{a}^\dagger$  and  $\hat{Y} = i(\hat{a}^\dagger - \hat{a})$ . If the single spin is only weakly excited, it behaves as an oscillator since the Bloch vector dynamics described by  $(\hat{\sigma}_x, \hat{\sigma}_y)$  is similar to the oscillator dynamics described by  $(\hat{X}, \hat{Y})$  as we heuristically set  $\hat{\sigma}_z = -1$  (remember that  $[\hat{\sigma}_-, \hat{\sigma}_+] = -\hat{\sigma}_z$ ). As quantified in the Holstein-Primakoff approximation introduced below, this similarity is increased as more spins are considered. To investigate the transition between the single spin and the oscillator results, we hence examine an ensemble of  $n$  spins as shown in Fig. 12.1(c). The total spin operator is  $\vec{S} = \sum_{i=1}^n \vec{\sigma}^{(i)}$  and the excitation lowering operator is  $\hat{S}_- = \sum_{i=1}^n \hat{\sigma}_-^{(i)}$ , with  $[\hat{S}_-, \hat{S}_+] = -\hat{S}_z$ , where  $\hat{S}_+ = \hat{S}_-^\dagger$ . Notice that, since we omit the factor 1/2 on the Pauli operators, conventionally used when defining the spin observables,  $\vec{S}/2$  ( $\vec{S}$ ) is (is not) an angular momentum. Symmetric states of the spin ensemble can be represented by an extension of the Bloch sphere picture of a single spin to a collective spin as shown in Fig. 12.2.

The Holstein-Primakoff transformation maps spin operators to bosonic creation and annihilation operators while conserving the commutation relations [123],

$$\begin{aligned}\hat{S}_z &= 2\hat{a}^\dagger\hat{a} - n, \\ \hat{S}_- &= \sqrt{n - \hat{a}^\dagger\hat{a}}\hat{a}, \\ \hat{S}_+ &= \hat{a}^\dagger\sqrt{n - \hat{a}^\dagger\hat{a}}.\end{aligned}\tag{12.2}$$

For a large ensemble  $n \gg 1$  and weak excitation, the second terms in the square roots are negligible such that  $\hat{S}_- \simeq \sqrt{n}\hat{a}$  and  $\hat{S}_+ \simeq \sqrt{n}\hat{a}^\dagger$ . This constitutes the HPA.

---

<sup>1</sup>Notice that this chapter assumes a different normalization of the quadratures than the previous.

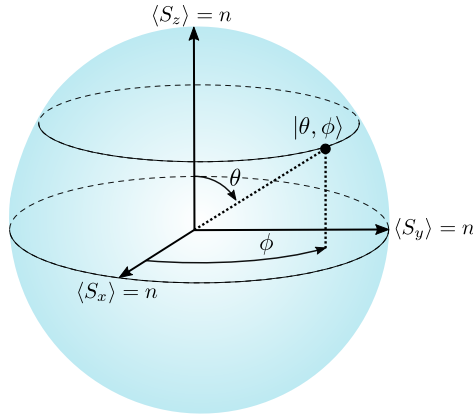


Figure 12.2: Bloch sphere representation of a collective spin with components  $(S_x, S_y, S_z)$ . The axes go from  $-n$  to  $n$ , the minimum and maximum eigenvalues for an ensemble with  $n$  spins. A spin coherent state  $|\theta, \phi\rangle$  is defined in terms of the Bloch angles  $\theta$  and  $\phi$ , [Eq. (12.22)].

### 12.1.1 Heisenberg equations of motion

The interaction between the system and the cavity field is described by a Tavis-Cummings-type Hamiltonian [297] ( $\hbar = 1$ )

$$\hat{H} = ig \left( \hat{d}\hat{a}_c^\dagger - \hat{d}^\dagger\hat{a}_c \right), \quad (12.3)$$

where for a single spin  $\hat{d} = \hat{\sigma}_-$ , for an ensemble of  $n$  spins  $\hat{d} = \hat{S}_-$ , and for an oscillator  $\hat{d} = \hat{a}$ . This yields the Heisenberg equation of motion for a general system operator  $\hat{q}$ ,

$$\dot{\hat{q}} = g \left( [\hat{q}, \hat{d}]\hat{a}_c^\dagger - [\hat{q}, \hat{d}^\dagger]\hat{a}_c \right). \quad (12.4)$$

Likewise, if  $\kappa$  denotes the output coupling through the cavity mirrors, the quantum Langevin equation for the cavity mode is,

$$\dot{\hat{a}}_c = g\hat{d} - \frac{\kappa}{2}\hat{a}_c + \sqrt{\kappa}\hat{b}. \quad (12.5)$$

In the bad cavity limit ( $g \ll \kappa$ ), we may assume that the cavity relaxes to a steady state faster than the other relevant time scales, i.e.,  $\dot{\hat{a}}_c = 0$ , so that

$$\hat{a}_c = \frac{2\hat{b}}{\sqrt{\kappa}} + \frac{2g\hat{d}}{\kappa}. \quad (12.6)$$

This shows how the cavity field is composed of the input field and a field generated by the system inside the cavity.

Although  $\hat{a}_c$  commutes with any system operator, the individual terms in Eq. (12.6) do not. Accordingly, the relative contributions to the evolution of the system operator in Eq. (12.4) depend on the ordering of  $\hat{a}_c^{(\dagger)}$  and the commutators. For a Hermitian operator  $\hat{q}$ ,  $\dot{\hat{q}}$  must also be Hermitian. Dalibard *et. al.* [298] offer the insight that by requiring each part to be separately Hermitian,  $\dot{\hat{q}}$  can be decomposed unambiguously into two terms with distinct physical meanings. Such splitting has been applied to study the underlying mechanisms in radiative energy corrections and spontaneous emission processes [298, 299]. Pursuing this line of reasoning, we may apply Eq. (12.6) and rewrite Eq. (12.4) as

$$\dot{\hat{q}} = (\dot{\hat{q}})_{\text{ff}} + (\dot{\hat{q}})_{\text{sr}}, \quad (12.7)$$

where

$$(\dot{\hat{q}})_{\text{ff}} = \frac{2g}{\sqrt{\kappa}} \left( [\hat{q}, \hat{d}] \hat{b}^\dagger - \hat{b} [\hat{q}, \hat{d}^\dagger] \right) \quad (12.8)$$

describes interactions with fluctuations in the input field, and

$$(\dot{\hat{q}})_{\text{sr}} = \frac{2g^2}{\kappa} \left( [\hat{q}, \hat{d}] \hat{d}^\dagger - \hat{d} [\hat{q}, \hat{d}^\dagger] \right) \quad (12.9)$$

describes electromagnetic self-reaction mediated by the cavity field.

### Oscillator

We consider first the case where the system is described by an oscillator degree of freedom,  $\hat{d} = \hat{a}$ . Here Eqs. (12.8) and (12.9) yield for the annihilation operator,

$$\begin{aligned} (\dot{\hat{a}})_{\text{ff}} &= -\frac{2g}{\sqrt{\kappa}} \hat{b}, \\ (\dot{\hat{a}})_{\text{sr}} &= -\frac{2g^2}{\kappa} \hat{a}. \end{aligned} \quad (12.10)$$

We thus obtain the equations of motion for the oscillator quadratures

$$\begin{aligned} \dot{\hat{X}} &= -\lambda(\hat{b} + \hat{b}^\dagger) - \frac{\gamma_p}{2} \hat{X} \\ \dot{\hat{Y}} &= i\lambda(\hat{b} - \hat{b}^\dagger) - \frac{\gamma_p}{2} \hat{Y}, \end{aligned} \quad (12.11)$$

where we have introduced the Purcell rate  $\gamma_p = 4g^2/\kappa$  and an effective coupling constant  $\lambda = 2g/\sqrt{\kappa}$ . The field fluctuations, represented by  $\hat{b}$ , drive the fluctuations of the oscillator quadratures while the self-reaction causes their damping.

### Collective spin ensemble

Consider now the case of an ensemble of  $n$  spin-1/2 particles inside the cavity. The ensemble couples linearly to the cavity field via  $\hat{d} = \hat{S}_-$ . By Eqs. (12.7)-(12.9), the equations of motion for  $\hat{S}_-$  and  $\hat{S}_z$  have contributions from both the field fluctuations and self reaction,

$$\begin{aligned} (\dot{\hat{S}}_-)_{\text{ff}} &= \frac{2g}{\sqrt{\kappa}} b \hat{S}_z, \\ (\dot{\hat{S}}_z)_{\text{ff}} &= -\frac{4g}{\sqrt{\kappa}} (\hat{S}_- b^\dagger + b \hat{S}_+), \end{aligned} \quad (12.12a)$$

$$\begin{aligned} (\dot{\hat{S}}_-)_{\text{sr}} &= \frac{2g^2}{\kappa} \hat{S}_- \hat{S}_z, \\ (\dot{\hat{S}}_z)_{\text{sr}} &= -\frac{8g^2}{\kappa} (\hat{S}_- \hat{S}_+). \end{aligned} \quad (12.12b)$$

The operator terms in  $(\dot{\hat{S}}_-)_{\text{ff}}$  and  $(\dot{\hat{S}}_z)_{\text{ff}}$  give rise to second order processes that contribute to the same order in  $g^2/\kappa$  as the processes in  $(\dot{\hat{S}}_-)_{\text{sr}}$  and  $(\dot{\hat{S}}_z)_{\text{sr}}$ . This follows by a formal integration of the equations over a small time interval  $\Delta t \rightarrow dt$ ,

$$\begin{aligned} [\hat{S}_-(t + \Delta t) - \hat{S}_-(t)]_{\text{ff}} &= \frac{2g}{\sqrt{\kappa}} \int_t^{t+\Delta t} dt' b(t') \hat{S}_z(t'), \\ [\hat{S}_z(t + \Delta t) - \hat{S}_z(t)]_{\text{ff}} &= \frac{4g}{\sqrt{\kappa}} \int_t^{t+\Delta t} dt' \left\{ \hat{S}_-(t') \hat{b}^\dagger(t') + \hat{b}(t') \hat{S}_+(t') \right\}, \end{aligned} \quad (12.13)$$

and substitution back in Eqs. (12.12a), keeping only terms to order  $g^2/\kappa$ ,

$$\begin{aligned} (\dot{\hat{S}}_-)_{\text{ff}} &= \frac{2g}{\sqrt{\kappa}} b \hat{S}_z - \frac{8g^2}{\kappa} \int_t^{t+\Delta t} dt' \left\{ b(t) \hat{S}_-(t') \hat{b}^\dagger(t') + \hat{b}(t) \hat{b}(t') \hat{S}_+(t') \right\}, \\ (\dot{\hat{S}}_z)_{\text{ff}} &= -\frac{4g}{\sqrt{\kappa}} (\hat{S}_- b^\dagger + b \hat{S}_+) - \frac{8g^2}{\kappa} \int_t^{t+\Delta t} dt' \left\{ \hat{b}(t') \hat{S}_z(t') \hat{b}^\dagger(t') + \hat{b}(t) \hat{S}_z(t') \hat{b}^\dagger(t') \right\}. \end{aligned} \quad (12.14)$$

Then applying Eq. (12.1) yields

$$\begin{aligned} (\dot{\hat{S}}_-)_{\text{ff}} &= \frac{2g}{\sqrt{\kappa}} b \hat{S}_z - \frac{4g^2}{\kappa} \left\{ (N+1) \hat{S}_- + M \hat{S}_+ \right\} \\ (\dot{\hat{S}}_z)_{\text{ff}} &= -\frac{4g}{\sqrt{\kappa}} \left( \hat{S}_- b^\dagger + b \hat{S}_+ \right) - \frac{16g^2}{\kappa} (N+1) \hat{S}_z, \end{aligned} \quad (12.15)$$

where we note that contributions by  $\delta$  functions evaluated at the lower integral limit are reduced by a factor of 2.

Hence by Eq. (12.7), combining Eqs. (12.12b) and (12.15), we arrive at

$$\dot{\hat{S}}_- = \frac{\gamma_p}{2} \hat{S}_- \hat{S}_z + \lambda b \hat{S}_z - \gamma_p \left\{ (N+1) \hat{S}_- + M \hat{S}_+ \right\}. \quad (12.16)$$

The two transverse spin components are given in terms of  $\hat{S}_-$  by  $\hat{S}_x = \hat{S}_- + \hat{S}_+$  and  $\hat{S}_y = i(\hat{S}_- - \hat{S}_+)$ . We thus obtain the operator equations of motion for the three spin components,

$$\begin{aligned} \dot{\hat{S}}_x &= \frac{\gamma_p}{2} \left( \hat{S}_- \hat{S}_z + \hat{S}_z \hat{S}_+ \right) + \lambda \left( \hat{b} + \hat{b}^\dagger \right) \hat{S}_z - \gamma_p \{N + M + 1\} S_x, \\ \dot{\hat{S}}_y &= i \frac{\gamma_p}{2} \left( \hat{S}_- \hat{S}_z - \hat{S}_z \hat{S}_+ \right) + i \lambda \left( \hat{b} - \hat{b}^\dagger \right) \hat{S}_z - \gamma_p \{N - M + 1\} S_y, \\ \dot{\hat{S}}_z &= -2\gamma_p \hat{S}_- \hat{S}_+ - 2\lambda \left( \hat{S}_- b^\dagger + b \hat{S}_+ \right) - 2\gamma_p (N+1) \hat{S}_z. \end{aligned} \quad (12.17)$$

The first term in all three equations is due to the radiation reaction terms and is independent of the properties of the incident noise. The remaining terms are due to the field fluctuations and depend explicitly on the input field properties.

## 12.2 Results

In the foregoing section we derived operator equations of motion for the quadratures of an oscillator and the components of a collective spin. Here we will show how these lead to equations of motion for mean values and variances and we will compare and discuss different limits of the theory.

### 12.2.1 Mean values and decay rates

The mean value equations discussed in this section yield the effective decay rates of the oscillator quadratures and of the spin components. From

Eq. (12.17) we find, for the three spin components,

$$\begin{aligned}\langle \dot{\hat{S}}_x \rangle &= \frac{\gamma_p}{2} \langle \hat{S}_- \hat{S}_z + \hat{S}_z \hat{S}_+ \rangle - \gamma_p (N + M + 1) \langle S_x \rangle \\ \langle \dot{\hat{S}}_y \rangle &= i \frac{\gamma_p}{2} \langle \hat{S}_- \hat{S}_z - \hat{S}_z \hat{S}_+ \rangle - \gamma_p (N - M + 1) \langle S_y \rangle \\ \langle \dot{\hat{S}}_z \rangle &= -2\gamma_p \langle \hat{S}_- \hat{S}_+ \rangle - 2\gamma_p (N + 1) \langle \hat{S}_z \rangle.\end{aligned}\quad (12.18)$$

For a single spin,  $\hat{\sigma}_- \hat{\sigma}_z = \hat{\sigma}_-$ ,  $\hat{\sigma}_z \hat{\sigma}_+ = \hat{\sigma}_+$ , and  $\hat{\sigma}_- \hat{\sigma}_+ = (\mathbb{I} - \hat{\sigma}_z)/2$  and Eq. (12.18) reduces to the equations for the relaxation of a spin-1/2 particle in a squeezed reservoir derived by Gardiner [124],

$$\begin{aligned}\langle \dot{\sigma}_x \rangle &= -\gamma_p \left( N + M + \frac{1}{2} \right) \langle \hat{\sigma}_x \rangle \\ \langle \dot{\sigma}_y \rangle &= -\gamma_p \left( N - M + \frac{1}{2} \right) \langle \hat{\sigma}_x \rangle \\ \langle \dot{\sigma}_z \rangle &= -\gamma_p (2N + 1) \langle \hat{\sigma}_z \rangle - \gamma_p.\end{aligned}\quad (12.19)$$

The relaxation rate of the spin is reduced along the squeezed axis ( $y$ ), while it is increased in the anti-squeezed direction ( $x$ ).

In the case of an oscillator, we have, by Eqs. (12.1) and (12.11),

$$\begin{aligned}\langle \dot{\hat{X}} \rangle &= -\frac{\gamma_p}{2} \langle \hat{X} \rangle \\ \langle \dot{\hat{Y}} \rangle &= -\frac{\gamma_p}{2} \langle \hat{Y} \rangle.\end{aligned}\quad (12.20)$$

The oscillator damping rates are independent of  $N$  and  $M$  and hence do not depend on the statistics of the input field.

To see how, for a collection of spins where the HPA is valid, the relaxation of the spin degrees of freedom is in agreement with the oscillator damping, we consider the limit of very many spins  $n \gg N, M \simeq O(1)$  in Eq. (12.18). Close to the south pole of the Bloch sphere,  $\hat{S}_z \simeq -n$  and we indeed obtain

$$\begin{aligned}\langle \dot{\hat{S}}_x \rangle &\simeq -\frac{n\gamma_p}{2} \langle S_x \rangle \\ \langle \dot{\hat{S}}_y \rangle &\simeq -\frac{n\gamma_p}{2} \langle S_y \rangle,\end{aligned}\quad (12.21)$$

equivalent to the mean value equations for oscillator quadratures (12.20) with  $\gamma_p \rightarrow n\gamma_p$ .

To illustrate the transition from the single spin results to the oscillator behavior close to the poles of the Bloch sphere, we consider a spin coherent

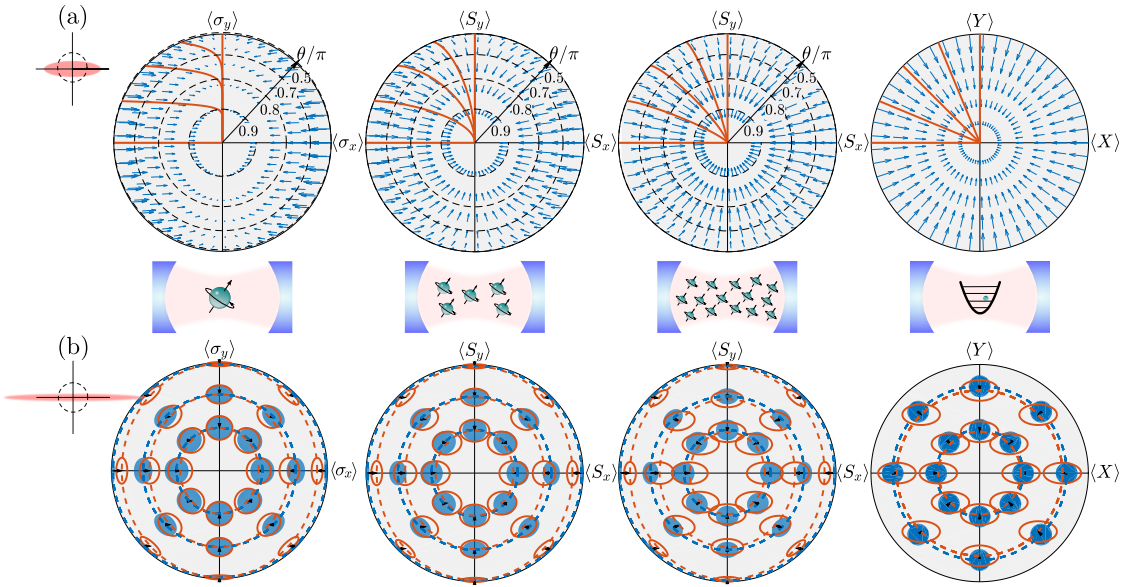


Figure 12.3: The first three panels in (a) and (b) illustrate the decay of a system with one, five and fifteen spins, respectively, in a squeezed bath with (a)  $N = 0.5$  and (b)  $N = 5$ . The plots show the lower half of the Bloch sphere projected on a plane with values of the polar angle marked by the dashed circles in (a). (a) Blue arrows indicate the magnitude and direction of the decay of a spin coherent state at each point with the red lines in the second quadrants showing how the collective spin decay progresses from different initial states. The right panel shows a similar plot for the quadrature plane of an oscillator, where the decay is symmetric. (b) Closed blue circles depict spin coherent states represented by their center coordinates  $(\langle \hat{S}_x \rangle, \langle \hat{S}_y \rangle)$  and error ellipses (see the main text). States are shown for different  $\phi$  and  $\theta = 0.55, 0.75, 0.87\pi$ . For plotting purposes, the error ellipses are scaled by factors 0.12 for  $n = 1$  spin, 0.25 for  $n = 5$  spins, and 0.4 for  $n = 15$  spins. The mean values and covariance matrix elements are evolved for a short time  $\Delta t = 0.008n\gamma_p^{-1}$  according to Eqs. (12.18) and (12.28). The dashed, blue circle (red ellipse) connects the mean values and the solid blue circles (open red ellipses) show the covariances of the states before (after) the short time evolution. The right panel shows a similar plot for the oscillator in an initial coherent state evolved for at time  $\Delta T = 0.1\gamma_p^{-1}$  by Eqs. (12.20) and (12.27).

state. Here all the spins point in the same direction determined by polar angles  $(\theta, \phi)$  on the sphere in Fig. 12.2 such that  $\langle \hat{S}_x \rangle = n \sin \theta \cos \phi$ ,  $\langle \hat{S}_y \rangle = n \sin \theta \sin \phi$ , and  $\langle \hat{S}_z \rangle = n \cos \theta$  with  $0 \leq \theta \leq \pi$  and  $0 \leq \phi \leq 2\pi$  [300],

$$|\theta, \phi\rangle = \bigotimes_{j=1}^n \left( \cos \frac{\theta}{2} |\uparrow\rangle_j + \sin \frac{\theta}{2} e^{i\phi} |\downarrow\rangle_j \right). \quad (12.22)$$

In such a state, the expectation values in Eq. (12.18) may readily be calculated, and the effective decay rates of the mean values of the total spin components at each point on the Bloch sphere are determined from our theory. It yields the evolution

$$\begin{aligned} \langle \theta, \phi | \dot{\hat{S}}_x | \theta, \phi \rangle &= -\gamma_x(n, \theta) \langle \theta, \phi | \hat{S}_x | \theta, \phi \rangle \\ \langle \theta, \phi | \dot{\hat{S}}_y | \theta, \phi \rangle &= -\gamma_y(n, \theta) \langle \theta, \phi | \hat{S}_y | \theta, \phi \rangle, \end{aligned} \quad (12.23)$$

where the  $n$  and  $\theta$ -dependent decay rates are

$$\begin{aligned} \gamma_x(n, \theta) &= \gamma_p \left\{ N + M + \frac{1}{2} - \frac{(n-1) \cos \theta}{2} \right\} \\ \gamma_y(n, \theta) &= \gamma_p \left\{ N - M + \frac{1}{2} - \frac{(n-1) \cos \theta}{2} \right\}. \end{aligned} \quad (12.24)$$

In the first three panels of Fig. 12.3(a), we show the Bloch sphere from below. The dashed circles mark different degrees of excitation, quantified by the polar angle  $\theta$ . The arrows indicates the magnitude and direction of the decay of the spin coherent state at each point, and the red lines in the second quadrants guide the eye along the spin decay. Results are shown for a single spin, five spins and fifteen spins, respectively, and for a moderate degree of squeezing ( $N = 0.2$ ). In the last panel, we show the quadrature plane of an oscillator degree of freedom. Here the arrows and solid lines show the decay of the mean quadratures given by Eq. (12.20). As predicted, a single spin exhibits a highly asymmetric decay where it quickly relaxes to  $\langle \hat{\sigma}_y \rangle \simeq 0$ , while the  $\langle \hat{\sigma}_x \rangle$  component decays on a much longer time scale. The oscillator, on the other hand, shows a completely symmetric decay in the two quadratures. As the number of spins increases, we see the expected transition between these two extremes, verifying, in this sense, the Holstein-Primakoff approximation.

We show in Fig. 12.4(a) the relaxation rates of the transverse spin components  $\gamma_x(n, \theta)$  and  $\gamma_y(n, \theta)$  as functions of  $n$  for different values of  $\theta$ . The results are shown for  $N = 0.05$ . As emphasized in Fig. 12.3, a single

spin has highly asymmetric rates but as the number of spins increases, the rates become similar and independent of  $N$  and  $M$ . Furthermore, the rates approach those of equivalent oscillator quadratures in the cases where the excitation is very low ( $\theta \simeq \pi$ ).

We can understand the fundamental difference between the single spin and the oscillator cases in terms of contributions to the decay rates from self-reaction and field fluctuations in Eq. (12.7). For both a weakly excited collective spin and an oscillator, self-reaction processes yield equivalent contributions,  $\gamma_p/2$  for the oscillator and  $n\gamma_p/2$  for the spins. Field fluctuations, on the other hand, do not contribute to the oscillator rate, whereas for the spins they cause spontaneous emission that in a squeezed reservoir is adjusted according to the squeezing parameters. The spin decay by self-reaction is, however, collectively enhanced by the number of spins  $n$  such that this contribution dominates the field fluctuations and the Holstein-Primakoff approximation becomes valid when many spins are present.

### 12.2.2 Second moments and Langevin noise

In the preceding section we showed that while the statistics of a squeezed reservoir directly influence the decay of a single spin, this effect gradually disappears as more spins are added to the cavity. With many weakly excited spins, the decay resembles that of an oscillator and the mean relaxation is independent of the field statistics. As shown in Eq. (12.11), however, the input field does enter in the equations of motion for the oscillator quadratures as Langevin noise terms. Hence, where a squeezed bath influences the decay rates of a single spin, it will influence the noise properties of an oscillator degree of freedom.

In this section, we probe these expectations by deriving and investigating equations of motion for the covariance matrix elements of the transverse spin components and study the limits of a single spin and of an oscillator in the case of low excitation. The non-linearity of a spin system induces non-zero higher moments and we do not expect the covariance matrix to fully characterize the evolution of collective spin states. Nevertheless, we take the (co)variances as indicators for the dynamical evolution of their dominating fluctuations.

The symmetrized covariance between two (noncommuting) observables  $A$  and  $B$  is defined as

$$C_{AB} \equiv \frac{1}{2} \langle \hat{A}\hat{B} + \hat{B}\hat{A} \rangle - \langle \hat{A} \rangle \langle \hat{B} \rangle. \quad (12.25)$$

If  $\hat{A} = \hat{B}$ , this is the variance,  $V_A \equiv C_{AA}$ .

The evolution of the (co)variances of the spin components and of the oscillator quadratures can be derived from the equations of motion of the observables in Sec. (12.1). Since the input field (12.1) is  $\delta$  correlated, when taking the time derivative of products of observables, we must employ Itô's formula [139] to obtain

$$\dot{(\hat{A}\hat{B})} = \dot{\hat{A}}\hat{B} + \hat{A}\dot{\hat{B}} + \dot{\hat{A}}\dot{\hat{B}}. \quad (12.26)$$

With this convention, the evolution of the oscillator quadrature covariance matrix follows from the equations of motion (12.11),

$$\begin{aligned} \dot{V}_X &= -\gamma_p \{V_X - (2N + 2M + 1)\} \\ \dot{V}_Y &= -\gamma_p \{V_Y - (2N - 2M + 1)\} \\ \dot{C}_{XY} &= -\gamma_p C_{XY}, \end{aligned} \quad (12.27)$$

where we applied Eq. (12.1). These expressions clearly show how the oscillator equilibrates with the squeezed input field to a steady state with  $V_X = 2N + 2M + 1$  and  $V_Y = 2N - 2M + 1$ . Notice that for a coherent state the  $+1$  terms in Eqs. (12.27) ensure that when  $N = M = 0$ , the variances do not change from  $V_X = V_Y = 1$ .

We may similarly derive equations of motion for the covariance matrix elements of the  $x$  and  $y$  components of a collective spin. From Eq. (12.17) we find after applying commutator relations,

$$\begin{aligned} \dot{V}_{S_x} &= -\gamma_p \left\{ (2N + 2M + 1) \left( V_{S_x} - \langle \hat{S}_z^2 \rangle \right) + \langle \hat{S}_z \rangle - C_{S_x, S_x \rightleftharpoons S_z} \right\}, \\ \dot{V}_{S_y} &= -\gamma_p \left\{ (2N - 2M + 1) \left( V_{S_y} - \langle \hat{S}_z^2 \rangle \right) + \langle \hat{S}_z \rangle - C_{S_y, S_y \rightleftharpoons S_z} \right\}, \\ \dot{C}_{S_x, S_y} &= -\gamma_p \left\{ (2N + 1) C_{S_x, S_y} - \frac{1}{2} (C_{S_x, S_y \rightleftharpoons S_z} + C_{S_y, S_x \rightleftharpoons S_z}) \right\}, \end{aligned} \quad (12.28)$$

where  $C_{A, B \rightleftharpoons C} \equiv \frac{1}{2} \left( \langle \hat{A}(\hat{B}\hat{C}) + (\hat{C}\hat{B})\hat{A} \rangle - \langle \hat{A} \rangle \langle \hat{B}\hat{C} + \hat{C}\hat{B} \rangle \right)$ . Note that the evolution in general depends on higher moments of the spin observables, signifying how the inherent non-linearity of spin systems does not preserve Gaussianity.

For a single spin,  $\hat{\sigma}_i \hat{\sigma}_j = i \epsilon_{ijk} \hat{\sigma}_k$ , where  $\epsilon_{ijk}$  is the Levi-Civita symbol and  $i, j, k \in \{x, y, z\}$ , implying that all higher moments are determined by the first moments. In particular,  $V_{\hat{\sigma}_x} = 1 - \langle \hat{\sigma}_x \rangle^2$  and  $V_{\hat{\sigma}_y} = 1 - \langle \hat{\sigma}_y \rangle^2$ , such that, since by Eq. (12.19) the transverse spin components relax to

zero in the steady state, their variances equilibrate to unity, independent of the squeezed environment. As discussed above, this is opposite to an oscillator degree of freedom.

To investigate how this discrepancy is bridged in the limit of many spins  $n \gg N, M$ , we consider a spin coherent state for which we note that, e.g.,  $V_{S_x}$  is proportional to  $n$ , while  $\langle \hat{S}_z^2 \rangle$  and  $C_{S_x, S_x=S_z}$  are proportional to  $n^2$ . Hence, to leading order in  $n$  we find

$$\begin{aligned} \dot{V}_{S_x} &= \gamma_p \left\{ (2N + 2M + 1) \langle \hat{S}_z^2 \rangle + C_{S_x, S_x=S_z} \right\} \\ \dot{V}_{S_y} &= \gamma_p \left\{ (2N - 2M + 1) \langle \hat{S}_z^2 \rangle + C_{S_y, S_y=S_z} \right\} \\ \dot{C}_{S_x, S_y} &\underset{n \gg 1}{=} \frac{\gamma_p}{2} (C_{S_x, S_y=S_z} + C_{S_y, S_x=S_z}). \end{aligned} \quad (12.29)$$

Close to the south pole ( $\hat{S}_z \simeq -n$ ), where we expect the HPA to be valid, the equations simplify further,

$$\begin{aligned} \dot{V}_{S_x} &= -n\gamma_p \{V_{S_x} - n(2N + 2M + 1)\}, \\ \dot{V}_{S_y} &= -n\gamma_p \{V_{S_y} - n(2N - 2M + 1)\}, \\ \dot{C}_{S_x, S_y} &\underset{\theta \simeq \pi}{=} -n\gamma_p C_{S_x, S_y}. \end{aligned} \quad (12.30)$$

That is, in these limits the noise properties of the collective spin comply with the oscillator results given in Eq. (12.27).

The transition from the single spin to an ensemble of many weakly excited spins, is illustrated in Fig. 12.3(b). Here we represent spin coherent states (12.22) as blue ellipses centered at  $(\langle \hat{S}_x \rangle, \langle \hat{S}_y \rangle)$  with radii along the major and minor axes given by  $(\sqrt{V_{S_a}}, \sqrt{V_{S_b}})$ , where  $V_{S_a}$  and  $V_{S_b}$  are the eigenvalues of the covariance matrix. Upon time evolving the mean values and the (co)variances for a short time  $\Delta t \ll \gamma_p^{-1}$  by the expressions given in Eqs. (12.18) and (12.28), the states transform into those shown as open, red ellipses. The rightmost panel shows a similar plot for an oscillator prepared in a coherent state and evolved under Eqs. (12.20) and (12.27). Dashed lines connecting the  $(\langle \hat{S}_x \rangle, \langle \hat{S}_y \rangle)$  values before and after the time evolution, respectively, show how the states move from a circular to an elliptic configuration, emphasizing the asymmetric rates of the decay. The uncertainty of a single spin evolves symmetrically in the two transverse spin components while that of an oscillator is squeezed according to the input field. As more spins are added, we see a clear transition between these two limiting cases. The resemblance of the large spin ensemble to the oscillator is more pronounced closer to the center corresponding to low

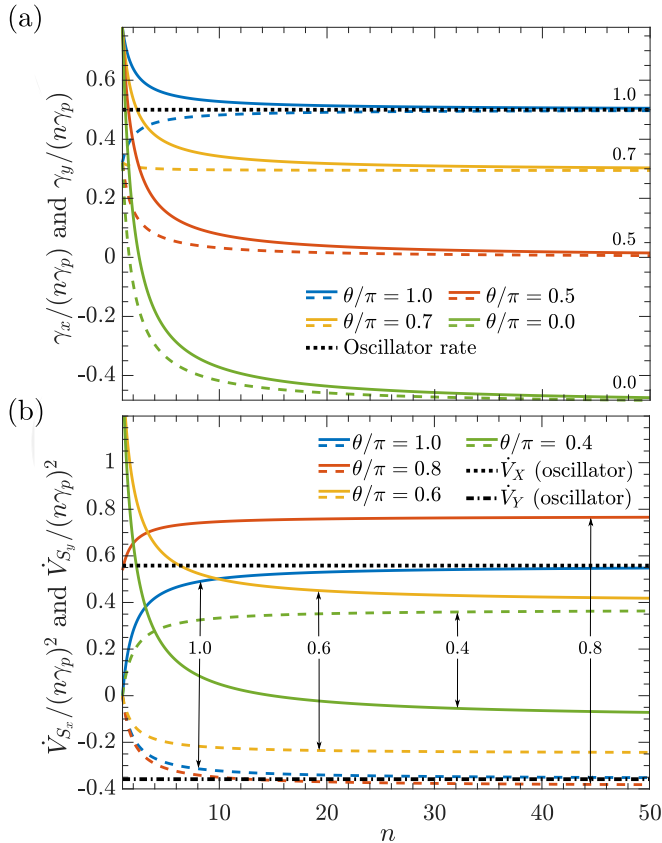


Figure 12.4: (a) Decay rates Eq. (12.24) of the  $S_x$  (solid lines) and  $S_y$  components (dashed lines) of a spin coherent state in a squeezed reservoir with  $N = 0.05$  shown as a function of the the number of spins  $n$  and for different mean excitations quantified by the Bloch angle  $\theta$  (values of  $\theta/\pi$  are assigned at the right-hand side of the figure). The dotted line shows the symmetric and squeezing independent decay rate  $\gamma_p/2$  of either quadrature of an oscillator. (b) Time derivatives Eqs. (12.28) of variances of the  $S_x$  (solid lines) and  $S_y$  (dashed lines) components of a spin coherent state in a squeezed reservoir with  $N = 0.05$  shown as a function of the the number of spins  $n$  and for different  $\theta$  with  $\phi = 0$  (values of  $\theta/\pi$  are assigned by the vertical arrows). The dotted and dash-dotted lines show the time derivatives of oscillator quadrature variances in similar settings, [Eqs. (12.27)].

excitation ( $\cos \theta \simeq -1$ ). These results are further quantified in Fig. 12.4(b), where we compare the time derivatives Eqs. (12.28) of the variances of the two transverse spin components as a function of the number of spins and for different mean excitations  $\theta$  to those of oscillator quadratures (12.27).

We note, finally, that our results confirm the findings of Ref. [301] which derives how the squeezing properties of an incoming field can be transferred to a spin ensemble and how this effect increases with the ensemble cooperativity (here equivalent to the number of spins). Reference [301] relies on a linearized model valid only for weak squeezing and considers the steady-state properties of the ensemble, whereas our treatment includes an analysis of the transient behavior and is valid for any amount of squeezing.

### 12.3 Discussion

In this chapter we have derived equations of motion for the first and second moments of the collective components of a spin ensemble coupled to a broadband squeezed radiation environment. We showed how the effect of the squeezing on the spin dynamics is transferred from the mean values of the components to their fluctuations as more spins are added to the ensemble. The results thereby link the limiting cases of a single spin, considered by Gardiner [124], and of a large ensemble described well in the Holstein-Primakoff approximation [123].

While we formulated our derivations in the Heisenberg picture, the model described in Sec. 12.1 can equivalently be treated in the Schrödinger picture by a master equation of the form (2.9) [278],

$$\dot{\rho} = \frac{\gamma_p}{2} \left\{ (N+1) \mathcal{D}[\hat{a}^\dagger, \hat{a}] + N \mathcal{D}[\hat{d}, \hat{d}^\dagger] - M \mathcal{D}[\hat{a}^\dagger, \hat{d}^\dagger] - M^* \mathcal{D}[\hat{d}, \hat{a}] \right\} \rho. \quad (12.31)$$

In the case of a single spin ( $\hat{d} = \hat{\sigma}_-$ ), the master equation yields  $(N, M)$ -dependent decay rates of the spin components as given in Eq. (12.19). From the structure of Eq. (12.31) it is not apparent that this dependence is lifted once more spins are added. Explicit calculations, properly taking commutator relations into account, show, however, that the master equation reproduces our results (12.18) for the mean components of a collective spin ( $\hat{d} = \hat{S}_-$ ), and that in the limit of many weakly excited spins ( $\hat{d} = \hat{a}$ ) the squeezing dependent damping terms cancel to realize Eq. (12.20). While the master equation formalism is useful for numerical calculations, it does not offer much insight into the physical mechanisms behind this

transition. Our formalism emphasizes how it occurs as collective radiation reaction processes dominate vacuum fluctuations in the coupling of a large spin system to a squeezed reservoir. Furthermore, the Heisenberg picture treatment allows us to consider second moments for which equations of motion are not easily derived from a master equation. The results obtained here suggest that the results and interpretations of fluorescence spectra and correlation functions of a spin system in a squeezed bath obtained by a master equation treatment in earlier studies should be revisited [302–304].

Ensembles of few and many effective spins have been the topic of numerous experimental studies and proposals. To mention a few, their implementations range from storage facilities for microwave excitations [305–307] and optical memories [308–310] to quantum information resources [311, 312], gain media in lasers and masers [313, 314], and to highly sensitive probes [8, 266, 313, 315]. In many of such applications and with the growing ability to engineer squeezing devices in the optical and microwave regimes [258–261], the employment of squeezed fields has the potential to enhance readout and performance. For instance, the signal-to-noise ratio in qubit readout can be exponentially increased by utilizing single-mode squeezing [271]. We believe that our simple model and main results, Eqs. (12.18) and (12.28), will be useful in the devising and evaluation of such protocols. As one example, our results quantify the circumstances under which squeezing of collective spin degrees of freedom [316] can be achieved by coupling to a squeezed radiation environment, [cf. Eq. (12.28) and Fig. 12.3(b)].

There is currently a high interest in superradiance effects and their possible applications [317–320]. Superradiance is associated with the enhanced collective radiative rates attained when a significant fraction of the emitters are excited [321]. This is outside the applicability of the Holstein-Primakoff oscillator approximation but tractable by our analysis.

Besides the insights into the interplay between damping and coherent dynamics in various applications, our study emphasizes a fundamental difference of the role of field fluctuation and radiation reaction between quantum systems with infinite (the oscillator) and low dimensional (single spin-1/2) Hilbert spaces. This difference becomes evident in the interaction with a squeezed environment, and observing the transition between these two extremes as more spins are put into resonance with a cavity may pose an interesting topic for experimental investigation in its own right.

# Conclusion and future directions

*“Now this is not the end. It is not even the beginning of the end. But it is, perhaps, the end of the beginning.”*

— Winston Churchill

Quantum mechanics promises intriguing new possibilities for the design of sensor devices with yet unseen precision and sensitivity, and with the rapid advancement of experimental and technological capabilities, the theoretical proposals and ideas in the field of quantum metrology are now more relevant than ever. Accordingly, it stands to reason that the high precision sensors and probes of tomorrow will employ and benefit from quantum effects.

During my PhD study, I have touched upon different aspects of quantum metrology with a special focus on the role of continuous quantum measurements, and this thesis presented the results of my research. I shall now conclude by summarising the main results, and, in the recognition that my inquiries as well as any research represent a beginning and not an end to questions worth asking, I would like to confabulate on a few future directions, inspired by the different projects.

Chapters 3, 4 and 5 investigated the implications of continuously monitoring or frequently measuring a quantum system with the purpose of estimating an unknown parameter (dynamically) encoded in its state. Our theory for the classical Fisher information reveals that, in general, efficient parameter inference from a system, which is interrogated for a

duration rather than just once, requires a full statistical analysis, offered by the Bayesian method. While the general results apply in a wide range of settings, the examples aimed to highlight generic features by focusing on small quantum systems. It would be interesting to adopt and apply the formalism to more complex and larger systems with a richer dynamics. Such studies could further reveal the role of many-body effects like phase transitions in quantum metrology [155, 322], and could, for instance, be accomplished in the matrix-product-state formalism [323] for which efficient methods for simulating continuous measurements exist [324].

We explained how the advantages of a full Bayesian analysis in the case of an interrogated quantum probe may be attributed to the role played by measurement backaction which quenches the state and thereby induces multi-time correlations in the signal recording with a strong dependence on the parameter in question. While the backaction is beneficial for a quantum probe whose fluorescence is monitored by photon counting or homodyne detection, the quantum Zeno effect becomes detrimental to the precision when a system is probed too strongly or too frequently. The difference between these two situations is that the fluorescence signal is the result of an intrinsic decoherence channel in the system, which left unmonitored would anyway be destructive to its sensing capabilities. Deliberate probing of an otherwise closed system, on the other hand, introduces on average an otherwise non-existing dephasing of the system state.

In either case, it is an attractive goal to harvest the benefits from continuous or frequent measurements while omitting the backaction. In Chapter 6 we showed how this is possible by employing a measurement controlled feedback, designed to exactly cancel the backaction while still obtaining a measurement record, thus allowing a topological transition in the system to be observed. There is one problem in applying the same procedure to parameter estimation scenarios: The correcting feedback depends explicitly on the state of the system prior to the measurement and this state depends on the exact value of the *unknown* parameter. In a preliminary study, I tried an adaptive strategy with a feedback designed at each instant according to the most likely parameter value as given by Bayes rule. The results suggest that such an approach is not able to provide a metrological advantage. One reason for this may be that the protocol is merely feeding information, which has already been extracted on the parameter, back into the system. Still, the idea of a continuous measurement controlled feedback for parameter estimation deserves further investigations, and it has indeed proven successful in a number of cases. For instance, the backaction of photon detection can be beneficially reversed if

the probe system is entangled with a second, perfect system which can be used to control the feedback [86].

There is also the possibility of designing a feedback with a more clever purpose than just cancelling backaction. One option is an adaptive scheme which, following a measurement or detection, rotates the system to the state most sensitive (as quantified by the Fisher information) to the unknown parameter around the, at that point in time, most likely value. Such a scheme has been proposed for phase measurements of optical modes [255] and it would be interesting to investigate if similar benefits can be identified in other settings. For example, in photon counting two ideas are to follow each detection by a rotation to the state which (a) is most sensitive to the unknown parameter or (b) would be most likely to rapidly emit the next photon. Interestingly, my initial calculations show that both strategies yield exactly the same Fisher information per time for estimating the Rabi frequency in the Hamiltonian (2.6). The reason is that (a) generates a higher information per photon but on average fewer photons in a given time and vice versa for (b).

Another option is to update auxiliary Hamiltonian parameters according to measurement outcomes; e.g., in order to adaptively bring a system close to criticality where it exhibits ultra-enhanced sensitivity to an unknown parameter [173]. This is also the intuitive behind the proposal presented in Chapter 7 where the idea is to exploit the sharp dip in the fluorescence spectrum around a dark resonance in a quantum system. We showed how an adaptive strategy, which randomly shifts the frequency of a probe laser every time a fluorescence photon is detected, produces a Lévy flight of that frequency. As a consequence, the frequency is exceedingly likely to be locked to the dark resonance in the spectrum, for the location of which it hence constitutes a very precise estimator. Despite an enhanced front factor in the scaling of the estimation sensitivity with the duration of the experiment  $T$  compared to conventional schemes, our example of a doubly-driven three-level system is still restricted to a  $1/\sqrt{T}$  functional dependency. However, this is not an intrinsic feature of our proposal but rather a consequence of the quadratic vanishing of the fluorescence signal around the dark resonance. One can easily imagine systems with a different spectral profile, allowing a better scaling,  $1/T^x$  with  $x > 1/2$ , and due to the non-ergodic dynamics there is non impediment against values of  $x > 1$  (super-Heisenberg scaling). As such, our proposal begs for further investigations and applications in different settings such as quantum many-body systems with non-trivial criticalities and spectral gaps; e.g., the Dirac cone in the electronic band structures of graphene

and topological insulators [325].

Chapters 8 and 9 change the focus from parameter estimation to hypothesis testing where the purpose is to discriminate a discrete set of possible Hamiltonians. A bound to our ability to perform this task by a hypothetical measurement on an open system and its environment was derived. The derivation is constructive in the sense that it explicitly evaluates (numerically) the positive-operator valued measure, needed to saturate the bound. Still, it is an open question how one can, in general, optimally approximate this highly non-local measurement in an experiment. While we approach this problem in Chapter 9 by considering continuous fluorescence detection combined with a final read-out of the state of the probe system, it would be a captivating and very relevant goal for future research to extend the intuition behind these examples to the formulation of a more general theory.

Where the first chapters of this thesis were concerned with efficient read-out of a parameter encoded in a quantum system, the proposed thermometer design in Chapter 10 takes a different angle on quantum metrology. It rather seeks and succeeds to reinforce the encoding of an unknown temperature in a quantum probe system, assuming that a perfect read-out measurement is available. In that specific example, the encoding is promoted by letting the sensor system, directly interacting with the thermal reservoir of interest, coherently transduce information to a second meter system, used in the read-out process. On a more general note, the idea of advantageously intervening with the way an unknown parameter is written to the state of a quantum systems holds interesting prospects which has this far not been devoted a proper attention in the quantum metrology community. True, results exist which show that it is not possible to improve the quantum Fisher information for estimating a parameter  $\theta$ , encoded by a unitary interaction  $U = e^{-i\hat{H}\theta}$  by the addition of a second control Hamiltonian, not depending on  $\theta$  [326]. Be that as it may, our thermometer shows that this is not the end of such inquiries. That device exhibits increased sensitivity to a parameter (temperature) which is encoded by an incoherent interaction with an environment, and this is achieved by the addition of a proper Hamiltonian interaction. A future study should seek to derive results which highlight in which settings and how it is possible to obtain a similar advantage in a more general framework of a parameter encoded by an incoherent interaction; e.g., via a Liouvillian superoperator of the form (2.10). Section 10.3 takes the first steps in this direction by seeking an understanding of the increased sensitivity from the

spectrum of the encoding Liouvillian.

The last two chapters 11 and 12 investigated implications and advantages of squeezing the uncertainty in the field used to probe a quantum system. The experiment and theory reported in Chapter 11 proves that it is possible to enhance the sensitivity in magnetic resonance detection by squeezing the uncertainty in the environment of a spin ensemble. At the same time, the theoretical study of that experiment sparked the investigation in Chapter 12 on the influence exercised by a squeezed environment on the dynamics of an ensemble of emitters with a focus on the very different reactions of a small and of a large ensemble. From a fundamental point of view, it would be rewarding to conduct an experiment with the purpose of probing the theoretical predictions of that theory.

The studies on continuous measurements in Chapters 3-7 and 9, seek to perform optimal data treatment and optimal measurement strategies, while accepting the limit imposed by quantum vacuum fluctuations in the signal. In light of the two final Chapters 11 and 12, a quest for further improvements by squeezing these uncertainties is a worthy undertaking. I have performed a preliminary study where the radiative environment in a homodyne detection setup (see Chapter 4), which aims to estimate a Rabi frequency in a two-level system (2.6), is squeezed. Unfortunately, the results suggest that squeezing actually diminishes the estimation precision! This can be understood since squeezing the relevant quadrature of the field effectively amounts to a stronger measurement, introducing a more pronounced Zeno effect of the measurement as studied in Chapter 5. Evidently, the decreased noise in the signal does not make up for the backaction dominated dynamics of the system as the squeezing is increased. A calculation of the associated quantum Fisher information shows, in fact, that it should be possible to increase the precision by instead anti-squeezing the quadrature holding the signal! The usage of squeezing in continuous measurements, taking into account the backaction in a Bayesian formulation, is thus clearly a topic which deserves further studies and may lead to valuable results.

With these final remarks, I conclude my PhD thesis in the opinion, hopefully shared by the reader, that the research presented here tackles some interesting and relevant problems in quantum metrology. I trust that my results and ideas may serve as an inspiration and a beginning to fantastic research directions in future projects.

# Supplemental material for Chapter 6

*This appendix pertains to the study presented in Chapter 6 and is reproduced from the supplemental material of Ref. [6].*

---

## A.1 Feedback master equation and optimal parameters

To describe the evolution of the density matrix of the system subject to measurement and feedback, we must apply Itô-calculus to treat the noise component of  $V(t)$  in the feedback  $\hat{H}_V$  as it is correlated with the noise in the SME (10) of the main text and yields a  $dW_t^2 = dt$  first order contribution in  $dt$ . Assuming no delay in the feedback channel and perfect detection ( $\eta = 1$ ), the stochastic master equation for a monitored system subject to continuous feedback has been derived by Wiseman and Milburn [134],

$$\begin{aligned}
 d\rho = & -i[\hat{H}(t), \rho]dt - i[\hat{H}_D(t), \rho]dt - i[\tilde{H}_V(t), \hat{\sigma}_y\rho + \rho\hat{\sigma}_y]dt \\
 & + \kappa\mathcal{D}[\hat{\sigma}_y]\rho dt + (\kappa\eta)^{-1}\mathcal{D}[\tilde{H}_V(t)]\rho dt \\
 & + \sqrt{\eta\kappa}\mathcal{H}[\hat{\sigma}_y - i\tilde{H}_V(t)/(\eta\kappa)]\rho dW_t,
 \end{aligned} \tag{A.1}$$

where  $\tilde{H}_V(t) = \hat{H}_V(t)/V(t)$ .

To derive the feedback parameters  $\alpha$ ,  $\beta$ ,  $a$  and  $b$  given in Eqs. (6.15) and (6.17) in Chapter 6, it is convenient to represent the density matrix in terms of the Bloch vector components as in Eq. (6.7). For  $\eta = 1$ , the stochastic feedback master equation Eq. (A.1) is equivalent to a set of stochastic Bloch equations,

$$\begin{aligned} dx &= dx_{\text{unitary}} + dx_{\text{ba}} + dx_{\text{fb}} \\ dy &= dx_{\text{unitary}} + dy_{\text{ba}} + dy_{\text{fb}} \\ dz &= dx_{\text{unitary}} + dy_{\text{ba}} + dy_{\text{fb}}, \end{aligned} \quad (\text{A.2})$$

where the first terms describe unitary evolution governed by the Hamiltonian,

$$\begin{aligned} dx_{\text{ba}} &= -2\kappa x dt - 2\sqrt{\kappa}xy dW_t \\ dy_{\text{ba}} &= 2\sqrt{\kappa}(1 - y^2)dW_t \\ dz_{\text{ba}} &= -2\kappa z dt - 2\sqrt{\kappa}yz dW_t \end{aligned} \quad (\text{A.3})$$

give the measurement backaction in the original stochastic master equation (6.11), and

$$\begin{aligned} dx_{\text{fb}} &= \kappa \left( -by - 2\beta - \frac{\beta^2}{2}x + \frac{\alpha\beta}{2}z \right) dt - \sqrt{\kappa}\beta y dW_t \\ dy_{\text{fb}} &= \kappa \left( -az + bx - \frac{(\alpha^2 + \beta^2)}{2}y \right) dt + \sqrt{\kappa}(\beta x - \alpha z) dW_t \\ dz_{\text{fb}} &= \kappa \left( ay + 2\alpha - \frac{\alpha^2}{2}z + \frac{\alpha\beta}{2}x \right) dt + \sqrt{\kappa}\alpha y dW_t \end{aligned} \quad (\text{A.4})$$

incorporate the extra terms associated with the feedback. The purpose of the feedback is to cancel both the deterministic and the stochastic effects of the probing. This requirement ( $0 = du_{\text{ba}} + du_{\text{fb}}$  for  $u = x, y, z$ ) can be met only for a pure state, obeying  $1 = x^2 + y^2 + z^2$ , and we readily identify how the feedback parameters should depend on the Bloch vector of the current state of the system,

$$\begin{aligned} \alpha &= 2z, \\ \beta &= -2x, \\ a &= -yz, \\ b &= xy. \end{aligned} \quad (\text{A.5})$$

These are the control parameters given in Eqs. (6.15) and (6.15).

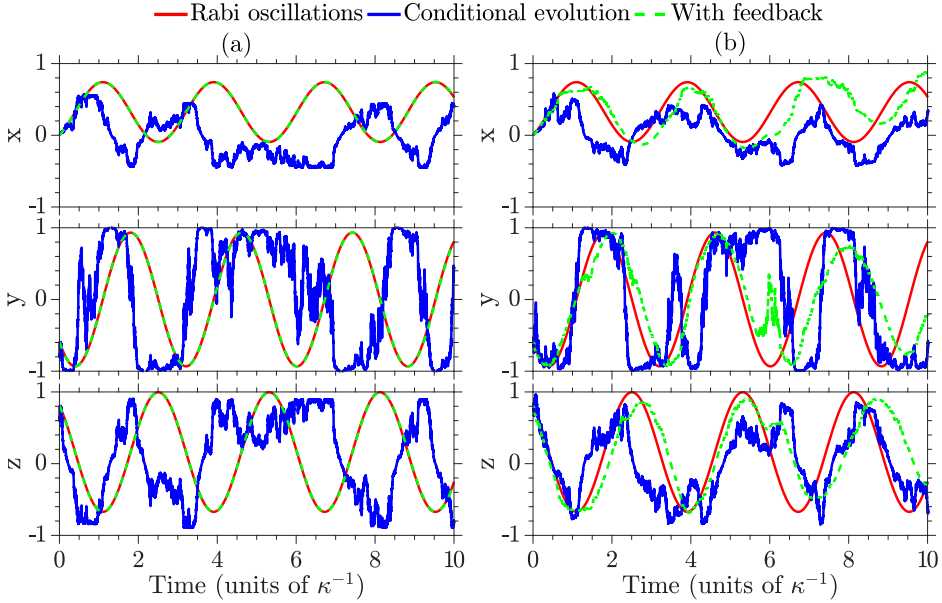


Figure A.1: Dynamical evolution of the three Bloch components of a two-level system subject to coherent Rabi oscillations (red curves). Monitoring of the state by continuous probing of the  $\sigma_y$  observable disturbs the evolution (noisy, green curve), but the system can be stabilized by feedback using the parameters Eq. (A.5) calculated from the expected Bloch components of the unmonitored system (dashed, blue curve). The Rabi frequency is  $\Omega = 2\kappa$  and the laser-atom detuning  $\delta = \kappa$ . For unit detection efficiency ( $\eta = 1$ ) in (a), the feedback completely eliminates the stochastic backaction while with imperfect detection ( $\eta = 0.8$ ) in (b) this is not possible.

To illustrate the accomplishments of the feedback protocol, we show in Fig. A.1 how the procedure can be used to stabilize monitored Rabi oscillations against measurement backaction. For unit detector efficiency in (a), we see perfect restoration of the Rabi oscillations, while a reduced detector efficiency  $\eta = 0.8$  in (b) prevents full recovery of the coherent dynamics.

The average evolution of a system subject to continuous probing and the compensating feedback obeys an *unconditional* master equation,

$$\begin{aligned}
 d\rho = & -i[\hat{H}(t), \rho]dt - i[\hat{H}_D(t), \rho]dt - i[\tilde{H}_V(t), \hat{\sigma}_y\rho + \rho\hat{\sigma}_y]dt \\
 & + \kappa\mathcal{D}[\hat{\sigma}_y]\rho dt + (\kappa\eta)^{-1}\mathcal{D}[\tilde{H}_V(t)]\rho dt.
 \end{aligned}
 \tag{A.6}$$

With the feedback parameters given in Eqs. (A.5) designed according to the Bloch components of the adiabatic eigenstate, the second term vanishes, but due to the slightly imperfect feedback, the latter three terms describe an effective attraction of the quasi-adiabatic state towards the instantaneous adiabatic eigenstate. The resulting modifications to the Chern number estimate from the measurement current are investigated in Chapter 6.

## A.2 Finite detector efficiency and a simple correction

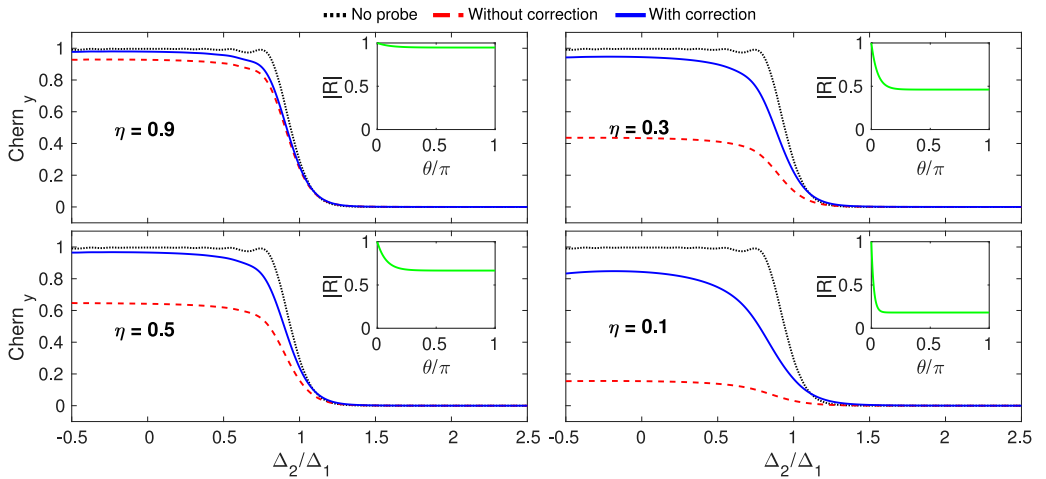


Figure A.2: The mean value of the Chern number for different values of  $\Delta_2/\Delta_1$  and for different values of the detection efficiency  $\eta$ . Curves are shown for the standard expression for the Chern number, Eq. (6.8) of the main text (dashed, red) and for the corrected expression, Eq. (A.7) (full, blue), taking into account the reduced purity of the quantum state when subject to imperfect detection. The black, dotted curve shows, as a reference, the results in the absence of probing. The insets depict the length of the Bloch vector as a function of the sweep parameter  $\theta = vt$ . Results are shown for  $\Omega_1 = \Delta_1/3$  and the optimized parameters (see main text);  $\Delta_1/2\pi = 16.1$  MHz,  $t_q = 0.96$   $\mu$ s and  $\kappa/2\pi = 0.37$  MHz.

As the cancellation of the measurement backaction is crucial to achieve the detection of the Chern number by probing the qubit during a few

quenches, we shall briefly explore the effect of imperfect detection for our protocol. A finite detector efficiency  $\eta$  imparts an effective non-monitored dissipation process with rate  $\kappa(1 - \eta)$ . As shown in Ref. [202], this is accompanied by a shortening of the Bloch vector over the duration of the Hamiltonian sweep and a corresponding reduction of the value of the estimated Chern number from the integral (6.8).

We illustrate this effect in Fig. A.2 for a system subject to our feedback by solving Eq. (A.6) for different values of the detector efficiency. The smaller values of  $\eta$  yield a larger reduction in the measurement results for the Chern number. It is evident that the ability of the feedback to (partially) restore the undisturbed evolution of the qubit is reduced under substantial imperfections in the detection.

The state dependent control parameters of the feedback Eqs. (A.5) were derived to stabilize the instantaneous state assuming perfect detection. In the case of imperfect detection, it must be noted that the same parameters do not maximize the purity and hence the length of the Bloch vector. An optimal scheme in the case of finite efficiency heterodyne detection is derived in the Supplemental Material of Ref. [205], and it stands to reason that a similar approach could be used to optimize the feedback parameters in the present measurement setup.

We choose not to pursue this further at this point. Instead we note that since the main contribution to the reduction in  $C_y$  stems from the shortened  $\sigma_y$  component of the Bloch vector, we may apply a simple post-processing procedure and replace the estimator, Eq. (6.8) of Chapter 6, by

$$C_y = - \int_0^\pi \frac{\Omega_1}{2v} \frac{\langle \hat{\sigma}_y \rangle}{|R(t)|} \sin \theta d\theta, \quad (\text{A.7})$$

where  $|R(t)| = \sqrt{x^2 + y^2 + z^2}$  is found by solving the unconditional master equation (A.6). We find that  $|R(t)|$  is only very weakly dependent on the detuning parameters, and we display in insets of Fig. A.2  $|R(t)|$  as a function of the sweep parameter  $\theta = vt$  for  $\Delta_2 = 2\Delta_1$ . It quickly drops to a constant value which is maintained during the remaining quench sequence. The blue curves in the main plots show how Eq. (A.7) yields fairly good estimates of the Chern number as long as  $\eta \gtrsim 0.3$ . Notice, however, that by Eq. (6.10) of Chapter 6, under finite detection efficiency, the noise is increased by a factor  $1/\sqrt{\eta}$  which must be remedied by a correspondingly larger number of repetitions  $N$ .

# Supplemental material for Chapter 7

*This appendix pertains to the study presented in Chapter 7 and is reproduced from the supplemental material of Ref. [5].*

---

## B.1 Effective emission rate for a laser driven $\Lambda$ -system

The laser driven  $\Lambda$ -system in Fig. 8.1 of Chapter 7 is described by the Hamiltonian

$$\hat{H} = \delta |0\rangle \langle 0| + \frac{\Omega}{2} (|2\rangle \langle 0| + |0\rangle \langle 2|) + \frac{\Omega}{2} (|2\rangle \langle 1| + |1\rangle \langle 2|), \quad (\text{B.1})$$

with laser atom detuning  $\delta$  and Rabi frequency  $\Omega$ .

The evolution of the density matrix  $\rho$  of the unobserved system is given by the master equation (2.9). Here the excited state spontaneous decay with rate  $\Gamma$  is represented by the relaxation operators  $\hat{c}_0 = \sqrt{\Gamma/2} |0\rangle \langle 2|$  and  $\hat{c}_1 = \sqrt{\Gamma/2} |1\rangle \langle 2|$ . The unobserved system relaxes to a steady state  $\rho^{(\text{ss})}$  (see Eq. (2.12)) from which follows the average properties of the emitted radiation. In particular, the average fluorescence rate is given by  $\tilde{R}(\delta) = \sum_i \text{Tr} \left( \hat{c}_i^\dagger \hat{c}_i \rho^{(\text{ss})} \right)$  where  $i = 0, 1$ , and the quantum regression

theorem yields Glauber's correlation function [327] for two photo emissions in channel  $i$  separated by a time  $\tau$ ,

$$G_i^{(2)}(\tau) = \text{Tr} \left( \hat{c}_i^\dagger \hat{c}_i e^{\mathcal{L}\tau} \left[ \hat{c}_i \rho^{(ss)} \hat{c}_i^\dagger \right] \right). \quad (\text{B.2})$$

The master equation can be unravelled into stochastic evolution corresponding to the random measurement backaction on the system due to detection of the emitted radiation by photon detectors, see Eq. (2.13). Whenever a photon is detected, the system jumps to the corresponding ground state,  $|\psi\rangle \rightarrow \hat{c}_i |\psi\rangle / \sqrt{\langle \psi | \hat{c}_i^\dagger \hat{c}_i | \psi \rangle}$ , while between photo detections the evolution of the (unnormalized) state  $|\tilde{\psi}\rangle$  is governed by an effective Hamiltonian,

$$\hat{H}_{\text{eff}} = \hat{H} - \frac{i}{2} \sum_i \hat{c}_i^\dagger \hat{c}_i, \quad (\text{B.3})$$

where the imaginary term represents the decay of the excited state. The eigenstates of  $\hat{H}_{\text{eff}}$ ,  $|\psi_j\rangle$  with eigenvalues  $\lambda_j$  represent decaying modes with decay rates  $\Gamma_j = -2\text{Im}(\lambda_j)$ . For weak driving, the largest of these rates is almost equal to  $\Gamma$  and the corresponding eigenstate is close to the bare atomic excited state, i.e., it has negligible statistical weight  $w_j^{(n)} = |\langle n | \psi_j \rangle|^2$  on the atomic ground states ( $n = 0, 1$ ). The two smallest rates  $\Gamma_-$  and  $\Gamma_+$ , on the other hand, are associated with the ground states, and hence they constitute the effective fluorescence rate right after a detector click. Their dependence on the detuning  $\delta$  is shown in Fig. B.1. Close to resonance  $\Gamma_-(\delta)$  tends quadratically to zero, while  $\Gamma_+(\delta)$  increases equivalently. This is because  $\Gamma_-(\delta \simeq 0) \simeq 0$  corresponds to the dark state superposition  $|\psi_-\rangle = (|0\rangle - |1\rangle) / \sqrt{2}$  while  $\Gamma_+(\delta \simeq 0) \simeq 2\Omega^2/\Gamma$  is the rate of excitation and emission from the bright state linear combination  $|\psi_+\rangle = (|0\rangle + |1\rangle) / \sqrt{2}$ .

Upon photo detection, the atom may, with probability  $w_+^{(0,1)} \simeq 1/2$ , continue to fluoresce at a rate  $\Gamma_+(\delta)$ , and hence quickly reemit, but it may also, with a probability  $w_-^{(0,1)} \simeq 1/2$ , continue to fluoresce at a rate  $\Gamma_-(\delta)$  corresponding to the pseudo dark state. The frequency dependent emission rate leading to non-ergodic dynamics close to resonance is thus given by  $R(\delta) = \Gamma_-(\delta)$ .

Our Lévy statistical analysis relies on the overall rather than the detailed shape of the emission rate from the ground states. In this spirit we note that the fluorescence rate  $\Gamma_-(\delta)$  as a function of the detuning is characterized by a dip with quadratic variation around  $\delta = 0$  due to the

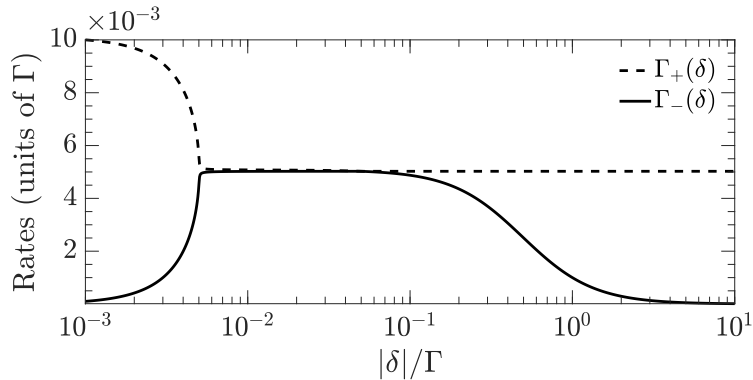


Figure B.1: Frequency dependent effective emission rates from the bright  $|\psi_+\rangle$  and dark  $|\psi_-\rangle$  state superpositions of the two ground states of a  $\Lambda$ -type system. The rates are even functions of  $\delta$  and results are shown for  $\Omega = 0.1\Gamma/\sqrt{2}$ .

dark state, a plateau where the rate is constant, and a tail where the decay follows a Lorentzian line shape due to off-resonant scattering. We hence approximate the rate by

$$R(\delta) = \begin{cases} \tau_0^{-1}(\delta/\delta_Q)^2, & |\delta| < \delta_Q \\ \tau_0^{-1}, & \delta_Q < |\delta| < \delta_L \\ \tau_0^{-1}(\delta_L/\delta)^2, & \delta_L < |\delta|. \end{cases} \quad (\text{B.4})$$

where the characteristic parameters are identified by matching the plateau to the maximum of  $\Gamma^{(-)}(\delta)$ , and requiring that  $R(\delta)$  represents the exact form in the limits  $\delta \simeq 0$  and  $\delta \gg 0$ . Though not a necessity for our analysis, we assume for simplicity that the coupling is weak ( $\Omega \ll \Gamma$ ). We then find by applying second order perturbation theory that

$$\begin{aligned} \tau_0 &= \frac{\Gamma}{\Omega^2}, \\ \delta_Q &= \sqrt{2} \frac{\Omega^2}{\Gamma}, \\ \delta_L &= \frac{\Gamma}{2}. \end{aligned} \quad (\text{B.5})$$

The approximation (B.4) is compared to the exact rate in Fig. 7.2 of the main text.

## B.2 Broad distributions and Lévy statistics

In this section we give a brief introduction to 'broad distributions' decaying slowly at large deviations. We will focus on the typical cases of power-law decays. Let  $\tau$  be a positive random variable distributed for large values according to

$$P(\tau) \underset{\text{large } \tau}{\simeq} \frac{\mu \tau_b^\mu}{\tau^{1+\mu}}, \quad (\text{B.6})$$

where the exponent  $\mu$  determines the decay of the tail towards zero. Normalizability requires  $\mu > 0$  and all moments  $\langle \tau^n \rangle$  for which  $n \geq \mu$  diverge.

The central limit theorem (CLT) concerns the asymptotic behavior of the sum  $T_N$  of  $N$  independent realizations of the probability distribution  $P(\tau)$ ,

$$T_N = \sum_{i=1}^N \tau_i, \quad (\text{B.7})$$

independent of the detailed shape of  $P(\tau)$ .

For  $\mu > 2$  both the mean  $\langle \tau \rangle$  and variance  $\sigma^2$  of  $\tau$  are finite, and defining a random variable  $\epsilon$  such that

$$T_N = \langle \tau \rangle N + \epsilon \sigma \sqrt{N}, \quad (\text{B.8})$$

the normal CLT ensures that for large  $N$ ,  $\epsilon$  is a Gaussian random variable with zero mean and unit variance. That is,  $T_N$  is normally distributed and  $T_N \rightarrow \langle \tau \rangle N$  for large  $N$ .

For  $\mu < 2$  the variance of  $\tau$  is formally infinite, and the normal CLT does not apply. Instead a generalized CLT has been proven by Lévy and Gnedenko [214, 215]. If  $1 < \mu < 2$  the mean value of  $\tau$  is finite, and by defining the Lévy increment  $\xi$  such that

$$T_N = \langle \tau \rangle N + \xi \tau_b N^{1/\mu}, \quad (\text{B.9})$$

the generalized CLT states that  $\xi$  is a random variable of order 1, distributed according to the completely asymmetric Lévy distribution  $L_\mu(\xi)$  which only depends on the value of  $\mu$ . Notice, however, that we still have  $T_N \rightarrow \langle \tau \rangle N$  for large  $N$ .

The most interesting case in the present work is  $\mu < 1$ , where even the mean of  $\tau$  is undefined. Then Eq. (B.9) becomes

$$T_N = \xi \tau_b N^{1/\mu}, \quad (\text{B.10})$$

where  $\xi$  is distributed as above, and we note that the sum Eq. (B.7) no longer scales proportionally with the number of terms, but rather is dominated by a few single terms; see Fig. 1.2.

### B.3 Recycling time distribution

Here we address the temporal dynamics and derive the probability distribution  $P_r(\tau_r)$  of the recycling time intervals  $\tau_r$ .

We introduce first the probability  $P_1(k)$  that the detuning returns to the PDS (defined in Chapter 5) for the first time at exactly  $k$  photon detection events after leaving the PDS. Notice that  $P_1(k)$  relates to the number of jumps and *not* to the duration  $\tau_r$  of the time spent outside the PDS. The probability  $P_{\text{trap}}(n)$  that the system occupies the PDS after the  $n^{\text{th}}$  detection event can be written as a sum over probabilities of already being trapped after  $n'$  events with probability  $P_{\text{trap}}(n')$ , leaving the PDS at  $n' + 1$  (which occurs with unit probability since  $\delta_{\text{PDS}} \ll \delta_{\text{max}}$ ) and returning after an additional  $n - n'$  steps with a probability  $P_1(n - n')$ ,

$$P_{\text{trap}}(n) = P_1(n) + \sum_{n'=0}^n P_{\text{trap}}(n')P_1(n - n'), \quad (\text{B.11})$$

where the first term accounts for a first return at  $n$  without any prior returns. We assume an initial detuning in the recycling region, and we have extended the summation limits to  $n' = 0$  and  $n' = n$  which is justified since  $P_{\text{trap}}(0) = 0$  and  $P_1(0) = 0$ .

The sum constitutes a convolution product, and we introduce the discrete Laplace transform (moment-generating function),

$$\mathcal{L}_d P(s) = \sum_{n=0}^{\infty} e^{-sn} P(n) \quad (\text{B.12})$$

realizing the relation between  $P_1(n)$  and  $P_{\text{trap}}(n)$ ,

$$\mathcal{L}_d P_1(s) = \frac{\mathcal{L}_d P_{\text{trap}}(s)}{1 + \mathcal{L}_d P_{\text{trap}}(s)}. \quad (\text{B.13})$$

This result is independent of any specific frequency-shifting protocol.

The main text investigates the case where after each detection event the detuning explores the interval  $\delta \in [-\delta_{\text{max}}, \delta_{\text{max}}]$  in a uniform manner. In such settings,  $P_{\text{trap}}(n)$  has a constant value

$$P_{\text{trap}}(n) = \frac{\delta_{\text{PDS}}}{\delta_{\text{max}}}, \quad (\text{B.14})$$

and Eq. (B.13) yields

$$\mathcal{L}_d P_1(s) = 1 - \frac{\delta_{\max}}{\delta_{\text{PDS}}} s. \quad (\text{B.15})$$

Since  $\mathcal{L}_d P_1(s)$  is a moment-generating function this implies that the average number of steps before the first return is finite and given by

$$\langle n \rangle = \frac{\delta_{\max}}{\delta_{\text{PDS}}}. \quad (\text{B.16})$$

The temporal duration of each step depends on the emission rate in the recycling region. In the main text we focus on the case  $\delta_Q \ll \delta_{\max} < \delta_L$ , where the recycling region is characterized by a frequency independent rate,  $R(\delta) = 1/\tau_0$ , and the average time  $\tau_0$  between two jumps is finite. The average first return time is then simply

$$\langle \tau_r \rangle = \langle n \rangle \tau_0. \quad (\text{B.17})$$

The finite mean value implies that the recycling times  $\tau_r$  follow normal statistics. In fact, it can be shown that the tail of  $P_r(\tau_r)$  follows an exponential law [328].

If the frequency-shifting is performed as an unconfined standard random walk Eq. (B.13) still applies and leads to a first return distribution with a power law tail

$$P_1(n) \underset{\text{large } n}{\simeq} \frac{1}{2\sqrt{2\pi}} \frac{\Delta\delta}{\delta_{\text{PDS}}} \frac{1}{n^{3/2}}, \quad (\text{B.18})$$

with  $\Delta\delta$  the average step size [226]. In this case  $\langle n \rangle$  diverges. The corresponding statistical behavior of the recycling times  $\tau_r$  is dominated by trapping in effective dark states at high  $\delta$  where, by Eq. (B.4),  $R(\delta) \propto 1/\delta^2$ . One finds [226] that  $P_r(\tau_r)$  then follows Eq. (B.6) with  $\mu_r = 1/4$  and  $\tau_{r,b} = \tau_0(\Delta\delta)^6/(\delta_{\text{PDS}}^4 \delta_L^2)$ , and that the recycling process is dominated by very long time intervals.

## B.4 Proportion of trapped trajectories

Here we derive the proportion of trajectories that will asymptotically for long times be trapped in the PDS with  $|\delta| < \delta_{\text{PDS}}$ . Due to the non-ergodic dynamics, the time average, unlike the ensemble average results, retains a stochastic contribution even in the long time limit.

The alternation between trapping and recycling periods defines a renewal process [329], and we introduce first the probability density functions  $S_R(t)$  of returning to the PDS region at time  $t$  independent of the number of previous return points and  $S_D(t)$  for departing at time  $t$  independent of previous departure points. That is,  $S_R(t)dt$  ( $S_D(t)dt$ ) is the probability of entering (departing) the PDS region in  $[t, t + dt]$ . The densities can be expressed in terms of each other and the trapping and recycling time distributions. For an initially un-trapped trajectory, we have

$$S_R(t) = P_r(t) + \int_0^t dt' S_D(t')P_r(t - t'), \quad (\text{B.19})$$

where the first term accounts for the probability of being trapped exactly at  $t$  and the second the case of escaping at  $t' \in [0, t]$  and returning at  $t$ . Similarly

$$S_D(t) = \int_0^t dt' S_R(t')P_t(t - t'). \quad (\text{B.20})$$

The integrals in the expressions (B.19 and (B.20) form convolution products, so performing Laplace transforms,  $\mathcal{L}g(s) = \int_0^\infty dt g(t)e^{-st}$ , and eliminating  $\mathcal{L}S_D(s)$ , we find

$$\mathcal{L}S_R(s) = \frac{\mathcal{L}P_r(s)}{1 - \mathcal{L}P(s)\mathcal{L}P_r(s)}. \quad (\text{B.21})$$

The ensemble average trapped proportion at time  $T$  can be written as an integral over time  $t'$  of the probability that the system entered the trap at time  $t'$  multiplied by the probability  $\psi(T - t')$  that the system remained in the trap until times later than  $T$ ,

$$f_E = \int_0^T dt' S_R(t')\psi(T - t'). \quad (\text{B.22})$$

Note that  $\psi(T - t')$  is itself an integral over the distribution  $P_t(T - t')$  of trapping times,

$$\psi(\tau) = \int_\tau^\infty d\tau' P_t(\tau').$$

The Laplace transform of the convolution Eq. (B.22) is

$$\mathcal{L}f_E(s) = \mathcal{L}S_R(s)\mathcal{L}\psi(s), \quad (\text{B.23})$$

with  $\mathcal{L}\psi(s) = (1 - \mathcal{L}P(s))/s$ . Inserting Eq. (B.21) we thus reach our final expression for the Laplace transform of the trapped proportion,

$$\mathcal{L}f_E(s) = \frac{\mathcal{L}P_r(s)}{1 - \mathcal{L}P_t(s)\mathcal{L}P_r(s)} \frac{1 - \mathcal{L}P_t(s)}{s}, \quad (\text{B.24})$$

revealing

$$f_E(T) = \int_0^T dt [S_R(t) - S_E(t)], \quad (\text{B.25})$$

which is very sensible.

With  $\mathcal{L}f_E(s)$  expressed in terms of the trapping and recycling time distributions we may apply our statistical model. A small  $s$  expansion (high  $\tau_t$ ) of the Laplace transform of  $P_t(\tau_t)$  as given in Eq. (7.2) yields to first order [226]

$$\mathcal{L}P_t(s) \simeq 1 - \Gamma(1 - \mu)(s\tau_b)^\mu, \quad (\text{B.26})$$

where  $\Gamma(x)$  is the Gamma-function. For the recycling distribution we focus on the case  $\delta_{\max} < \delta_L$ , where the mean recycling time is finite so that

$$\mathcal{L}P_r(s) = 1 - s \langle \tau_r \rangle \quad (\text{B.27})$$

for small  $s$ . Then by Eq. (B.24)

$$\mathcal{L}f_E(s) = \frac{1}{s} - \frac{\langle \tau_r \rangle}{\Gamma(1 - \mu)(s\tau_b)^\mu}, \quad (\text{B.28})$$

and one can finally show that asymptotically as  $T \rightarrow \infty$ , the inverse transform gives

$$f_E(T) \simeq 1 - \frac{\sin(\pi\mu)}{\pi} \frac{\langle \tau_r \rangle}{\tau_b^\mu T^{1-\mu}}. \quad (\text{B.29})$$

For a discussion of cases in which  $\delta_{\max} > \delta_L$ , the reader is referred to Ref. [226].

## B.5 Asymptotic frequency distribution

The asymptotic proportion of trajectories with  $|\delta| < \delta_{\text{PDS}}$  is given by  $f_E(T)$ . The asymptotic distribution  $\mathcal{P}(\delta, T)$  of this proportion is found by

integrating the probability of entering the trap at a time  $t'$  with a given  $\delta$  and not leaving before the final time  $T$ ,

$$\mathcal{P}(\delta, T) = \rho(\delta) \int_0^T dt' S_R(t') \phi(T - t'|\delta), \quad (\text{B.30})$$

where  $\rho(\delta) = 1/2\delta_{\text{PDS}}$  is normalized, so  $f_E(T) = \int_{-\delta_{\text{PDS}}}^{\delta_{\text{PDS}}} d\delta \mathcal{P}(\delta, T)$ , and we define the probability to leave the trap after a time  $\tau$  conditioned on the value of  $\delta$ ,

$$\phi(\tau|\delta) = \int_{\tau}^{\infty} d\tau' P_t(\tau'|\delta). \quad (\text{B.31})$$

As it turns out, the time-dependent distribution of frequencies  $\delta \leq \delta_{\text{PDS}}$  *within* the trap is self-similar for different times and can in general be factorized as

$$\mathcal{P}(\delta, T) = h(T)G(q). \quad (\text{B.32})$$

We restrict our attention to the case  $\delta_{\text{max}} < \delta_L$  with infinite average trapping time and finite recycling times, and we refer to [226] for derivations when the recycling is also non-ergodic. From Eq. (B.21) and Eq. (B.26) it follows that the small  $s$  expansion of the Laplace transform of the renewal density function is  $\mathcal{L}S_R(s) = (s\tau_b)^{-\mu}/\Gamma(1 - \mu)$ , so that for large times  $S_R(t) \simeq \sin(\pi\mu)\tau_b^{-\mu}t^{\mu-1}/\pi$ . One finds then the height of the distribution,

$$h(T) = \left( \frac{\tau_{\text{PDS}}}{\tau_b} \right)^{\mu} \frac{\sin(\pi\mu)}{\pi\mu\delta_T}. \quad (\text{B.33})$$

The form factor is defined as a function of  $q = \delta/\delta_T$  as

$$G(q) = \mu \int_0^1 du u^{\mu-1} e^{-(1-\mu)q^{1/\mu}}, \quad (\text{B.34})$$

which for  $\mu = 1/2$  can be expressed as  $G(q) = D(q)/q$ , where  $D(q)$  is the Dawson function. The tails of  $G(q)$  are like a Lorentzian  $\sim 1/2q^2$  and the area is  $\pi^{3/2}/2$ .  $G(q)$  is compared to a Lorentzian with the same tails and a Gaussian with the same FWHM and normalization in Fig. B.2. Notice that the distribution is not as narrow as the Lorentzian close to the central frequencies.

The resulting properties of  $\mathcal{P}(\delta, T)$  are discussed in Sec. 7.2.2.

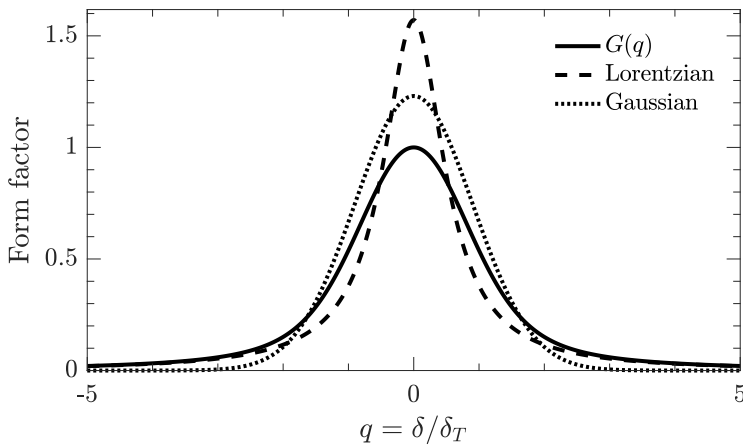


Figure B.2: The form factor  $G(q)$  Eq. (B.34) of  $\mathcal{P}(\delta, T)$  is compared to a Lorentzian with the same tails ( $\propto 1/2q^2$ ), and a Gaussian with the same FWHM (2.13). All distributions are normalized to an area  $\pi^{3/2}/2$ .

# Bibliography

- [1] A. H. Kiilerich and K. Mølmer, Estimation of atomic interaction parameters by photon counting, *Phys. Rev. A* **89**, 052110 (2014).
- [2] A. H. Kiilerich and K. Mølmer, Parameter estimation by multichannel photon counting, *Phys. Rev. A* **91**, 012119 (2015).
- [3] A. H. Kiilerich and K. Mølmer, Quantum Zeno effect in parameter estimation, *Phys. Rev. A* **92**, 032124 (2015).
- [4] A. H. Kiilerich and K. Mølmer, Bayesian parameter estimation by continuous homodyne detection, *Phys. Rev. A* **94**, 032103 (2016).
- [5] A. H. Kiilerich and K. Mølmer, Random search for a dark resonance, *Phys. Rev. A* **95**, 022110 (2017).
- [6] P. Xu, A. H. Kiilerich, R. Blattmann, Y. Yu, S.-L. Zhu, and K. Mølmer, Measurement of the topological Chern number by continuous probing of a qubit subject to a slowly varying Hamiltonian, *Phys. Rev. A* **96**, 010101 (2017).
- [7] D. Tan, N. Foroozani, M. Naghiloo, A. H. Kiilerich, K. Mølmer, and K. W. Murch, Homodyne monitoring of postselected decay, *Phys. Rev. A* **96**, 022104 (2017).
- [8] A. Bienfait, P. Campagne-Ibarcq, A. H. Kiilerich, X. Zhou, S. Probst, J. J. Pla, T. Schenkel, D. Vion, D. Esteve, J. J. L. Morton, et al., Magnetic resonance with squeezed microwaves, *Phys. Rev. X* **7**, 041011 (2017).
- [9] A. H. Kiilerich and K. Mølmer, Relaxation of an ensemble of two-level emitters in a squeezed bath, *Phys. Rev. A* **96**, 043855 (2017).
- [10] A. H. Kiilerich and K. Mølmer, Multistate and multihypothesis discrimination with open quantum systems, *Phys. Rev. A* **97**, 052113 (2018).
- [11] A. H. Kiilerich and K. Mølmer, Hypothesis testing with a continuously monitored quantum system, *Phys. Rev. A* **98**, 022103 (2018).
- [12] J. J. Sørensen, M. Dalgaard, A. H. Kiilerich, K. Mølmer, and J. Sherson, Quantum control with measurements and quantum Zeno dynamics, arXiv preprint arXiv:1806.07793 (2018).
- [13] A. H. Kiilerich, A. De Pasquale, and V. Giovannetti, A dynamical approach to ancilla assisted quantum thermometry, arXiv preprint arXiv:1807.11268 (2018).
- [14] Nobelprize.org, The Nobel Prize in Physics 2012, Nobel Media AB 2014 (2018).
- [15] N. Lambert, Y.-N. Chen, Y.-C. Cheng, C.-M. Li, G.-Y. Chen, and F. Nori, Quantum biology, *Nat. Phys.* **9**, 10 (2013).
- [16] G. S. Engel, T. R. Calhoun, E. L. Read, T.-K. Ahn, T. Mančal, Y.-C. Cheng, R. E. Blankenship, and G. R. Fleming, Evidence for wavelike energy transfer through quantum coherence in photosynthetic systems, *Nature* **446**, 782 (2007).

- [17] H. Lee, Y.-C. Cheng, and G. R. Fleming, Coherence dynamics in photosynthesis: protein protection of excitonic coherence, *Science* **316**, 1462 (2007).
- [18] E. Collini, C. Y. Wong, K. E. Wilk, P. M. G. Curmi, P. Brumer, and G. D. Scholes, Coherently wired light-harvesting in photosynthetic marine algae at ambient temperature, *Nature* **463**, 644 (2010).
- [19] N. Killoran, S. F. Huelga, and M. B. Plenio, Enhancing light-harvesting power with coherent vibrational interactions: A quantum heat engine picture, *The Journal of Chemical Physics* **143**, 155102 (2015).
- [20] E. M. Gauger, E. Rieper, J. J. L. Morton, S. C. Benjamin, and V. Vedral, Sustained quantum coherence and entanglement in the avian compass, *Phys. Rev. Lett.* **106**, 040503 (2011).
- [21] D. Deutsch, Quantum theory, the Church–Turing principle and the universal quantum computer, *Proc. R. Soc. Lond. A* **400**, 97 (1985).
- [22] A. Steane, Quantum computing, *Reports on Progress in Physics* **61**, 117 (1998).
- [23] P. W. Shor, Polynomial-time algorithms for prime factorization and discrete logarithms on a quantum computer, *SIAM review* **41**, 303 (1999).
- [24] C. H. Bennett and D. P. DiVincenzo, Quantum information and computation, *Nature* **404**, 247 (2000).
- [25] R. P. Feynman, Simulating physics with computers, *International journal of theoretical physics* **21**, 467 (1982).
- [26] S. Lloyd, Universal quantum simulators, *Science* pp. 1073–1078 (1996).
- [27] S. Barrett, K. Hammerer, S. Harrison, T. E. Northup, and T. J. Osborne, Simulating quantum fields with cavity QED, *Phys. Rev. Lett.* **110**, 090501 (2013).
- [28] N. Gisin, G. Ribordy, W. Tittel, and H. Zbinden, Quantum cryptography, *Rev. Mod. Phys.* **74**, 145 (2002).
- [29] N. Gisin and R. Thew, Quantum communication, *Nat. Photonics* **1**, 165 (2007).
- [30] F. Caruso, S. F. Huelga, and M. B. Plenio, Noise-enhanced classical and quantum capacities in communication networks, *Phys. Rev. Lett.* **105**, 190501 (2010).
- [31] R. Alicki and M. Fannes, Entanglement boost for extractable work from ensembles of quantum batteries, *Phys. Rev. E* **87**, 042123 (2013).
- [32] D. Ferraro, M. Campisi, G. M. Andolina, V. Pellegrini, and M. Polini, High-power collective charging of a solid-state quantum battery, *Physical review letters* **120**, 117702 (2018).
- [33] V. Giovannetti, S. Lloyd, and L. Maccone, Quantum metrology, *Phys. Rev. Lett.* **96**, 010401 (2006).
- [34] V. Giovannetti, S. Lloyd, and L. Maccone, Quantum-enhanced measurements: Beating the standard quantum limit, *Science* **306**, 1330 (2004).
- [35] G. Tóth and I. Apellaniz, Quantum metrology from a quantum information science perspective, *Journal of Physics A: Mathematical and Theoretical* **47**, 424006 (2014).
- [36] P. Neumann, I. Jakobi, F. Dolde, C. Burk, R. Reuter, G. Waldherr, J. Honert, T. Wolf, A. Brunner, J. H. Shim, et al., High-precision nanoscale temperature sensing using single defects in diamond, *Nano Letters* **13**, 2738 (2013).
- [37] J.-M. Yang, H. Yang, and L. Lin, Quantum dot nano thermometers reveal heterogeneous local thermogenesis in living cells, *ACS nano* **5**, 5067 (2011).

- [38] G. Kucsko, P. C. Maurer, N. Y. Yao, M. Kubo, H. J. Noh, P. K. Lo, H. Park, and M. D. Lukin, Nanometre-scale thermometry in a living cell, *Nature* **500**, 54 (2013).
- [39] D. M. Toyli, F. Charles, D. J. Christle, V. V. Dobrovitski, and D. D. Awschalom, Fluorescence thermometry enhanced by the quantum coherence of single spins in diamond, *Proceedings of the National Academy of Sciences* **110**, 8417 (2013).
- [40] F. Seilmeier, M. Hauck, E. Schubert, G. J. Schinner, S. E. Beavan, and A. Högele, Optical thermometry of an electron reservoir coupled to a single quantum dot in the millikelvin range, *Physical Review Applied* **2**, 024002 (2014).
- [41] F. Haupt, A. Imamoglu, and M. Kroner, Single quantum dot as an optical thermometer for millikelvin temperatures, *Physical Review Applied* **2**, 024001 (2014).
- [42] M. Brunelli, S. Olivares, M. Paternostro, and M. G. A. Paris, Qubit-assisted thermometry of a quantum harmonic oscillator, *Phys. Rev. A* **86**, 012125 (2012).
- [43] C. Sabín, A. White, L. Hackermuller, and I. Fuentes, Impurities as a quantum thermometer for a Bose-Einstein condensate, *Scientific reports* **4**, 6436 (2014).
- [44] M. A. Taylor, J. Janousek, V. Daria, J. Knittel, B. Hage, H.-A. Bachor, and W. P. Bowen, Biological measurement beyond the quantum limit, *Nat. Photonics* **7**, 229 (2013).
- [45] M. A. Taylor and W. P. Bowen, Quantum metrology and its application in biology, *Physics Reports* **615**, 1 (2016).
- [46] N. P. Mauranyapin, L. S. Madsen, M. A. Taylor, M. Waleed, and W. P. Bowen, Evanescent single-molecule biosensing with quantum-limited precision, *Nat. Photonics* **11**, 477 (2017).
- [47] K. McKenzie, D. A. Shaddock, D. E. McClelland, B. C. Buchler, and P. K. Lam, Experimental demonstration of a squeezing-enhanced power-recycled michelson interferometer for gravitational wave detection, *Phys. Rev. Lett.* **88**, 231102 (2002).
- [48] K. Goda, O. Miyakawa, E. E. Mikhailov, S. Saraf, R. Adhikari, K. McKenzie, R. Ward, S. Vass, A. J. Weinstein, and N. Mavalvala, A quantum-enhanced prototype gravitational-wave detector, *Nat. Phys.* **4**, 472 (2008).
- [49] G. M. Harry and the LIGO Scientific Collaboration, Advanced ligo: the next generation of gravitational wave detectors, *Classical and Quantum Gravity* **27**, 084006 (2010).
- [50] J. Aasi, J. Abadie, B. P. Abbott, R. Abbott, T. D. Abbott, M. R. Abernathy, C. Adams, T. Adams, P. Addesso, R. X. Adhikari, et al., Enhanced sensitivity of the ligo gravitational wave detector by using squeezed states of light, *Nat. Photonics* **7**, 613 (2013).
- [51] The LIGO Scientific Collaboration, A gravitational wave observatory operating beyond the quantum shot-noise limit, *Nat. Phys.* **7**, 962 (2011).
- [52] R. C. Jaklevic, J. Lambe, A. H. Silver, and J. E. Mercereau, Quantum interference effects in Josephson tunneling, *Phys. Rev. Lett.* **12**, 159 (1964).
- [53] R. A. Kamper and M. B. Simmonds, Broadband superconducting quantum magnetometer, *App. Phys. Lett.* **20**, 270 (1972).
- [54] W. Wasilewski, K. Jensen, H. Krauter, J. J. Renema, M. V. Balabas, and E. S. Polzik, Quantum noise limited and entanglement-assisted magnetometry, *Phys. Rev. Lett.* **104**, 133601 (2010).

- [55] I. Baumgart, J.-M. Cai, A. Retzker, M. B. Plenio, and C. Wunderlich, Ultrasensitive magnetometer using a single atom, *Phys. Rev. Lett.* **116**, 240801 (2016).
- [56] V. Petersen, L. B. Madsen, and K. Mølmer, Magnetometry with entangled atomic samples, *Phys. Rev. A* **71**, 012312 (2005).
- [57] D. Budker and M. Romalis, Optical magnetometry, *Nat. Phys.* **3**, 227 (2007).
- [58] J. M. Taylor, P. Cappellaro, L. Childress, L. Jiang, D. Budker, P. R. Hemmer, A. Yacoby, R. Walsworth, and M. D. Lukin, High-sensitivity diamond magnetometer with nanoscale resolution, *Nat. Phys.* **4**, 810 (2008).
- [59] D. J. Wineland, J. J. Bollinger, W. M. Itano, F. L. Moore, and D. J. Heinzen, Spin squeezing and reduced quantum noise in spectroscopy, *Phys. Rev. A* **46**, R6797 (1992).
- [60] D. J. Wineland, J. J. Bollinger, W. M. Itano, and D. J. Heinzen, Squeezed atomic states and projection noise in spectroscopy, *Phys. Rev. A* **50**, 67 (1994).
- [61] A. Facon, E.-K. Dietsche, D. Grosso, S. Haroche, J.-M. Raimond, M. Brune, and S. Gleyzes, A sensitive electrometer based on a Rydberg atom in a Schrödinger-cat state, *Nature* **535**, 262 (2016).
- [62] F. Armata, L. Latmiral, A. D. K. Plato, and M. S. Kim, Quantum limits to gravity estimation with optomechanics, *Phys. Rev. A* **96**, 043824 (2017).
- [63] K. Koźdoń, I. T. Durham, and A. Dragan, Measuring acceleration using the Purcell effect, *Quantum* **2**, 83 (2018).
- [64] R. Nair and M. Tsang, Far-field superresolution of thermal electromagnetic sources at the quantum limit, *Phys. Rev. Lett.* **117**, 190801 (2016).
- [65] M. Tsang, R. Nair, and X.-M. Lu, Quantum theory of superresolution for two incoherent optical point sources, *Phys. Rev. X* **6**, 031033 (2016).
- [66] A. Chrostowski, R. Demkowicz-Dobrzański, M. Jarzyna, and K. Banaszek, On super-resolution imaging as a multiparameter estimation problem, *International Journal of Quantum Information* **15**, 1740005 (2017).
- [67] J. P. Dowling and K. P. Seshadreesan, Quantum optical technologies for metrology, sensing, and imaging, *Journal of Lightwave Technology* **33**, 2359 (2015).
- [68] W. P. Schleich, K. S. Ranade, C. Anton, M. Arndt, M. Aspelmeyer, M. Bayer, G. Berg, T. Calarco, H. Fuchs, E. Giacobino, et al., Quantum technology: from research to application, *Appl. Phys. B* **122**, 130 (2016).
- [69] V. Giovannetti, S. Lloyd, and L. Maccone, Advances in quantum metrology, *Nat. Photonics* **5**, 222 (2011).
- [70] C. L. Degen, F. Reinhard, and P. Cappellaro, Quantum sensing, *Rev. Mod. Phys.* **89**, 035002 (2017).
- [71] M. G. A. Paris, Quantum estimation for quantum technology, *International Journal of Quantum Information* **07**, 125 (2009).
- [72] S. F. Huelga, C. Macchiavello, T. Pellizzari, A. K. Ekert, M. B. Plenio, and J. I. Cirac, Improvement of frequency standards with quantum entanglement, *Phys. Rev. Lett.* **79**, 3865 (1997).
- [73] J. Kołodyński and R. Demkowicz-Dobrzański, Phase estimation without a priori phase knowledge in the presence of loss, *Phys. Rev. A* **82**, 053804 (2010).
- [74] R. Demkowicz-Dobrzański, J. Kołodyński, and M. Guță, The elusive Heisenberg limit in quantum-enhanced metrology, *Nat. Commun.* **3**, 1063 (2012).

- [75] J. F. Haase, A. Smirne, J. Kołodyński, R. Demkowicz-Dobrzański, and S. F. Huelga, Precision limits in quantum metrology with open quantum systems, arXiv preprint arXiv:1807.11882 (2018).
- [76] M. W. Mitchell, J. S. Lundeen, and A. M. Steinberg, Super-resolving phase measurements with a multiphoton entangled state, *Nature* **429**, 161 (2004).
- [77] T. Nagata, R. Okamoto, J. L. O'Brien, K. Sasaki, and S. Takeuchi, Beating the standard quantum limit with four-entangled photons, *Science* **316**, 726 (2007).
- [78] S. Slussarenko, M. M. Weston, H. M. Chrzanowski, L. K. Shalm, V. B. Verma, S. W. Nam, and G. J. Pryde, Unconditional violation of the shot-noise limit in photonic quantum metrology, *Nat. Photonics* **11**, 700 (2017).
- [79] M. Naghiloo, A. N. Jordan, and K. W. Murch, Achieving optimal quantum acceleration of frequency estimation using adaptive coherent control, *Phys. Rev. Lett.* **119**, 180801 (2017).
- [80] A. Smirne, A. Lemmer, M. B. Plenio, and S. F. Huelga, Improving the precision of frequency estimation via long-time coherences, arXiv preprint arXiv:1808.03664 (2018).
- [81] W. Dür, M. Skotiniotis, F. Fröwis, and B. Kraus, Improved quantum metrology using quantum error correction, *Phys. Rev. Lett.* **112**, 080801 (2014).
- [82] E. M. Kessler, I. Lovchinsky, A. O. Sushkov, and M. D. Lukin, Quantum error correction for metrology, *Phys. Rev. Lett.* **112**, 150802 (2014).
- [83] T. Unden, P. Balasubramanian, D. Louzon, Y. Vinkler, M. B. Plenio, M. Markham, D. Twitchen, A. Stacey, I. Lovchinsky, A. O. Sushkov, et al., Quantum metrology enhanced by repetitive quantum error correction, *Phys. Rev. Lett.* **116**, 230502 (2016).
- [84] S. Zhou, M. Zhang, J. Preskill, and L. Jiang, Achieving the Heisenberg limit in quantum metrology using quantum error correction, *Nat. Commun.* **9**, 78 (2018).
- [85] Q.-S. Tan, Y. Huang, X. Yin, L.-M. Kuang, and X. Wang, Enhancement of parameter-estimation precision in noisy systems by dynamical decoupling pulses, *Phys. Rev. A* **87**, 032102 (2013).
- [86] T. Gefen, D. A. Herrera-Martí, and A. Retzker, Parameter estimation with efficient photodetectors, *Phys. Rev. A* **93**, 032133 (2016).
- [87] M. B. Plenio and S. F. Huelga, Sensing in the presence of an observed environment, *Phys. Rev. A* **93**, 032123 (2016).
- [88] B. L. Higgins, D. W. Berry, S. D. Bartlett, H. M. Wiseman, and G. J. Pryde, Entanglement-free Heisenberg-limited phase estimation, *Nature* **450**, 393 (2007).
- [89] H. Mabuchi, Dynamical identification of open quantum systems, *Quantum and Semiclassical Optics: Journal of the European Optical Society Part B* **8**, 1103 (1996).
- [90] J. Gambetta and H. M. Wiseman, State and dynamical parameter estimation for open quantum systems, *Phys. Rev. A* **64**, 042105 (2001).
- [91] M. Tsang, Continuous quantum hypothesis testing, *Phys. Rev. Lett.* **108**, 170502 (2012).
- [92] S. Gammelmark and K. Mølmer, Bayesian parameter inference from continuously monitored quantum systems, *Phys. Rev. A* **87**, 032115 (2013).
- [93] P. Haikka, Y. Kubo, A. Bienfait, P. Bertet, and K. Mølmer, Proposal for detecting a single electron spin in a microwave resonator, *Phys. Rev. A* **95**, 022306 (2017).

- [94] A. Bayat, B. Alkurtass, P. Sodano, H. Johannesson, and S. Bose, Measurement quench in many-body systems, *Phys. Rev. Lett.* **121**, 030601 (2018).
- [95] W. M. Itano, D. J. Heinzen, J. J. Bollinger, and D. J. Wineland, Quantum Zeno effect, *Phys. Rev. A* **41**, 2295 (1990).
- [96] W. M. Itano, Perspectives on the quantum Zeno paradox, *J. Phys.: Conf. Ser.* **196**, 012018 (2009).
- [97] C. M. Caves, K. S. Thorne, R. W. P. Drever, V. D. Sandberg, and M. Zimmermann, On the measurement of a weak classical force coupled to a quantum-mechanical oscillator. I. Issues of principle, *Rev. Mod. Phys.* **52**, 341 (1980).
- [98] A. A. Clerk, M. H. Devoret, S. M. Girvin, F. Marquardt, and R. J. Schoelkopf, Introduction to quantum noise, measurement, and amplification, *Rev. Mod. Phys.* **82**, 1155 (2010).
- [99] K. W. Murch, S. J. Weber, C. Macklin, and I. Siddiqi, Observing single quantum trajectories of a superconducting quantum bit, *Nature (London)* **502**, 211 (2013).
- [100] P. Campagne-Ibarcq, P. Six, L. Bretheau, A. Sarlette, M. Mirrahimi, P. Rouchon, and B. Huard, Observing quantum state diffusion by heterodyne detection of fluorescence, *Phys. Rev. X* **6**, 011002 (2016).
- [101] S. Hacohe-Gourgy, L. S. Martin, E. Flurin, V. V. Ramasesh, K. B. Whaley, and I. Siddiqi, Quantum dynamics of simultaneously measured non-commuting observables, *Nature* **538**, 491 (2016).
- [102] J. P. Garrahan and I. Lesanovsky, Thermodynamics of quantum jump trajectories, *Phys. Rev. Lett.* **104**, 160601 (2010).
- [103] J. M. Hickey, S. Genway, I. Lesanovsky, and J. P. Garrahan, Thermodynamics of quadrature trajectories in open quantum systems, *Phys. Rev. A* **86**, 063824 (2012).
- [104] S. Gammelmark, B. Julsgaard, and K. Mølmer, Past quantum states of a monitored system, *Phys. Rev. Lett.* **111**, 160401 (2013).
- [105] M. K. Pedersen, J. J. W. H. Sørensen, M. C. Tichy, and J. F. Sherson, Many-body state engineering using measurements and fixed unitary dynamics, *New J. Phys.* **16**, 113038 (2014).
- [106] C. W. Helstrom, Quantum detection and estimation theory, *J. Stat. Phys.* **1**, 231 (1969).
- [107] K. Jacobs, Feedback control for communication with non-orthogonal states, *Quantum Information & Computation* **7**, 127 (2007).
- [108] A. De Pasquale, D. Rossini, R. Fazio, and V. Giovannetti, Local quantum thermal susceptibility, *Nat. Commun.* **7**, 12782 (2016).
- [109] L. A. Correa, M. Mehboudi, G. Adesso, and A. Sanpera, Individual quantum probes for optimal thermometry, *Phys. Rev. Lett.* **114**, 220405 (2015).
- [110] A. De Pasquale, K. Yuasa, and V. Giovannetti, Estimating temperature via sequential measurements, *Phys. Rev. A* **96**, 012316 (2017).
- [111] S. Campbell, M. G. Genoni, and S. Deffner, Precision thermometry and the quantum speed limit, *Quantum Science and Technology* (2018).
- [112] S. Jevtic, D. Newman, T. Rudolph, and T. M. Stace, Single-qubit thermometry, *Phys. Rev. A* **91**, 012331 (2015).
- [113] T. M. Stace, Quantum limits of thermometry, *Phys. Rev. A* **82**, 011611 (2010).
- [114] P. P. Hofer, J. B. Brask, M. Perarnau-Llobet, and N. Brunner, Quantum thermal machine as a thermometer, *Phys. Rev. Lett.* **119**, 090603 (2017).

- [115] V. Mukherjee, A. Zwick, A. Ghosh, and G. Kurizki, High precision multi-temperature quantum thermometry via dynamical control, arXiv preprint arXiv:1711.09660 (2017).
- [116] P. P. Hofer, J. B. Brask, and N. Brunner, Fundamental limits on low-temperature quantum thermometry, arXiv preprint arXiv:1711.09827 (2017).
- [117] L. Pezzé and A. Smerzi, Mach-Zehnder interferometry at the Heisenberg limit with coherent and squeezed-vacuum light, Phys. Rev. Lett. **100**, 073601 (2008).
- [118] E. S. Polzik, J. Carri, and H. J. Kimble, Spectroscopy with squeezed light, Phys. Rev. Lett. **68**, 3020 (1992).
- [119] V. G. Lucivero, R. Jiménez-Martínez, J. Kong, and M. W. Mitchell, Squeezed-light spin noise spectroscopy, Phys. Rev. A **93**, 053802 (2016).
- [120] E. L. Hahn, Spin echoes, Phys. Rev. **80**, 580 (1950).
- [121] C. W. Gardiner and M. J. Collett, Input and output in damped quantum systems: Quantum stochastic differential equations and the master equation, Phys. Rev. A **31**, 3761 (1985).
- [122] C. W. Gardiner and P. Zoller, *Quantum Noise: A Handbook of Markovian and Non-Markovian Quantum Stochastic Methods with Applications to Quantum Optics* (Springer, Berlin, 2004).
- [123] T. Holstein and H. Primakoff, Field dependence of the intrinsic domain magnetization of a ferromagnet, Phys. Rev. **58**, 1098 (1940).
- [124] C. W. Gardiner, Inhibition of atomic phase decays by squeezed light: A direct effect of squeezing, Phys. Rev. Lett. **56**, 1917 (1986).
- [125] L. A. Clark, A. Stokes, M. M. Khan, G. Wang, and A. Beige, Quantum-enhanced metrology without entanglement based on optical cavities with feedback, PHOTOPTICS conference proceedings p. 223 (2017).
- [126] H. Carmichael, *An Open Systems Approach to Quantum Optics - Lectures Presented at the Université Libre de Bruxelles October 28 to November 4, 1991* (Springer, Berlin Heidelberg, 1993).
- [127] Q. Ficheux, S. Jezouin, Z. Leghtas, and B. Huard, Dynamics of a qubit while simultaneously monitoring its relaxation and dephasing, Nat. Commun. **9**, 1926 (2018).
- [128] W. Wieczorek, S. G. Hofer, J. Hoelscher-Obermaier, R. Riedinger, K. Hammerer, and M. Aspelmeyer, Optimal state estimation for cavity optomechanical systems, Phys. Rev. Lett. **114**, 223601 (2015).
- [129] M. Guță, Fisher information and asymptotic normality in system identification for quantum Markov chains, Phys. Rev. A **83**, 062324 (2011).
- [130] A. Negretti and K. Mølmer, Estimation of classical parameters via continuous probing of complementary quantum observables, New J. Phys. **15**, 125002 (2013).
- [131] R. A. Fisher, On the mathematical foundations of theoretical statistics, Philosophical Transactions of the Royal Society **A 222**, 309–368 (1922).
- [132] H. Cramér, *Mathematical methods of statistics (PMS-9)* (Princeton University Press, 2016).
- [133] H.-P. Breuer and F. Petruccione, *The theory of open quantum systems* (Oxford University Press on Demand, 2002).
- [134] H. M. Wiseman and G. J. Milburn, *Quantum Measurement and Control* (Cambridge University Press, Cambridge, 2010).

- [135] E. M. Purcell, H. C. Torrey, and R. V. Pound, Resonance absorption by nuclear magnetic moments in a solid, *Phys. Rev.* **69**, 37 (1946).
- [136] A. Bienfait, J. J. Pla, Y. Kubo, X. Zhou, M. Stern, C. C. Lo, C. D. Weis, T. Schenkel, D. Vion, D. Esteve, et al., Controlling spin relaxation with a cavity, *Nature* (2016).
- [137] D. Tan, S. J. Weber, I. Siddiqi, K. Mølmer, and K. W. Murch, Prediction and retrodiction for a continuously monitored superconducting qubit, *Phys. Rev. Lett.* **114**, 090403 (2015).
- [138] J. Dalibard, Y. Castin, and K. Mølmer, Wave-function approach to dissipative processes in quantum optics, *Phys. Rev. Lett.* **68**, 580 (1992).
- [139] K. Jacobs, *Stochastic Processes for Physicists* (Cambridge University Press, Cambridge, 2010).
- [140] S. Gammelmark and K. Mølmer, Fisher Information and the quantum Cramér-Rao sensitivity limit of continuous measurements, *Phys. Rev. Lett.* **112**, 170401 (2014).
- [141] C. Cătană, M. van Horsen, and M. Guță, Asymptotic inference in system identification for the atom maser, *Phil. Trans. R. Soc. A* **370**, 5308 (2012).
- [142] C. Ferrie, C. E. Granade, and D. G. Cory, How to best sample a periodic probability distribution, or on the accuracy of Hamiltonian finding strategies, *Quantum Inf. Process.* **12**, 611 (2013).
- [143] D. Burgarth, V. Giovannetti, A. N. Kato, and K. Yuasa, Quantum estimation via sequential measurements, *New J. Phys.* **17**, 113055 (2015).
- [144] I. Schwartz, J. Roszkopf, S. Schmitt, B. Tratzmiller, Q. Chen, L. P. McGuinness, F. Jelezko, and M. B. Plenio, Blueprint for nanoscale NMR, arXiv preprint arXiv:1706.07134 (2017).
- [145] S. L. Braunstein and C. M. Caves, Statistical distance and the geometry of quantum states, *Phys. Rev. Lett.* **72**, 3439 (1994).
- [146] A. S. Holevo, *Probabilistic and statistical aspects of quantum theory*, vol. 1 (Springer Science & Business Media, 2011).
- [147] H. Yuen and M. Lax, Multiple-parameter quantum estimation and measurement of nonselfadjoint observables, *IEEE Transactions on Information Theory* **19**, 740 (1973).
- [148] C. W. Helstrom and R. Kennedy, Noncommuting observables in quantum detection and estimation theory, *IEEE Transactions on Information Theory* **20**, 16 (1974).
- [149] S. L. Braunstein, C. M. C., and G. Milburn, Generalized uncertainty relations: Theory, examples, and Lorentz invariance, *Annals of Physics* **247**, 135 (1996).
- [150] R. D. Gill and M. Guță, On asymptotic quantum statistical inference, *IMS Collections* (9), 2013 pp. 105–127 (2011).
- [151] L. Seveso, M. A. C. Rossi, and M. G. A. Paris, Quantum metrology beyond the quantum Cramér-Rao theorem, *Phys. Rev. A* **95**, 012111 (2017).
- [152] P. Zanardi, P. Giorda, and M. Cozzini, Information-theoretic differential geometry of quantum phase transitions, *Phys. Rev. Lett.* **99**, 100603 (2007).
- [153] D. Šafránek, Simple expression for the quantum Fisher information matrix, *Phys. Rev. A* **97**, 042322 (2018).
- [154] K. Mølmer, Hypothesis testing with open quantum systems, *Phys. Rev. Lett.* **114**, 040401 (2015).

- [155] K. Macieszczak, M. Guță, I. Lesanovsky, and J. P. Garrahan, Dynamical phase transitions as a resource for quantum enhanced metrology, *Phys. Rev. A* **93**, 022103 (2016).
- [156] L. Cortez, A. Chantasri, L. P. García-Pintos, J. Dressel, and A. N. Jordan, Rapid estimation of drifting parameters in continuously measured quantum systems, *Phys. Rev. A* **95**, 012314 (2017).
- [157] E. Greplova, E. A. Laird, G. A. D. Briggs, and K. Mølmer, Conditioned spin and charge dynamics of a single-electron quantum dot, *Phys. Rev. A* **96**, 052104 (2017).
- [158] E. Greplova, C. K. Andersen, and K. Mølmer, Quantum parameter estimation with a neural network, arXiv preprint arXiv:1711.05238 (2017).
- [159] H. L. Van Trees, *Detection, estimation, and modulation theory, part I: detection, estimation, and linear modulation theory* (John Wiley & Sons, 2004).
- [160] M. Tsang, Conservative classical and quantum resolution limits for incoherent imaging, *Journal of Modern Optics* **65**, 1385 (2018).
- [161] M. Hassani, C. Macchiavello, and L. Maccone, Digital quantum estimation, *Phys. Rev. Lett.* **119**, 200502 (2017).
- [162] V. Delaubert, N. Treps, C. Fabre, H. A. Bachor, and P. Réfrégier, Quantum limits in image processing, *EPL (Europhysics Letters)* **81**, 44001 (2008).
- [163] A. Negretti, C. Henkel, and K. Mølmer, Quantum-limited position measurements of a dark matter-wave soliton, *Phys. Rev. A* **77**, 043606 (2008).
- [164] H. Paul, Photon antibunching, *Rev. Mod. Phys.* **54**, 1061 (1982).
- [165] D. R. Cox, *Renewal Theory* (Methuen, London, 1962).
- [166] W. Feller, *An Introduction to Probability Theory and Its Application* (Wiley, New York, 1968), chap. 9, 3rd ed.
- [167] A. Blais, J. Gambetta, A. Wallraff, D. I. Schuster, S. M. Girvin, M. H. Devoret, and R. J. Schoelkopf, Quantum-information processing with circuit quantum electrodynamics, *Phys. Rev. A* **75**, 032329 (2007).
- [168] J. Q. You and F. Nori, Quantum information processing with superconducting qubits in a microwave field, *Phys. Rev. B* **68**, 064509 (2003).
- [169] R. O. Duda, P. E. Hart, and D. G. Stork, *Pattern Classification* (John Wiley and Sons, Inc., New York, 2000).
- [170] A. H. Kiilerich and K. Mølmer, Unpublished, (2018).
- [171] B. R. Mollow, Power spectrum of light scattered by two-level systems, *Phys. Rev.* **188**, 1969 (1969).
- [172] L. Zhang, A. Datta, and I. A. Walmsley, Precision metrology using weak measurements, *Phys. Rev. Lett.* **114**, 210801 (2015).
- [173] M. Mehboudi, L. A. Correa, and A. Sanpera, Achieving sub-shot-noise sensing at finite temperatures, *Phys. Rev. A* **94**, 042121 (2016).
- [174] B. Misra and E. C. G. Sudarshan, The zeno's paradox in quantum theory, *Journal of Mathematical Physics* **18**, 756 (1977).
- [175] F. Schäfer, I. Herrera, S. Cherukattil, C. Lovecchio, F. S. Cataliotti, F. Caruso, and A. Smerzi, Experimental realization of quantum Zeno dynamics, *Nat. Commun.* **5**, 3194 (2014).
- [176] M. C. Fischer, B. Gutiérrez-Medina, and M. G. Raizen, Observation of the quantum Zeno and anti-Zeno effects in an unstable system, *Phys. Rev. Lett.* **87**, 040402 (2001).

- [177] S. Maniscalco, F. Francica, R. L. Zaffino, N. Lo Gullo, and F. Plastina, Protecting entanglement via the quantum Zeno effect, *Phys. Rev. Lett.* **100**, 090503 (2008).
- [178] A. Beige, D. Braun, B. Tregenna, and P. L. Knight, Quantum computing using dissipation to remain in a decoherence-free subspace, *Phys. Rev. Lett.* **85**, 1762 (2000).
- [179] J. D. Franson, B. C. Jacobs, and T. B. Pittman, Quantum computing using single photons and the Zeno effect, *Phys. Rev. A* **70**, 062302 (2004).
- [180] G. J. Milburn, Quantum zeno effect and motional narrowing in a two-level system, *J. Opt. Soc. Am. B* **5**, 1317 (1988).
- [181] A. Peres, Zeno paradox in quantum theory, *American Journal of Physics* **48**, 931 (1980).
- [182] C. Bonato, M. S. Blok, H. T. Dinani, D. W. Berry, M. L. Markham, D. J. Twitchen, and R. Hanson, Optimized quantum sensing with a single electron spin using real-time adaptive measurements, *Nat. Nanotechnol.* **11**, 247 (2016).
- [183] A. E. B. Nielsen and K. Mølmer, Stochastic master equation for a probed system in a cavity, *Phys. Rev. A* **77**, 052111 (2008).
- [184] L. S. Schulman, Continuous and pulsed observations in the quantum Zeno effect, *Phys. Rev. A* **57**, 1509 (1998).
- [185] J. M. Kosterlitz and D. J. Thouless, Ordering, metastability and phase transitions in two-dimensional systems, *Journal of Physics C: Solid State Physics* **6**, 1181 (1973).
- [186] D. J. Thouless, M. Kohmoto, M. P. Nightingale, and M. den Nijs, Quantized hall conductance in a two-dimensional periodic potential, *Phys. Rev. Lett.* **49**, 405 (1982).
- [187] F. D. M. Haldane, Nonlinear field theory of large-spin heisenberg antiferromagnets: Semiclassically quantized solitons of the one-dimensional easy-axis néel state, *Phys. Rev. Lett.* **50**, 1153 (1983).
- [188] C. Nayak, S. H. Simon, A. Stern, M. Freedman, and S. D. Sarma, Non-abelian anyons and topological quantum computation, *Reviews of Modern Physics* **80**, 1083 (2008).
- [189] V. Gritsev and A. Polkovnikov, Dynamical quantum Hall effect in the parameter space, *Proceedings of the National Academy of Sciences* **109**, 6457 (2012).
- [190] M. D. Schroer, M. H. Kolodrubetz, W. F. Kindel, M. Sandberg, J. Gao, M. R. Vissers, D. P. Pappas, A. Polkovnikov, and K. W. Lehnert, Measuring a topological transition in an artificial spin-1/2 system, *Phys. Rev. Lett.* **113**, 050402 (2014).
- [191] Q. Niu, D. J. Thouless, and Y.-S. Wu, Quantized Hall conductance as a topological invariant, *Phys. Rev. B* **31**, 3372 (1985).
- [192] M. Fruchart and D. Carpentier, An introduction to topological insulators, *Comptes Rendus Physique* **14**, 779 (2013).
- [193] M. V. Berry, Classical adiabatic angles and quantal adiabatic phase, *Journal of Physics A: Mathematical and General* **18**, 15 (1985).
- [194] S.-S. Chern, A simple intrinsic proof of the Gauss-Bonnet formula for closed Riemannian manifolds, *Ann. Math.* **45**, 747 (1944).
- [195] K. von Klitzing, The quantized Hall effect, *Rev. Mod. Phys.* **58**, 519 (1986).
- [196] F. D. M. Haldane, Model for a quantum Hall effect without Landau levels: Condensed-matter realization of the "parity anomaly", *Phys. Rev. Lett.* **61**, 2015 (1988).

- [197] Y. Zhang, Y.-W. Tan, H. L. Stormer, and P. Kim, Experimental observation of the quantum Hall effect and Berry's phase in graphene, *Nature* **438**, 201 (2005).
- [198] K. W. Murch, S. J. Weber, K. M. Beck, E. Ginossar, and I. Siddiqi, Reduction of the radiative decay of atomic coherence in squeezed vacuum, *Nature (London)* **499**, 62 (2013).
- [199] M. Hatridge, S. Shankar, M. Mirrahimi, F. Schackert, K. Geerlings, T. Brecht, K. M. Sliwa, B. Abdo, L. Frunzio, S. M. Girvin, et al., Quantum back-action of an individual variable-strength measurement, *Science* **339**, 178 (2013).
- [200] S. J. Weber, A. Chantasri, J. Dressel, A. N. Jordan, K. W. Murch, and I. Siddiqi, Mapping the optimal route between two quantum states, *Nature* **511**, 570 (2014).
- [201] K. Jacobs and D. A. Steck, A straightforward introduction to continuous quantum measurement, *Contemporary Physics* **47**, 279 (2006).
- [202] L. Henriot, A. Sclocchi, P. P. Orth, and K. Le Hur, Topology of a dissipative spin: Dynamical Chern number, bath-induced nonadiabaticity, and a quantum dynamo effect, *Phys. Rev. B* **95**, 054307 (2017).
- [203] H. F. Hofmann, G. Mahler, and O. Hess, Quantum control of atomic systems by homodyne detection and feedback, *Phys. Rev. A* **57**, 4877 (1998).
- [204] J. Wang and H. M. Wiseman, Feedback-stabilization of an arbitrary pure state of a two-level atom, *Phys. Rev. A* **64**, 063810 (2001).
- [205] P. Campagne-Ibarcq, S. Jezouin, N. Cottet, P. Six, L. Bretheau, F. Mallet, A. Sarlette, P. Rouchon, and B. Huard, Using spontaneous emission of a qubit as a resource for feedback control, *Phys. Rev. Lett.* **117**, 060502 (2016).
- [206] R. Vijay, C. Macklin, D. H. Slichter, S. J. Weber, K. W. Murch, R. Naik, A. N. Korotkov, and I. Siddiqi, Stabilizing rabi oscillations in a superconducting qubit using quantum feedback, *Nature* **490**, 77 (2012).
- [207] T. Bitter and D. Dubbers, Manifestation of Berry's topological phase in neutron spin rotation, *Phys. Rev. Lett.* **59**, 251 (1987).
- [208] D. Suter, K. T. Mueller, and A. Pines, Study of the Aharonov-Anandan quantum phase by NMR interferometry, *Phys. Rev. Lett.* **60**, 1218 (1988).
- [209] H. R. Gray, R. M. Whitley, and C. R. Stroud, Coherent trapping of atomic populations, *Opt. Lett.* **3**, 218 (1978).
- [210] K.-J. Boller, A. Imamoglu, and S. E. Harris, Observation of electromagnetically induced transparency, *Phys. Rev. Lett.* **66**, 2593 (1991).
- [211] A. Nagel, L. Graf, A. Naumov, E. Mariotti, V. Biancalana, D. Meschede, and R. Wynands, Experimental realization of coherent dark-state magnetometers, *EPL (Europhysics Letters)* **44**, 31 (1998).
- [212] C. L. Holloway, J. A. Gordon, S. Jefferts, A. Schwarzkopf, D. A. Anderson, S. A. Miller, N. Thaicharoen, and G. Raithel, Broadband Rydberg atom-based electric-field probe for SI-traceable, self-calibrated measurements, *IEEE Transactions on Antennas and Propagation* **62**, 6169 (2014).
- [213] M. Stähler, S. Knappe, C. Affolderbach, W. Kemp, and R. Wynands, Picotesla magnetometry with coherent dark states, *EPL (Europhysics Letters)* **54**, 323 (2001).
- [214] P. Lévy, *Théorie de l'addition des variables aléatoires* (Gauthier-Villars, Paris, 2010), 2nd ed.

- [215] J.-P. Bouchaud and A. Georges, Anomalous diffusion in disordered media: statistical mechanisms, models and physical applications, *Physics reports* **195**, 127 (1990).
- [216] D. W. Sims, E. J. Southall, N. E. Humphries, G. C. Hays, C. J. A. Bradshaw, J. W. Pitchford, A. James, M. Z. Ahmed, A. S. Brierley, M. A. Hindell, et al., Scaling laws of marine predator search behaviour, *Nature* **451**, 1098 (2008).
- [217] G. M. Viswanathan, S. V. Buldyrev, S. Havlin, M. G. E. Da Luz, E. P. Raposo, and H. E. Stanley, Optimizing the success of random searches, *Nature* **401**, 911 (1999).
- [218] D. Brockmann, L. Hufnagel, and T. Geisel, The scaling laws of human travel, *Nature* **439**, 462 (2006).
- [219] A. Corral, Universal earthquake-occurrence jumps, correlations with time, and anomalous diffusion, *Phys. Rev. Lett.* **97**, 178501 (2006).
- [220] B. Mandelbrot, The variation of certain speculative prices, *The Journal of Business* **36**, 394 (1963).
- [221] R. N. Mantegna and H. E. Stanley, Turbulence and financial markets, *Nature* **383**, 587 (1996).
- [222] D. S. Novikov, M. Drndic, L. S. Levitov, M. A. Kastner, M. V. Jarosz, and M. G. Bawendi, Lévy statistics and anomalous transport in quantum-dot arrays, *Phys. Rev. B* **72**, 075309 (2005).
- [223] F. Bardou, J. P. Bouchaud, O. Emile, A. Aspect, and C. Cohen-Tannoudji, Subrecoil laser cooling and Lévy flights, *Phys. Rev. Lett.* **72**, 203 (1994).
- [224] F. J. Harris, On the use of windows for harmonic analysis with the discrete fourier transform, *Proceedings of the IEEE* **66**, 51 (1978).
- [225] J. Reichel, F. Bardou, M. B. Dahan, E. Peik, S. Rand, C. Salomon, and C. Cohen-Tannoudji, Raman cooling of cesium below 3 nk: New approach inspired by Lévy flight statistics, *Phys. Rev. Lett.* **75**, 4575 (1995).
- [226] F. Bardou, J. P. Bouchaud, A. Aspect, and C. C. Tannoudji, *Lévy Statistics and Laser Cooling* (Cambridge University Press, Cambridge, 2002).
- [227] L. A. Clark, A. Stokes, and A. Beige, Quantum-enhanced metrology with the single-mode coherent states of an optical cavity inside a quantum feedback loop, *Phys. Rev. A* **94**, 023840 (2016).
- [228] D. Ha and Y. Kwon, Complete analysis for three-qubit mixed-state discrimination, *Phys. Rev. A* **87**, 062302 (2013).
- [229] M. Rosati, G. De Palma, A. Mari, and V. Giovannetti, Optimal quantum state discrimination via nested binary measurements, *Phys. Rev. A* **95**, 042307 (2017).
- [230] C. W. Helstrom, J. W. S. Liu, and J. P. Gordon, Quantum-mechanical communication theory, *Proceedings of the IEEE* **58**, 1578 (1970).
- [231] E. Davies, Information and quantum measurement, *IEEE Transactions on Information Theory* **24**, 596 (1978).
- [232] A. Peres and D. R. Terno, Optimal distinction between non-orthogonal quantum states, *Journal of Physics A: Mathematical and General* **31**, 7105 (1998).
- [233] K. M. R. Audenaert, J. Calsamiglia, R. Muñoz Tapia, E. Bagan, L. Masanes, A. Acín, and F. Verstraete, Discriminating states: the quantum Chernoff bound, *Phys. Rev. Lett.* **98**, 160501 (2007).
- [234] K. Li, Discriminating quantum states: the multiple Chernoff distance, *The Annals of Statistics* **44**, 1661 (2016).

- [235] L. Vandenberghe and S. Boyd, Semidefinite programming, *SIAM review* **38**, 49 (1996).
- [236] J. Bae and W.-Y. Hwang, Minimum-error discrimination of qubit states: Methods, solutions, and properties, *Phys. Rev. A* **87**, 012334 (2013).
- [237] Y. C. Eldar, A. Megretski, and G. C. Verghese, Designing optimal quantum detectors via semidefinite programming, *IEEE Transactions on Information Theory* **49**, 1007 (2003), ISSN 0018-9448.
- [238] M. Grant and S. Boyd, CVX: Matlab software for disciplined convex programming, version 2.1, <http://cvxr.com/cvx> (2014).
- [239] M. Grant and S. Boyd, Graph implementations for nonsmooth convex programs, in *Recent Advances in Learning and Control*, edited by V. Blondel, S. Boyd, and H. Kimura (Springer-Verlag Limited, 2008), Lecture Notes in Control and Information Sciences, pp. 95–110, [http://stanford.edu/~boyd/graph\\_dcp.html](http://stanford.edu/~boyd/graph_dcp.html).
- [240] N. Ohlsson, R. K. Mohan, and S. Kröll, Quantum computer hardware based on rare-earth-ion-doped inorganic crystals, *Optics Communications* **201**, 71 (2002).
- [241] J. H. Wesenberg, K. Mølmer, L. Rippe, and S. Kröll, Scalable designs for quantum computing with rare-earth-ion-doped crystals, *Phys. Rev. A* **75**, 012304 (2007).
- [242] J. D. Jackson, *Classical electrodynamics* (John Wiley & Sons, 2007).
- [243] F. R. Graf, A. Renn, U. P. Wild, and M. Mitsunaga, Site interference in Stark-modulated photon echoes, *Phys. Rev. B* **55**, 11225 (1997).
- [244] R. L. Ahlefeldt, W. D. Hutchison, and M. J. Sellars, Characterisation of  $\text{EuCl}_3 \cdot 6\text{H}_2\text{O}$  for multi-qubit quantum processing, in *Quantum Electronics Conference & Lasers and Electro-Optics (CLEO/IQEC/PACIFIC RIM), 2011* (IEEE, 2011), pp. 1791–1793.
- [245] D. Jaksch, J. I. Cirac, P. Zoller, S. L. Rolston, R. Côté, and M. D. Lukin, Fast quantum gates for neutral atoms, *Phys. Rev. Lett.* **85**, 2208 (2000).
- [246] L. Childress, M. V. G. Dutt, J. M. Taylor, A. S. Zibrov, F. Jelezko, J. Wrachtrup, P. R. Hemmer, and M. D. Lukin, Coherent dynamics of coupled electron and nuclear spin qubits in diamond, *Science* **314**, 281 (2006).
- [247] J. R. Maze, J. M. Taylor, and M. D. Lukin, Electron spin decoherence of single nitrogen-vacancy defects in diamond, *Phys. Rev. B* **78**, 094303 (2008).
- [248] T. H. Taminiau, J. J. T. Wagenaar, T. van der Sar, F. Jelezko, V. V. Dobrovitski, and R. Hanson, Detection and control of individual nuclear spins using a weakly coupled electron spin, *Phys. Rev. Lett.* **109**, 137602 (2012).
- [249] N. Zhao, J. Honert, B. Schmid, M. Klas, J. Isoya, M. Markham, D. Twitchen, F. Jelezko, R.-B. Liu, H. Fedder, et al., Sensing single remote nuclear spins, *Nat. Nanotechnol.* **7**, 657 (2012).
- [250] F. Albarelli, M. A. C. Rossi, D. Tamascelli, and M. G. Genoni, Restoring Heisenberg scaling in noisy quantum metrology by monitoring the environment, arXiv preprint arXiv:1803.05891 (2018).
- [251] G. T. Foster, L. A. Orozco, H. M. Castro-Beltran, and H. J. Carmichael, Quantum state reduction and conditional time evolution of wave-particle correlations in cavity QED, *Phys. Rev. Lett.* **85**, 3149 (2000).
- [252] S. Gerber, D. Rotter, L. Slodička, J. Eschner, H. J. Carmichael, and R. Blatt, Intensity-field correlation of single-atom resonance fluorescence, *Phys. Rev. Lett.* **102**, 183601 (2009).

- [253] L. Zhang, H. B. Coldenstrodtt-Ronge, A. Datta, G. Puentes, J. S. Lundeen, X.-M. Jin, B. J. Smith, M. B. Plenio, and I. A. Walmsley, Mapping coherence in measurement via full quantum tomography of a hybrid optical detector, *Nat. Photonics* **6**, 364 (2012).
- [254] F. Verstraete, A. C. Doherty, and H. Mabuchi, Sensitivity optimization in quantum parameter estimation, *Phys. Rev. A* **64**, 032111 (2001).
- [255] H. M. Wiseman, Adaptive phase measurements of optical modes: Going beyond the marginal  $q$  distribution, *Phys. Rev. Lett.* **75**, 4587 (1995).
- [256] M. Brunelli, S. Olivares, and M. G. A. Paris, Qubit thermometry for micromechanical resonators, *Phys. Rev. A* **84**, 032105 (2011).
- [257] J. Dittmann, On the Riemannian geometry of finite dimensional mixed states, in *Seminar Sophus Lie* (1993), vol. 3, pp. 73–87.
- [258] U. L. Andersen, T. Gehring, C. Marquardt, and G. Leuchs, 30 years of squeezed light generation, *Physica Scripta* **91**, 053001 (2016).
- [259] T. Eberle, S. Steinlechner, J. Bauchrowitz, V. Händchen, H. Vahlbruch, M. Mehmet, H. Müller-Ebhardt, and R. Schnabel, Quantum enhancement of the zero-area Sagnac interferometer topology for gravitational wave detection, *Phys. Rev. Lett.* **104**, 251102 (2010).
- [260] B. Yurke, P. G. Kaminsky, E. A. Whittaker, A. D. Smith, A. H. Silver, and R. W. Simon, Squeezing thermal microwave radiation, in *Squeezed and nonclassical light* (Springer, 1989), pp. 57–71.
- [261] X. Zhou, V. Schmitt, P. Bertet, D. Vion, W. Wustmann, V. Shumeiko, and D. Esteve, High-gain weakly nonlinear flux-modulated Josephson parametric amplifier using a SQUID array, *Phys. Rev. B* **89**, 214517 (2014).
- [262] H. Nha and H. J. Carmichael, Proposed test of quantum nonlocality for continuous variables, *Phys. Rev. Lett.* **93**, 020401 (2004).
- [263] S. L. Braunstein and H. J. Kimble, Teleportation of continuous quantum variables, *Phys. Rev. Lett.* **80**, 869 (1998).
- [264] A. Furusawa, J. L. Sørensen, S. L. Braunstein, C. A. Fuchs, H. J. Kimble, and E. S. Polzik, Unconditional quantum teleportation, *Science* **282**, 706 (1998).
- [265] S. L. Braunstein and P. van Loock, Quantum information with continuous variables, *Rev. Mod. Phys.* **77**, 513 (2005).
- [266] A. Bienfait, J. J. Pla, Y. Kubo, M. Stern, X. Zhou, C. C. Lo, C. D. Weis, T. Schenkel, M. L. W. Thewalt, D. E. D. Vion, et al., Reaching the quantum limit of sensitivity in electron spin resonance, *Nat. Nanotechnol.* **11**, 253 (2016).
- [267] A. Schweiger and G. Jeschke, *Principles of pulse electron paramagnetic resonance* (Oxford University Press, New York, 2001).
- [268] R. Movshovich, B. Yurke, P. G. Kaminsky, A. D. Smith, A. H. Silver, R. W. Simon, and M. V. Schneider, Observation of zero-point noise squeezing via a Josephson-parametric amplifier, *Phys. Rev. Lett.* **65**, 1419 (1990).
- [269] F. Mallet, M. A. Castellanos-Beltran, H. S. Ku, S. Glancy, E. Knill, K. D. Irwin, G. C. Hilton, L. R. Vale, and K. W. Lehnert, Quantum state tomography of an itinerant squeezed microwave field, *Phys. Rev. Lett.* **106**, 220502 (2011).
- [270] N. Didier, A. Kamal, W. D. Oliver, A. Blais, and A. A. Clerk, Heisenberg-limited qubit read-out with two-mode squeezed light, *Phys. Rev. Lett.* **115**, 093604 (2015).

- [271] N. Didier, J. Bourassa, and A. Blais, Fast quantum nondemolition readout by parametric modulation of longitudinal qubit-oscillator interaction, *Phys. Rev. Lett.* **115**, 203601 (2015).
- [272] A. Eddins, S. Schreppler, D. M. Toyli, L. S. Martin, S. Hacothen-Gourgy, L. C. G. Govia, H. Ribeiro, A. A. Clerk, and I. Siddiqi, Stroboscopic qubit measurement with squeezed illumination, *Phys. Rev. Lett.* **120**, 040505 (2018).
- [273] L. C. G. Govia and A. A. Clerk, Enhanced qubit readout using locally generated squeezing and inbuilt Purcell-decay suppression, *New J. of Phys.* **19**, 023044 (2017).
- [274] M. A. Castellanos-Beltran and K. W. Lehnert, Widely tunable parametric amplifier based on a superconducting quantum interference device array resonator, *Appl. Phys. Lett.* **91**, 083509 (2007).
- [275] N. Bergeal, F. Schackert, M. Metcalfe, R. Vijay, V. E. Manucharyan, L. Frunzio, D. E. Prober, R. J. Schoelkopf, S. M. Girvin, and M. H. Devoret, Phase-preserving amplification near the quantum limit with a Josephson ring modulator, *Nature* **465**, 64 (2010).
- [276] C. Macklin, K. O'Brien, D. Hover, M. E. Schwartz, V. Bolkhovskiy, X. Zhang, W. D. Oliver, and I. Siddiqi, A near-quantum-limited Josephson traveling-wave parametric amplifier, *Science* **350**, 307 (2015).
- [277] M. H. Devoret and R. J. Schoelkopf, Superconducting circuits for quantum information: an outlook, *Science* **339**, 1169 (2013).
- [278] C. W. Gardiner and M. J. Collett, Input and output in damped quantum systems: Quantum stochastic differential equations and the master equation, *Phys. Rev. A* **31**, 3761 (1985).
- [279] A. Bienfait, Magnetic Resonance with Quantum Microwaves, PhD thesis, Université Paris-Saclay (2016).
- [280] W. Wustmann and V. Shumeiko, Parametric resonance in tunable superconducting cavities, *Phys. Rev. B* **87**, 184501 (2013).
- [281] S. Boutin, D. M. Toyli, A. V. Venkatramani, A. W. Eddins, I. Siddiqi, and A. Blais, Effect of higher-order nonlinearities on amplification and squeezing in Josephson parametric amplifiers, *Phys. Rev. Applied* **8**, 054030 (2017).
- [282] G. Wolfowicz, A. M. Tyryshkin, R. E. George, H. Riemann, N. V. Abrosimov, P. Becker, H.-J. Pohl, M. L. W. Thewalt, S. A. Lyon, and J. J. L. Morton, Atomic clock transitions in silicon-based spin qubits, *Nature nanotechnology* **8**, 561 (2013).
- [283] C. D. Weis, C. C. Lo, V. Lang, A. M. Tyryshkin, R. E. George, K. M. Yu, J. Bokor, S. A. Lyon, J. J. L. Morton, and T. Schenkel, Electrical activation and electron spin resonance measurements of implanted bismuth in isotopically enriched silicon-28, *Appl. Phys. Lett.* **100**, 172104 (2012).
- [284] J. J. Pla, A. Bienfait, G. Pica, J. Mansir, F. A. Mohiyaddin, Z. Zeng, Y. M. Niquet, A. Morello, T. Schenkel, J. J. L. Morton, et al., Strain-induced spin-resonance shifts in silicon devices, *Phys. Rev. Applied* **9**, 044014 (2018).
- [285] J. Y. Mutus, T. C. White, R. Barends, Y. Chen, Z. Chen, B. Chiaro, A. Dunsworth, E. Jeffrey, J. Kelly, A. Megrant, et al., Strong environmental coupling in a Josephson parametric amplifier, *Appl. Phys. Lett.* **104**, 263513 (2014).
- [286] T. Roy, S. Kundu, M. Chand, A. M. Vadiraj, A. Ranadive, N. Nehra, M. P. Patankar, J. Aumentado, A. A. Clerk, and R. Vijay, Broadband parametric

- amplification with impedance engineering: Beyond the gain-bandwidth product, *Appl. Phys. Lett.* **107**, 262601 (2015).
- [287] T. Sleator, E. L. Hahn, C. Hilbert, and J. Clarke, Nuclear-spin noise, *Phys. Rev. Lett.* **55**, 1742 (1985).
- [288] D. M. Toyli, A. W. Eddins, S. Boutin, S. Puri, D. Hover, V. Bolkhovsky, W. D. Oliver, A. Blais, and I. Siddiqi, Resonance fluorescence from an artificial atom in squeezed vacuum, *Phys. Rev. X* **6**, 031004 (2016).
- [289] A. M. Tyryshkin, S. Tojo, J. J. L. Morton, H. Riemann, N. V. Abrosimov, P. Becker, H.-J. Pohl, T. Schenkel, M. L. W. Thewalt, K. M. Itoh, et al., Electron spin coherence exceeding seconds in high-purity silicon, *Nature materials* **11**, 143 (2012).
- [290] K. W. Murch, S. J. Weber, K. M. Beck, E. Ginossar, and I. Siddiqi, Reduction of the radiative decay of atomic coherence in squeezed vacuum, *Nature* **499**, 62 (2013).
- [291] H. J. Carmichael, A. S. Lane, and D. F. Walls, Resonance fluorescence from an atom in a squeezed vacuum, *Phys. Rev. Lett.* **58**, 2539 (1987).
- [292] J. I. Cirac, Interaction of a two-level atom with a cavity mode in the bad-cavity limit, *Phys. Rev. A* **46**, 4354 (1992).
- [293] B. J. Dalton, Z. Ficek, and S. Swain, Atoms in squeezed light fields, *Journal of Modern Optics* **46**, 379 (1999).
- [294] G. M. Palma and P. L. Knight, Phase-sensitive population decay: The two-atom Dicke model in a broadband squeezed vacuum, *Phys. Rev. A* **39**, 1962 (1989).
- [295] G. S. Agarwal and R. R. Puri, Cooperative behavior of atoms irradiated by broadband squeezed light, *Phys. Rev. A* **41**, 3782 (1990).
- [296] M. Xu, D. A. Tieri, and M. J. Holland, Simulating open quantum systems by applying SU(4) to quantum master equations, *Phys. Rev. A* **87**, 062101 (2013).
- [297] M. Tavis and F. W. Cummings, Exact solution for an  $N$ -molecule—radiation-field Hamiltonian, *Phys. Rev.* **170**, 379 (1968).
- [298] J. Dalibard, J. Dupont-Roc, and C. Cohen-Tannoudji, Vacuum fluctuations and radiation reaction: identification of their respective contributions, *Journal de Physique* **43**, 1617 (1982).
- [299] D. Meschede, W. Jhe, and E. A. Hinds, Radiative properties of atoms near a conducting plane: An old problem in a new light, *Phys. Rev. A* **41**, 1587 (1990).
- [300] J. M. Radcliffe, Some properties of coherent spin states, *Journal of Physics A: General Physics* **4**, 313 (1971).
- [301] L. Vernac, M. Pinard, V. Josse, and E. Giacobino, Collective atomic spin squeezing and control, *Eur. Phys. J. D* **18**, 129 (2002).
- [302] A. S. Shumovsky and T. Quang, Spectral and statistical properties of collective resonance fluorescence in a squeezed vacuum, *Journal of Physics B: Atomic, Molecular and Optical Physics* **22**, 131 (1989).
- [303] T. Quang, M. Koziarowski, and L. H. Lan, Collective resonance fluorescence in a squeezed vacuum, *Phys. Rev. A* **39**, 644 (1989).
- [304] J. Cirac and L. Sánchez-Soto, Collective resonance fluorescence in a strongly squeezed vacuum, *Optics Communications* **77**, 26 (1990).
- [305] H. Wu, R. E. George, J. H. Wesenberg, K. Mølmer, D. I. Schuster, R. J. Schoelkopf, K. M. Itoh, A. Ardavan, J. J. L. Morton, and G. A. D. Briggs, Storage of multiple

- coherent microwave excitations in an electron spin ensemble, *Phys. Rev. Lett.* **105**, 140503 (2010).
- [306] Y. Kubo, I. Diniz, A. Dewes, V. Jacques, A. Dréau, J.-F. Roch, A. Auffeves, D. Vion, D. Esteve, and P. Bertet, Storage and retrieval of a microwave field in a spin ensemble, *Phys. Rev. A* **85**, 012333 (2012).
  - [307] C. Grezes, B. Julsgaard, Y. Kubo, M. Stern, T. Umeda, J. Isoya, H. Sumiya, H. Abe, S. Onoda, T. Ohshima, et al., Multimode storage and retrieval of microwave fields in a spin ensemble, *Phys. Rev. X* **4**, 021049 (2014).
  - [308] M. Lovrić, D. Suter, A. Ferrier, and P. Goldner, Faithful solid state optical memory with dynamically decoupled spin wave storage, *Phys. Rev. Lett.* **111**, 020503 (2013).
  - [309] P. Jobez, C. Laplane, N. Timoney, N. Gisin, A. Ferrier, P. Goldner, and M. Afzelius, Coherent spin control at the quantum level in an ensemble-based optical memory, *Phys. Rev. Lett.* **114**, 230502 (2015).
  - [310] A. I. Lvovsky, B. C. Sanders, and W. Tittel, Optical quantum memory, *Nat. Photon.* **3**, 706 (2009).
  - [311] A. Imamoglu, D. D. Awschalom, G. Burkard, D. P. DiVincenzo, D. Loss, M. Sherwin, and A. Small, Quantum information processing using quantum dot spins and cavity QED, *Phys. Rev. Lett.* **83**, 4204 (1999).
  - [312] K. R. Motes, B. Q. Baragiola, A. Gilchrist, and N. C. Menicucci, Encoding qubits into oscillators with atomic ensembles and squeezed light, *Phys. Rev. A* **95**, 053819 (2017).
  - [313] J. G. Bohnet, A superradiant laser and spin squeezed states: Collective phenomena in a rubidium cavity QED system for enhancing precision measurements, PhD thesis, University of Colorado at Boulder (2014).
  - [314] A. Yoshimi, K. Asahi, K. Sakai, M. Tsuda, K. Yogo, H. Ogawa, T. Suzuki, and M. Nagakura, Nuclear spin maser with an artificial feedback mechanism, *Physics Letters A* **304**, 13 (2002).
  - [315] A. Apellaniz, Lower bounds on quantum metrological precision, PhD thesis, University of the Basque Country (2017).
  - [316] J. Ma, X. Wang, C. P. Sun, and F. Nori, Quantum spin squeezing, *Physics Reports* **509**, 89 (2011).
  - [317] V. V. Temnov and U. Woggon, Superradiance and subradiance in an inhomogeneously broadened ensemble of two-level systems coupled to a low- $q$  cavity, *Phys. Rev. Lett.* **95**, 243602 (2005).
  - [318] D. Meiser and M. J. Holland, Steady-state superradiance with alkaline-earth-metal atoms, *Phys. Rev. A* **81**, 033847 (2010).
  - [319] M. A. Norcia and J. K. Thompson, Cold-strontium laser in the superradiant crossover regime, *Phys. Rev. X* **6**, 011025 (2016).
  - [320] D. A. Tieri, M. Xu, D. Meiser, J. Cooper, and M. J. Holland, Theory of the crossover from lasing to steady state superradiance, arXiv:1702.04830 (2017).
  - [321] M. Gross and S. Haroche, Superradiance: An essay on the theory of collective spontaneous emission, *Physics reports* **93**, 301 (1982).
  - [322] M. M. Rams, P. Sierant, O. Dutta, P. Horodecki, and J. Zakrzewski, At the limits of criticality-based quantum metrology: Apparent super-Heisenberg scaling revisited, *Phys. Rev. X* **8**, 021022 (2018).

- [323] U. Schollwöck, The density-matrix renormalization group in the age of matrix product states, *Annals of Physics* **326**, 96 (2011).
- [324] S. Gammelmark and K. Mølmer, Simulating local measurements on a quantum many-body system with stochastic matrix product states, *Phys. Rev. A* **81**, 012120 (2010).
- [325] H. Zhang, C.-X. Liu, X.-L. Qi, X. Dai, Z. Fang, and S.-C. Zhang, Topological insulators in  $\text{Bi}_2\text{Se}_3$ ,  $\text{Bi}_2\text{Te}_3$  and  $\text{Sb}_2\text{Te}_3$  with a single Dirac cone on the surface, *Nat. Phys.* **5**, 438 (2009).
- [326] A. De Pasquale, D. Rossini, P. Facchi, and V. Giovannetti, Quantum parameter estimation affected by unitary disturbance, *Phys. Rev. A* **88**, 052117 (2013).
- [327] R. J. Glauber, The quantum theory of optical coherence, *Phys. Rev.* **130**, 2529 (1963).
- [328] G. Weiss, *Random Walk Theory and Applications* (North-Holland, Amsterdam, 2010).
- [329] E. Cinlar, Markov renewal theory, *Advances in Applied Probability* **1**, 123 (1969).